New methods for high resolution 3D imaging with X-rays

Dissertation

zur Erlangung des akademischen Grades

doctor rerum naturalium

(Dr. rer. nat.)

im Fach Physik

eingereicht an der

Mathematisch-Naturwissenschaftlichen Fakultät

der Humboldt-Universität zu Berlin

von

Christoph Pratsch

Präsidentin der Humboldt-Universität zu Berlin

Prof. Dr.-Ing. Dr. Sabine Kunst

Dekan der Mathematisch-Naturwissenschaftlichen Fakultät

Prof. Dr. Elmar Kulke

Gutachter/innen: 1. Prof. Dr. Gerd Schneider

2. Prof. Dr. Günter Schmahl
3. Prof. Dr. Christoph Koch

Tag der mündlichen Prüfung: 22.09.2017

Contents

List of Figures

Abstract

X-ray imaging offers a large penetration depth, good element contrast and short wavelength. This unique combination enables imaging of thick samples at high resolution, thus bridging the current gap between optical microscopy and electron microscopy. As a result, X-ray imaging has become an extremely valuable tool for many applications in life and materials sciences.

Among the X-ray imaging methods, 3D X-ray microscopy based on nanoscale soft X-ray tomography has to date found the widest application, most notably in the life sciences. However, the principles of tomographic reconstruction based on linear projection are already violated for most biological cells, since their thickness exceeds the depth of focus of current zone plate objectives. This problem only worsens as the lateral resolution of zone plate objectives improve to 10 nm. To understand the effect of the limited depth of focus on tomographic reconstructions, we have investigated the imaging process in the X-ray microscope using a 3D cell phantom. We find that only a sub-region of the phantom lying within the depth of field is resolved at the resolution given by the X-ray objective, whereas phantom structures outside of this region are increasingly blurred. Furthermore, consistent with experimental observations of real specimens, we find that the obtainable 3D resolution for soft X-ray tomography of biological specimens is limited to about 30 nm. For some applications this 3D resolution is insufficient, and moreover in many cases specimen thickness exceeds the depth of focus thereby reducing the resolution outside of the specimen's central region. As a consequence, in this thesis we have used the 3D phantom to investigate the performance of alternative 3D nanoscale X-ray imaging methods in order to provide guidance for future developments in X-ray microscopy.

In light microscopy, the confocal principle is an established method for 3D optical sectioning. Here we have investigated the 3D resolution performance of its X-ray counterpart, the confocal scanning transmission soft X-ray microscope. In confocal light microscopy, image formation includes an incoherent process due to fluorescent light emission from the specimen. As a result, the 3D resolution for an infinitely small detector is given by the square of the point spread function of the objective. In contrast, in confocal X-ray microscopy, the interaction of X-rays with the object leads to an attenuation and phase shift of the incident wave. As a result, image formation in the X-ray confocal microscope must be based on the wave propagation of coherent X-rays. Here we simulate the X-ray confocal microscope assuming a zone plate objective with 10 nm lateral resolution. We show that this confocal setup achieves a lateral resolution comparable to that obtained for the transmission soft X-ray microscope. However, the depth resolution is significantly worse yielding only 300 nm. Although this poorer depth resolution degrades the overall 3D resolution performance of the confocal X-ray microscope, the confocal

approach has the advantage that it is a direct imaging method without the need for the complex computational algorithms currently required for the tomographic reconstructions of the transmission X-ray microscope. Nevertheless, we conclude that the confocal X-ray microscope is not superior to the current soft X-ray tomography approach, at least with current X-ray objectives that yield only low depth resolution.

In this thesis, we also investigate another completely new approach to 3D X-ray imaging that is based on scanning X-ray microscopy combined with focused ion beam milling, which we term FIB-SXM (Focused Ion Beam – Scanning X-ray Microscopy). In FIB-SXM, a high resolution Fresnel zone plate generates a nanoscale focal spot that is scanned over the surface of the object. At each scanned spot, photoelectrons are emitted from the object in proportion to the local absorption coefficients at that location. The surface scan therefore yields the image of the top layer of the specimen to a depth corresponding to the escape depth of the electrons. To generate 3D data, a focused ion beam is then used to remove the surface layer, and then the spot scan is repeated at the new surface. Iteration of milling and scanning therefore builds up a 3D image stack in the slice and view mode. In this thesis, we have evaluated the 3D resolution performance of FIB-SXM by simulating the image formation process. We show that FIB-SXM can achieve an isotropic resolution of 10 nm due to the short escape length (< 10 nm) of the emitted electrons and the small size of the focal spot. Surprisingly, we also find that FIB-SXM, by virtue of its electron detection mode, can operate at a dose three orders of magnitude lower than any transmission technique. Thus FIB-SXM offers high isotropic resolution at significantly lower dose, and as such overcomes severe limitations of all current transmission methods for 3D X-ray imaging.

Another limitation of current soft X-ray microscopy methods is time resolution. Although free electron lasers (FELs) provide short X-ray pulses with femtosecond resolution, imaging with these short coherent X-ray pulses is very challenging. In this thesis, we propose a new holography approach based on Fourier transform holography and novel diffractive optical elements. Our method differs from previous soft X-ray Fourier transform holography approaches by using a diffractive optical element to generate the illumination of both the sample and the reference. The main advantages of the new method are its fast imaging, extended field of view and its decoupling of optics and sample. To investigate the resolution performance of the new method we perform both theoretical calculations and proof of concept experiments using synchrotron light from BESSY II. Our experimental and theoretical results reveal the potential of this holography method for future imaging experiments at FELs.

Finally, for all lens-based soft X-ray imaging experiments, it is critical to understand the imaging performance of Fresnel zone plates. While effects of systematic

zone positioning errors have been known for a long time, the effects of random zone-positioning errors have remained unclear. Zone plates are mainly produced by electron beam lithography and planar etching techniques. For hard X-rays, an alternative zone plate fabrication approach is based on alternately coating a micro-wire with two different materials. With this process, very thin zone layers with very high aspect ratios can be deposited. However, depending on the fabrication method, random zone positioning errors may introduce strong aberrations. To understand these effects, we studied the effects of positioning errors on zone plate resolution using different random fluctuations. We found that random errors significantly decreased the contrast transfer of X-ray microscopes. We also determined an upper bound for the mean acceptable variance of the zone-plate deposition rate.

In summary, we have characterized the limitations of the most powerful and widely used 3D X-ray imaging approach, transmission X-ray microscopy with tomographic reconstruction. We show that 3D resolution in this approach is limited by the depth of field. To investigate alternatives, we perform simulations of a confocal transmission X-ray microscope and a FIB-SXM. We show that FIB-SXM is a very promising approach that could offer 3D isotropic resolution at 10 nm with dramatically improved signal to noise. We also introduce a new holography method that could prove beneficial for full field imaging with short coherent X-ray pulses and yield new insights into ultrafast physics.

Zusammenfassung

Die Vorteile der Röntgenmikroskopie bestehen darin, dass Röntgenlicht eine hohe Eindringtiefe, einen guten Elementkontrast und eine kurze Wellenlänge aufweist. Diese einzigartige Kombination ermöglicht die Abbildung von dicken Proben mit hoher Auflösung und überbrückt so die Lücke zwischen der optischen Mikroskopie und der Elektronenmikroskopie. Damit haben sich röntgenbasierte Mikroskopiemethoden zu einem äußerst wertvollen Werkzeug für viele Anwendungen in den Material- und Lebenswissenschaften entwickelt.

Unter den röntgenbasierten, bildgebenden Verfahren hat die 3D-Röntgenmikroskopie auf Basis der Röntgentomographie bislang, vor allem in der Biologie, die breiteste Anwendung gefunden. Allerdings sind die Prinzipien der tomographischen Rekonstruktion, die auf der linearen Projektion beruhen, bereits für die meisten biologischen Zellen verletzt, da deren Dicke die Schärfentiefe der gegenwärtigen Zonenplatten übersteigt. Dieses Problem verschärft sich, wenn man die laterale Auflösung der Zonenplattenobjektive auf 10 nm erhöht. Um den Effekt der begrenzten Schärfentiefe auf die tomographischen Rekonstruktionen zu verstehen, haben wir die Bildentstehung im Röntgenmikroskop auf Basis eines 3D-Zellphantoms untersucht. Wir fanden, dass nur ein Teilbereich des Phantoms, welcher innerhalb der Schärfentiefe liegt, mit der Auflösung des Röntgenobjektivs aufgelöst wird. Mit zunehmender Entfernung von diesem Bereich, werden die Phantomstrukturen zunehmend verschwommener abgebildet. In Übereinstimmung mit experimentellen Beobachtungen an realen Proben haben wir weiterhin festgestellt, dass die erzielbare 3D-Auflösung für die weiche Röntgentomographie für biologischen Proben auf etwa 30 nm begrenzt ist. Für manche Anwendungen ist diese 3D-Auflösung unzureichend. Zusätzlich übersteigt die Probendicke in vielen Fällen die Schärfentiefe, wodurch die Auflösung außerhalb des zentralen Bereichs der Probe zusätzlich verringert wird. Daher haben wir in dieser Arbeit das 3D-Phantom verwendet, um die Leistung von alternativen röntgenbasierten, 3D-bildgebenden Verfahren zu untersuchen. Diese Untersuchungen geben uns eine Orientierung für zukünftige Entwicklungen.

In der Lichtmikroskopie ist das konfokale Prinzip eine etablierte 3D-Bildgebungsmethode. In dieser Arbeit haben wir das röntgenbasierte Gegenstück, die konfokale Rastermikroskopie mit weicher Röntgenstrahlung, auf die erzielbare 3D-Auflösung untersucht. Bei der konfokalen Lichtmikroskopie enthält die Bildentstehung einen inkohärenten Prozess aufgrund der Fluoreszenz der Probe. Daraus resultierend ergibt sich die 3D-Auflösung für einen unendlich kleinen Detektor durch das Quadrat der Punktspreizfunktion des Objektivs. Im Gegensatz dazu führt bei der konfokalen Röntgenmikroskopie die Wechselwirkung von Röntgenstrahlen mit dem Objekt zu einer Dämpfung und Phasenverschiebung der einfallenden Welle. Folglich muss die Bildentstehung im konfokalen Röntgenmikroskop

auf der Wellenausbreitung kohärenter Röntgenstrahlen basieren. Hier simulieren wir das konfokale Röntgenmikroskop unter der Annahme eines Zonenplattenobjektivs mit 10 nm lateraler Auflösung. Wir zeigen, dass dieser konfokale Aufbau eine laterale Auflösung erreicht, die mit der des konventionellen transmissionsbasierten Röntgenmikroskops vergleichbar ist. Allerdings beträgt die Tiefenauflösung lediglich 300 nm. Obwohl diese schlechtere Tiefenauflösung die 3D-Auflösung des konfokalen Röntgenmikroskops verschlechtert, hat der konfokale Ansatz den Vorteil, dass es sich um ein direktes Abbildungsverfahren handelt, welches ohne komplexe Algorithmen auskommt. Tomographische Rekonstruktionen hingegen erfordern einen hohen Rechenaufwand und eine komplexe Vorbereitung der Daten. Trotzdem ist das konfokale Röntgenmikroskop dem heutigen weichen röntgenbasierten Tomographieansatz unterlegen, zumindest mit aktuellen Röntgenobjektiven, die nur eine geringe Tiefenauflösung aufweisen.

In dieser Arbeit untersuchen wir auch einen weiteren, völlig neuen Ansatz für ein röntgenbasiertes, bildgebendes Verfahren, der auf einer Kombination aus Rasterröntgenmikroskopie und fokussiertem Ionenstrahlfräsen basiert. Dieser Ansatz wird hier als FIB-SXM (Focused Ion Beam Scanning X-ray Microscopy) bezeichnet. Bei der FIB-SXM erzeugt eine hochauflösende Fresnel-Zonenplatte einen Brennfleck im Nanometerbereich, der über die Oberfläche des Objekts gescannt wird. An jedem abgetasteten Punkt werden Photoelektronen vom Objekt in Abhängigkeit von den lokalen Absorptionskoeffizienten an dieser Stelle emittiert. Die Oberflächenabtastung ergibt daher das Bild der oberen Schicht der Probe bis zu einer Tiefe, die der Austrittstiefe der Elektronen entspricht. Um 3D-Daten zu erhalten, wird dann ein fokussierter Ionenstrahl verwendet, um die Oberflächenschicht zu entfernen. Die neu entstandende Oberfläche wird erneut mit dem Brennfleck abgescannt. Iterationen von Fräsen und Scannen bauen so einen 3D-Bildstapel im Slice- und View-Modus auf. In dieser Arbeit haben wir die erreichbare 3D-Auflösung für FIB-SXM durch Simulation der an der Bildentstehung beteiligten Prozesse simuliert. Wir zeigen, dass FIB-SXM aufgrund der kurzen Austrittslänge ($<$10 nm) der emittierten Elektronen und der geringen Größe des Brennflecks sowie der hohen Präzision Fräsvorgangs eine isotrope Auflösung von 10 nm erreichen kann. Überraschenderweise finden wir auch, dass FIB-SXM aufgrund seines Elektronenerfassungsmodus bei einer drei Größenordnungen niedrigeren Dosis arbeiten kann als röntgenbasierte Transmissionsmethoden. Somit bietet FIB-SXM eine hohe isotrope Auflösung bei einer signifikant niedrigeren Dosis und überwindet so eine der stärksten Beschränkungen aller gängigen röntgenbasierten Transmissionsverfahren für die 3D-Bildgebung.

Eine weitere Einschränkung der derzeitigen Mikroskopieverfahren im weichen Röntgenbereich ist die Zeitauflösung. Obwohl freie Elektronenlaser (FELs) kurze Röntgenpulse mit Femtosekundenauflösung bieten, ist die Abbildung mit diesen

kurzen, kohärenten Pulsen eine große Herausforderung. In dieser Arbeit schlagen wir einen neuen Holographieansatz vor, der auf der Basis der Fourier-Transformations-Holographie beruht. Unsere Methode unterscheidet sich von früheren Holographieansätzen durch die Verwendung eines diffraktiven optischen Elements, um die Beleuchtung sowohl der Probe als auch der Referenz zu erzeugen. Die Hauptvorteile der neuen Methode sind die schnelle Bildgebung, das erweiterte Sichtfeld und die Entkopplung von Optik und Probe. Um die Auflösung der neuen Methode zu untersuchen, führten wir sowohl theoretische Berechnungen als auch Experimente mit Synchrotronstrahlung von BESSY II durch. Unsere experimentellen und theoretischen Ergebnisse zeigen das Potential dieser Holographiemethode für zukünftige Experimente an FELs.

Für alle linsenbasierten, bildgebenden Experimente im Röntgenbereich ist es entscheidend, die Abbildungseigenschaften von Fresnel-Zonenplatten zu verstehen. Während die Auswirkungen von systematischen Zonenpositionierungsfehlern seit Langem bekannt sind, sind die Effekte von zufälligen Zonenpositionierungsfehlern unklar geblieben. Zonenplatten werden hauptsächlich durch Elektronenstrahllithographie und planare Ätztechniken hergestellt. Für harte Röntgenstrahlen beruht ein alternativer Zonenplattenherstellungsansatz darauf, abwechselnd einen Mikrodraht mit zwei verschiedenen Materialien zu beschichten. Mit diesem Verfahren können sehr dünne Zonenschichten mit sehr hohen Aspektverhältnissen abgeschieden werden. Abhängig von dem Herstellungsverfahren können jedoch zufällige Zonenpositionierungsfehler zu starken Aberrationen führen. Um diese Effekte zu verstehen, untersuchten wir die Auswirkungen von Positionierungsfehlern auf das Auflösungsvermögen der Zonenplatten unter Verwendung unterschiedlicher zufälliger Fluktuationen. Wir fanden heraus, dass zufällige Fehler zu einer deutlichen Reduktion der Kontrastübertragung führen können. Wir haben auch eine obere Schranke für die mittlere akzeptierbare Varianz der Zonenabscheidungsrate bestimmt.

In der Arbeit haben wir die Grenzen der weit verbreiteten tomographischen Rekonstruktion von 3D-Proben mittels Transmissionsröntgenmikroskopie charakterisiert. Wir zeigen, dass die 3D-Auflösung mit diesem Ansatz durch die Schärfentiefe begrenzt ist. Zur Untersuchung von Alternativen führten wir Simulationen zur Bildentstehung in einem konfokalen Röntgenmikroskop und einem FIB-SXM durch. Wir zeigen, dass FIB-SXM ein vielversprechender Ansatz ist, der eine isotrope 3D-Auflösung um die 10 nm erreichen kann und zusätzlich ein drastisch verbessertes Signal-Rausch-Verhältnis bieten könnte. Wir stellen auch eine neue Holographiemethode vor, die sich für Vollfeldabbildungen mit kurzen kohärenten Röntgenpulsen als vorteilhaft erweisen und neue Einsichten in die ultraschnelle Physik liefern könnte.

Notation

Throughout the thesis, parentheses (()) are either used to indicate a new symbol without explicitly defining it, e. g. the electric field (E) or to group mathematical expressions, e. g. $2 \cdot (1 + 1) = 4$. Square brackets ([]) are used for arguments of functions, for closed intervals and citations, e. g. $\exp[0] = 1$, $1 \in [0, 1]$ or [51].

Nomenclature

dr_N	outermost zone width
CDI	coherent diffraction imaging
CSTXM	confocal scanning transmission X-ray microscope
DOE	diffractive optical element
DOF	depth of focus
ePIE	extended ptychography iterative engine
FEL	free electron laser
FFT	fast Fourier transform
FIB	focused ion beam
FIB-SXM	focused ion beam milling scanning X-ray microscope
FTH	Fourier transform holography
FWHM	full width half maximum
FZP	Fresnel zone plate
MTF	modulation transfer function
NA	numerical aperture
NFFA	wide-angle near and far field approximation
OSA	order sorting aperture
OTF	optical transfer function
PSF	(intensity/ amplitude) point spread function
rms	root mean square

SNR	signal to noise ratio
STXM	scanning transmission X-ray microscope
TXM	transmission X-ray microscope

Chapter 1

Introduction

Microscopes play an important role for industrial applications and natural science. In particular, microscopy has found many applications in life science, for example by studying diseases at the cellular level. In energy research, microscopy plays a crucial role for the development of efficient energy storage devices.

The first light microscopes were developed in the Netherlands around 1620. In 1873, Abbe noted that light microscopes are diffraction limited by the wavelength. Their best achievable resolution is about half of the wavelength of the light used. In practice, conventional light microscopes can only resolve structures of about a quarter micrometer. Although their resolution is limited, their easy usage and versatility make them the most commonly used type of microscopes. They have become valuable tools for biology, physics and materials science. This versatility is partly due to the efforts made to develop different contrast mechanisms. These variations of the light microscope enable the study of otherwise invisible samples. The different contrast methods include dark field, Zernike phase contrast and differential interference contrast microscopy.

Smaller structures than given by Abbe limit can be resolved by modern super-resolution methods. Photoactivated localization microscopy (PALM) [4] and stochastic optical reconstruction microscopy (STORM) [71] use statistic analysis of fluorescence signals to overcome the diffraction limit. Other super resolution methods such as stimulated emission depletion microscopy (STED) [37] and ground state depletion microscopy (GSD) [36] use non-linear excitation of fluorophores to increase the resolution. While in these super-resolution microscopes, the center of the fluorophores is determined with up to a precision of a few nanometers, the non-fluorescent cellular structures surrounding the fluorophores are not imaged.

In 1924, de Broglie published his hypothesis that matter exhibits a wave-like behavior. The transmission electron microscope (TEM) [47] makes use of the sig-

nificantly shorter de Broglie wavelength of electrons permitting atomic resolution. However, due to the strong inelastic scattering of the electrons in the sample, the resolution decreases with increased thickness of the sample. In practice, TEM applications are limited to sub-micrometer thin samples. Another form of electron microscopy is scanning electron microscopy (SEM). In SEM, a focused electron beam is raster scanned over the surface of a sample. The electron beam generates secondary and back-scattered electrons which carry information about the surface topology of the sample. Additionally, characteristic X-rays are also generated which can be used to analyze the elemental composition of the sample.

Similar to electrons, X-rays have significantly shorter wavelengths than visible light. Therefore, X-ray microscopes can potentially achieve very high resolution. In addition, X-rays have the advantage that they can penetrate thicker objects than electrons can. Furthermore, X-rays exhibit a stronger energy and material-dependent element contrast. This contrast is due to atomic inner-shell transitions. One energy range which is well suited for biological applications is the so-called water window between the K-absorption of carbon (283 eV) and oxygen (531 eV). Since cell structures mainly consist of carbon rich proteins embedded in water, they exhibit a strong natural element contrast in the water window [107]. Due to this contrast, cells can be studied at these energies without artificially staining their structures [77].

Microscopy Method	Resolutions 2D	Object thickness	Interaction / Contrast	Limitation
LM	$\approx$ 200 nm		absorption/ phase shift	wavelength
SI	$\approx$ 100 nm		fluorescence	wavelength
Super-resolution	$\approx$ 10 nm		fluorescence	SNR
TXM	10 nm	$<$10 µm	absorption/ phase shift	SNR/optics
TEM	$<$ 0.1 nm	$<$0. 5 µm	inelastic / elastic scattering	SNR
SEM	$<$ 1 nm	surface	surface information	sample
SNOM	$\approx$ 30 nm	surface	surface information	tip

Table 1.1: *Comparison of different microscopy methods. (Light microscopy (LM), structured illumination (SI), super-resolution methods, transmission X-ray microscopy (TXM), transmission electron microscopy (TEM), scanning electron microscopy (SEM) and scanning near field optical microscopy (SNOM).) Note that X-ray imaging offers a unique combination of high resolution and large object thickness.*

In table 1.1, different microscopy methods are compared with regard to their

resolution for typical biological samples. It is noteworthy that soft X-ray microscopy is almost ideally suited for studying the ultra-structure of cells since it combines high penetration depth, high 3D resolution and photon energy dependent object contrast. The combination of these three properties enables the imaging of whole cells in their almost natural state. Both soft X-ray microscopy and light microscopy can image whole cells. Therefore, X-ray imaging is also well suited for correlative light and X-ray microscopy. The correlative microscopy approach combines the information about the cellular ultra-structure obtained by soft X-ray imaging with functional properties imaged by fluorescence light microscopy [34, 82].

Over the last decades, various X-ray microscopy methods have been developed. One class of X-ray imaging techniques makes use of X-ray lenses. These so-called Fresnel zone plates were suggested for X-ray microscopy in the 1950s [58, 2] and first experiments were conducted in the 70s [75]. This class contains full field transmission soft X-ray microscopy (TXM) [77] and scanning soft X-ray transmission microscopy (STXM) [45, 60]. Both methods have found many applications in life and materials sciences. Currently, full field transmission soft X-ray microscopy generates the best images of whole cells. One of the main challenges in the development of lens based soft X-ray microscopy was that for this photon energy range (100 eV - 5 keV) the ratio between absorption and phase shift is too large to manufacture efficient refractive lenses. Therefore, soft X-ray microscopes use diffractive optics, the previously mentioned Fresnel zone plates. These optics are technically challenging to manufacture with high apertures (see chapter 8). In contrast to their refractive counterparts in light microscopy, Fresnel zone plates generate several focal spots which correspond to different orders of diffraction and the positions of these focal spots depends on the wavelength. In practice, Fresnel zone plates have an efficiency of 5 - 35 percent [64, 103], because the incident intensity is distributed into many orders of diffraction but only one order is used for imaging.

An alternative approach, namely lens-less X-ray imaging techniques, is based on Fraunhofer diffraction theory. These techniques recover the image of a sample from its far-field scattering signal [23, 20]. According to Fraunhofer diffraction theory, the far-field scattering pattern of a complex scalar wave is proportional to the Fourier transform of the wave. Since the scattering signal is directly detected, no lens is needed and theoretically the resolution should only depend on the aperture created by the propagation distance and the dimensions of the detector. However, X-ray detectors are only sensitive to the incident intensity. Hence, the information carried in the phase of the complex wave is lost. This phase is needed to deduce the real space image of the sample from its reciprocal space scattering signal. Therefore, the phase of the signal has to be recovered by auxiliary means. The

recovery of the real space image is further complicated if the signal to noise ratio is low. The signal to noise ratio depends on the strength of the scattering signal which is typically low for non- crystalline, weak contrast samples, such as cells. The signal to noise ratio can be increased by exposing the sample to higher doses but most biological samples are damaged by large radiation doses. Due to these limitations, high resolution imaging of such samples with lens-less methods is challenging.

Life science is one of the most important but also most difficult applications for soft X-ray imaging. Cells are true 3D nanoscale objects and their internal structure typically covers a wide range of dimensions. Currently, the most detailed X-ray based 3D images of whole cells are achieved with soft X-ray transmission microscopes. However, the 3D resolution is anisotropic and limited to about 30 nm which is still much coarser than most of the cellular structures [83, 34]. In this thesis, we will analyze the fundamental limitations of TXM tomography by numerical and theoretical means. Furthermore, new concepts for high resolution soft X-ray imaging will be presented.

Currently, transmission X-ray microscopes operate at many electron storage rings around the world, and have been used to solve biological and medical problems [12, 44, 34, 6]. For a long time, the improvements in resolution were driven by better optics which improved the lateral resolution. Nowadays, soft X-ray microscopes have reached a point where improvements in the lateral resolution no longer translate into better 3D resolution. This is mainly due to the decrease of the depth of focus (DOF) with increased lateral resolution. The depth of focus limits the 3D resolution since the reconstruction of the sample is done via tomography. For tomography, one takes a series of images under different rotation angles. One central assumption in tomography is that the images are generated through a projection along a ray. This assumption is violated as soon as the depth of focus is smaller than the sample. In addition, the effects produced by a fixed partially coherent illumination and by dose induced chemical breakdown also increase with higher resolution. In order to study the different effects and analyze their impact on the tomographic 3D reconstruction, incoherent and partially coherent simulation methods for transmission X-ray microscopes are developed in chapter 4.

In this thesis, a new concept for direct 3D imaging with soft X-rays is also analyzed. It is based on optical sectioning and raster-scanning of a sample. This concept is also used by confocal light microscopy. In these microscopes, the image is generated by scanning the sample through a common focal point of condenser and objective and detecting the transmitted signal with a point-like detector. This setup has the advantage that the signal originates from a small area around the common focal point of the lenses. A 3D image is then directly generated by correlating the positioning data with the detected signal strength. Since no additional steps for alignment and 3D reconstruction are necessary, such methods directly

generate a 3D image stack. The properties and capabilities of such a confocal scanning transmission soft X-ray microscope (CSTXM) are analyzed in chapter 5.

A completely different 3D imaging approach compared to the previously mentioned transmission methods is based on combining high resolution surface imaging by X-rays and high precision surface removal. An analogous approach is the combination of scanning electron microscopy and focused ion beam milling (FIB-SEM) to produce high resolution 3D images. This FIB-SEM method was originally developed for the semiconductor industry but has now also been successfully applied to cryogenic biological samples [74]. In this thesis, a similar method is analysed which is based on scanning soft X-ray microscopy and photoelectron detection for surface imaging. In this FIB-SXM approach, a soft X-ray beam is focused onto the surface of the sample. Photoelectrons are emitted from the illuminated surface layer. Due to the relatively low photon energy of soft X-rays, the generated electrons also have relatively low energies. Therefore, the electrons can only escape from a thin surface layer ($<$10 nm). Thus, the method has an excellent depth resolution. Using X-rays instead of electrons has the additional advantage of a significantly better element contrast for cells. In chapter 6, we introduce this novel 3D imaging approach and investigate its potential performance by numerical simulations.

New X-ray sources, like free electron lasers, now offer short-pulsed, coherent X-ray beams and allow to tackle new scientific questions. In particular, imaging with a single femtosecond-pulse enables the analysis of fast processes [65]. These new coherent sources also require novel approaches for X-ray imaging. In chapter 7, a new approach to Fourier transform holography is introduced. It is based on newly designed diffractive optical elements. The experimental results obtained with these diffractive optical elements are presented. In addition, possible applications for full field imaging with short pulses from free electron lasers are discussed. Furthermore, lens based soft X-ray transmission microscopy methods may also potentially profit from using specially designed diffractive optical elements. A new approach combines in-line holography and transmission soft X-ray microscopy. The setup presented in appendix D allows the use of information from in-line holograms without increasing the dose on the sample. In the same chapter, a discussion is included of how diffractive optical elements can potentially improve existing setups for soft X-ray Zernike and dark field contrast.

In summary, this thesis aims to improve our understanding of the soft X-ray optical setups for high resolution 3D imaging. We investigate the imaging performance of different setups by numerical simulations, which allows us to compare different optical setups and to evaluate their potential performance.

Chapter 2

Current Status of 2D and 3D X-ray Imaging

In the following chapters, we investigate the properties of different soft X-ray imaging methods. In this chapter, we introduce the required theory and present a selection of the most common soft X-ray imaging methods.

2.1 Advantages of Soft X-ray Imaging

Soft X-rays offer a unique combination of large penetration depth, good element contrast and short wavelength for microscopy. The short wavelength is a significant advantage in comparison to light microscopy since the diffraction limited resolution improves according to the Abbe diffraction limit. For biological samples embedded in water, the penetration depth of soft X-rays is larger than most cells. For comparison, the penetration depth of vacuum ultraviolet light is much smaller so that only very thin samples or surfaces are accessible for imaging. [1]

Hard X-rays have a higher penetration depth but provide a significantly lower natural contrast for biological samples leading to higher doses for the same signal to noise ratio [81]. Both the penetration depth and the contrast depend on the interaction between X-rays and the material of the sample. Therefore, the image of a sample generated by the microscope depends on the interaction between X-rays and sample. In order to understand the imaging process within a microscope, we now first describe the interaction between soft X-rays and matter. Then, we analyze the propagation of a scattering signal to the detector.

[1] Most biological samples are contained in water. The attenuation length (decrease of the intensity to $1/e$) for water at 520eV is $\approx$ 9.1µm. At 50eV it is only $\approx$ 46nm. [CXRO http://henke.lbl.gov/]

2.1.1 The Interaction Between Soft X-rays and Material [2]

Soft X-rays interact with a sample by elastic and inelastic scattering. In the soft X-ray range between 100eV and 2keV, the dominating inelastic process is absorption while other effects like Thomson or Compton scattering are negligible. The absorption process either generates a free photoelectron or lifts a bound electron into an unoccupied energy state. The excited atom returns to a lower energy state by filling the vacancy with an electron from an outer shell. The excess energy is released either via the emission of a photon with a characteristic energy (fluorescence) or the emission of an outer shell electron (non-radiative Auger process). If an electron is emitted, this electron can generate secondary electrons via inelastic scattering.

The rate of absorption is material dependent. The difference in absorption between materials is used as a contrast mechanism in soft X-ray imaging. Related to the absorption is the deposition of energy within the sample which results in fast, free electrons and finally in broken chemical bonds. Some samples, such as cells, are relatively sensitive and should generally only be imaged under cryogenic conditions [81]. Alternatively, short pulses (of a few femtoseconds) can be used. During the pulse, the atoms cannot move significantly from their original position although the chemical bonds might break [59]. Therefore, the image shows the sample in its natural state.

For the elastic scattering process, the X-rays are viewed as electromagnetic waves[3]. Hence, they produce a force on the bound electrons of the atoms in the material. This force drives an oscillation of these electrons. Thus, the electrons generate a secondary field which produces a phase shift of the incident field. The amount of phase shift depends on the atomic composition of the material and is described for each atom by the real part (f_1) of the so-called atomic scattering factor (f). The imaginary parts of the atomic scattering factors (f_2) describe the attenuation of the wave field due to absorption (see also [1]). On a macroscopic scale, the interaction between material and X-rays is characterized by the complex refractive index ($n\,[\lambda]$). The refractive index is often written as

$$n = 1 - \delta\,[\lambda] + i\beta\,[\lambda]\,. \tag{2.1}$$

Here, β describes the attenuation of the wave and δ is the phase shift in comparison to the propagation in vacuum. If one neglects the interaction of neighboring atoms on the inner atomic energy states, the refractive index of a material can also be

[2] The propagation of X-rays and their interaction with material is well described in literature. Here, we follow [1] and [62].

[3] The theory that follows holds only for scalar, monochromatic and static fields. Nevertheless, it is a sufficiently good approximation for the considered imaging methods.

written as the weighted sum of the (forward) atomic scattering factors over the type of atoms

$$n = 1 - \sum_a \frac{n_a r_e \lambda^2}{2\pi} \left(f_{1,a}^{(0)} - i f_{2,a}^{(0)} \right). \tag{2.2}$$

Here, n_a is the number of atoms of type "a" per unit volume, r_e is the classical electron radius ($\approx 2.8 \cdot 10^{-15}$ m) and λ is the wavelength of the X-rays.

The inhomogeneous scalar Helmholtz equation (2.3) describes the propagation of a scalar field (U) within an inhomogeneous medium.[4] In this formula, the refractive index characterizes the interaction between the scalar field and the sample.

$$\Delta U + k_0^2 n^2 U = 0 \tag{2.3}$$

The scalar field U is identified with the field of X-rays, Δ is the Laplacian and $k_0 = \frac{2\pi}{\lambda}$ is the wave number. It is common to rewrite the complex valued scalar field U as the product of an amplitude $A = \sqrt{I}$ and a phase term $\exp[i\varphi]$. Here, I is the intensity and takes non-negative values while φ takes values in the real numbers.

The inhomogeneous scalar Helmholtz equation holds in the absence of free current and charge densities in a non-magnetic, slowly varying and weakly scattering material and can be derived under these conditions from the Maxwell equations [62, pp.70 (2.28)]. Generally, finding solutions of equation (2.3) is a challenging problem but for some special cases an explicit solution has been obtained. We now investigate one example which is essential for the simulations in later chapters.

The solution to the inhomogeneous Helmholtz equation for a plane wave traveling along the z-axis through a homogeneous material with refractive index $n = 1 - \delta + i\beta$ can be solved. Since the plane wave is constant for a fixed z, the Laplacian in (2.3) reduces to a second derivative in z and the propagation is described by

$$\frac{\partial^2}{\partial z^2} U + k_0^2 n^2 U = 0.$$

For a constant refractive index, the solution of the differential equation is given by[5]

$$U[z] = U[z_0] \exp\left[k_0 \left(i\left(1-\delta\right) - \beta\right)\left(z - z_0\right)\right]. \tag{2.4}$$

Here, $U[z_0]$ is the value of the field in the z_0-plane. According to equation (2.4), the amplitude of the wave decreases by $\exp[-k_0\beta(z - z_0)]$ and the phase changes

[4] We assume that U is monochromatic and static.

[5] Here, a choice of sign in the exponential is necessary. Here, it is chosen such that a plane wave traveling in the positive z direction is given by $U[z] = U_0 \exp[i\,(k\,z - \omega t)]$.

relative to the one in vacuum by $\exp\left[-ik_0\delta\left(z-z_0\right)\right]$. This result is strictly speaking only valid for a plane wave and homogeneous material. Nevertheless, it is also the key assumption of the projection approximation for forward propagating waves in weakly scattering samples. The projection approximation is used in numerical simulations during so-called multislice algorithms.

Another simplification is the first Born approximation which assumes that the incident field is not significantly changed by the presence of the sample. Therefore, the interaction of the sample with the incident field is well described without taking into account the interaction of the field produced by the sample with the sample itself. Both approximations will be discussed in detail in chapter 3.

The Propagation of X-rays in Vacuum

It is assumed that the X-rays are well described by a scalar field U. The free space propagation of a wave is then described by the homogeneous Helmholtz equation (2.5)

$$\Delta U + k_0^2 U = 0 \tag{2.5}$$

which results from the inhomogeneous Helmholtz equation (2.3) for $n = 1$. An outgoing spherical wave

$$U_{r'}^{spherical}\left[r\right] = \frac{\exp\left[ik_0\left|r-r'\right|\right]}{\left|r-r'\right|}$$

is a Green function to the homogeneous Helmholtz equation. That is, it solves the fundamental equation

$$\left(\Delta + k_0^2\right)\left[U_{r'}^{spherical}\right] = -4\pi\delta\left[r-r'\right].$$

This fact is also used in the (first) Born approximation which approximates the inhomogeneous Helmholtz equation (2.3) by an inhomogeneous homogeneous Helmholtz equation

$$\Delta U + k_0^2 U \;\; = \;\; f.$$

Here, f is a function which depends on n and on an approximation of U. For the case of an incident plane wave, this equation implies that the far field pattern is related to a spherical cut of the Fourier transform of f.

A slightly different Green function is used to solve the propagation in a homogeneous medium from an input plane at z_0 to an output plane at z_1. The situation is shown in figure 2.1. Here, we assume that the two planes are perpendicular to the z-axis. Then, the Rayleigh-Sommerfeld diffraction integral of the first kind describes the propagation by

$$U\left[x_1, y_1, z_1\right] = \frac{1}{i\,\lambda}\int_{-\infty}^{\infty}\int_{-\infty}^{\infty} U\left[x_0, y_0, z_0\right]\frac{z_1 - z_0}{r_{01}}\frac{\exp\left[i\,k\,r_{01}\right]}{r_{01}}\,\mathbf{d}x_0\mathbf{d}y_0. \tag{2.6}$$

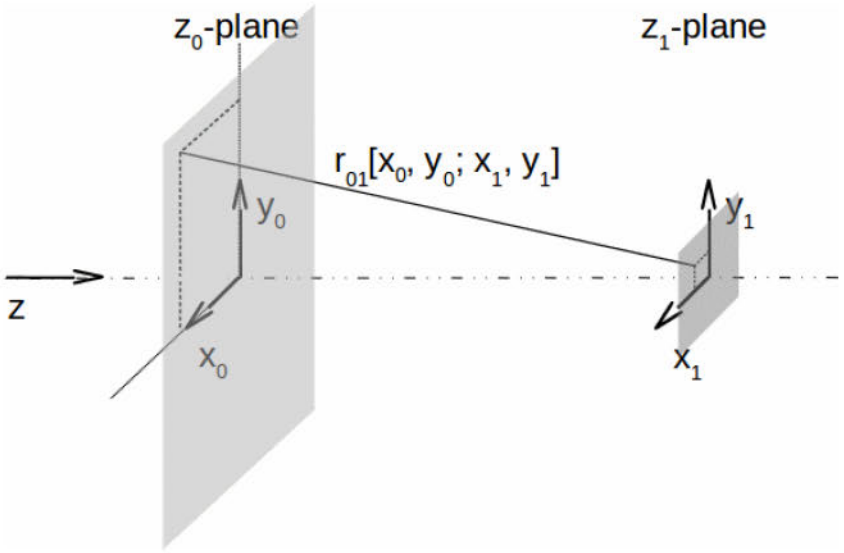

Figure 2.1: *Schematic illustration of the notation used. It is assumed that the wave propagates from the z_0 plane to the z_1 plane.*

Here, we use $k = k_0 n$ and define the function[6]

$$r_{01} = \sqrt{(x_1 - x_0)^2 + (y_1 - y_0)^2 + (z_1 - z_0)^2}.$$

For a thin object and a sufficiently large distance between object and detector, the diffracted field is approximated by the Fresnel diffraction integral

$$\begin{aligned} U[x,y,z] \;\approx\; & -\frac{ik_0 \exp[ik_0 z]}{2\pi z} \exp\left[\frac{ik_0}{2z}\left(x^2+y^2\right)\right] \\ & \int_{\mathbb{R}^2} U[x',y',0] \exp\left[\frac{ik_0}{2z}\left(x'^2+y'^2\right)\right] \exp\left[\frac{-ik_0}{z}\left(x'\,x + y'\,y\right)\right] \mathrm{d}x'\,\mathrm{d}y'. \end{aligned} \tag{2.7}$$

Here, it is assumed that $U[x', y', 0]$ is the wave field at the exit face of the thin sample. Typically for applications in diffraction microscopy, the sample is small

[6] This formula is usually deduced from the Helmholtz-Kirchhoff theorem by using the Green function

$$U^{RS}_{r'}[r] \;=\; \frac{\exp[ik\,|r-r'|]}{|r-r'|} - \frac{\exp[ik\,|r-r'_*|]}{|r-r'_*|}.$$

Here, r'_* is the mirror reflection of r' with respect to the plane z_0. The Helmholtz-Kirchhoff theorem states $\int_{\partial\Omega}\left(G^Q \frac{\partial}{\partial n} U - U \frac{\partial}{\partial n} G^Q\right) \mathrm{d}\sigma = 4\pi U[Q]$ for any Green function G^Q and can be deduced from an application of the Helmholtz equation to the Gauss divergence theorem. See [62] p.18ff.

enough and the distance between sample and detector is sufficiently large such that the Fraunhofer approximation is valid

$$U[x,y,z] \approx -\frac{ik_0 \exp[ik_0 z]}{2\pi z} \exp\left[\frac{ik_0}{2z}(x^2+y^2)\right] \int_{\mathbb{R}^2} U[x',y',0] \exp\left[\frac{-ik_0}{z}(x'x+y'y)\right] \mathrm{d}x'\,\mathrm{d}y'. \tag{2.8}$$

The far field is then proportional to the Fourier transform of the field $U[x',y',0]$.

Lens-less imaging methods try to invert either equation (2.7) or equation (2.8). The aim is to recover the refractive index distribution of the object. Soft X-ray detectors only detect the intensity of the incident X-rays. Therefore, the phase information of the far field is lost. But the phase information is needed, in order to use equation (2.7) or equation (2.8) to measure respectively the refractive index or the field at the exit face. The main difference between the existing lens-less methods is the way this phase information is recovered. We now give a short overview of lens-less and lens based soft X-ray imaging methods for non-crystalline samples that can be described by the scalar wave theory.

2.2 Lens-less Methods for 2D and 3D X-ray Imaging

2.2.1 Coherent Diffraction Imaging (CDI)

The underlying physical concept of coherent diffraction imaging is that the diffraction pattern produced by a quasi monochromatic wave and a scattering sample contains information about the three dimensional scattering process and thus also about the structure of the sample. We first study the case of a thin sample illuminated by a plane wave. It is assumed that the conditions for the scalar wave approximation are always fulfilled. Let us assume that the sample is thin in the z-direction and has a constant refractive index along this direction

$$n[x,y,z] = \begin{cases} n[x,y] & z_0 - \Delta z \le z \le z_0 \\ 1 & else \end{cases}.$$

Here, Δz is the thickness of the sample. According to the projection approximation, the resulting field is

$$\begin{aligned} U[x,y,z_0] &= U_0 \exp[ik_0 (n[x,y,z_0]-1)\Delta z] \\ &\approx U_0 (1 + (i\delta - \beta) k_0 \Delta z). \end{aligned}$$

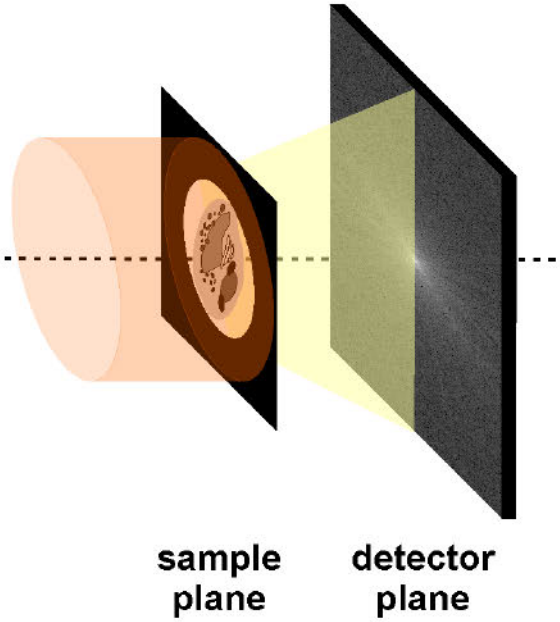

(a) Coherent diffraction imaging setup

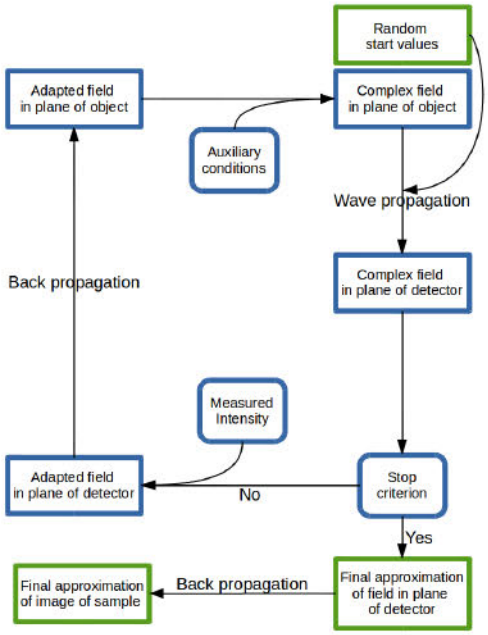

(b) Reconstruction algorithm

Figure 2.2: *In figure 2.2a, a classical coherent diffraction imaging setup is shown [55]. It consists of a sample and a detector. The sample is coherently illuminated and the diffraction pattern is recorded on the detector. The reconstruction of the image is done numerically, for example with the error reduction algorithm [24] as illustrated in figure 2.2b.*

In a classical CDI experiment, the distance between sample and detector is large so that the Fraunhofer approximation is applicable. Let the detector be located at z_D. Then, equation (2.8) yields

$$\begin{aligned} U[x,y,z_D] &= \frac{ik_0 \exp[ik_0(z_D-z_0)]}{2\pi(z_D-z_0)} \exp\left[\frac{ik_0(x^2+y^2)}{2(z_D-z_0)}\right] \\ &\quad \int_{\mathbb{R}^2} U[x',y',z_0] \exp\left[-ik_0\frac{x'x+y'y}{z_D-z_0}\right] \mathrm{d}x'\mathrm{d}y' \\ &\approx \frac{ik_0 \exp[ik_0(z_D-z_0)]}{2\pi(z_D-z_0)} \exp\left[\frac{ik_0(x^2+y^2)}{2(z_D-z_0)}\right] \\ &\quad \int_{\mathbb{R}^2} U_0(1+(i\delta-\beta)k_0\Delta z) \exp\left[-ik_0\frac{x'x+y'y}{z_D-z_0}\right] \mathrm{d}x'\mathrm{d}y'. \end{aligned}$$

With this equation, one can reconstruct $U[x,y,z_0]$ from $U[x,y,z_D]$. But the detectors only measure the intensity $\left(I = U\overline{U}[x,y,z_D]\right)$ of a diffracted wave. As previously mentioned, the phase information is lost. Hence, the reconstruction

is only possible if additional a priori information is available. In particular, it is assumed that the sample is isolated and ideally sparse or small. This recovery problem is also known as the "phase problem".

The first step to a solution was found in 1952. Sayre noticed that the Bragg diffraction pattern can be oversampled relative to Shannon's theorem [73]. This is also true if the sample has a restricted support instead of being crystalline. By oversampling the diffraction pattern, the lost phase can be recovered. Iterative solvers based on this principle have been used to solve the phase problem. First, the Gerchberg Saxton algorithm [27] and later the faster converging hybrid input output algorithm [24] have been developed, followed by the first successful experiments in 1999 [55].

The setup of a CDI experiment is comparatively simple and good results have been achieved with artificial test samples. However, this technique requires isolated samples. Therefore, CDI has not gone beyond the stage of imaging artificial objects (see table 2.4).

2.2.2 Ptychography

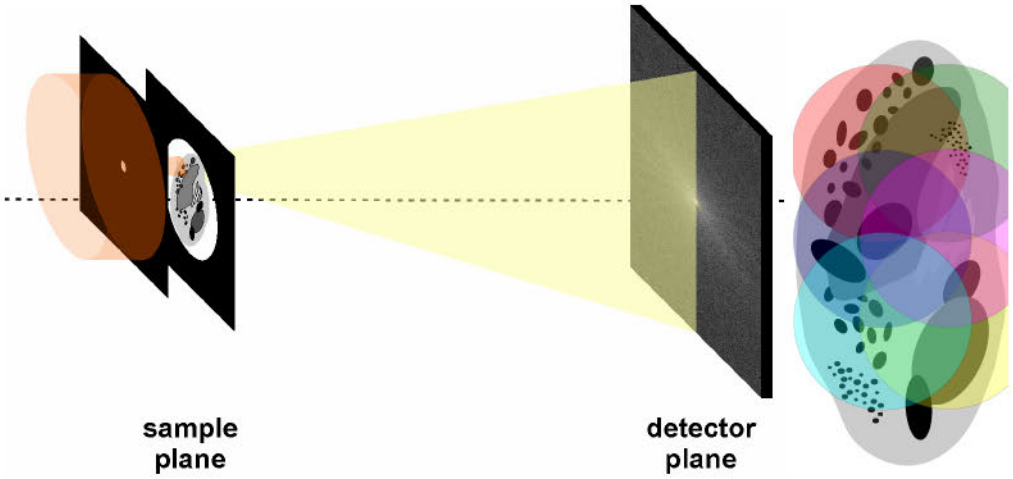

(a) Schematic setup of a ptychography experiment **(b)** Scan pattern

Figure 2.3: *In a ptychography setup as shown in figure 2.3a, a coherently illuminated spot is scanned over the sample. For each position, the diffraction pattern is recorded on the detector [39]. The reconstruction of the image is done numerically. Ambiguities are eliminated due to an overlap of the illuminated patches, as shown in figure 2.3b.*

Ptychography is conceptually similar to CDI. However, instead of illuminating the whole sample coherently with a plane wave, in ptychography one uses a coherent,

focused beam. The beam is scanned over the sample in an overlapping pattern, as shown in figure 2.3. The overlapping regions are used to generate the needed oversampling to solve the phase problem. Therefore, the method allows to image extended samples. The overlap also solves the ambiguity of the classical CDI setup.

This method was first introduced to solve the phase problem for electron diffraction [39] and generalized in 2004 [20] to other diffraction patterns. It is now also applicable to X-ray imaging. In 2009, the first algorithm for the simultaneous reconstruction of the transmission function of the sample and the illuminating field was proposed [50].

It has been shown that ptychography can achieve high resolution on strongly scattering artificial samples. It is also used to image biological samples [14] but the resolution achieved on those samples is still significantly lower (see table 2.4).

2.2.3 Holography

The idea of holography was developed by Gabor in the early 1940s [25]. Mainly two approaches are useful for high resolution soft X-ray imaging. They are called in-line holography and Fourier transform holography [106]. An in-line holography setup consists of a focusing optic, a sample and a detector. The focus of the beam lies a bit before or behind the sample. The defocused beam passes through the sample and the resulting diffracted wave (U_s) interferes with the non-diffracted beam (U_0) on the detector. Therefore, the signal on the detector is

$$\begin{aligned} I_{detector} &= |U_0 + U_s|^2 \\ &= U_0\overline{U_0} + \overline{U_0}U_s + U_0\overline{U_s} + U_s\overline{U_s} \\ &\approx U_0\overline{U_0} + \overline{U_0}U_s + U_0\overline{U_s}. \end{aligned}$$

In the last line, we used the fact that the sample is typically weakly scattering so that the point-wise product[7] of the scattered wave with itself is small. The reconstruction is done by first multiplying this signal with U_0 and back-propagating the result to the plane of the sample

$$P_{-z_s}\left[U_0^2\overline{U_0} + \underline{U_0\overline{U_0}U_s} + U_0^2\overline{U_s}\right]. \tag{2.9}$$

Here, P_{-z} is the back-propagator and z_s is the distance between sample and detector. The underlined term generates the reconstruction of the sample. It is assumed that the Fraunhofer approximation is valid and that the non-diffracted beam is a

[7] With the point-wise product, we mean the Hadamard product, i.e. $\forall x : \left(U\overline{U}\right)[x] = U[x]\,\overline{U}[x]$.

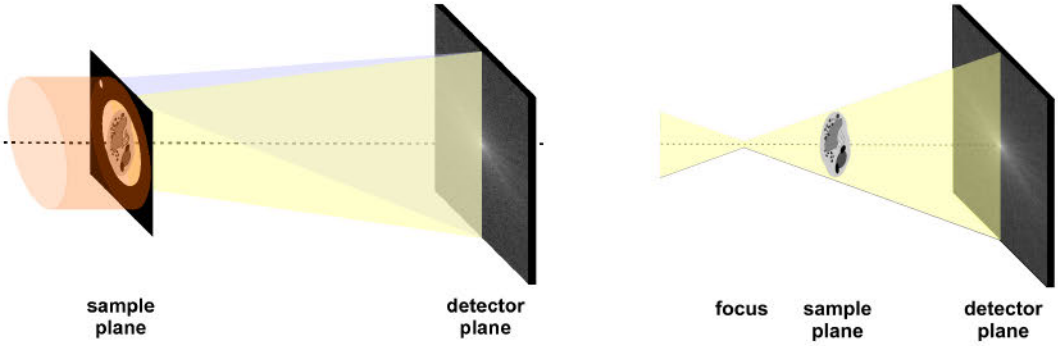

(a) Fourier transform holography setup **(b)** In-line holography setup

Figure 2.4: The two classical setups for X-ray holography are shown [92, 106].
(a) The classical Fourier transform holography setup consists of an opaque screen, with a transparent, small reference and a larger sample area. The interference between the light scattered by the reference hole and the light scattered by the sample is detected in the far ″eld. A simple Fourier transform produces an image of the sample.
(b) The classical in-line holography setup uses a focused reference. The propagat-ing wave front interacts with the sample and generates an in-line hologram on the detector.

parabolic wave.

$$U_0[x,y] = \exp\left[ik\frac{x^2+y^2}{2z_s}\right].$$

Then, (2.9) is equal to

$$\begin{aligned} &P_{-z_s}\left[\exp\left[ik\frac{x^2+y^2}{2z_s}\right] + \underline{U_s} + \exp\left[ik\frac{x^2+y^2}{z_s}\right]\overline{U_s}\right] \\ =&P_{-z_s}\left[\exp\left[ik\frac{x^2+y^2}{2z_s}\right]\right] + \underline{P_{-z_s}[U_s]} + P_{-z_s}\left[\exp\left[ik\frac{x^2+y^2}{z_s}\right]\overline{U_s}\right]. \end{aligned}$$

Here, we used the fact that the back-propagator is linear which can be deduced from equation (2.8). Therefore, the three terms in the preceding equation can be considered separately. The first term produces a scaled version of the non-diffracted beam and the last term generates the so-called twin image. The underlined term produces the wave field due to the sample in the z_s plane. A major problem is the presence of speckles. In addition, the twin image and the reconstruction are not spatially separated, which reduces the achievable image quality. The twin image problem is solved by Fourier transform holography.

A Fourier transform holography setup consists of a sample and a reference, as shown in figure 2.4. Both have to be illuminated coherently so that the signal on the

detector results from the interference of the light diffracted by either the reference or the sample. As in the in-line holography case, the intensity on the detector is given by $I_{detector} = |\psi_{reference} + \psi_{sample}|^2$. Applying the same reconstruction steps as before yields the same three terms. This time, the twin image is shifted so that the reconstruction of the sample and the twin image is separated. As a consequence, this method, unlike in-line holography, is not limited to weakly scattering samples. For more details, see 7.3.

Current Fourier transform holography approaches use a separate reference and sample field which have to be illuminated coherently. Therefore, this approach requires a high degree of spatial coherence and uses only a small part of the incident photons. X-ray holography has not visualized the ultra-structure of cells. However, it has found applications for time resolved imaging of magnetic structures under extreme conditions ([65]). In particular, time resolved imaging by holography using short pulse free electron laser radiation offers new scientific studies. Therefore, in chapter 7, a new approach to Fourier transform holography is introduced which enables imaging of extended samples potentially with one short X-ray pulse.

2.3 Lens Based Methods

As their name suggests, lens based methods use lenses for the imaging of the sample. Lenses are optical elements that change the phase of an incident wave. Ordinary, collecting refractive lenses with focal length (f) create a phase shift of

$$T[x,y] \propto \exp\left[-\frac{ik_0\left(x^2+y^2\right)}{2f}\right].$$

Such lenses can be used to image a point source or to focus light into a small spot. For soft X-ray imaging, refractive lenses are ill-suited since all materials have an unfavorable ratio between absorption and phase shift. Hence, diffractive optics are used, namely the so-called Fresnel zone-plates (FZP) which consist of concentric rings [75]. They are characterized by their outermost zone width (dr_N) and their (first order) focal length (f). In table 2.1, some typical examples for properties of Fresnel zone-plates as used for soft X-ray imaging are given. The profile of a binary Fresnel zone-plate can be expanded into a sine series

$$T[r] = \frac{1}{2} + \frac{2}{\pi}\sum_{m=1,3\ldots}^{\infty}\frac{1}{m}\sin\left[k_0\frac{m}{2f}r^2\right].$$

By using the decomposition of sine functions into exponential functions

$$\sin[x] = \frac{1}{2i}\left(\exp[ix] - \exp[-ix]\right),$$

the transmission profile can be rewritten as

$$T[r] = \frac{1}{2} + \frac{2}{\pi} \sum_{m=1,3\ldots}^{\infty} \frac{1}{2im} \left(\exp\left[\frac{ik_0 r^2}{2\frac{f}{m}}\right] - \exp\left[-\frac{ik_0 r^2}{2\frac{f}{m}}\right] \right). \quad (2.10)$$

The underlined part is obviously similar to the transmission function of a collecting lens with focal length f/m. The parameter m defines the order of diffraction. We now show that the underlined part focuses a plane wave at f/m.

dr_N	f	Ø	DOF	N	δ
40 nm	1.5 mm	90 µm	2.7 µm	566	49 nm
25 nm	0.95 mm	90 µm	1.0 µm	911	31 nm
10 nm	0.38 mm	90 µm	0.17 µm	2271	12 nm

Table 2.1: *Selected properties of Fresnel zone-plates (FZP) at a wavelength of $\lambda = 2.4\,nm$. Here, dr_N is the outermost zone width, f is the focal length and Ø is the diameter of the FZP. From the data, one can derive the depth of focus ($DOF \approx 4dr_N^2/\lambda$), the number of zones ($N$) and the lateral resolution ($\delta \approx 1.22\,dr_N$).*

According to the Fresnel approximation (2.7), a plane wave that illuminates a disc $\mathbb{D}_d = \{(x,y)\,|\,x^2+y^2 < d\}$ with the transmission function $\frac{-1}{2i\pi m} \exp\left[-\frac{ik_0 r^2}{2f/m}\right]$ generates at a distance f/m the field

$$\begin{aligned} U_{\frac{f}{m}}[x,y] \approx & -\frac{ik_0 \exp[ik_0 f/m]}{2\pi\, f/m} \exp\left[\frac{ik_0\,(x^2+y^2)}{2f/m}\right] \int_{\mathbb{D}_{d_{FZP}}} \frac{-1}{2i\pi m} \exp\left[-\frac{ik_0 r^2}{2f/m}\right] \\ & \exp\left[\frac{ik_0}{2f/m}\,(x'^2+y'^2)\right] \exp\left[\frac{-ik_0}{f/m}\,(x'x+y'y)\right] \mathrm{d}x'\,\mathrm{d}y' \\ \approx & -\frac{ik_0 \exp[ik_0 f/m]}{2\pi\, f\ \ /m} \exp\left[\frac{ik_0\,(x^2+y^2)}{2f/m}\right] \\ & \frac{-1}{2i\pi m} \int_{\mathbb{D}_{d_{FZP}}} \exp\left[\frac{-ik_0}{f\ \ m}\,(x'x+y'y)\right] \mathrm{d}x'\,\mathrm{d}y'. \end{aligned}$$

A Fresnel zone-plate has only a finite diameter (d_{FZP}), therefore, the integration has to be restricted to the area of the zone-plate. This yields

$$U_{\frac{f}{m}}[x,y] \approx \frac{k_0 \exp[ik_0 f/m]}{4\pi^2 f} \exp\left[\frac{ik_0\,(x^2+y^2)}{2f\ \ m}\right] \int_{\mathbb{D}_{d_{FZP}}} \exp\left[\frac{-ik_0}{f\ m}\,(x'x+y'y)\right] \mathrm{d}x'\,\mathrm{d}y'.$$

This integral yields the well known Airy pattern. Therefore, the m-th part of the transmission function in equation (2.10) focuses the plane wave at a distance f/m behind the zone-plate. Hence, Fresnel zone-plates can be used for imaging like thin lenses but one has to suppress the contributions of other diffraction orders.

2.3.1 Scanning Transmission X-ray Microscope (STXM)

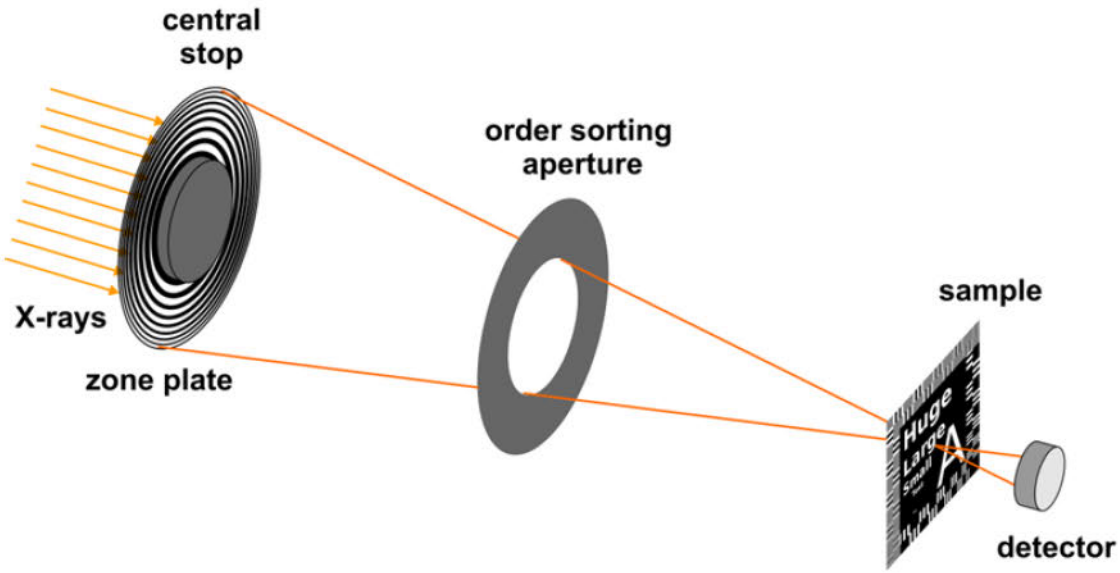

Figure 2.5: *X-ray optical setup of a scanning transmission X-ray microscope. For a diffraction limited resolution, the focusing optic has to be coherently illuminated. An order sorting aperture is required to block all unwanted orders. The produced focal spot is raster scanned over the sample and the transmitted intensity is detected* [77, 45].

The optical setup of a scanning transmission X-ray microscope is shown in figure 2.5. A focusing optic creates a diffraction limited spot. This spot is scanned over the sample. The transmitted light is detected for each scanning position. The change in transmission yields the image of the sample. Since the Fresnel zone-plate has several diffraction orders, an order sorting aperture is needed to block the unwanted orders. The achievable resolution of the microscope depends on the size of the focal spot and the precision of the positioning.

Different contrast modes have been realized. By using an array detector with spatial resolution, the implementation of differential phase-contrast and dark field imaging is feasible [40]. This type of transmission microscope is also easily modified for ptychography by equipping it with a pixel detector.

The first scanning transmission X-ray microscopes were constructed during the 1980s [77, 45] with first development in the 1970s [41].

2.3.2 Transmission X-ray Microscope (TXM)

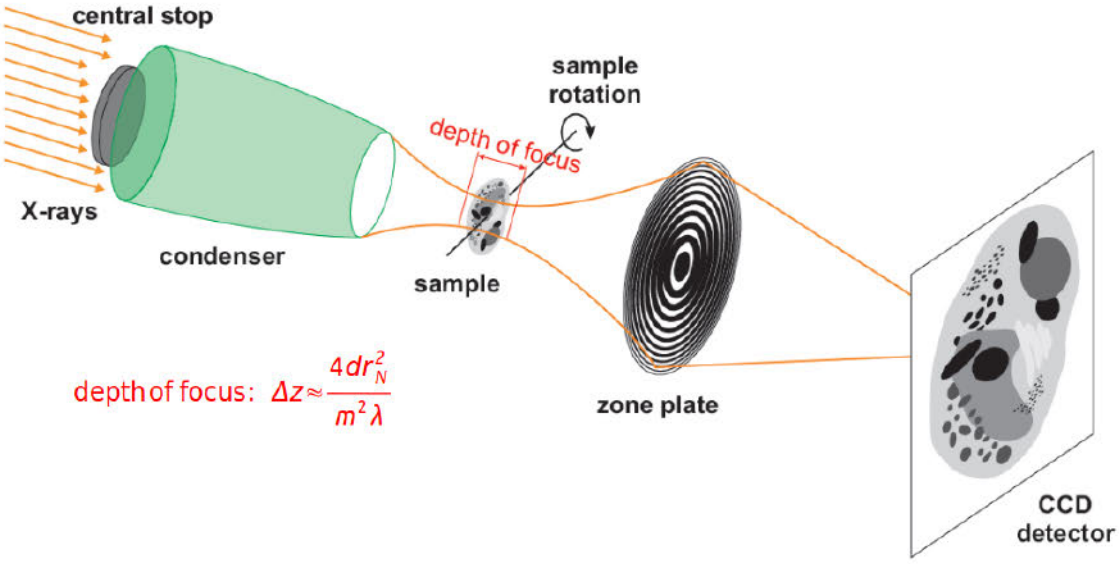

(a) X-ray optical setup of a soft X-ray transmission microscope

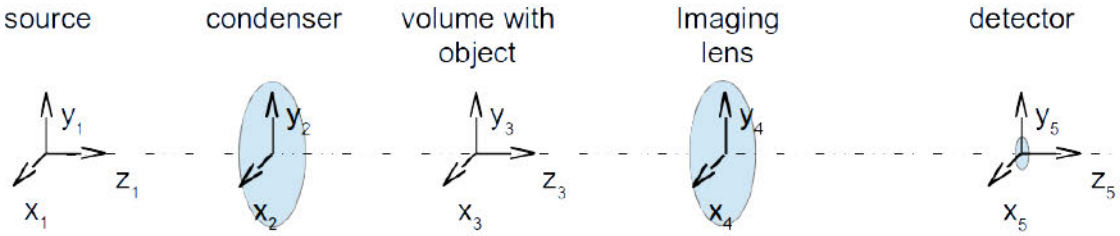

(b) Coordinatesystems

Figure 2.6: *Setup of a transmission X-ray microscope. In* **(a)**, *the layout of the HZB soft X-ray microscope is sketched [83, image by S. Werner]. It is based on an elliptically shaped glass capillary which acts as mirror condenser by total reflection. The second key component is a high resolution Fresnel zone-plate objective. In* **(b)**, *the corresponding coordinates are shown. These coordinates are used in subsequent chapters for simulations.*

Fresnel zone-plate based transmission soft X-ray full-field microscopy started in the 1970s [77, 60] and is now a well established technique for 3D high resolution imaging of biological samples [44][8]. The general setup is shown in figure 2.6.

[8] The development of reflection based X-ray microscopes dates back to the 1950s [63]. However,

Like a bright-field microscope in the visible spectrum, the main components of a TXM are a light source, a condenser, a sample, an objective and a detector. The condenser focuses the incident X-ray beam to illuminate the sample. The objective collects the X-rays after they have been diffracted by the sample and generates an image of the sample on the detector. The detector is usually a directly illuminated charge-coupled device (CCD). For 3D reconstructions, the sample is placed on a tilt stage and imaged through a series of tilt angles. Each image represents a 2D projection of the 3D sample. From the series of projections, the 3D transmission of the sample is reconstructed via tomography.

Our understanding of the imaging process in the TXM is based on the Fresnel approximation (2.7). We now use the notation illustrated in figure 2.6. A field in the z_3 plane in front of the Fresnel zone-plate is imaged by the zone-plate to the z_5 plane where the detector is located. We assume that $z_4 = 0$ is the position of the zone-plate. It is assumed that the Fresnel zone-plate is used in the first order of diffraction and we neglect all other orders. According to equation (2.10),[9] the first diffraction order acts on the field by multiplying it with $T \propto \exp\left[-\frac{ik_0\left(x_4^2+y_4^2\right)}{2f}\right]$. Let us also introduce the shorthand $z_{ij} := z_j - z_i$. Then, one can apply equation (2.7) for the propagation of the field from z_3 to z_4 and from z_4 to z_5.

$$\begin{aligned} U_{z_5} \approx & -\cancel{\frac{ik_0 \exp\left[ikz_{45}\right]}{2\pi\, z_{45}} \exp\left[\frac{ik_0\left(x_5^2+y_5^2\right)}{2z_{45}}\right]} \int_{\mathbb{R}^2} U_{z_4}\left[x', y', 0\right] \\ & \exp\left[\frac{ik_0}{2z_{45}}\left(x'^2+y'^2\right)\right] \exp\left[\frac{-ik_0}{z_{45}}\left(x'\,x_5 + y'\,y_5\right)\right] \mathrm{d}x'\,\mathrm{d}y' \end{aligned}$$

and

$$\begin{aligned} U_{z_4} \approx & -\cancel{\frac{ik_0 \exp\left[ik_0 z_{34}\right]}{2\pi\, z_{34}}} \exp\left[\frac{ik_0\left(x_4^2+y_4^2\right)}{2z_{34}}\right] T\left[x_4, y_4\right] \int_{\mathbb{R}^2} U_{z_3}\left[x', y', 0\right] \\ & \exp\left[\frac{ik_0}{2z_{34}}\left(x'^2+y'^2\right)\right] \exp\left[\frac{-ik_0}{z_{34}}\left(x'\,x_4 + y'\,y_4\right)\right] \mathrm{d}x'\,\mathrm{d}y' \end{aligned}$$

We will here ignore the crossed-out terms since they result only in a constant scaling of the final intensity $U_{z_5}\overline{U_{z_5}}$. By rearranging and inserting T, one gets

$$\begin{aligned} U_{z_5} \propto & \int_{\mathbb{R}^2}\int_{\mathbb{R}^2} \exp\left[\frac{ik_0\left(x_4'^2+y_4'^2\right)}{2}\left(\frac{1}{z_{34}}+\frac{1}{z_{45}}-\frac{1}{f}\right)\right] U_{z_3}\left[x_3', y_3', 0\right] \cancel{\exp\left[\frac{ik_0}{2z_{34}}\left(x_3'^2+y_3'^2\right)\right]} \\ & \exp\left[\frac{-ik_0}{z_{34}}\left(x_3'\,x_4' + y_3'\,y_4'\right)\right] \mathrm{d}x_3'\,\mathrm{d}y_3' \exp\left[\frac{-ik_0}{z_{45}}\left(x_4'\,x_5 + y_4'\,y_5\right)\right] \mathrm{d}x_4'\,\mathrm{d}y_4'. \end{aligned}$$

better images are in general produced by Fresnel zone-plate based TXM.

[9] Here, we neglected all other orders of diffraction of the Fresnel zone-plate. Due to the usually geometry of the TXM experiments, this has no significantly impact on the imaging properties.

Since the field of view is typically small, the argument in the crossed-out part is small and the exponential can be approximated by one. Then, the resulting integral is proportional to the Fourier transform of the Fourier transform of U_{z_3}, as long as the thin lens formula $\left(\frac{1}{z_{34}} + \frac{1}{z_{45}} = \frac{1}{f}\right)$ is satisfied. Due to the properties of the Fourier transform, this is proportional to an upside down and left right interchanged version of U_{z_3}.[10] A detailed discussion of the 3D imaging properties of the TXM is given in chapter 4. In the same chapter, the properties and limits of a transmission X-ray microscope are numerically investigated and compared to experimental data.

2.4 Comparison of Lens-less and Lens Based Methods

Table 2.4 shows an overview summarizing published experimental results for different X-ray imaging approaches.

A direct comparison of the different X-ray imaging methods is difficult since resolution and quality of the image depend strongly on the sample. Generally speaking, ptychography delivers good results for high contrast and highly ordered objects. Typically, lens-less methods require strong scattering signals into high diffraction angles.

Lens based methods like TXM and STXM, generally are superior for low contrast, non-periodic and weakly scattering samples, which are typical for life science.

[10] More accurately, one can use substitution and equation (E.2) to show that the absolute value of the field U_{z_5} is proportional to a scaled, upside down and left right interchanged version of the absolute value of the field U_{z_3}.

	2D resolution		3D resolution		Limitations
	Test objects	Real objects	Test objects	Real objects	
Microscopy (TXM / STXM)	10 nm (multi-layer structure) [69]	12 nm (IC stacks) [68]	-	26 nm (vaccinia virus) [6]	2D: zone-plate optics 3D: depth of focus
Ptychography	5 nm (multi-layer structure) [86]	18 nm (LiFePO4 nano-crystals) [86]	16 nm (porous SiO2 structure coated with Ta) [38]	-	high dose strongly scattering samples detectors with high dynamic range
Holography	46 nm (Siemens star) [26]	50 nm (magnetic domains) [18]	-	140 nm (diatom) [31]	reference wave or nano-pinhole twin image problem speckles
Coherent diffraction imaging (CDI)	10 - 13 nm (gold spheres) [11]	35 nm (red blood cells) [105]	50 nm (gold spheres on pyramid shaped SiN membrane) [10]	-	isolated objects no unique phase retrieval solution detectors with high dynamic range

Table 2.4: Resolutions of X-ray imaging methods as reported in the literature. Note that different samples were used, which complicates the comparison.

Chapter 3

Numerical Methods for Soft X-ray Imaging

In the following chapters, we use numerical simulations to investigate the properties of different soft X-ray imaging methods. In this chapter, we introduce the methods laying the groundwork for subsequent chapters. Specifically, the description of the propagation of X-rays in a homogeneous medium as presented in the previous chapter is extended to a few special cases. These cases are later used in the numerical simulations. The following chapter is based on [19] and [62].

3.1 Simulating the Propagation of Soft X-rays in Free Space

For simulations of the imaging methods, we must compute the propagation in a homogeneous medium from an input plane to an output plane. As in section 1 of the previous chapter, we assume that the propagation occurs in the absence of free current and charge densities in a non-magnetic, slowly varying and weakly scattering material. As shown, the Rayleigh-Sommerfeld diffraction integral of the first kind describes the propagation between two planes perpendicular to the optical axis in z_1 and z_0. It is given by

$$U\left[x_1, y_1, z_1\right] = \frac{1}{i\,\lambda} \int_{-\infty}^{\infty} \int_{-\infty}^{\infty} U\left[x_0, y_0, z_0\right] \frac{z_1 - z_0}{r_{01}} \frac{\exp\left[i\,k\,r_{01}\right]}{r_{01}} \mathbf{d}x_0 \mathbf{d}y_0. \tag{3.1}$$

Here, λ is the wavelength of the monochromatic light and $k = \frac{2\pi}{\lambda}$ is the wave number. The distance between two points (x_0, y_0, z_0) and (x_1, y_1, z_1) is denoted by r_{01}. A schematic of the coordinate system is shown in figure 3.1. Equation (3.1) is not well suited for numerical simulations since the numerical integration

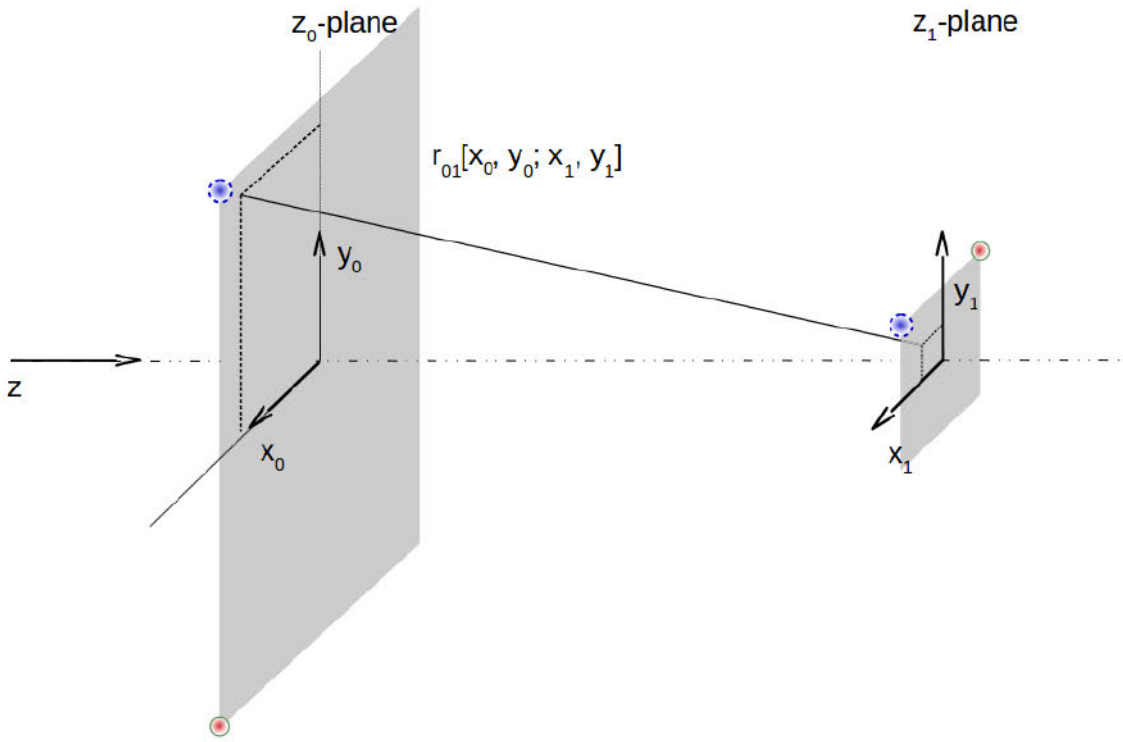

Figure 3.1: *Schematic of the notation used. The red and blue spots correspond to the extremal positions considered in figure 3.2.*

is time consuming. Therefore, this expression has to be transformed into a more convenient form. One such form results in the angular spectrum method (ASM). In order to efficiently implement formula (3.1), the integral is expressed as

$$\begin{aligned} U[x_1, y_1, z_1] &= \frac{1}{i\lambda}\int_{-\infty}^{\infty}\int_{-\infty}^{\infty} U[x_0, y_0, z_0] \\ &\quad \cdot \frac{\exp\left[i\,k\sqrt{(z_1-z_0)^2+(x_1-x_0)^2+(y_1-y_0)^2}\right]}{(z_1-z_0)^2+(x_1-x_0)^2+(y_1-y_0)^2}\,(z_1-z_0)\,\mathbf{d}x_0\mathbf{d}y_0 \\ &= \frac{1}{i\lambda}\int_{\mathbb{R}^2} U[x_0, y_0, z_0]\cdot h[x_1-x_0, y_1-y_0, z_1-z_0]\;\mathbf{d}x_0\mathbf{d}y_0 \end{aligned} \tag{3.2}$$

where h is defined by

$$h[x, y, z] := \frac{\exp\left[i\,k\sqrt{z^2+x^2+y^2}\right]}{z^2+x^2+y^2}.$$

By definition of the convolution $f * g[t] := \int_{\mathbb{R}} f[\tau]\cdot g[t-\tau]\;\mathbf{d}\tau$, the right side of equation (3.2) is a convolution integral. This integral has to be discretized for

computer based simulations. The discrete Fourier transform of a signal y of length N is denoted by $Y = \mathcal{FFT}[y]$. Using the circular convolution theorem on

$$\begin{aligned} \mathcal{FFT}^{-1}[X \cdot Y]|_n &= const \cdot \left(\sum_{l=0}^{N-1} x_l \cdot (y_N)_{n-l} \right) \\ &= const \cdot (x * y_N)_n , \end{aligned}$$

the convolution can be computed with the aid of the fast Fourier transform (FFT) with $O(N \log N)$ operations [13]. Here, (y_N) is the periodic extension of y. For large optical elements such as the ones typically used in soft X-ray microscopy, this approach is superior to a direct evaluation of the integral since the latter needs $O(N^2)$ computational operations.

In order to prevent artifacts caused by the circular convolution, the function U has to have finite support in the z_0 plane. Additionally, U has to be restricted and h has to be padded with zeros so that the circular nature of the convolution does not affect the result. Since a convolution operator is used, the resolutions in the z_0 and in the z_1 plane are equal. This can pose difficulties if either the regions of interest or required resolutions differ significantly between the planes. For example, for soft X-ray microscopy at 2.4 nm, a typical Fresnel zone plate has a diameter of about 100 µm while the focal spot has an FWHM on the order of a few tens of nanometers.

Alternatively, equation (3.1) can be approximated by using the paraxial assumption. This approximation assumes that the direction of propagation is essentially along the optical axis and that the field is restricted to a tight neighborhood of the optical axis.[1] With these requirements, the square root in the exponential function is approximated by its Taylor expansion

$$\sqrt{(z_1 - z_0)^2 + (x_1 - x_0)^2 + (y_1 - y_0)^2} \approx (z_1 - z_0) + \frac{(x_1 - x_0)^2 + (y_1 - y_0)^2}{2(z_1 - z_0)}. \quad (3.3)$$

We obtain the well known Fresnel approximation

$$\begin{aligned} U[x_1, y_1, z_1] \approx & \frac{\exp[i\,k\,(z_1 - z_0)]}{i\,\lambda\,(z_1 - z_0)} \exp\left[i\,k\,\frac{x_1^2 + y_1^2}{2\,(z_1 - z_0)} \right] \int_{-\infty}^{\infty} \int_{-\infty}^{\infty} \\ & U[x_0, y_0, z_0] \exp\left[i\,k\,\frac{x_0^2 + y_0^2}{2\,(z_1 - z_0)} \right] \exp\left[-i\,k\,\frac{x_1 x_0 + y_1 y_0}{(z_1 - z_0)} \right] \mathbf{d}x_0 \mathbf{d}y_0. \end{aligned} \quad (3.4)$$

The Fresnel approximation has the advantage that the integral can be computed by using a two dimensional Fourier transform. This is especially helpful for numerical

[1] Throughout the thesis, we assume that the optical axis is located at $(x_i, y_i) = 0$.

simulations since the two dimensional fast Fourier transform is much faster than the numerical integration. A matlab implementation of the Fresnel approximation is included in the supplementary part of this work in appendix A.

One disadvantage of the Fresnel approximation is that the paraxial assumption must hold in both planes. For the simulation of the imaging performance of lens based microscopes with high numerical apertures ($NA > 0.1$), the Fresnel approximation is not applicable. Nevertheless, the region of the focal plane with non-negligible intensity is tightly centered around the optical axis. Therefore, it is possible to use a different Taylor approximation of the square root. This results in the wide-angle near and far field approximation (NFFA) which we use for calculations of optics with numerical apertures larger than 0.1. The NFFA is described in the following section.

3.1.1 The Wide-angle Near and Far Field Approximation (NFFA)

The wide-angle near and far field approximation (NFFA) is best used for applications where either the input or the output plane is much larger than the other plane. For example, this is the case for high NA optical elements, i.e. $NA > 0.1$. For such applications, it is useful to utilize a different approximation in the Rayleigh-Sommerfeld diffraction integral (equation (3.1)) for r_{01} instead of equation (3.3).

The distance $r_{01}\left[x_0, y_0; x_1, y_1\right]$ as a function of the position of the points of interest in the two planes is dominated by either the (x_0, y_0) or the (x_1, y_1) values. We now introduce a better suited approximation which takes the given geometry into account.

Firstly, the case of a larger input plane is considered.

Here, we introduce the approximation

$$r_{01} \approx \sqrt{z^2 + x_0^2 + y_0^2}\sqrt{1+h},$$

using $z := z_1 - z_0$. The function h is here given by:

$$\begin{aligned} h &= \frac{x_1^2 + y_1^2}{z^2 + x_0^2 + y_0^2} - \frac{2\left(x_1 x_0 + y_1 y_0\right)}{z^2 + x_0^2 + y_0^2} \\ &\approx \frac{x_1^2 + y_1^2}{\sqrt{z^2}\sqrt{z^2 + x_0^2 + y_0^2}} - \frac{2\left(x_1 x_0 + y_1 y_0\right)}{z^2 + x_0^2 + y_0^2}. \end{aligned}$$

For the following computations, it is convenient to introduce the abbreviation

$$r_n := \sqrt{z^2 + x_n^2 + y_n^2}\,,\ n \in \{0, 1\}\,.$$

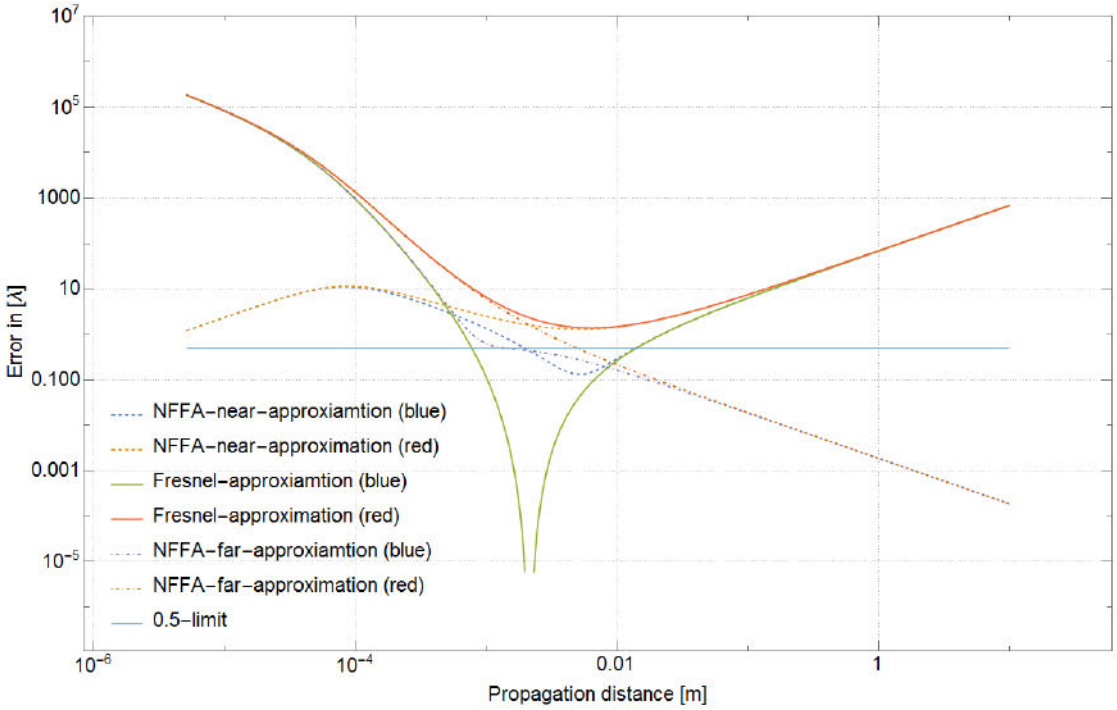

Figure 3.2: *These graphs show the errors of the approximated distance (equation (3.3) and equation (3.5)) in units of the wavelength over the propagation distance. The graphs correspond to the approximation used for the NFFA (near dashed, far dot-dashed) and the Fresnel approximations (line). The dimension of the output plane depends on the input plane since the numerical propagators link the resolution, number of discretization points, plane dimensions and propagation distance (as explained in the supplement in appendix A). The points* (x_0, y_0) *and* (x_1, y_1) *are chosen in such a way that they represent extremal cases for the approximations. These extremal cases correspond to positions marked with the red and blue points in figure 3.1.*
In this example, we assumed that the input plane is a square of 100 µm and is discretized by 2048×2048 *points. The figure illustrates that under these conditions, the outer parts of the FOV are no longer within the scope of application of the approximations since the total approximation error lies above* $\lambda/2$.

With these notations and the Taylor expansion of

$$\begin{aligned}\sqrt{1+h} &= 1+\frac{h}{2}-\frac{h^2}{8}\dots \\ &\approx 1+\frac{h}{2},\end{aligned}$$

the distance r_{01} is approximated by

$$r_{01} \approx r_0 \left(1 + \frac{x_1^2 + y_1^2}{2\sqrt{z^2}\sqrt{z^2 + x_0^2 + y_0^2}} - \frac{x_1 x_0 + y_1 y_0}{z^2 + x_0^2 + y_0^2} \right). \tag{3.5}$$

This approximation significantly improves the estimation of the distance between the extreme points in the two planes if it is compared to the one used for the Fresnel approximation. The approximation errors are shown in figure 3.2. Inserting equation (3.5) into the Rayleigh-Sommerfeld diffraction integral (3.1) yields

$$\begin{aligned} U[x_1, y_1, z_1] \approx & \frac{1}{i\lambda} \int_{\mathbb{R}^2} U[x_0, y_0, z_0] \frac{z}{r_0^2} \\ & \exp\left[i\frac{2\pi}{\lambda} \left(\sqrt{z^2 + x_0^2 + y_0^2} + \frac{x_1^2 + y_1^2}{2\,z} - \frac{x_1 x_0 + y_1 y_0}{\sqrt{z^2 + x_0^2 + y_0^2}} \right) \right] \mathrm{d}x_0 \mathrm{d}y_0. \end{aligned} \tag{3.6}$$

In order to efficiently solve this integral equation, the fast Fourier transform has to be used. Hence, the same conditions have to be satisfied as in the case of the Fresnel approximation. This implies that the discretization points (x_0, y_0) should be chosen in such a way that they satisfy the following equation

$$\frac{x_1 x_0 + y_1 y_0}{\sqrt{z^2 + x_0^2 + y_0^2}} \stackrel{!}{=} \frac{x_1 x_s + y_1 y_s}{z}.$$

Here, x_s and y_s are the regular equidistant grid points used in the implementation of the Fresnel approximation based propagator. A simple calculation shows that

$$x_0 = \frac{x_s}{\sqrt{1 - \frac{x_s^2 + y_s^2}{z^2}}} \text{ and } y_0 = \frac{y_s}{\sqrt{1 - \frac{x_s^2 + y_s^2}{z^2}}}$$

satisfy this condition. Since this choice of sampling points corresponds to a variable transformation of the integration variable, the volume element changes according to the theorem of integral transformation.

$$\det \begin{bmatrix} \partial_{x_s} x_0[x_s, y_s] & \partial_{y_s} x_0[x_s, y_s] \\ \partial_{x_s} y_0[x_s, y_s] & \partial_{y_s} y_0[x_s, y_s] \end{bmatrix} = \frac{z^4}{(z^2 - x_s^2 - y_s^2)^2}$$

Using the transformation $\Phi : (x_s, y_s) \mapsto \left(\frac{x_s}{\sqrt{1 - \frac{x_s^2 + y_s^2}{z^2}}}, \frac{y_s}{\sqrt{1 - \frac{x_s^2 + y_s^2}{z^2}}} \right) = (x_0, y_0)$ and the identity $r_0 := \sqrt{z^2 + x_0^2 + y_0^2} = \sqrt{\frac{z^4}{z^2 - x_s^2 - y_s^2}}$, $U[x_1, y_1, z_1]$ is approximated by

$$U\left[x_1,y_1,z_1\right] \approx \frac{1}{i\lambda}\exp\left[i\frac{2\pi}{\lambda}\frac{x_1^2+y_1^2}{2z}\right]\int_{\mathbb{R}^2} U\left[\frac{x_s}{\sqrt{1-\frac{x_s^2+y_s^2}{z^2}}},\frac{y_s}{\sqrt{1-\frac{x_s^2+y_s^2}{z^2}}},z_0\right] \cdot\frac{z}{z^2-x_s^2-y_s^2}\exp\left[i\frac{2\pi}{\lambda}\left(\sqrt{\frac{z^4}{z^2-x_s^2-y_s^2}}-\frac{(x_1x_s+y_1y_s)}{z}\right)\right]\mathrm{d}x_s\mathrm{d}y_s.$$

The inverse formula is given by:

$$U\left[\frac{x_s}{\sqrt{1-\frac{x_s^2+y_s^2}{z^2}}},\frac{y_s}{\sqrt{1-\frac{x_s^2+y_s^2}{z^2}}},z_0\right] \approx \exp\left[-i\frac{2\pi}{\lambda}\sqrt{\frac{z^4}{z^2-x_s^2-y_s^2}}\right]\frac{z^2-x_s^2-y_s^2}{z}\int_{\mathbb{R}^2} i\lambda U\left[x_1,y_1,z_1\right] \cdot\exp\left[-i\frac{2\pi}{\lambda}\left(\frac{x_1^2+y_1^2}{2z}-\frac{(x_1x_s+y_1y_s)}{z}\right)\right]\mathrm{d}x_1\mathrm{d}y_1.$$

Secondly, the case of a larger output plane is considered.

This case is needed for the propagation from a focal plane to a second lens. As in the previous case, we approximate the distance by its Taylor approximation with regard to the coordinates of the larger plane. Now, we use $x_1^2+y_1^2 \ll z^2$ which results in the approximation

$$r_{01} \approx r_1\left(1+\frac{x_0^2+y_0^2}{2z^2}-\frac{(x_1x_0+y_1y_0)}{z^2+x_1^2+y_1^2}\right).$$

This yields again

$$U\left[x_1,y_1,z_1\right] \approx \frac{1}{i\lambda}\int_{\mathbb{R}^2} U\left[x_0,y_0,z_0\right]\frac{z}{r_1^2} \exp\left[i\frac{2\pi}{\lambda}\left(\sqrt{z^2+x_1^2+y_1^2}+\frac{x_0^2+y_0^2}{2\,z}-\frac{(x_1x_0+y_1y_0)}{\sqrt{z^2+x_1^2+y_1^2}}\right)\right]\mathrm{d}x_0\mathrm{d}y_0. \tag{3.7}$$

This time, the variables (x_1,y_1) are modified in the following way

$$x_1 = \frac{x_s}{\sqrt{1-\frac{x_s^2+y_s^2}{z^2}}} \text{ and } y_1 = \frac{y_s}{\sqrt{1-\frac{x_s^2+y_s^2}{z^2}}}$$

where (x_s,y_s) are now the regular grid points of the Fresnel approximation in the output plane. Since the variables of integration have not changed, the volume element does not change either. Using this relation between x_1,y_1 and x_s,y_s yields

$$U[x_1, y_1, z_1] \approx \frac{1}{i\lambda} \exp\left[i\frac{2\pi}{\lambda}\sqrt{\frac{z^4}{z^2 - x_s^2 - y_s^2}}\right]\left(\frac{z^2 - x_s^2 - y_s^2}{z^3}\right) \int_{\mathbb{R}^2} U[x_0, y_0, z_0] \exp\left[i\frac{2\pi}{\lambda}\left(\frac{x_0^2 + y_0^2}{2\,z} - \frac{x_s x_0 + y_s y_0}{z}\right)\right] \mathrm{d}x_0 \mathrm{d}y_0.$$

This integral approximation can again be solved by a Fourier transform. Therefore, the inverse approximation is given by:

$$U[x_0, y_0, z_0] \approx i\lambda \exp\left[-i\frac{2\pi}{\lambda}\frac{x_0^2 + y_0^2}{2\,z}\right] \int_{\mathbb{R}^2} U[x_1[x_s, y_s], y_1[x_s, y_s], z_1] \left(\frac{z^3}{z^2 - x_s^2 - y_s^2}\right) \exp\left[i\frac{2\pi}{\lambda}\frac{x_s x_0 + y_s y_0}{z} - \sqrt{\frac{z^4}{z^2 - x_s^2 - y_s^2}}\right] \mathrm{d}x_s \mathrm{d}y_s.$$

As previously stated, the wide-angle near and far field approximation is best used for applications where either the input or the output plane is much larger than the other. In most applications in this work, one gains little by using it since for small numerical apertures, the Fresnel approximation is almost as good. A typical case is shown in figure 3.3. However, in the case of large numerical apertures ($NA \gg 0.1$) the NFFA should be used. This was for example the case for the design of the diffractive optical element for the plasma based soft X-ray laser Fourier transform holography experiment in chapter 7. The typically large free space propagation distances between optic and focus also induce a second set of problems which is now further analyzed.

3.1.2 Converging Waves and the Fresnel Approximation

A common example for wave propagation is the focal pattern of a lens. It is also a good example to motivate the next set of approximations. For the focal pattern of a lens with high numerical aperture, the previously described approximations harbor some intrinsic problems.

The transmission function of a thin lens of focal length (f) and radius r_{max} is

$$T_{lens}[x, y] := \begin{cases} \exp\left[-ik\frac{x^2+y^2}{2f}\right] & x^2 + y^2 < r_{max}^2 \\ 0 & x^2 + y^2 \geq r_{max}^2 \end{cases}.$$

A simulation of the focal pattern resulting from a plane wave illuminating a lens is shown in figure 3.4. The images in 3.4b reveal one of the fundamental problems

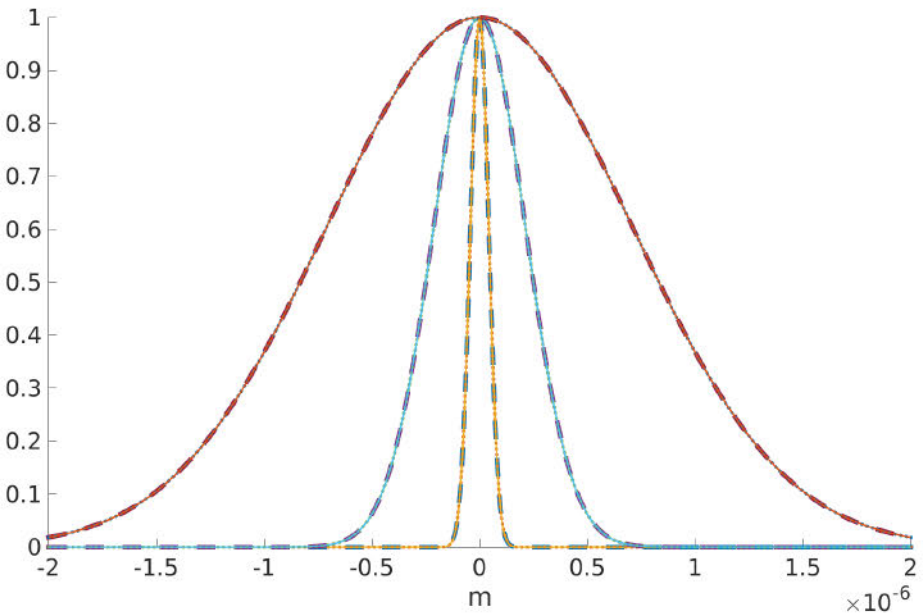

Figure 3.3: *A comparison between the analytic propagation of Gaussian beams (line) and the Fresnel (dots) and NFFA (dashed) based propagation.*
The Gaussian beams have a waist of 60, 300 and 1000 nm. The parameters for the simulation include a field of view of 2000x2000 pixels at 6 nm resolution. The radius of the aperture is 100 µm and the distance between the focal plane and the plane of the aperture is 0.5 mm. The wavelength is $\lambda = 2.4$ nm.

of the previous approximations. If the phase of the wave oscillates rapidly in comparison to the step size of the discretization, the undersampling of the wave generates numerical artifacts, the so-called Moire patterns.

For this reason, in numerical simulations it is sometimes advisable to separate one of the fields e.g. $U[x, y, z_0]$ or $U[x, y, z_1]$ into a simple fast oscillating function combined with an arbitrary, slowly varying function. An example is a converging wave front emerging from an optical element with focusing properties. In this case, the fast oscillating function is a converging spherical wave and the properties of the optical element are encoded in the slowly oscillating function (U_d) which modulates the spherical wave. That is $U[x_0, y_0, z_0] \stackrel{!}{=} U_d[x_0, y_0, z_0] \cdot \exp\left[-i\frac{2\pi}{\lambda} r_0\right]$. In this case, the modified equation (3.6) becomes

$$U[x_1, y_1, z_1] \approx \frac{1}{i\lambda} \int_{\mathbb{R}^2} U_d[x_0, y_0, z_0] \frac{z}{r_0^2} \exp\left[i\frac{2\pi}{\lambda}\left(\frac{x_1^2 + y_1^2}{2\,z} - \frac{(x_1 x_0 + y_1 y_0)}{\sqrt{z^2 + x_0^2 + y_0^2}}\right)\right] \mathrm{d}x_0 \mathrm{d}y_0.$$

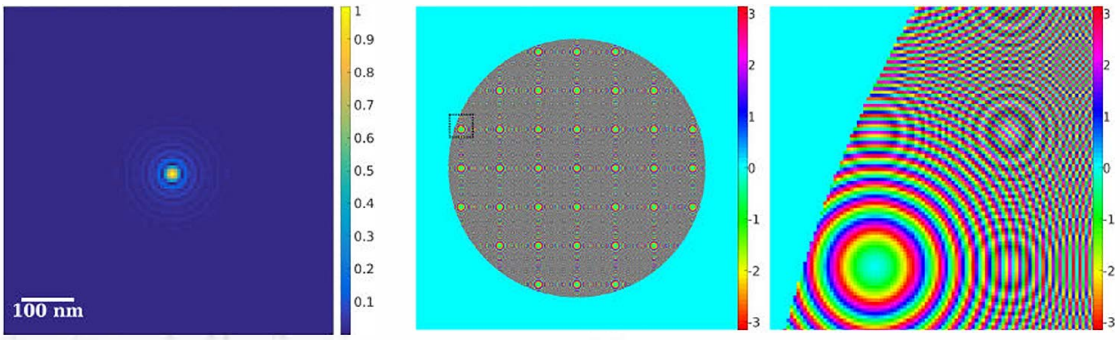

(a) Focal pattern of a lens **(b)** Moire patterns of the phase

Figure 3.4: *Simulation of the focal pattern of a lens illuminated by a plane wave. The discretization in the plane of the lens was chosen to be coarser than the fastoscillations of the transmission function. Except for the radius of the aperture, all parameters for the simulation are identical to the parameters from figure 3.3. The radius of the aperture is 40 µm. In figure 3.4a, the focal pattern is shown. The lens is illuminated by a plane wave and the pattern is computed with the Fresnel approximation. In figure 3.4b, the discretized phase is shown and the Moire patterns of the phase in the plane of the lens are obvious. This pattern results from an undersampling in the code of the Fresnel propagator. The right image shows the marked region enlarged so that the pixels are visible.*

Similar calculations analogously to the NFFA case of a larger input plane yield

$$U[x_1, y_1, z_1] \approx \frac{1}{i\lambda} \int_{\mathbb{R}^2} U_d \left[\frac{x_s}{\sqrt{1 - \frac{x_s^2+y_s^2}{z^2}}}, \frac{y_s}{\sqrt{1 - \frac{x_s^2+y_s^2}{z^2}}}, z_0 \right] \frac{z}{z^2 - x_s^2 - y_s^2} \cdot \exp\left[i \frac{2\pi}{\lambda} \left(\frac{x_1^2 + y_1^2}{2z} - \frac{(x_1 x_s + y_1 y_s)}{z} \right) \right] \mathrm{d}x_s \mathrm{d}y_s$$

and

$$U_d \left[\frac{x_s}{\sqrt{1 - \frac{x_s^2+y_s^2}{z^2}}}, \frac{y_s}{\sqrt{1 - \frac{x_s^2+y_s^2}{z^2}}}, z_0 \right] \approx \frac{z^2 - x_s^2 - y_s^2}{z} \int_{\mathbb{R}^2} i\lambda U[x_1, y_1, z_1] \cdot \exp\left[-i \frac{2\pi}{\lambda} \left(\frac{x_1^2 + y_1^2}{2z} - \frac{(x_1 x_s + y_1 y_s)}{z} \right) \right] \mathrm{d}x_1 \mathrm{d}y_1. \tag{3.8}$$

Equipped with these approximations, we can now simulate the free space propagations in our microscope. Before we start to study the still missing propagation through the sample, we describe how the partial derivatives of the field depend on the propagation distance and how we can use them to recover the phase of the field.

name	formula	advantage	disadvantage
Angular Spectrum Method (ASM)	convolution	applicable to a wide range of distances and plane sizes	not directly invertible same resolution in both planes
Fresnel approximation	Fourier transform	fast directly invertible	only valid for a small range of distances and plane sizes resolution in planes changes
NFFA	Fourier transform	fast directly invertible	only valid for a moderate range of distances and plane sizes grid is not equidistant resolution in planes changes

Table 3.1: *Comparison of the scope and advantages of the scalar propagators. In order to choose the best scalar propagator for a given task, one has to compare their disadvantages and advantages. For example, the ASM is often a bad choice for an iterative algorithm since it is not directly invertible.*

3.1.3 Propagation of Waves and Partial Derivatives in Different Planes

Sometimes, it is convenient to write the slowly varying function U_d as

$$U_d[x,y] = \exp[i\Phi[x,y]].$$

This is for example the case if higher orders of a FZP are considered. Usually, Φ cannot be recovered from a discretised U_d due to ambiguities of the covering $t \in \mathbb{R} \mapsto \exp[i\,t] \in \mathbb{S}^1 \subset \mathbb{C}$. Nevertheless, due to the relationship between U and U_d, the following steps lead to an explicit formula for Φ. Firstly, the partial derivatives of U_d are considered:

$$\begin{aligned}
\partial_x U_d &= \partial_x \exp[i\Phi] \\
&= \exp[i\Phi]\; i\,\partial_x\Phi \\
&= i\,U_d\,\partial_x\Phi \\
\partial_y U_d &= \cdots = i\,U_d\,\partial_y\Phi.
\end{aligned}$$

We can now deduce for any continuous Φ and continuous path $\Gamma : [0,1] \mapsto \mathbb{R}^2$ which starts in (x_0, y_0) and ends in (x, y) that

$$\begin{aligned}
\mathrm{d}U_d &= i\,U_d\,\mathrm{d}\Phi \\
\Phi[x,y] &= -i \int_\Gamma \frac{\overline{U_d}\mathrm{d}U_d}{\overline{U_d}U_d}\,\mathrm{d}s + \Phi[x_0,y_0].
\end{aligned}$$

Since $\mathrm{d}U_d$ and U_d can be computed independently from U, this expression resolves the ambiguity of Φ.

We now deduce U_d in one plane using U from another plane. The following calculation explicitly shows the relationship between U_d and U

$$\partial_{x_s} U_d\left[x\left[x_s,y_s\right],y\left[x_s,y_s\right]\right] \overset{(3.8)}{\approx} \partial_{x_s}\left(\frac{z^2-x_s^2-y_s^2}{z}\int_{\mathbb{R}^2} i\lambda U\left[x_1,y_1,z_1\right] \cdot\exp\left[-i\frac{2\pi}{\lambda}\left(\frac{x_1^2+y_1^2}{2z}-\frac{(x_1x_s+y_1y_s)}{z}\right)\right]\mathrm{d}x_1\mathrm{d}y_1\right).$$

If U satisfies the conditions of the theorem of differentiation under the integral sign, the partial differentiation follows from the product rule

$$\begin{aligned}\partial_{x_s} U_d \;=-\;& \frac{(z^2-x_s^2-y_s^2)}{z} \int_{\mathbb{R}^2} 2\pi\frac{x_1}{z}U\left[x_1,y_1,z_1\right]\exp\left[-i\frac{2\pi}{\lambda}\left(\frac{x_1^2+y_1^2}{2z}-\frac{(x_1x_s+y_1y_s)}{z}\right)\right]\mathrm{d}x_1\mathrm{d}y_1 \\ &-\frac{2\,x_s}{z}\int_{\mathbb{R}^2} i\lambda U\left[x_1,y_1,z_1\right]\exp\left[-i\frac{2\pi}{\lambda}\left(\frac{x_1^2+y_1^2}{2z}-\frac{(x_1x_s+y_1y_s)}{z}\right)\right]\mathrm{d}x_1\mathrm{d}y_1.\end{aligned}$$

Numerical simulations showed that the direct implementation of this formula is unstable and yields the correct solution only for sufficiently small derivatives. Hence, we primarily use it as an independent criterion to verify that a separation of a wave into a fast and a slowly oscillating function is justified.

A better working approach for the iterative phase reconstruction of Φ from U is shown in section 7.2.1 where it is used for the design of binary diffractive optical elements.

3.2 Simulating the Propagation of Soft X-rays in a Medium

In the last section, we studied the free space propagation of scalar waves. In order to include a sample into our microscopy simulations, we now study the propagation in an inhomogeneous medium. As mentioned in section §1, the inhomogeneous scalar Helmholtz equation

$$\Delta U + k_0^2 n^2 U = 0 \tag{3.9}$$

describes the propagation of a scalar field U within an inhomogeneous but slowly varying and weakly scattering material. In general, this equation is challenging, but some special cases are solved more easily and these solutions can be used to find numeric approximations to complex propagation problems. For the simulations in this thesis, we use the paraxial approximation, the (first) Born approximation and the projection approximation, or modified versions of these approximations.

If the light propagates essentially along the optical axis, the paraxial approximation simplifies the computations. For the paraxial approximation, the wave-field U is rewritten as the product of an enveloping function $\tilde{U}$ and a plane wave propagating along the optical axis (here z) $U = \tilde{U}[x, y, z] \exp[ik_0 z]$. Since it is assumed that the enveloping function is now slowly varying in z, the following inequality holds: $\left|\frac{\partial^2 \tilde{U}}{\partial z^2}\right| \ll \left|k_0 \frac{\partial \tilde{U}}{\partial z}\right|$. Substituting this into the Helmholtz equation yields:

$$\begin{aligned}
\left(\Delta + k_0^2 n^2\right) \tilde{U}[x, y, z] \exp[ik_0 z] &= 0 \\
\left(\Delta_\perp \tilde{U} + \cancel{\partial_{z,z} \tilde{U}} + 2\,i\,k_0\,\partial_z \tilde{U} - k_0^2 \tilde{U} + k_0^2 n^2 \tilde{U}\right) \exp[ik_0 z] &= 0 \\
\approx \left(\Delta_\perp \tilde{U} + 2\,i\,k_0\,\partial_z \tilde{U} + k_0^2 \left(n^2 - 1\right) \tilde{U}\right) \exp[ik_0 z] &= 0 \\
\approx \left(\Delta_\perp \tilde{U} + 2\,i\,k_0\,\partial_z \tilde{U} + k_0^2 \left(n^2 - 1\right) \tilde{U}\right) &= 0 \qquad (3.10)
\end{aligned}$$

which is equivalent to

$$\begin{aligned}
\Delta_\perp U + 2ik_0 \left(\partial_z U - ik_0 U\right) + k_0^2 \left(n^2 - 1\right) U &= 0 \\
\Delta_\perp U + 2ik_0 \partial_z U + k_0^2 \left(n^2 + 1\right) U &= 0.
\end{aligned}$$

This equation is vital for the simulations. In the simulations, it is numerically approximated. One example is the first Born approximation.

The First Born Approximation

The first Born approximation assumes that the incident field is not significantly changed due to the presence of the object. Therefore, the interaction of the object with the incident field is well described without taking into account the interaction of the field produced by the object with the object itself. For the first Born approximation applied to the paraxial approximation of the Helmholtz equation, the scalar wave-field $\tilde{U}$ is separated into an incident field $\tilde{U}_0$ which satisfies the paraxial homogeneous Helmholtz equation and a scattered field $\tilde{U}_s$. Applying this approach to equation (3.10) yields:

$$\begin{aligned}
\Delta_\perp \tilde{U}_0 + 2\,i\,k_0\,\partial_z \tilde{U}_0 &= 0 \\
\Delta_\perp \tilde{U} + 2\,i\,k_0\,\partial_z \tilde{U} + k_0^2\left(n^2-1\right)\tilde{U} &= 0 \\
\Delta_\perp \left(\tilde{U}_0 + \tilde{U}_s\right) + 2\,i\,k_0\,\partial_z \left(\tilde{U}_0 + \tilde{U}_s\right) + k_0^2\left(n^2-1\right)\left(\tilde{U}_0 + \tilde{U}_s\right) &= 0.
\end{aligned}$$

Using the decomposition, we obtain

$$\Delta_\perp \tilde{U}_s + 2ik_0\partial_z \tilde{U}_s + k_0^2\left(n^2-1\right)\left(\tilde{U}_0 + \cancel{\tilde{U}_s}\right) = 0.$$

Since the first Born approximation is used, the contribution of $\tilde{U}_s$ to the last sum is assumed to be negligible. Hence, the last equation can be approximated by

$$\Delta_\perp \tilde{U}_s + 2ik_0\partial_z \tilde{U}_s \approx k_0^2\left(1-n^2\right)\tilde{U}_0. \tag{3.11}$$

The convolution kernel of the Fresnel propagator is a Green function (fundamental solution) to this equation. Therefore, the solution is given by

$$\begin{aligned}
U_s\left[x,y,z\right] = \int_{\mathbb{R}^3} &\frac{\exp\left[ik_0\left(z-z'\right)\right]}{i\lambda} \exp\left[ik_0 \frac{\left(x-x'\right)^2 + \left(y-y'\right)^2}{2\left(z-z'\right)}\right] \\
&k_0^2\left(n^2-1\right) U_0\left[x',y',z'\right] \mathrm{d}x'\,\mathrm{d}y'\,\mathrm{d}z'.
\end{aligned} \tag{3.12}$$

The Projection Approximation

A second way to approximate equation (3.10) is to assume that the change of the field orthogonal to the propagation direction is slow so that the $\Delta_\perp \tilde{U}$ part is negligible. Then, the equation can directly be solved

$$\begin{aligned}
2\,i\,k_0\,\partial_z \tilde{U} &\approx k_0^2\left(1-n^2\right)\tilde{U} \\
\Longrightarrow \tilde{U}\left[x,y,z\right] &\approx \tilde{U}\left[x,y,z_0\right] \exp\left[\frac{k_0}{2i}\int_{z_0}^{z}\left(1-n^2\left[x,y,z'\right]\right)\mathrm{d}z'\right].
\end{aligned} \tag{3.13}$$

The resulting formula is also called the projection approximation.

The Multislice Method

For our simulations, we usually use a version of the multislice method [21, 95]. In this approximation, the inhomogeneous medium is subdivided into slices perpendicular to the direction of the wave propagation. The main idea is to separate the diffraction caused by the propagation through the slice and the phase and amplitude shift caused by the inhomogeneous medium in the slice.

If the slice starts at z and ends at $z + \Delta z$, the field $U[x, y, z]$ is propagated to $z + \Delta z$ by any wave propagator for a homogeneous medium. The effect of the inhomogeneous medium is then taken into account by multiplying with

$$\exp\left[\frac{k_0}{2i}\int_z^{z+\Delta z}\left(1 - n^2[x, y, z']\right)\mathrm{d}z'\right]$$

as in the projection approximation. It should be highlighted that this approximation differs from the first Born approximation since it includes the attenuation of the incident wave.

Classical implementations use Fourier transform based convolution in each propagation step. It is well known that these numerical implementations produce artifacts along the border of the simulated field which propagate further into the center for successive slices.[2] Since in our simulations, only X-rays passing through the optics are important, we chose to ignore evanescent waves and use a combination of Fresnel forward and backward propagation for the free propagation step. The advantage of this method in comparison to the commonly used direct layer to layer propagation is that we can pad the starting field in such a way that the artifacts do not occur in the region of interest. A sufficiently large padding protects the region of interest since the artifacts propagate inwards at approximately the same angle as the aperture of the lens.

Summary

In this chapter, we have introduced the basics of all the numerical methods used in this thesis. These numerical methods are used in the following chapters to simulate and analyze different soft X-ray imaging methods. We start our analysis in the next chapter with soft X-ray based tomography.

[2] These artifacts can be suppressed by including perfectly matched layers.

Chapter 4

Simulation of 3D Soft X-ray Imaging by Tomography

Soft X-ray 3D nanoscale imaging is a complex process. As discussed before, one of the most successful approaches is based on tomography. Classical tomography assumes that light travels through the object along straight, parallel beams without any diffraction. Along these paths, the intensity decreases in accordance with the Beer-Lambert law.

In a full-field soft X-ray transmission microscopy setup, X-ray lenses form an enlarged image of the object. For soft X-rays, the optics are Fresnel zone plates which are diffraction based and have a depth of focus similar or smaller than the thickness of the sample. Therefore, the Beer-Lambert law based line integral approach of classical tomography is not perfectly fulfilled.

4.1 A Cell-like Phantom for Tomography

In order to study the imaging properties of an optical system, it is essential to define a well-suited 3D test object. Properties like the resolution, the depth of focus, the field of view and the contrast transfer can be deduced by comparing the image of the object with the original object. Our simulations will show that some properties of the optical system are only apparent in images of extended 3D objects.

In this thesis, different soft X-ray setups for 3D imaging of cryogenic biological samples are investigated and compared. A good example for the 3D imaging capabilities of a transmission soft X-ray microscope is shown in figure 4.1. For the numerical investigations a cell like phantom is required. This phantom should reflect the most important structures of cells. Our phantom contains long annular objects which have similar optical properties to microtubules as well as filled

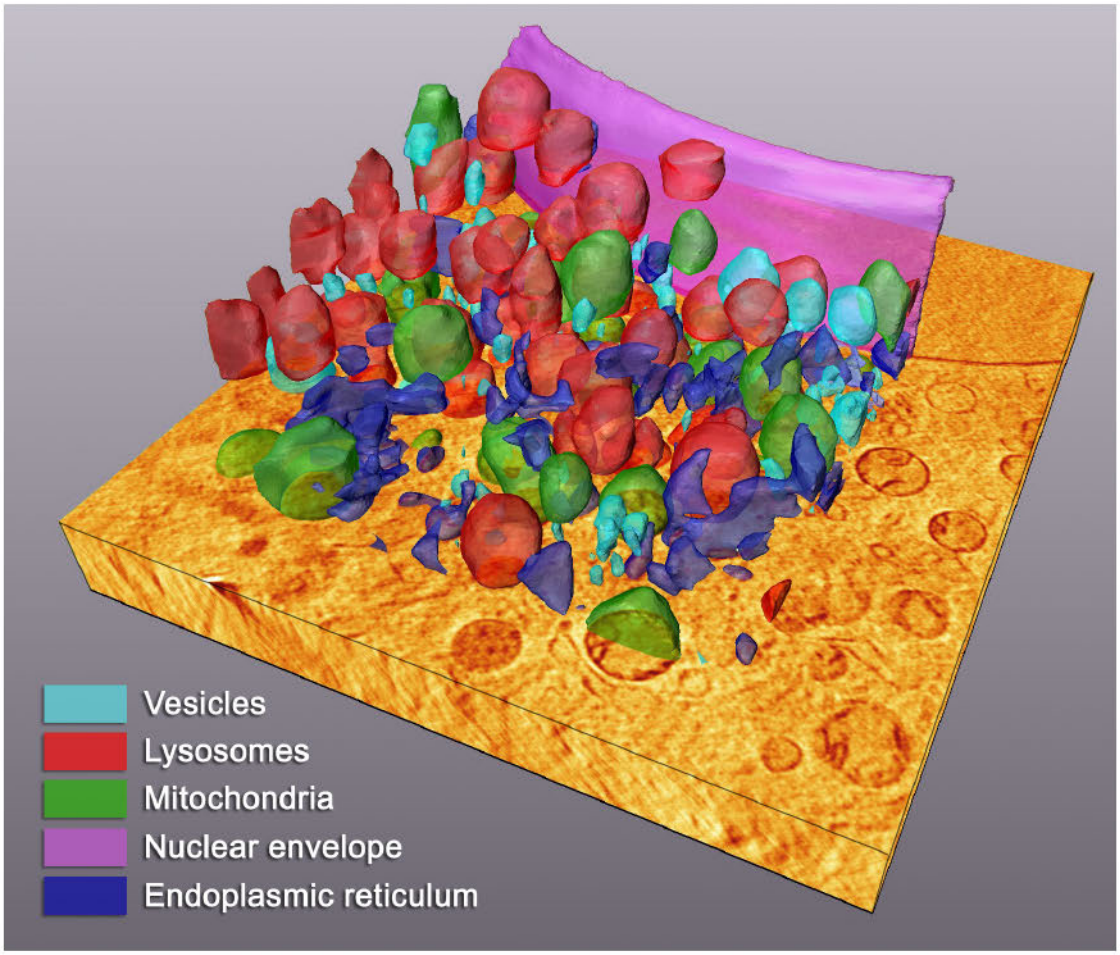

Figure 4.1: *This volumetric rendering highlights the discernible components of the cytoplasm as well as the nuclear envelope. The original TXM based tomogram is shown in orange. A complete description of the method as well as the sample and additional images are presented in [83]. Image was provided by the authors of [83], and used with their permission.*

cylinders which represent chromatin. Membranes are simulated by elliptical surfaces with a thickness of a few nanometers. The phantom has to be larger than the depth of focus in order to include the effects of image degeneration due to the limited depth of focus.

The complex refractive index for each type of phantom structure incorporates their known molecular composition. In addition, the complex refractive indices for microtubules and chromatin take into account that these biological structures are hydrated. In contrast, the inside of membranes are hydrophobic and thus contain almost no additional water. The average empirical formulas for the components

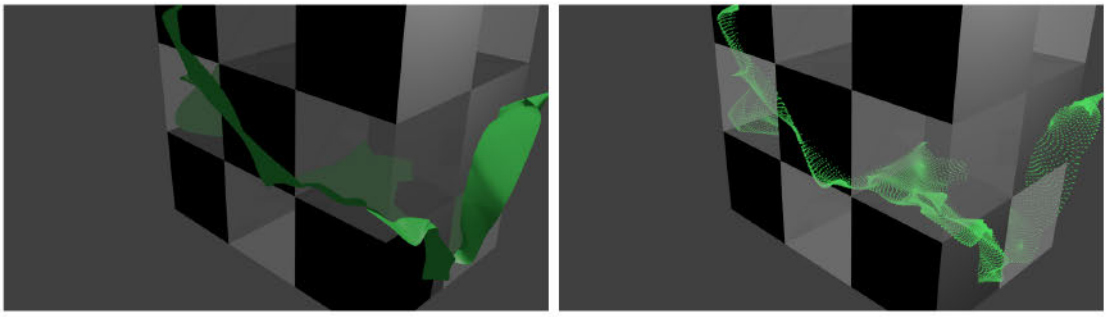

(a) Non-discretized version **(b)** Discretized version

Figure 4.2: *Discretization of a biological membrane for the TXM simulation. The black and transparent boxes represent voxels while the green surface respectively dots represent a membrane.*

are given in table 4.1

The creation of a 3D phantom seems simple. One could, for example, start with an orthogonal 3D grid and identify the nodes of the grid with the surrounding volume. These voxels represent the structures of the phantom. The optical properties of each voxel are defined by the optical properties of the phantom at the center of the voxel, i.e. at the position of the node. Unfortunately, this approach is not feasible on a normal computer since the amount of memory needed for the storage of the phantom would be quite large. For example, a volume of $1\,\mu m^3$ at a resolution of 2.5 nm requires 1 GB of data storage. Additionally, the computational time needed to rotate the phantom is also quite long. Even worse is the effect that the sampling on the grid generates aliasing artifacts. This results in an extremely small allowable discretization step size well below the resolution and wavelength used for imaging (see also figure 4.3).

Another approach is more convenient for phantoms which mainly consist of one medium and some sparse structures, the latter occupying only a small fraction of the volume. For the subsequent simulations, it is necessary that the phantom is discretized on a grid, with each node representing a small voxel. In contrast to the previous approach, the optical parameters of the voxels are calculated by averaging over randomly chosen sub sampling points. The random data set is created by overlaying the volume of the particles with a cloud of randomly chosen sampling points, as illustrated in figure 4.2. The optical properties of each sampling point are set in accordance to the optical properties of the component that the sampling point represents. In this way, the object is now described as a set of points together with an optical point density. In order to obtain a good approximation, the randomly chosen points have to be homogeneously distributed.[1] It should be

[1] One can achieve a homogeneous distribution by describing the component as embedded

noted that this approach does not generate an exact copy of the object and that the discretization still generates a small error. However, aliasing effects are reduced due to the random nature of the underlying sampling points. A comparison between the two approaches is shown in figure 4.3. Additionally, the latter approach has the advantage that it reduces the computational effort to rotate and shift the phantom.[2]

Cell component	Chemical formula	Volume (nm^3)	Chemical formula with H_2O	Density $\left(\frac{g}{cm^3}\right)$	δ-value at 2.4 nm	β-value at 2.4 nm
Chromatin	C_{8151} H_{12797} N_{2791} O_{3240} P_{292} S_{24}	523	C_{8151} H_{29604} N_{2791} O_{11644} P_{292} S_{24}	1.306	8.36E-4	1.57E-4
Microtubule	C_{2186} H_{3365} N_{591} O_{684} S_{25}	536	C_{2186} H_{4429} N_{591} O_{121} S_{25}	1.426	10.03E-4	2.37E-4
Membrane	C_{74176} H_{113200} N_{2066} O_{15424} P_{1120} S_{400}	536	-	1.167	9.09E-4	2.12E-4
Cytoplasm	-	1000	C_{2186} H_{65651} N_{591} O_{31827} S_{23}	1.036	5.7E-4	0.37E-4
Water	H_2O	-	-	1	5.3E-4	0.21E-4

Table 4.1: *Empirical formulas and X-ray optical properties of some selected cell components.*

manifolds. By using a chart of the corresponding manifold, a density mapping can be deduced from the fundamental determinant.

[2]The values for the complex index of refraction were estimated with the help of the data listed in the Henke tables which can be found e.g. on the CXRO webpage: http://henke.lbl.gov/optical_constants/getdb2.html. They result from equation (2.2).

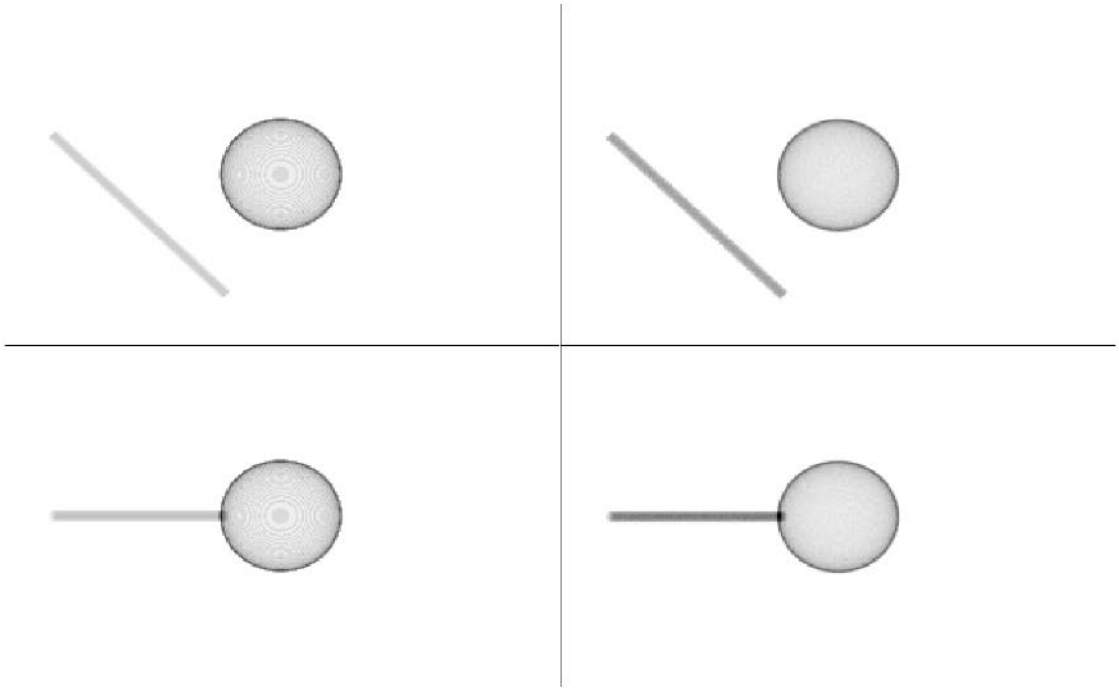

Figure 4.3: *Two orthogonal projections of a phantom consisting of a hollow sphere and a filled cylinder for two construction algorithms. The resulting cylinder on the left side looks flat and the sphere shows aliasing artifacts.*
Left: *Object discretised on an orthogonal grid. A voxel is filled if the center is located inside the object's borders.*
Right: *The object is approximated by a cloud of randomized points. The value of a voxel is the weighted sum of all points of the cloud that lie within the voxel's border.*

4.2 Transmission Soft X-ray Microscopy

In what follows, the performance of transmission soft X-ray microscopes for biological samples is studied. As described in chapter 2, an extended sample is illuminated with a wide X-ray spot in the transmission X-ray microscope (TXM). The X-ray optical setup is illustrated in figure 2.6a. The partial coherence factor

$$\left(\sigma = \frac{NA_C}{NA_O}\right)$$

characterizes the degree of coherence introduced by the ratio of the numerical aperture of the condenser (NA_C) and objective (NA_O). A value close to 0 corresponds to a high degree of coherence, while for $\sigma \gg 1$ the degree of coherence is dominated by the coherence of the source.

The illuminating photons are partly absorbed by the sample. The resulting wave field is collected by a Fresnel zone plate which forms an image on the detector. The description of the imaging process is especially simple if a fully incoherent illumination is assumed. For incoherent illumination, the imaging process can be described by the transmittance of the object and the 3D incoherent point spread function of the FZP. This description is based on a lateral convolution. The 3D incoherent point spread function of the FZP represents the image on the detector of an on-axis point source at given distance in front of the FZP.

4.2.1 Incoherent TXM Simulation

If the illumination of the sample is to a good approximation incoherent, the 3D incoherent point spread function of the FZP can be used to approximate the resulting image of the sample. In this case, the sample is imaged based on absorption contrast.

For the simulation, we use the phantom described in section §4.1, which represents typical biological structures. In order to obtain a 3D image of the phantom, a series of images under different tilt angles is simulated. Tomographic reconstructions of the phantom are computed from this tilt series. The theory behind tomography is explained in section 4.2.2.

An early implementation used an incoherent version of the first Born approximation. The first Born approximation and the algorithm work well for thin samples. The first Born approximation is also used to analyze the imaging process of weakly scattering samples. Similar to the coherent case, the signal is divided into an incident field I_0 and a scattered field I_s. Since we assume that the scattered field is much weaker than the incident field, its interaction with the sample is negligible. We assume that the imaging process is linear in intensities. By considering the signal that a single point source at (x, y, z) generates on the detector, one gets a function $F : \mathbb{R}^2 \times \mathbb{R}^3 \to \mathbb{R}$. This function allows us to compute the resulting image of a complicated intensity distribution $I_s : \mathbb{R}^3 \to \mathbb{R}$. Let S be the support of the sample. The signal on the detector (at $(\hat{x}, \hat{y})$) is then given by

$$\begin{aligned} I[\hat{x}, \hat{y}] &\approx I_0 - I_s \\ &= I_0[\hat{x}, \hat{y}] - \int_S F[\hat{x}, \hat{y}, x, y, z]\, I_s[x, y, z]\, \mathrm{d}x\, \mathrm{d}y\, \mathrm{d}z. \end{aligned}$$

If it is assumed that for a fixed z plane, the image of a point source near the optical axis is similar to the one on the axis, the integration can be simplified. Under these conditions, the image of an off-axis point source is the same as the image of an on-axis source which is translated from the axis with a (z-dependent) factor of magnification M. Therefore, the function F depends only on the difference between $(\hat{x}, \hat{y})$ and $M \cdot (x, y)$. From now on, the resulting function is called

the $(IPSF)$. The signal on the detector is now given by

$$I[\hat{x},\hat{y}] = I_0[\hat{x},\hat{y}] - \int IPSF[\hat{x} - M[z]\,x, \hat{y} - M[z]\,y, z]\, I_s[x,y,z]\,\mathrm{d}x\,\mathrm{d}y\,\mathrm{d}z.$$

In an abuse of notation, we now introduce a scaled version of $IPSF$ without introducing a new name. The image of a z-slice (S_z) of the phantom is then given by

$$I \approx I_0 - \int_{S_z} IPSF\left[\frac{1}{M}\hat{x} - x, \frac{1}{M}\hat{y} - y, z\right] I_s[x,y,z]\,\mathrm{d}x\,\mathrm{d}y\,\mathrm{d}z.$$

which can be computed by convolution. We started our investigations by implementing this algorithm. It was later rejected because it produced in some cases bad results, such as negative intensities. Since this approximation does not take into account the depletion of the incident radiation, a scattering signal which is stronger than the original signal can be produced.[3] In order to account for the attenuation of the incident wave, we use an approach which is very similar to beam propagation and the multislice method for waveguides and transmission electron microscopy [95, 21]. We start by dividing the phantom into slices perpendicular to the direction of the propagation. Let us assume that the thickness (Δz) of such a slice is significantly smaller than the depth of focus. Then, we can apply the projection approximation (equation (3.13)) so that each slice is characterized by the 2D transmission function

$$\begin{aligned} T_z[x,y] &= \exp\left[\int_z^{z+\Delta z} -2k\beta[x,y,z]\;\mathrm{d}z\right] \\ &= \exp\left[-2k\overline{\beta}[x,y]\;\Delta z\right]. \end{aligned}$$

Due to the discretization, the absorption coefficient $\overline{\beta}$ is averaged over the voxel.

The absorption in the slice reduces the signal on the detector in comparison to the unperturbed beam. The quotient of obscured to unperturbed signal is called the relative signal. Since the illumination is incoherent, the next slice modifies the image on the detector again in the same way. According to this approach, the resulting relative signal on the detector is the product of the relative signals of each slice

$$I[\hat{x},\hat{y}] \approx I_0[\hat{x},\hat{y}] \prod_{z_i} \frac{\int_{\mathbb{R}^2} IPSF\left[\frac{1}{M}\hat{x} - x, \frac{1}{M}\hat{y} - y, z_i\right] I[x,y,z_i]\, T_{z_i}[x,y]\,\mathrm{d}x\,\mathrm{d}y}{\int_{\mathbb{R}^2} IPSF\left[\frac{1}{M}\hat{x} - x, \frac{1}{M}\hat{y} - y, z_i\right] I[x,y,z_i]\,\mathrm{d}x\,\mathrm{d}y}. \quad (4.1)$$

[3] For example, a $0.3\,\mu\mathrm{m}$ thick layer of ice has at $\lambda = 2.4\,\mathrm{nm}$ a transmission of ≈ 0.9676 according to equation (3.13). But with the first Born approximation, the value would be ≈ 0.9673 for the case of incoherent absorption contrast. For a coherent system, the first Born approximation has already broken down since $\frac{|U_0+U_s|^2}{|U_0|^2} \approx 1.14$ in accordance with equation (3.11).

Here, z_i is the z coordinate of the face of each slice as used in the definition of T_z. I_0 is the intensity on the detector without the sample. A matlab implementation of this approach is explained in section B.2.2.

4.2.2 3D Imaging with Tomography

As described in the previous section, the detectors of soft X-ray transmission microscopes usually only gather a two dimensional image. This image represents a projection along the direction of the optical axis. Nevertheless, it is feasible to recover the three dimensional structure of an investigated sample. One of the most successful methods is soft X-ray tomography. In the following, a short introduction is given which follows the explanations in [19]. It is assumed that the three dimensional structure is represented by a function $g : \mathbb{R}^3 \to \mathbb{C}$. The Radon transformation enables recovery of the function g from its projections.[4]

The main idea is to use a rotation of the reference frame. The transformation is

$$T_\theta : \begin{pmatrix} x \\ y \\ z \end{pmatrix} \mapsto \begin{pmatrix} x' \\ y' \\ z' \end{pmatrix} = \begin{pmatrix} \cos[\theta] & 0 & \sin[\theta] \\ 0 & 1 & 0 \\ -\sin[\theta] & 0 & \cos[\theta] \end{pmatrix} \begin{pmatrix} x \\ y \\ z \end{pmatrix}.$$

The inverse transformation of this rotation is given by

$$T_\theta^{-1} : \begin{pmatrix} x' \\ y' \\ z' \end{pmatrix} \mapsto \begin{pmatrix} x \\ y \\ z \end{pmatrix} = \begin{pmatrix} \cos[\theta] & 0 & -\sin[\theta] \\ 0 & 1 & 0 \\ \sin[\theta] & 0 & \cos[\theta] \end{pmatrix} \begin{pmatrix} x' \\ y' \\ z' \end{pmatrix}.$$

Let $g : (x, y, z) \in \mathbb{R}^3 \to \mathbb{C}$ be a function and $p_\theta : (x', y') \to \mathbb{C}$ be a family of projections defined by

$$\begin{aligned} p_\theta[x', y'] : &= \int_{\mathbb{R}} g \circ T_\theta^{-1}[x', y', z']\, dz' \\ &= \int_{\mathbb{R}} g[x'\cos[\theta] - z'\sin[\theta], y', x'\sin[\theta] + z'\cos[\theta]]\, dz'. \end{aligned}$$

The projections are along the z' axis of the rotated reference frame. It is now convenient to consider each y slice separately. We therefore now drop the y dimension.

[4] In soft X-ray tomography, one assumes that the function g is equal to the attenuation coefficient (μ). According to the Beer-Lambert law, the change of measured intensity along a straight line from p_0 to p_1 is equal to the exponential of the negative of the integral of the attenuation coefficient along the line, i.e $I[p_1] = I_0[p_0] \exp\left[\int_0^{|p_1-p_0|} -\mu\left[s\frac{p_1-p_0}{|p_1-p_0|} + p_0\right] \mathrm{d}s\right]$. Therefore, one has $\ln\left[\frac{I[p_1]}{I[p_0]}\right] = \int_0^{|p_1-p_0|} -\mu\left[s\frac{p_1-p_0}{|p_1-p_0|} + p_0\right] \mathrm{d}s$.

The projection slice theorem relates the one dimensional Fourier transform P_θ of p_θ and the two dimensional Fourier transform G of g along a corresponding θ-slice.

$$\begin{aligned} P_\theta[f] &:= \int_{\mathbb{R}} p_\theta[x'] \exp[-i\,2\pi f \cdot x']\,\mathrm{d}x' \\ &= \int_{\mathbb{R}^2} g'[x', z'] \exp[-i\,2\pi f \cdot x']\,\mathrm{d}z'\mathrm{d}x' \\ &= \int_{\mathbb{R}^2} g[x'\cos[\theta] - z'\sin[\theta], x'\sin[\theta] + z'\cos[\theta]] \exp[-i\,2\pi f \cdot x']\,\mathrm{d}x'\mathrm{d}z' \\ &= \int_{\mathbb{R}^2} g[x, z] \exp[-i\,2\pi f \cdot (x\cos[\theta] + z\sin[\theta])]\,\mathrm{d}x\,\mathrm{d}z \\ &=: G[f\cos[\theta], f\sin[\theta]]. \end{aligned} \tag{4.2}$$

With this relationship between P_θ and G, g can be reconstructed from P_θ alone.

$$\begin{aligned} g[x, z] &= \int_{\mathbb{R}^2} G[f_x, f_z] \exp[i2\pi(f_x x + f_z z)]\,\mathrm{d}f_x\,\mathrm{d}f_z \\ &= \int_0^\pi \int_{\mathbb{R}} G[f\cos[\theta], f\sin[\theta]] \exp[i2\pi f(x\cos[\theta] + y\sin[\theta])]\,|f|\,\mathrm{d}f\,\mathrm{d}\theta \end{aligned} \tag{4.3}$$

According to equation (4.2), the inner integral is given by:

$$\begin{aligned} &\int_{\mathbb{R}} G[f\cos[\theta], f\sin[\theta]] \exp[i2\pi f(x\cos[\theta] + y\sin[\theta])]\,|f|\,\mathrm{d}f \\ = &\int_{\mathbb{R}} f P_\theta[f] \operatorname{sign}[f] \exp[i2\pi f x']\,\mathrm{d}f. \end{aligned}$$

By the convolution theorem, the last integral is equal to

$$\begin{aligned} &\int_{\mathbb{R}} f P_\theta[f] \cdot \operatorname{sign}[f] \exp[i2\pi f x']\,\mathrm{d}f \\ = &\left(\int_{\mathbb{R}} f P_\theta[f] \exp[i2\pi f x']\,\mathrm{d}f\right) * \left(\int_{\mathbb{R}} \operatorname{sign}[f] \exp[i2\pi f x']\,\mathrm{d}f\right) \\ = &\frac{1}{i2\pi}\frac{\partial}{\partial x'} p_\theta[x'] * \frac{-1}{i\pi x'} \\ = &\frac{1}{2\pi^2}\int_{\mathbb{R}} \frac{\partial p_\theta[\hat{x}]}{\partial \hat{x}} \frac{1}{x' - \hat{x}}\mathrm{d}\hat{x}. \end{aligned}$$

This finally leads to the recovery of $g[x, z]$ from the projections p_θ by equation (4.3)

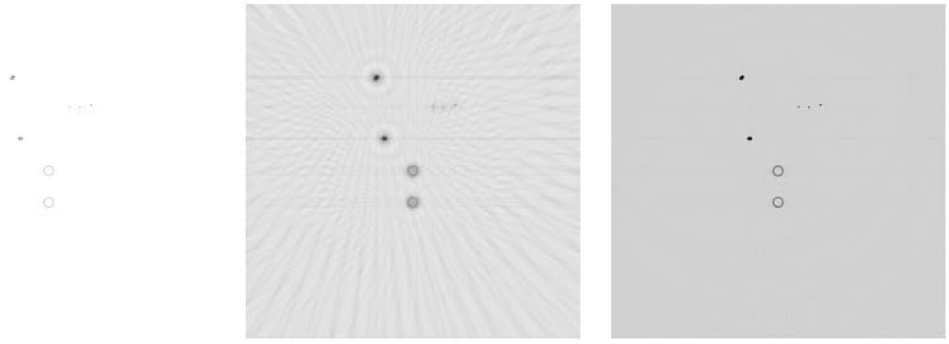

(a) Phantom **(b)** -90° to 90° in 5° steps **(c)** -90° to 90° in 1° steps

Figure 4.4: *The effect of the choice of tilt steps on the tomographic reconstruction is visualized. The reconstructions are based on ray projections.*
(a) *Projection of the phantom*
(b) *Reconstruction based on projections from -90° to 90° at 5° steps*
(c) *Reconstruction based on projections from -90° to 90° at 1° steps*

$$\begin{aligned} g[x,z] &= \int_0^{\pi} \frac{1}{2\pi^2} \int_{\mathbb{R}} \frac{\partial p_\theta[\hat{x}]}{\partial \hat{x}} \frac{1}{x' - \hat{x}} \mathrm{d}\hat{x}\, \mathrm{d}\theta \\ &= \int_0^{\pi} \frac{1}{2\pi^2} \int_{\mathbb{R}} \frac{\partial p_\theta[\hat{x}]}{\partial \hat{x}} \frac{1}{x\cos[\theta] + y\sin[\theta] - \hat{x}} \mathrm{d}\hat{x}\, \mathrm{d}\theta. \end{aligned}$$

We now reintroduce the previously dropped dimension y and finally get

$$g[x,y,z] = \int_0^{\pi} \frac{1}{2\pi^2} \int_{\mathbb{R}} \frac{\partial p_\theta[\hat{x},y]}{\partial \hat{x}} \frac{1}{x' - \hat{x}} \mathrm{d}\hat{x}\, \mathrm{d}\theta.$$

Intrinsically, this approach has some experimentally and theoretically challenging features. Typically, the sample is rotated and a certain number of projections are taken. In practice, it is often not possible to rotate the sample by $\pm 90°$. For a perfect reconstruction of g, theoretically all projections in the θ-values from 0 to π are needed. The fact that only a finite number of them are taken reduces the sampling in Fourier space. Therefore, only a band limited approximation of g is recovered. Tilt steps that are too large result in artifacts, as shown in figure 4.4. Furthermore, if the θ-values are limited to less than the full 180°, the reconstruction includes missing cone artifacts. The "missing cone" refers to the missing cone of projections and, therefore, to the missing cone in the coverage of Fourier space. The effect on the reconstruction is shown in figure 4.5.

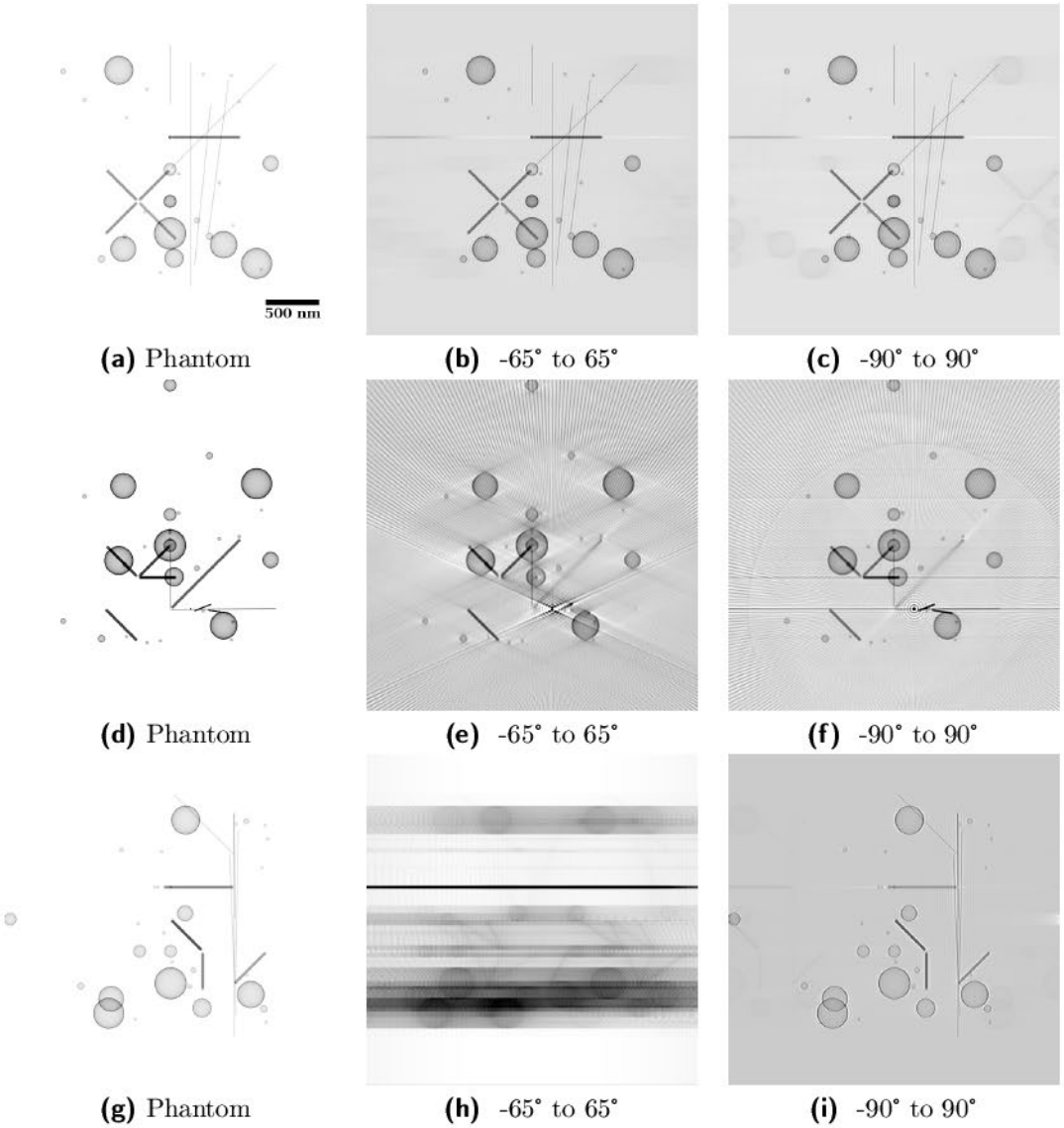

Figure 4.5: *Missing cone artifacts due to the limited range of tilt of the projections. The reconstructions are based on classical tomography assumptions. The resulting 3D tomographic reconstruction is then projected along one direction. In each row, a different projection direction is shown.* ***(a-c)*** *projection along the optical axis;* ***(d-f)*** *projection along the rotational axis;* ***(g-i)*** *projection perpendicular to the optical and rotational axis. In the first column, projections of the phantom are shown, while in the second column projections of the tomographic reconstruction for a data set of -65° to 65° with a 1° step size are shown. In the last column, projections of the tomographic reconstruction for a data set of -90° to 90° with a 1° step size are shown.*

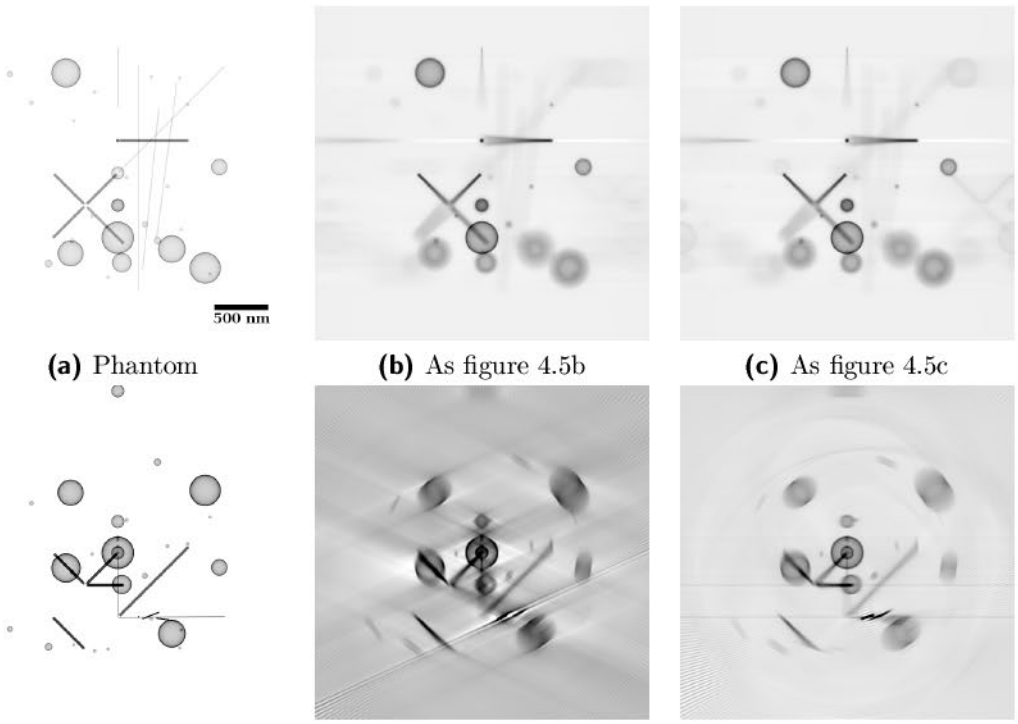

(a) Phantom **(b)** As figure 4.5b **(c)** As figure 4.5c

(d) Phantom **(e)** As figure 4.5e **(f)** As figure 4.5f

Figure 4.6: *The violation of the projection slice theorem due to the limited depth of focus causes additional artifacts in the tomographic reconstruction. The 3D tomographic reconstruction is again projected as in the previous figure but now the effect of the limited depth of focus on the reconstruction is included.*
In the upper row (a-c), the projection along the optical axis is shown. In the lower row, the projection is along the direction of the rotational axis. The first column shows the phantom, while the second and third columns show tomographic reconstructions from data sets with angles from -65° to 65° (b,e) and -90° to 90° (c,f) in 1° steps. The simulations were performed for a Fresnel zone plate with outermost zone width of $dr_N = 10\,nm$.

Additionally, the imaging properties of high resolution Fresnel zone plates violate the assumptions used in the projection slice theorem (4.2). The soft X-ray beam spreads out due to the wave nature of the light. Therefore, the projection assumption of the projection slice theorem is not perfectly fulfilled. Instead, the images on the detector are described by the integral given in equation (4.1). This integral is essentially a convolution with the point-spread function of the zone plate. The resulting effect on the reconstruction is shown in figure 4.6. Parts of

the sample which are outside the depth of focus appear blurred. Only within the depth of focus, the line integral is a good approximation.

4.2.3 Comparison of Experimental TXM Images and Incoherent Simulation

In this section, we compare experimental data with a simulation for the case of an incoherent illumination. In an abuse of notation we will call the simulation incoherent. The sample consists of Au spheres with a polymer core with a diameter of 270 nm on a carbon-foil with 2.4 µm holes. The sample was imaged under tilt angles from -70° to 70° in 1° steps. The final 3D reconstruction was performed with the weighted back-propagation algorithm as implemented in TomoJ [54].

A comparison between an experimental image and the result of an incoherent simulation is shown in figure 4.7. The comparison shows that the depth of focus is similar, but some features of the experimental data are not explained by this model. These features include halos around the holes, as well as an increased contrast at their edges. The experimental data exhibits an asymmetric blurring

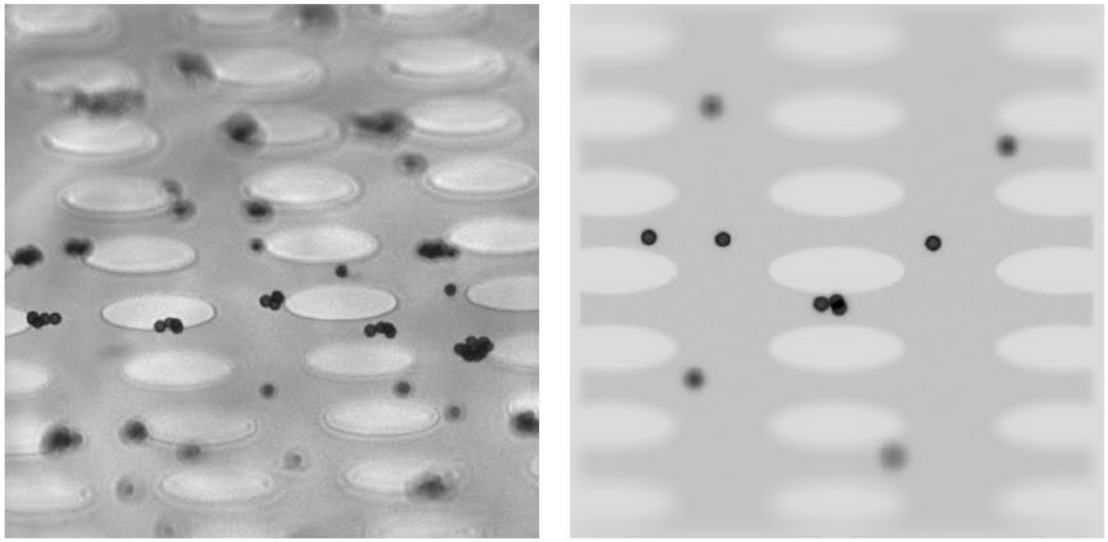

(a) Experimental TXM image **(b)** Incoherent TXM simulation

Figure 4.7: *Comparison of real TXM and simulated incoherent images. The tilt is 70° and the FZP has a* $dr_N = 40\,\text{nm}$.
(a) *An image of 270 nm hollow Au spheres on a carbon foil with 2.4 µm holes is shown. The image was taken with the TXM at the U41-FSGM beamline at the Helmholtz Zentrum Berlin.*
(b) *An incoherent simulation of a similar object as in figure 4.7a is shown.*

of the nanoparticles in regard to the distance to the focal plane. This effect is not observed in the simulation.

A comparison between the 3D tomographic reconstruction from experimental data and the corresponding reconstruction from a series of incoherent simulations is presented in figure 4.8. We show selected slices from these reconstructions. One slice is perpendicular to the optical axis while the other slice is perpendicular to the tilt axis. The reconstructions show a higher degree of similarity.

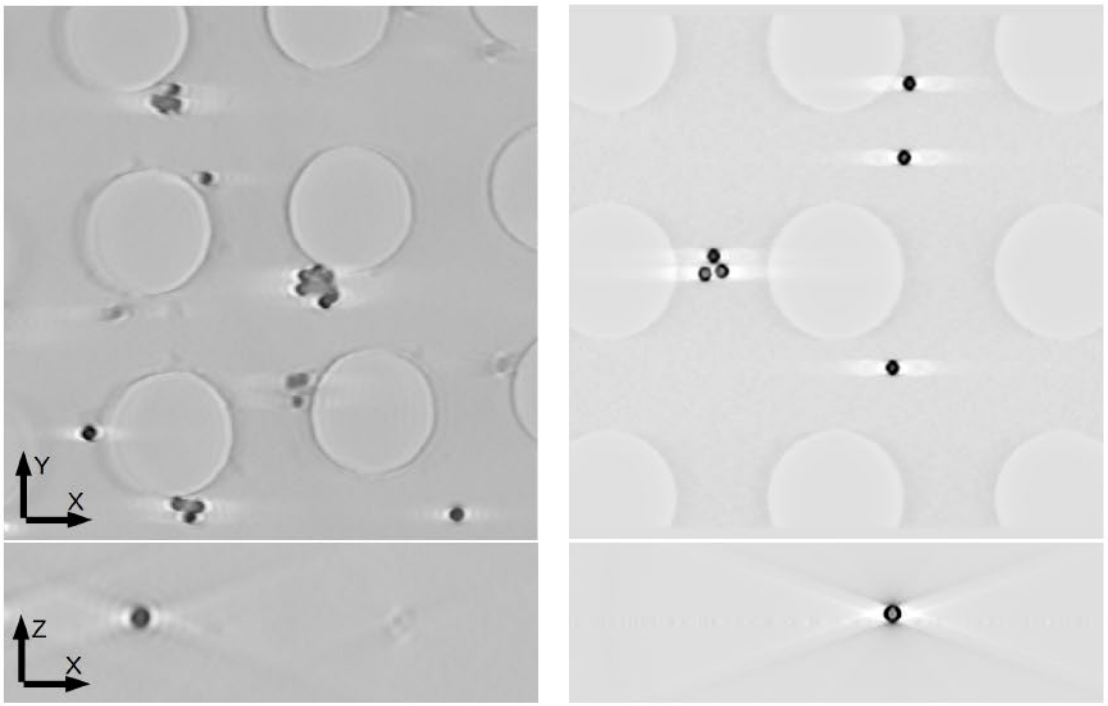

(a) Reconstruction experiment **(b)** Reconstruction incoherent

Figure 4.8: *Comparison of real TXM and simulated incoherent tomograms. The xy-slice is orthogonal to the optical axis. The xz-slice is orthogonal to the rotation axis and shows the effect of the missing cone artifacts.*
(a) *Tomographic reconstruction of the experimental data from figure 4.7a.*
(b) *Tomographic reconstruction of the simulated data from figure 4.7b.*

4.2.4 Partially Coherent TXM Simulation

The assumption of an incoherent illumination does not perfectly describe the imaging process in our TXM. This is due to a mismatch between the numerical aperture of the condenser and the imaging Fresnel zone plate which results in a partially coherent illumination of the sample. Therefore, a simulation of a partially coherent TXM was developed and implemented. In other works, finite difference methods

(FDM) were used to solve the 3D propagation through the sample [85]. Since FDM are known to produce artifacts and are relatively slow, a different approach is used. In addition, the imaging properties of the condenser are included.

The simulation steps are:

1. construction of a phantom
2. calculation of the set of inbound illuminating fields
3. description of the propagation through the phantom for each field according to a modified multislice approach as described in section 3.2
   (a) propagation through a single layer
   (b) free space propagation to the second optic
   (c) free space back-propagation to the next layer
4. propagation to the detector
5. integration of the results on the detector

The details of the proposed workflow are now explained. The algorithm for the construction of the phantom is very similar to the one described earlier in section §4.1. The only difference is that planes perpendicular to the optical axis differ in the step size of their discretization. For the second step of the simulation, the partially coherent illumination is separated into fully coherent components. Due to the experimental setup, the partially coherent illumination can be approximated by a finite number of (fully coherent) source points which are mutually incoherent. For each coherent source, the propagation through the TXM is well described by the coherent propagators described in chapter 3. The resulting intensity distributions are integrated on the detector over all sources.

For step 3, we use explicitly invertible propagators. This leads to different transverse resolutions for z-slices along the optical axis. For details about the implementation, see also section B.2.3. Each point source illuminates mainly a small part of the phantom. This property is used implicitly on several occasions. It allows the separation of the resulting field in the plane of the second optic into the product of a fast oscillating spherical wave and a much slower oscillating function. This approximation is essential in order to use a reasonably large discretization in the planes of the optics.[5]

We now explain the details of a single propagation step and start with introducing a few notations:

[5] Remark: For large numerical apertures, another propagator has to be used which is no longer equidistant in the plane of the second optic. The difference in transverse resolution and distance to the lens introduces additional errors.

U_0 is the scalar field of the current layer.

$1 - \overline{\delta} + i\overline{\beta}$ is the mean complex index of refraction of the voxel.

Δz is the thickness along the z-direction.

k is the wavenumber.

z is the distance to the objective lens.

$P_{z^*}[U]$ is the free space propagator for the distance z^*.

$P_{z^*}^{-1}[U]$ is the inverse of the free space propagator.

Then, the scalar field (U_{next}) at the next z-layer is estimated from the scalar field (U_{last}) at the previous layer by

$$U_{next} \approx P_{z-\Delta z}^{-1}\left[P_z\left[U_{last}\right]\right] \cdot \exp\left[ik\left(-\overline{\delta} + i\overline{\beta}\right)\Delta z\right].$$

In the propagation and back-propagation step, one has to take into account the separation into spherical wave and slowly oscillating function. This results in an additional multiplication of the slowly varying part with another slowly oscillating function.

$$\begin{aligned} U_{last}[r] &= U_{slow,last}[r] \exp\left[ik\frac{r^2}{2z}\right] \stackrel{!}{=} U_{next}[r] \\ U_{next} &= U_{slow,next} \exp\left[ik\frac{r^2}{2(z-\Delta z)}\right] \\ \Longrightarrow \quad & U_{slow,next} = U_{slow,last} \exp\left[ik\frac{-\Delta z\, r^2}{2(z-\Delta z)z}\right] \end{aligned}$$

A propagation step leads to a small change in resolution. This change depends on the original resolution, the propagation distance, the size (N) of the discretised field and the wavelength (λ) of the light. If the resolution in the first plane is Δx_{z_1}, the resolution in the plane of the optic is given by:

$$\Delta x_{z_{opt}} = \frac{\lambda\left(z_{opt} - z_1\right)}{\Delta x_{z_1} N}.$$

Since the resolution in the plane of the optic has to be kept constant, the new resolution in the next layer is

$$\Delta x_{z_1+\Delta z} = \frac{\left(z_{opt} - z_1 - \Delta z\right)}{\left(z_{opt} - z_1\right)} \Delta x_{z_1}.$$

Hence, the physical sizes of the planes decrease as they come closer to the optic. This indicates already one of the main restrictions of the algorithm. If the illumination has a significant intensity close to the borders of the field of view, the algorithm's results are not well suited for the simulation. Under these conditions, one gets significant artifacts along the borders. This is a well known problem of similar algorithms like the split step method. Methods exist to reduce the resulting numerical artifacts for those algorithms. For example, perfectly matched layers can be used to reduce the effect of reflection at the borders. In this method, the field of view is padded with an absorbing outer layer.

Once the last layer is reached, the resulting field is again propagated to the second optic. The resulting field is modified by the transmission function of the optic.[6] Subsequently, the field is propagated to the detector. As previously mentioned, partial coherence is included by integrating the resulting intensity distribution of different source points in the plane of the detector.

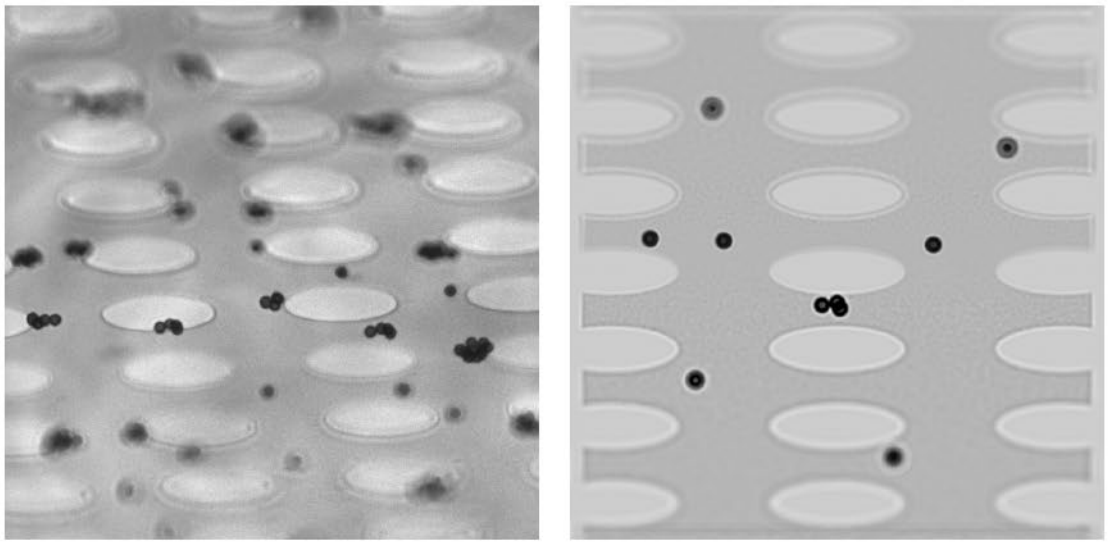

(a) Experimental TXM image **(b)** Partially coherent TXM simulation

Figure 4.9: *Comparison of experimental TXM and simulated partially coherent data.*
(a) *Hollow Au spheres with a diameter of 270 nm on a carbon foil with 2.4 µm holes were imaged in the TXM.*
(b) *A partially coherent simulation of a similar object as in figure 4.9a. The tilt is 70° and the FZP has a* $dr_N = 40\,\mathrm{nm}$.

[6] Here, we assume that the optic acts as a thin lens with focal length f, and therefore, the transmission function is: $T[r] = \chi_{r<r_{max}}[r] \cdot \exp\left[-ik\frac{r^2}{2f}\right]$.

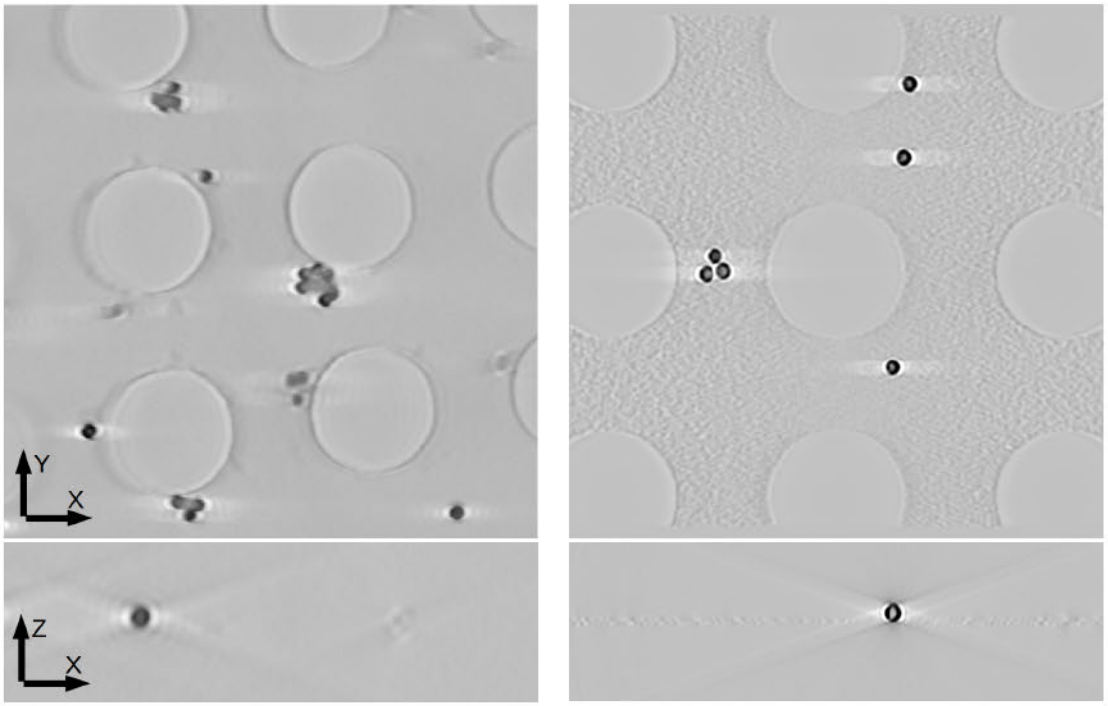

(a) Reconstruction experiment **(b)** Reconstruction partially coherent

Figure 4.10: *Comparison of experimental TXM and simulated partially coherent based tomograms.*
(a) *Tomographic reconstruction of the experimental data from figure 4.9a.*
(b) *Tomographic reconstruction of the simulated data from figure 4.9b.*

Discussion of the Numerical Results

In figure 4.9, a comparison between an experimental image and the result of a partially coherent simulation is shown. The images show that the depth of focus is similar and most features of the experimental data, such as contrast inversion, are better reproduced by this model than by the incoherent one.

In figure 4.10, a comparison is shown between a tomogram from experimental images and the corresponding tomogram from a series of partially coherent simulations. The images in the experimental and simulated series are now more alike, and also the tomograms are more alike. For example, the effects along the edges of the holes in the foil are reproduced. Nevertheless, the impact of the partial coherence on the tomogram seems to be rather minor.

One approach to decrease the impact of the depth of focus on the tomographic 3D reconstruction is based on deconvolution [61]. This approach is based on equation (4.1). Theoretically a deconvolution can be used to recover the 3D information from a series of defocused images. This information could be used to extend the

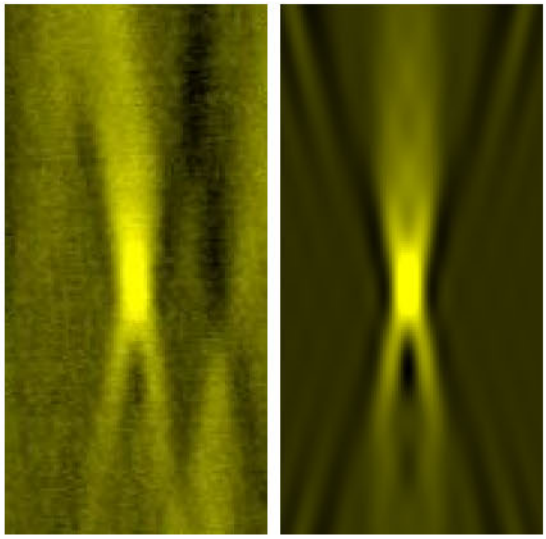

(a) Data **(b)** Simulation

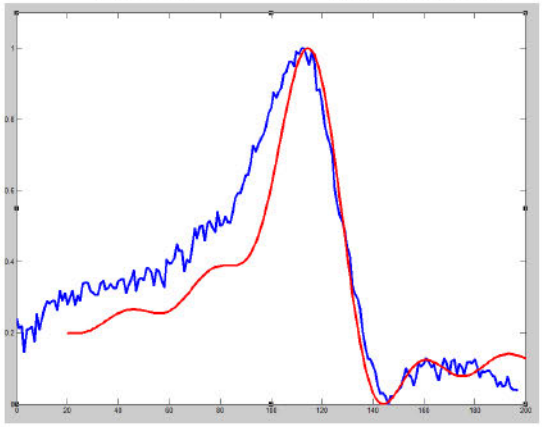

(c) Comparison of the on-axis intensity.

Figure 4.11: *Comparison of finite depth of focus effects for 310 eV and an FZP with $dr_N = 25\,nm$. A 60 nm Au nanosphere is imaged. Due to partially coherent illumination. an asymmetry is observed along the optical axis (vertical).*

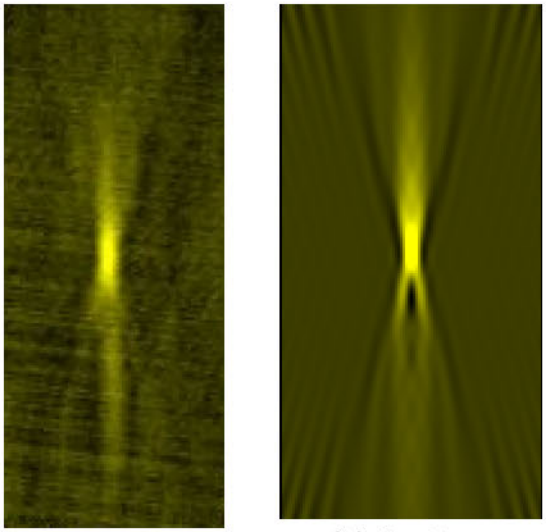

(a) Data **(b)** Simulation

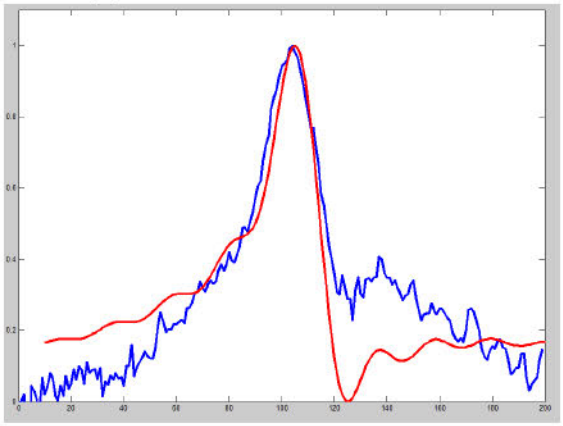

(c) Comparison of the on-axis intensity.

Figure 4.12: *Comparison of finite depth of focus effects for 510 eV and an FZP with $dr_N = 25\,nm$.* A detailed analysis of the results is given in [53].

region for which the projection approximation of tomography is fulfilled. For this deconvolution approach, the point spread function (PSF) of the imaging system must be well known. We measured the PSF along the optical axis by moving a 60 nm gold nanoparticle. The experimental data in figure 4.11 and figure 4.12 show that the resulting axial intensity profile is asymmetrical. Our simulations showed

that a purely absorbing particle generates a symmetric pattern. Therefore, the image of such a small particle in the TXM is already strongly dependent on its complex refractive index. For the numerical simulation, we used a similar, partially coherent algorithm as for the presented partially coherent TXM simulations. More details are published in [53].

Summary

We showed that the imaging properties of high resolution Fresnel zone plates violate the assumptions used in the projection slice theorem (4.2). For samples with the dimensions of a typical cell, the soft X-ray beam spreads out due to the wave nature of the light and therefore, the projection assumption of the projection slice theorem is not perfectly fulfilled. Instead, the image on the detector is even for the incoherent case described by the result of the integral given in equation (4.1), which is essentially a convolution with the point-spread function of the zone plate. For partially coherent TXM setups, similar effects occur, as observed in figure 4.9. Therefore, parts of the sample that are outside the depth of focus are blurred for some tilts in the image series, and the quality of the tomographic reconstruction is thereby reduced. Additionally, artifacts are observed for tomographic reconstructions based on limited tilt series, e.g. series with tilts well below $\pm 90°$ or with step sizes that are too large.

To circumvent these problems, one either can restrict the sample thickness or use higher photon energies. The latter leads to an increase of the depth of focus but decreases the contrast which increases the dose on the sample. The dose problem can be compensated by using phase contrast based imaging methods [76]. For some samples, like thick tissue, neither solution is feasible. Although, several groups world wide are working on improving soft X-ray tomography, no breakthroughs have yet been achieved [46, 61, 85]. Hence, alternative reconstruction algorithms or imaging methods are required. In the following chapters, the performance of novel, soft X-ray based 3D imaging approaches are investigated.

Chapter 5

Confocal Scanning Transmission Microscopy for Direct 3D Imaging

In the previous chapter, it was shown that the tomographic approach has severe limitations for 3D imaging on the nanoscale due to the limited depth of focus of high resolution, soft X-ray objectives. However, the limited depth of focus can also be used to directly image 3D objects. This is used for example in confocal light microscopy, which is an established method for 3D imaging in light microscopy. In this chapter, we investigate whether this method can be transferred to soft X-ray imaging. The concept of confocal light microscopy was developed in the 1950s and patented by Marvin Minsky in 1957 [56].

Several optical setups for confocal light microscopy exist and one of them is diagrammed in figure 5.1. The success of confocal light microscopy is based on the fact that it allows direct acquisition of image slices within thick samples. This feature is also known as optical sectioning. By stacking adjacent slices, one obtains a 3D stack which represents the 3D structure of the sample.

In the following, the basic concept of confocal light microscopy and the related concept of optical sectioning are explained. Afterwards, we discuss how these concepts can be transferred to soft X-ray imaging.

5.1 The Incoherent Confocal Microscope

The optical setup of a confocal light microscope is diagrammed in figure 5.1. The setup consists of a light source, a condenser, a sample, an objective and a point like detector. In a confocal setup, the position of condenser and objective are chosen such that the image of the light source and the pre-image of the point detector

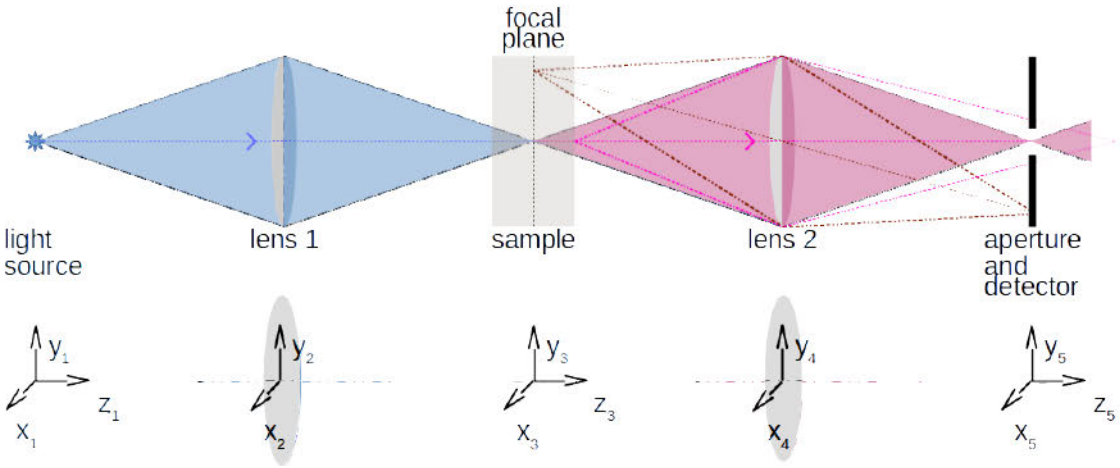

Figure 5.1: *Optical setup of a confocal light microscope. Lens 1 acts as condenser while lens 2 acts as objective. In the case of a confocal light microscope with a fluorescent sample, a filter can be used to separate the fluorescence signal. The red (out of focus), the brown (off-axis) and black (on-axis, in focus) ray paths show that out of focus components are suppressed by the aperture detector combination.*

coincide (see figure 5.1[1]). The ray optical paths shown in figure 5.1 suggest that such a setup suppresses background light and out of focus contributions.

The majority of confocal light microscopes use the incoherent imaging mode, which is usually based on fluorescence. In this mode, a diffraction limited spot generates a secondary signal (at a different wavelength) which is collected by the objective and detected with a point-like detector. It is assumed that the strength of the induced secondary signal is proportional to the local intensity of the focal spot. Furthermore, one assumes that the secondary signal is fully incoherent. The fact that the objective images the secondary signal onto a point-like detector leads to the increase in lateral and depth resolution in comparison to a transmission microscope with equivalent numerical aperture.

In the next section, we will explain this resolution increase. A preliminary explanation is based on geometric optics. As shown in figure 5.1, background light and out of focus contribution are suppressed for well chosen distances between the focusing optic, the second collecting optic and the aperture and detector combination. This allows 3D imaging of thick samples by optical sectioning.

[1]In confocal light microscopy, reflection based setups also exist which we will not consider here since soft X-rays exhibit only weak reflection.

5.1.1 The Mathematical Description of the Incoherent Confocal Microscope

In order to deduce a wave optical description of the imaging process, the intensity of the exciting light in the focal spot of the condenser has to be determined. For simplicity, a point-like source at s_0 is assumed.[2] Under this condition, the first lens generates a diffraction limited spot in the area of the sample. Therefore, the resulting intensity (I_3) at a point r in the region of the sample is given by

$$\begin{aligned} I_3[r] &= \left| \int \delta[s - s_0]\, PSF_1[s, r]\, \mathrm{d}s \right|^2 \\ &= |PSF_1[s_0, r]|^2 \\ &= IPSF_1[s_0, r]. \end{aligned} \tag{5.1}$$

Here, $PSF_1[s, r]$ is the amplitude point spread function of the first optic and $IPSF_1[s, r]$ is the intensity point spread function. The index in I_3 is used to illustrate that this is the intensity in the z_3 region without sample interaction.

We now determine the strength of the secondary signal. Since this signal is usually produced by fluorescence, we call it from now on the fluorescence signal. Furthermore, it is assumed that the resulting fluorescence signal is linearly dependent on the intensity in the focal spot[3]. The total strength of the fluorescence signal is, therefore, proportional to $\int_{\mathbb{R}^3} I_3[r]\, \alpha[r]\, \mathrm{d}r$. Here, $\alpha[r]$ represents the likelihood of an excitation of the fluorescence. Furthermore, we assume that the attenuation of the exciting light and the fluorescence is negligible.

We now study the image of a single fluorophore which is situated in r_0. Let its value be $\alpha[r] := \alpha_0 \cdot \delta[r - r_0]$. This spot now is imaged by the second optic. On the detector, it generates at the point r_{det} the signal

$$\begin{aligned} I_5[r_{det}] &= \int_{\mathbb{R}^3} I_3[r]\, \alpha[r]\; IPSF_2[r, r_{det}]\, \mathrm{d}r \\ &= I_3[r_0]\, \alpha_0 IPSF_2[r_0, r_{det}]. \end{aligned} \tag{5.2}$$

Here, the incoherent point spread function $IPSF_2[r, r_{det}]$ has to be used since it is assumed that the fluorescence signal is emitted fully incoherently. The index in I_5 is used to illustrate that this is the intensity in the detector region which results

[2] A slightly more general description assumes a source which can be separated into a finite sum of fully coherent but mutually incoherent distributions $\sigma_S[s]$. Then, the intensity results from $I_3[r] = \sum_S \left| \int_{s \in S} \sigma_S[s]\, PSF_1[s, r]\, \mathrm{d}s \right|^2$.

[3] For fluorescence, this assumption holds if saturation effects can be neglected and the mean time between two consecutive absorptions of a photon is larger than the time needed for the emission of the fluorescence photon.

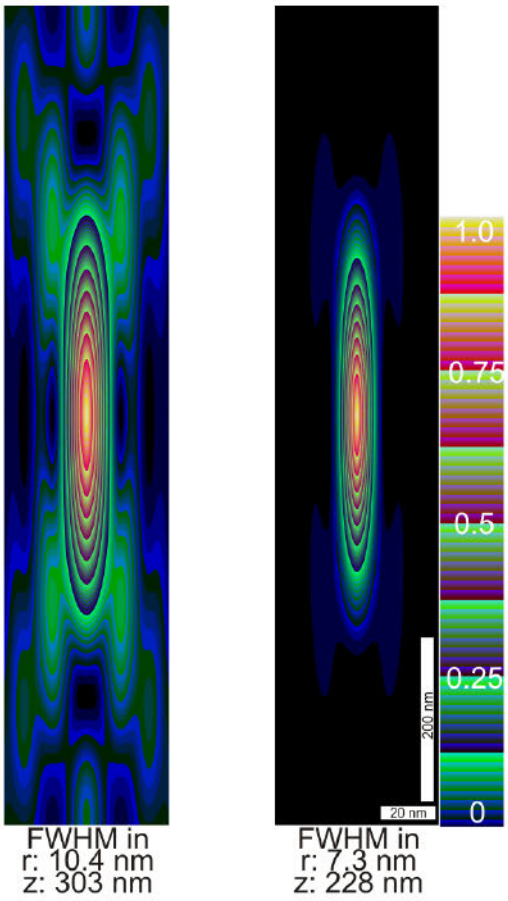

Figure 5.2: *Comparison of the incoherent point spread function of a Fresnel zone plate with $dr_N = 10\,nm$ (left) and the intensity point spread function for the incoherent confocal microscope with a point detector (right). The increased localization of the PSF of the confocal microscope results in an increased resolution.*

from the fluorescence of the sample. If the spot is now moved by Δr, the resulting signal at the same position on the detector is

$$\begin{aligned} I_5\left[r_{det}\right] &= \int_{\mathbb{R}^3} I_3\left[r\right] \alpha_0 \delta\left[r - (r_0 + \Delta r)\right]\, IPSF_2\left[r, r_{det}\right] \mathrm{d}r \\ &= I_3\left[r_0 + \Delta r\right] \alpha_0 IPSF_2\left[r_0 + \Delta r, r_{det}\right]. \end{aligned} \tag{5.3}$$

To compute the intensity on the detector for an arbitrary distribution of fluorophores, we use the fact that the integral is linear and that the fluorescence based emission signals are mutually incoherent. The resulting signal of multiple fluorescent spots is, therefore, simply the sum (or integral for a continuous distribution) of the signals. Therefore, it suffices to compute the signal produced by a single fluorescent spot. The resulting image of an intricate distribution of fluorescent particles is given by the convolution of the single spot signal and the particle distribution.

Equation (5.3) can be further simplified by applying equation (5.1)

$$I_5\left[r_{det}\right] = IPSF_1\left[s_0, r_0 + \Delta r\right] \cdot IPSF_2\left[r_0 + \Delta r, r_{det}\right] \alpha_0.$$

The image of an intricate distribution of fluorescent particles (a) is therefore given by

$$I_a\left[r'\right] = \left(IPSF_1\left[s_0, r\right] \cdot IPSF_2\left[r, r'\right]\right) * a\left[r\right].$$

Hence, the effective point spread function of the incoherent confocal microscope is under these conditions the product of the incoherent point spread functions of the two lenses. This leads to an increased resolution as visualized in figure 5.2 in comparison to a transmission microscope with equivalent numerical aperture.

In the soft X-ray region, fluorescence is weak for light elements and additionally only a relatively small part of the fluorescence signal can be collected due to the small numerical aperture.[4] Therefore, a fluorescence based confocal scanning X-ray microscope requires a large dose which is most likely above the destruction threshold of biological samples. Hence, for high resolution imaging of the cellular ultra-structure, a transmission system as shown in figure 5.3 is preferred. For such a system, the previous description of image formation is not valid. Instead, such an optical setup has to be described in a coherent setting.

5.2 The Coherent Confocal Microscope

The presented confocal soft X-ray scanning microscopy setup is based on Fresnel zone plates instead of refractive lenses (see figure 5.3,[90]). Zone plates produce several focal spots each at a different focal length. Therefore, an order sorting aperture is necessary to block unwanted diffraction orders and select only one order for image formation. As known from confocal light microscopy, the confocal setup of the second objective in conjunction with the pinhole is supposed to remove light that originates from planes outside the depth of focus. In light microscopy, the lateral resolution and the depth of focus (DOF) are within the same range due to high numerical aperture objectives. For X-ray optics, the depth

[4] For higher atomic numbers, a setup with crossed Fresnel lenses is sometimes used for X-ray fluorescence (XRF) microscopy. Although this setup is not strictly speaking a confocal setup, it nevertheless uses a similar concept to achieve an increased lateral and depth resolution and to mitigate the problems generated by a long depth of focus for 3D imaging. For XRF, the DOF is significantly longer than for the confocal STXM since the X-ray fluorescence of heavier elements is at higher energies (e.g. Fe @ 6.4 keV) [98, 43]. In the soft X-ray region, such an instrument is unlikely to work with biological samples since the dominating path of decay of core vacancies for low atomic numbers is the non-radiative Auger process [1]. Therefore, the required dose for imaging is well above the destruction threshold of such samples.

(FWHM)	Conventional LM	Confocal LM 1 AU < R	Confocal LM R<0.25 AU
Optical slice thickness	not definable	$\sqrt{\left(\frac{0.88\lambda_{em}}{n-\sqrt{n^2-NA^2}}\right)^2+\left(\frac{\sqrt{2}n\,R}{NA}\right)^2}$	$\frac{0.64\overline{\lambda}}{n-\sqrt{n^2-NA^2}}$
		(410 nm)	(213 nm)
Axial resolution	$\frac{1.67\,\lambda_{em}}{NA^2}$	$\frac{0.88\lambda_{exc}}{n-\sqrt{n^2-NA^2}} \overset{NA\leq 0.5}{\approx} \frac{1.67n\,\lambda_{exc}}{NA^2}$	$\frac{0.64\overline{\lambda}}{n-\sqrt{n^2-NA^2}} \overset{NA\leq 0.5}{\approx} \frac{1.28n\overline{\lambda}}{NA^2}$
	(278 nm)	(292 nm ≈ 278 nm)	(212 nm ≈ 213 nm)
Lateral resolution	$\frac{0.51\lambda_{em}}{NA}$	$\frac{0.51\lambda_{exc}}{NA}$	$\frac{0.37\overline{\lambda}}{NA}$
	(10.2 nm)	(10.2 nm)	(7.4 nm)

Table 5.1: Rule of thumb formulas for confocal light microscopy (LM) [104]. Two cases are considered depending on the radius (R) of the detector. The lower numbers represent the hypothetical results for $\lambda_{em} \approx \lambda_{exc} = 2.4\,\text{nm}$, $NA = 0.12$ ($dr_N \approx 10\text{nm}$) and $n \approx 1$.
(AU: airy unit, $\overline{\lambda} := \sqrt{2}\lambda_{em}\lambda_{exc}/\sqrt{\lambda_{em}^2+\lambda_{exc}^2}$, λ_{exc}: excitation wavelength, λ_{em}: emission wavelength)

of focus is significantly larger than the lateral resolution since only relatively low numerical aperture (NA) optics are available due to difficulties in the manufacturing of high resolution X-ray objectives. For example, a state of the art Fresnel zone plate with an outermost zone width of $\text{dr}_\text{N} = 10$ nm has at 0.5 keV photon energy a numerical aperture of NA=0.12. Since the proposed transmission system uses only one wavelength and the signal propagates coherently, the analysis of a confocal transmission microscope is more challenging than in the incoherent case. It has been studied in [29] for light microscopy with the help of coherent transfer functions and 3D transmission cross-coefficients. Since the computational load of this approach exceeded our available resources, a different approach was used to predict the expected performance of such a system. Pivotal for the simulation is that the setup of a confocal transmission microscope shares similarities with a transmission microscope. The main difference is that the initial illumination is fully coherent, the detector is point-like and the image is generated by scanning the sample. Therefore, virtually the same simulation as for the partially coherent TXM can be used to simulate the confocal microscope. An implementation is described in detail in the supplement in section B.2.1[5].

[5]One should be aware that the convolution with a point spread function is a bad approximation for this imaging mode since the detected signal is not a sum of point like sources as in the case of a fluorescence confocal setup.

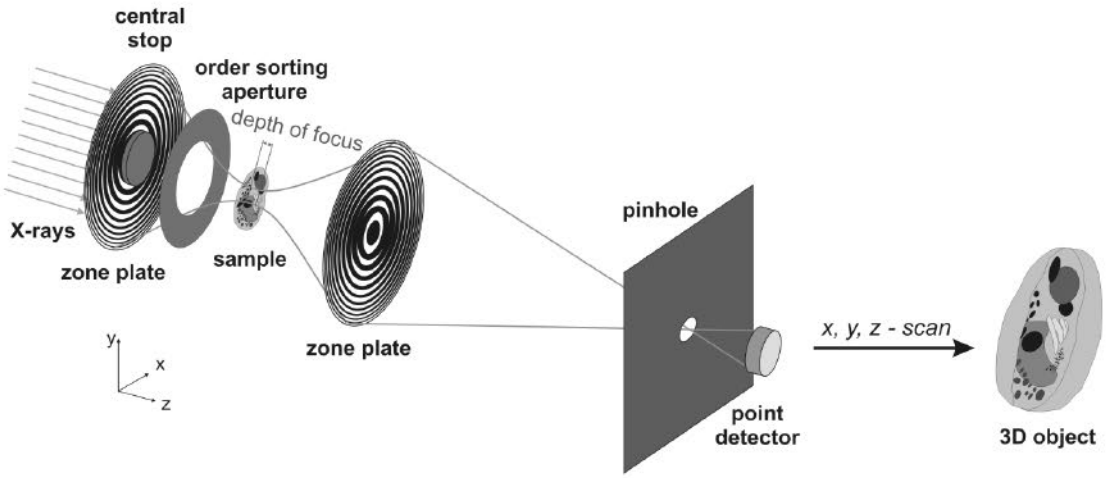

Figure 5.3: *X-ray optical setup of the confocal STXM. The partially coherent photons are focused by a zone plate onto the object plane. An order sorting aperture in combination with a central stop blocks zero order light and higher orders of the zone plate. A second zone plate collects the light that is transmitted by the sample and images it onto a pinhole in front of the detector plane. The pinhole suppresses light scattered from out of focus planes. It also reduces off-axis light from the focal plane. By raster scanning the object, its 3D image is formed. Image provided by S. Werner*

5.2.1 The Mathematical Description of the Coherent Confocal Microscope

In order to study the coherent, confocal system, the first Born approximation is commonly used (see [29]), which is valid for thin or sparse objects.

Analysis of the Confocal System Using the First Born Approximation

The first Born approximation assumes that the incident field is not significantly changed due to the presence of the object. Therefore, the interaction of the object with the incident field is well described without taking into account the interaction of the field produced by the object with the object itself. The notation used for the different parts of the system is shown in figure 5.3.

Since the focal spot is supposed to be diffraction limited, it is assumed that the source is fully coherent. Let it generate the field U_1. Then, the illumination which is incident on the sample is given by

$$U_3[r] = \int_{s \in Source} U_1[s]\, PSF_1[s, r]\, \mathrm{d}s.$$

Without the sample, the illumination is simply imaged by the second objective

lens onto the detector. The resulting field in the plane of the detector is given by

$$U_5[v] = \int_{r \in R} PSF_2[r, v] \int_{s \in Source} U_1[s]\, PSF_1[s, r]\, \mathrm{d}s\, \mathrm{d}r.$$

Here, R is a plane orthogonal to the optical axis. The signal (S) on the detector results from the integrated intensity over the area of the detector

$$S = \int_{v \in Detector} |U_5[v]|^2\, \mathrm{d}v.$$

In the presence of a sample, the incident field U_3 is perturbed. Since the first Born approximation is used, this generates just another field $U_{obj,3}$ and does not change the field U_3. We now have to propagate the field generated by the object to the detector.

In the plane of the second lens, the field generated by the object is according to equation (3.12)

$$\begin{aligned} U_{obj,4}[x_4, y_4, z_4] \;=\; & \int_{(x',y',z') \in Sample} \frac{\exp[ik_0(z_4 - z')]}{i\lambda} \exp\left[ik_0 \frac{(x_4 - x')^2 + (y_4 - y')^2}{2(z_4 - z')}\right] \\ & \cdot k_0^2 \left(n^2[x', y', z'] - 1\right) U_3[x', y', z']\, \mathrm{d}x'\, \mathrm{d}y'\, \mathrm{d}z'. \end{aligned}$$

This field is first modified by the transmission function of the optic, and the result has to be propagated to the detector. Since the coherent point spread function PSF_2 already includes both the transmission properties of the optic and the propagation from the region of the sample to the second optic, it can be used directly to compute the contribution of the sample to the signal. This approach leads to the following equation for the contribution of the sample to the field on the detector

$$U_{obj,5}[v] \;=\; \int_{r \in Sample} PSF_2[r, v]\; k_0^2 \left(n^2[r] - 1\right) U_3[r]\; \mathrm{d}r.$$

Since the incident field depends only on the source, this is equivalent to

$$\begin{aligned} U_{obj,5}[v] \;=\; & \int_{r \in Sample} PSF_2[r, v]\; k_0^2 \left(n^2[r] - 1\right) \\ & \int_{s \in Source} U_1[s]\, PSF_1[s, r]\, \mathrm{d}s\, \mathrm{d}r. \end{aligned}$$

Finally, the signal (S) on the detector results now from the interference of the two propagated fields

$$S \;=\; \int_{v \in Detector} |U_5[v] + U_{obj,5}[v]|^2\, \mathrm{d}v.$$

The signal is therefore,

$$\begin{aligned} S &= \int_{v\in Detector} \left|U_5\left[v\right] + U_{obj,5}\left[v\right]\right|^2 \mathrm{d}v \\ &= \int_{v\in Detector} \left| \int_{r\in Sample} PSF_2\left[r,v\right] \left(\delta\left[r_z\right] + k_0^2\left(n^2\left[r\right]-1\right)\right) \right. \\ &\quad \left. \int_{s\in Source} U_1\left[s\right] PSF_1\left[s,r\right] \mathrm{d}s\,\mathrm{d}r \right|^2 \mathrm{d}v. \end{aligned}$$

The delta distribution in the last equation describes the field without sample.

If the source is not fully coherent, the focal spot is not diffraction limited. In this case, the source has to be separated into series of mutually incoherent fields $U_1^{(j)}$. Each of these fields is propagated through the system and the resulting incoherent sum yields the signal on the detector.

Analysis of the Confocal System Without the First Born Approximation

In X-ray microscopy, thick samples are often used. For thick samples, the first Born approximation is no longer perfectly fulfilled. Instead, a multislice approach is used to simulate the resulting images. A comparison of the experimental setups shows that the confocal and the transmission soft X-ray microscope share similarities. Hence, an almost identical algorithm to the one presented in section 4.2.4 is used to calculate the distribution on the intensity detector for each scanned position. The algorithm for the creation of the phantom is identical to the one in section 4.2.4.

Essentially, the confocal simulation is for each position of the scan a fully coherent TXM simulation with a point source. At each position of the scan, the following steps are undertaken:

1. The phantom is translated to the scan position.

2. For the condenser facing first face of the phantom, the scalar field of an on-axis point-like source imaged by the condenser is computed.

3. This scalar field is propagated through the (translated) phantom by the same multislice algorithm as in section 4.2.4.

4. The resulting field at the exit face of the phantom is propagated through the objective to the detector.

5. The intensity in the area corresponding to the point-like detector is integrated. This value represents the signal at the scanned position.

5.2.2 Results of the Simulation

The performance of a confocal transmission setup was analyzed numerically with the multislice based simulation. As samples, we used four spheres which have a

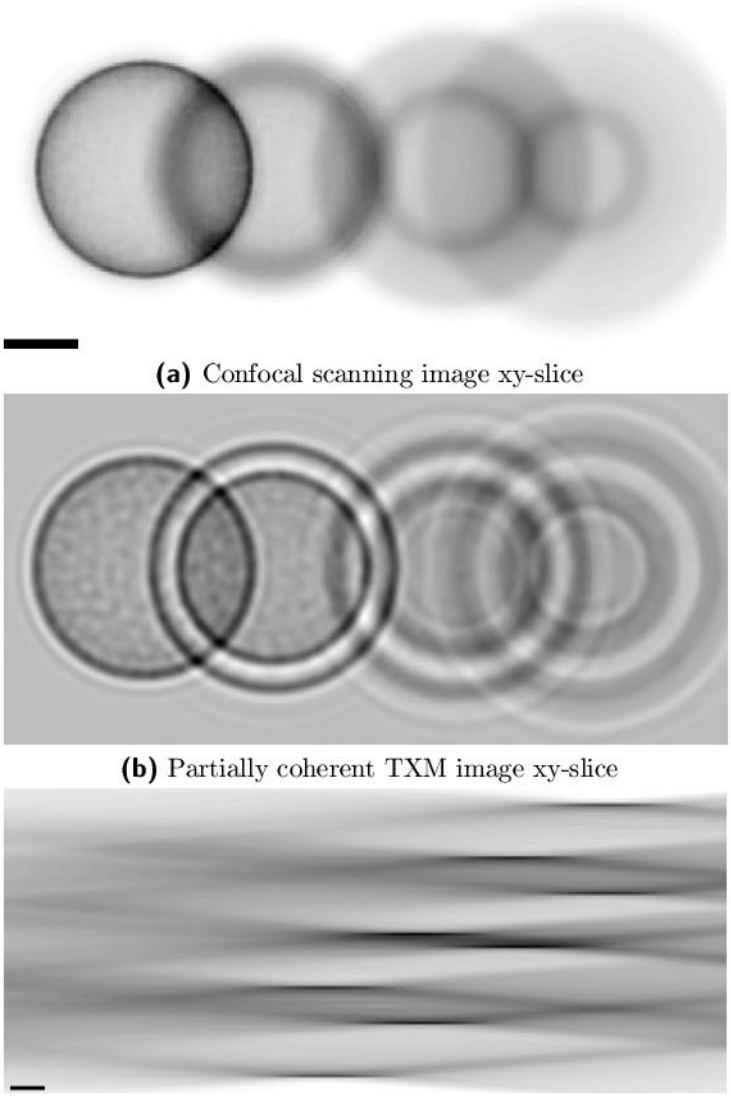

(a) Confocal scanning image xy-slice

(b) Partially coherent TXM image xy-slice

(c) Confocal scanning image xz-slice

Comparison of the imaging performance of a confocal STXM and a partially coherent TXM. The images show four spheres. Each sphere has a diameter of 300 nm and simulates a 4 nm thick cellular membrane. They are separated in depth by 300 nm.
The limited depth resolution is obvious (c).
Two 10 nm FZP were used for the confocal simulation (a,c), while for the TXM simulation a 10 nm FZP objective in combination with a condenser which is equivalent to a 40 nm FZP was used (b). Scale bars are 100 nm.

Figure 5.4: *Comparison of confocal and TXM 3D imaging performance.* ***(a)*** *The confocal image of the xy-slice focused on the center of the left sphere.* ***(b)*** *The same slice as a TXM image.* ***(c)*** *The confocal image of the xz-slice through the center of the spheres.*

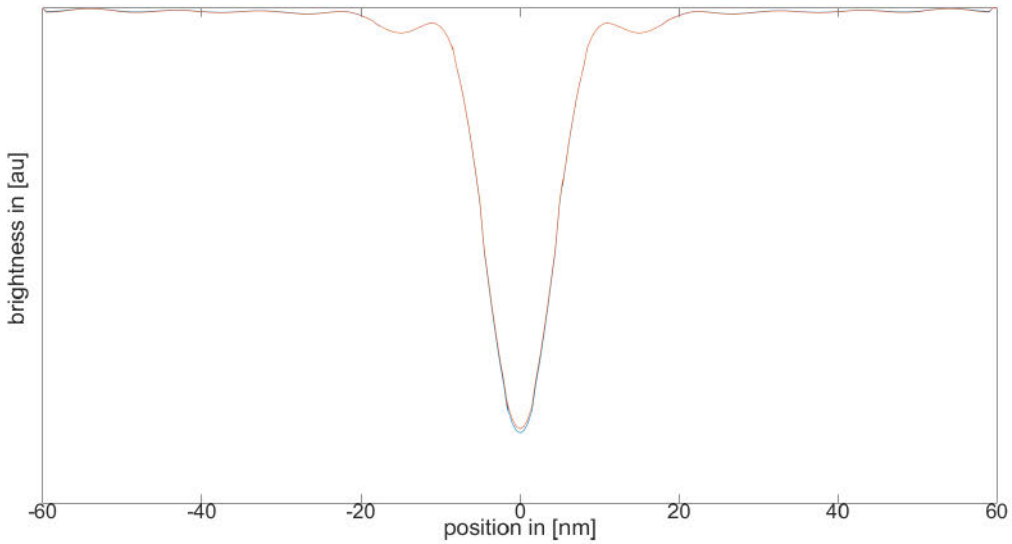

(a) *Line scan along the transversal direction*

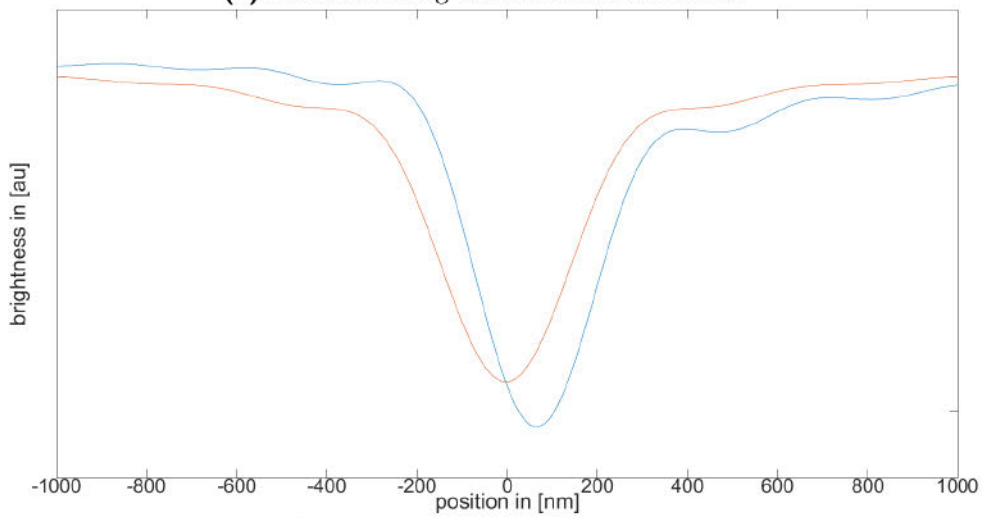

(b) *Line scan along the optical axis*

Figure 5.5: *To estimate the resolution of a confocal STXM, the image of a thin line-like object was simulated. The FZPs used have a dr_N of 10 nm. The red line represents an object with pure absorption contrast, while the blue line reflects phase shift and absorption similar to a cellular membrane.* ***(a)*** *The lateral resolution is about 9.6 nm (FWHM).* ***(b)*** *The depth resolution is about 350 nm (FWHM), which is lower than the DOF for TXM imaging (170 nm). Note, that the image is phase sensitive.*

diameter of 300 nm and are separated in depth by 300 nm. They represent 4 nm thick cellular membranes. We compared the resulting confocal images to TXM images with equivalent objectives. Our results are shown in 5.4. From these results,

we conclude that a confocal STXM produces a 3D image but the resolution is anisotropic. A comparison of the xy-views of the confocal STXM and the partially coherent TXM image shows that the latter exhibits significant coherence induced artifacts which are not present in the confocal image. The investigated confocal STXM shows no such artifacts. The reason is that the imaging process of two scanning points is independent in time and the numerical aperture of both optics match. From the xz-view of the spheres, one can conclude that the depth resolution for the confocal STXM is in this setup about 350 nm (FWHM) (see 5.5b), while the depth of focus of a TXM is about 170 nm at the same $\mathrm{dr_N}$. See also table 2.1.

Summary

In this chapter, we have theoretically analyzed the performance of a confocal scanning X-ray microscope for 3D nanoscale imaging. In contrast to confocal microscopes in the optical regime which operate under incoherent conditions, the confocal X-ray microscope operates under either coherent or partially coherent conditions. In the optical regime, the lateral resolution of a confocal microscope improves by ~60% compared to the single objective. In addition, defocused planes are removed by the confocal setup with pinhole detector. The axial resolution in the optical confocal microscope is only 2 to 3 times worse than the lateral resolution.

In this thesis, we showed that the confocal X-ray microscope requires a more complex description with coherent wave propagation through the object that incorporates both attenuation and phase shift. We find that the lateral resolution does not improve significantly over the single X-ray objective. Furthermore, the relatively low numerical aperture of zone plates in the soft X-ray regime yields a depth resolution that is 30-fold larger than the lateral resolution. Therefore, the 3D resolution in the X-ray confocal microscope is highly anisotropic, which significantly reduces its applicability for 3D analysis of biological specimens. Nevertheless, the well-defined focal spot of the X-ray confocal microscope might trigger other applications, for example when coupled with ultrashort pulses emitted from X-ray lasers.

Chapter 6

Novel 3D Imaging by a Combined FIB and SXM with Photoelectron Detection

Nanoscale soft X-ray imaging has yielded unprecedented views into native and synthetic structures, but as the investigations in the previous chapters showed, it is also subject to limitations for 3D imaging. A new imaging approach is presented in this chapter, which potentially can overcome some of the main limitations. The new approach is studied by numerical simulations. In addition, its performance concerning the signal to noise ratio is analytically investigated.

6.1 Introduction to FIB-SXM

The new imaging approach is based on the detection of emitted photoelectrons generated by a scanned nanoscale X-ray beam [84]. This strategy naturally achieves a depth resolution of less than 10 nm due to the short escape length of photoelectrons. Those emitted at depths beyond 10 nm are rapidly absorbed before they escape the specimen. A 3D image is generated by removing the surface layer with milling by a focused ion beam (FIB). FIB is now widely used to remove surface layers at a resolution of 10 nm or less with minimal impact on the specimens [74]. Note that by raster scanning the sample as shown in figure 6.1, the 3D image is obtained directly without computational processing. In the following, we will analyze theoretically and numerically the 3D imaging performance of the focused ion beam

milling based scanning X-ray microscopy by photoelectron detection (FIB-SXM) setup.

6.1.1 Setup

The general setup for FIB-SXM is shown in figure 6.1. The setup consists of a focused ion beam column, a channeltron with an in-lens objective and a translation stage for the sample. The in-lens objective consists of a high-resolution Fresnel zone plate (FZP) with a central stop and an order sorting aperture (OSA). The OSA is matched to the central stop and selects one order of diffraction.

The concept uses a focused ion beam column to prepare a flat surface. The surface is then raster scanned with the focal spot of the Fresnel zone plate. For soft X-rays and light elements, the absorbed photons generate mainly photoelectrons. They are detected by the channeltron. We assume that the detected signal is proportional to the absorption of the surface layer[1]. Two different types of signal can be detected.

Firstly, one can choose to detect only Auger electrons. For this mode, the analysis of the signal to noise ratio is relatively straight forward and will be done in section §6.3. Secondly, one can detect all secondary electrons. These electrons include low energy electrons produced by the interaction of the Auger electrons with the atoms of the sample. To predict the exact local and energetic distribution of these secondary electrons is challenging. We therefore skip this analysis. Intuitively, the expected amount of secondary electrons should correspond to the local absorption coefficient since the latter determines the energy which is deposited into the surface area.

Both methods are expected to generate good contrast in biological samples. The intrinsic resolution is given by the lateral dimensions of the focal spot and the escape depth of the electrons. The escape depth of electrons at these energies is small so that a very good depth resolution is expected. To generate 3D images, the specimen is fixed on a sample holder with three degrees of freedom in translation. The sample is imaged layer by layer. One starts with the raster scan of the first layer. Then, the second layer is produced by removing the first layer by FIB milling. For biological samples, cryo-fixation is used to suppress artifacts due to radiation damage. For cryogenic samples, surface layers of about 10 nm have already been removed by FIB [74]. In these experiments, the embedding of ions proved to be no problem.

[1]This assumption will lead to an improved contrast in FIB-SXM in comparison to other soft X-ray transmission methods for biological samples since the signal is $\propto 1 - \exp[-\mu\Delta z] \approx \mu\Delta z$ (FIB-SXM), respectively $\propto \exp[-\mu\Delta z] \approx 1 - \mu\Delta z$ (transmission).

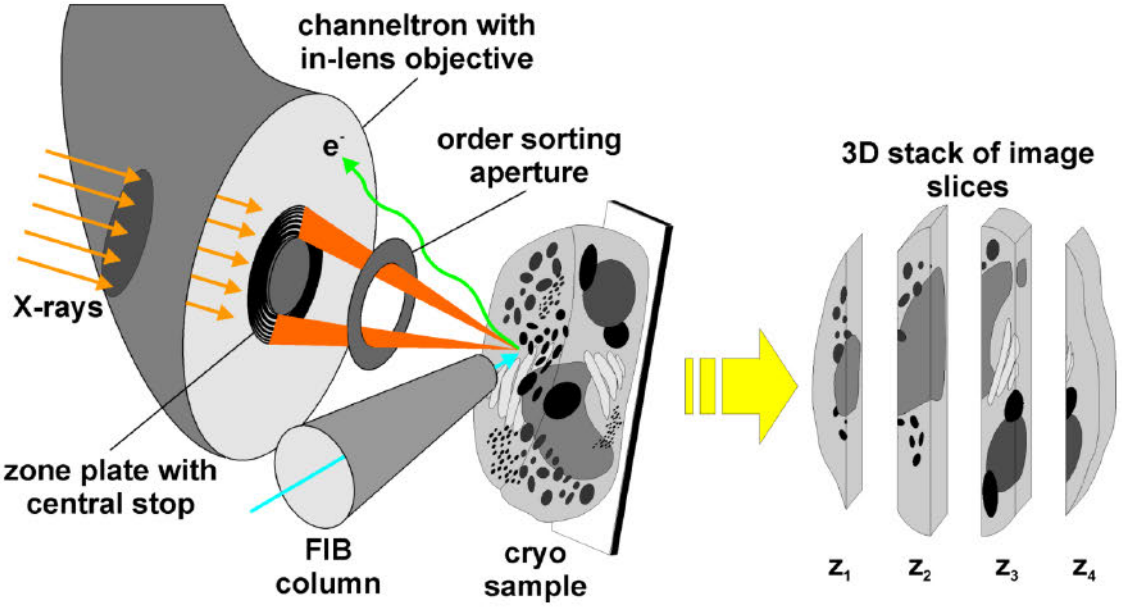

Figure 6.1: *Optical setup of the dual beam FIB-SXM (focused ion beam scanning X-ray microscope) with photoelectron detection. Soft X-ray light (orange arrows) is focused by a zone plate to a diffraction limited 10 nm spot on a cryo-preserved specimen. The photoelectrons (green arrow), emitted from the specimen, emerge only from a thin surface layer of the specimen and are detected by a channeltron surrounding the zone plate. The 10 nm X-ray spot is scanned to produce a 2D image of the specimen's surface (z1), and then FIB is used to remove a 10 nm – thick layer from the surface. Thus, an iteration of SXM followed by FIB milling yields images of successive surface layers (z2, z3 ,z4) finally generating a 3D image stack of the specimen at isotropic resolution. Image provided by S.Werner*

6.2 Simulation

We begin our investigation of the imaging capabilities of the new FIB-SXM method by comparing the FIB-SXM and the TXM images of a phantom since the latter is in my opinion currently the best soft X-ray method for imaging of whole cells. The phantom simulates a typical eukaryotic cell and includes filaments with the optical properties of cellular microtubules and spherical vesicles with the optical properties of cellular membranes.

The FIB-SXM simulation includes the point spread function of the Fresnel zone plate and the depth dependent escape probability of the Auger electrons. For the simulation, it is assumed that the number of Auger electrons is directly proportional to the absorption coefficient. They are emitted in any direction with equal likelihood and the probability to escape the sample decreases exponentially

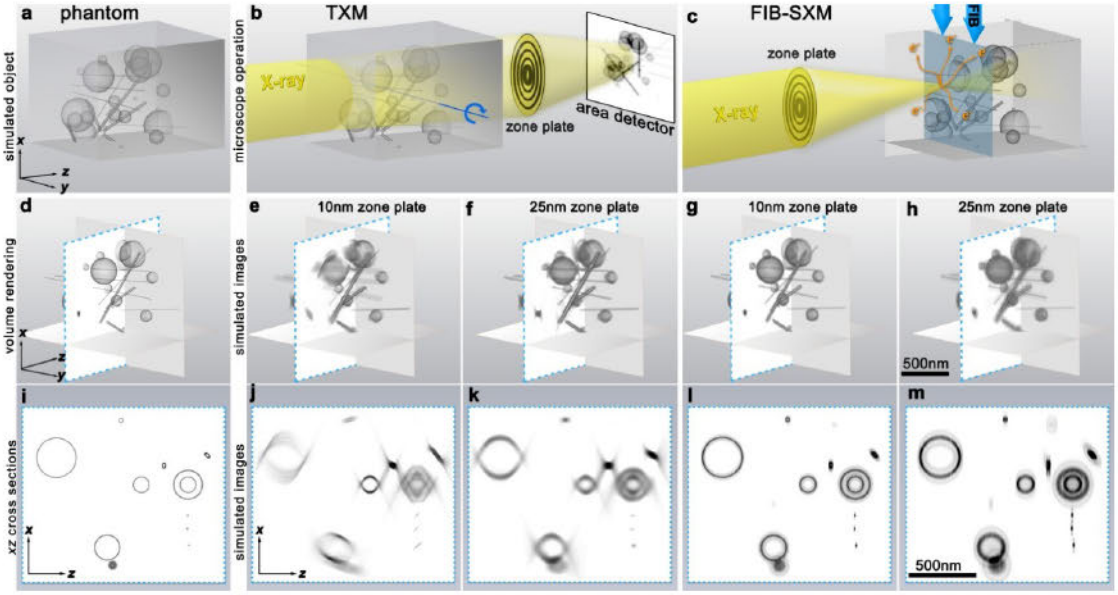

Figure 6.2: *This simulation compares the FIB-SXM and the TXM imaging modes. Imaged is a phantom that corresponds to a biological sample. The phantom object consists of hollow spheres with a 4 nm thick shell composed of membrane lipids and proteins, and 25 nm diameter rods of microtubule protein* ***(a, d** and **i)**.
The X-ray optical setup of the TXM ***(b)*** *and the FIB-SXM* ***(c)*** *are also illustrated. In the TXM, the entire sample is illuminated by X-rays (yellow). The light transmitted by the object is then imaged by the zone plate objective onto the detector, generating a 2D projection image. To image the 3D structure of the sample, a series of images at different angles is taken. A volume rendering of the resulting reconstructions is shown for a 10 nm zone plate in* ***(e)*** *and a 25 nm zone plate in* ***(f)***. *In the third row, an xz slice of the phantom* ***(i)*** *is compared to the same slice from the TXM reconstruction with a 10 nm* ***(j)*** *or 25 nm zone plate* ***(k)***.
In the FIB-SXM, the X-rays (yellow) are focused to a diffraction limited spot on the sample. The photoelectrons produced are detected, and a 2D image is obtained by scanning the spot over the surface. To recover the 3D information, the surface layer is successively removed by FIB milling (blue arrows). A volume rendering of the resulting reconstructions is shown for a 10 nm zone plate in ***(g)*** *and a 25 nm zone plate in* ***(h)***. *In the third row, an xz slice of the phantom* ***(i)*** *is compared to the same slice from the FIB-SXM reconstruction with a 10 nm* ***(l)*** *or 25 nm zone plate* ***(m)***.
The FIB-SXM images are faithful renderings of the phantom, subject only to blurring produced by the zone plate objective. In contrast, the TXM images show a more distorted phantom with artifacts created by the reconstruction process.

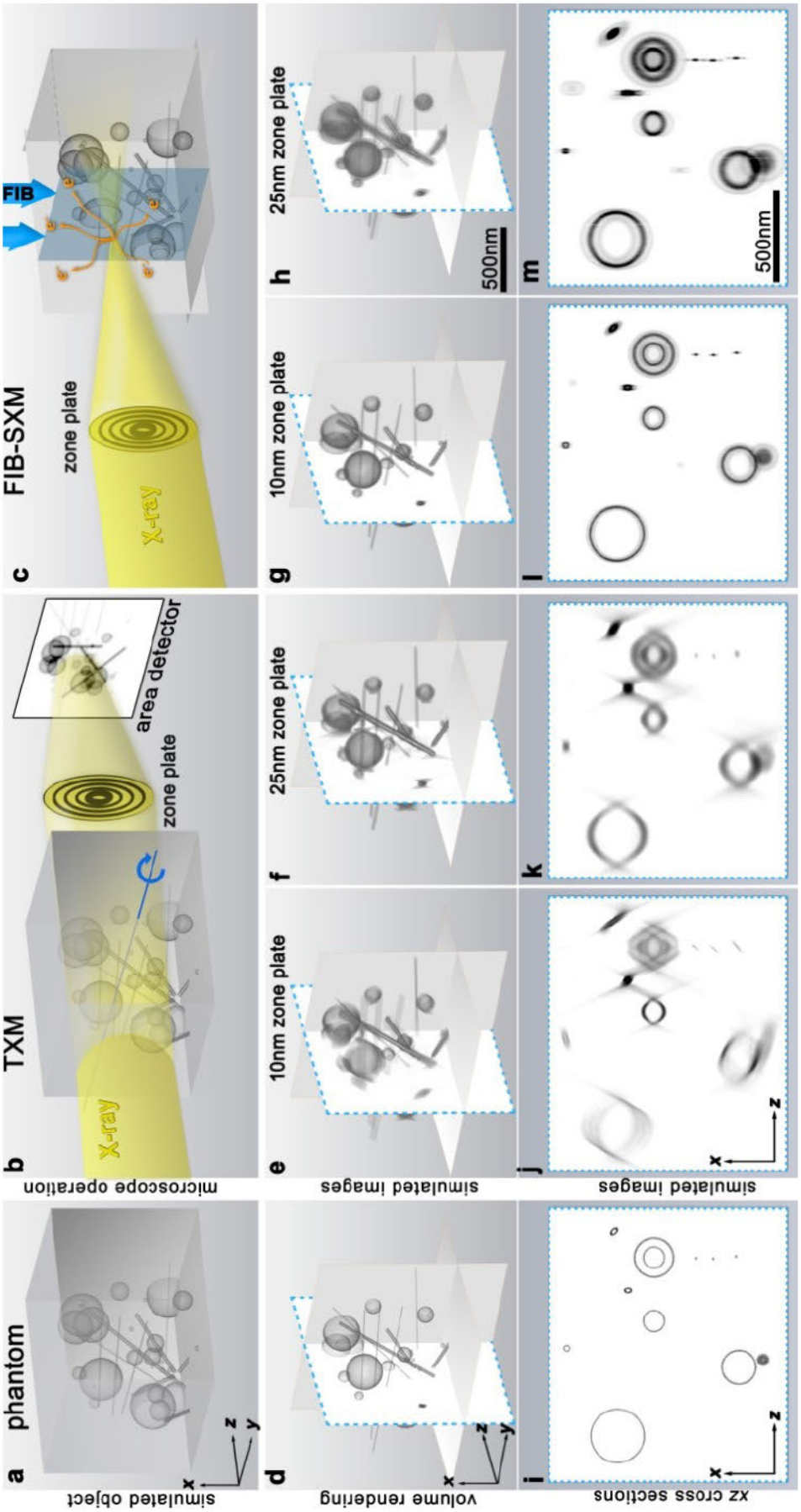

Figure 6.3: Large version of figure 6.2

with the length of the path to the surface. The probability of the electrons to escape the sample is based on the electron effective attenuation lengths in ice [66].

For the TXM simulation, we use the incoherent algorithm described in chapter 4. The 3D image is generated by tomography. This simulation includes the effects of defocus due to the incoherent 3D intensity point spread function and the missing wedge artifacts.

The results are shown in figure 6.2 and figure 6.3. From a direct comparison of figures d to h, one notices the improved image quality of the FIB-SXM in comparison to the tomographic reconstructions. FIB-SXM does not suffer from the same depth of focus restrictions as seen in figure j and l. Since the FIB-SXM image is directly generated in 3D, no artifacts occur due to the 3D reconstruction algorithm.

6.3 Signal to Noise Ratio for FIB-SXM and TXM

As previously mentioned, soft biological samples are damaged by large X-ray doses. Hence, the achievable resolution of any X-ray imaging method depends not only on the resolution of the imaging system, but also on the signal to noise level achievable with a prescribed dose. The aim of the following calculations is to approximate the required dose for a prescribed contrast, resolution and signal to noise level for FIB-SXM.

According to the Rose criterion, a signal to noise ratio (SNR) of at least 5 is needed to reliably distinguish features. The SNR is here defined as the quotient of the expected signal to the standard variation of the signal, i.e. $SNR := \frac{\mathbb{E}[S]}{SD[S]}$ where $\mathbb{E}[S]$ and $SD[S]$ are the mean and standard variation of the signal (S).

6.3.1 Signal to Noise Level for the FIB-SXM

We now consider the FIB-SXM signals produced by two cuboids which differ only in the material. Due to the difference in the material, both cuboids generate a different number of detected photoelectrons (Y_i). The signal is the difference between the two detected electron counts $S = Y_1 - Y_2$.

The electron signal produced by a cuboid results from two random processes. Firstly, we have the number of incoming photons N_i. This number is usually described by a Poisson distribution. In an abuse of notation, we will call the distribution and the expected value N_i. Secondly, each of these photons has a certain (independently identically distributed) probability to be absorbed in the cuboid. For soft X-ray absorption, fluorescence is negligible so each absorbed photon produces one or two Auger electrons. Since the end results are similar, we assume here that both materials produce only one electron in the detectable

energy range.[2] The amount of produced electrons is hence $Y_i = \sum_{l=1}^{N_i} Z_{i,l}$ where the distribution of $Z_{i,l}$ is given by a Bernoulli distribution with parameter $p_i \approx 1 - \exp[-\mu_i \Delta z] \approx \mu_i \Delta z$. Here, μ_i and Δz are the absorption coefficient and thickness of the cuboid respectively. Since both cuboids have the same dimensions, the expected number of incident photons is the same, i.e $\mathbb{E}[N_i] = N$.

From this, plus the Wald equation and the Blackwell-Girshick equation (see E.3.1), a straightforward calculation produces the SNR. We start with the definition of the signal to noise ratio

$$SNR := \frac{\mathbb{E}[S]}{\sqrt{Var[S]}}.$$

The expected value of the signal S follows from

$$\begin{aligned} \mathbb{E}[S] &= \mathbb{E}[Y_1 - Y_2] \\ &\overset{Wald}{=} \mathbb{E}[N_1]\mu_1 \Delta z - \mathbb{E}[N_2]\mu_2 \Delta z \\ &= N(\mu_1 - \mu_2)\Delta z, \end{aligned}$$

and the variance of S

$$\begin{aligned} Var[S] &= Var[Y_1 - Y_2] \\ &= Var[Y_1] + Var[Y_2] - 2Cov[Y_1, Y_2] \\ &= Var[Y_1] + Var[Y_2] \\ &\overset{6.1}{=} N(\mu_1 + \mu_2)\Delta z. \end{aligned}$$

In the calculation of the variance, we use the fact that the variance of each $Y_i, i = 1, 2$, follows from the Blackwell-Girshick equation

$$\begin{aligned} Var[Y_i] &\overset{Black}{=} \mathbb{E}[N_i] Var[Z_{i,1}] + \mathbb{E}[Z_{i,1}]^2 Var[N_i] \\ &= N\mu_i \Delta z (1 - \mu_i \Delta z) + (\mu_i \Delta z)^2 N \\ &= N\mu_i \Delta z. \end{aligned} \tag{6.1}$$

Therefore, the signal to noise ratio is

[2] See later calculation for the case of two electrons.

$$\begin{aligned} SNR &:= \frac{\mathbb{E}[S]}{\sqrt{Var[S]}} \\ &= \frac{N(\mu_1 - \mu_2)\Delta z}{\sqrt{N(\mu_1 + \mu_2)\Delta z}} \\ &= \frac{\sqrt{N\Delta z}(\mu_1 - \mu_2)}{\sqrt{(\mu_1 + \mu_2)}}. \end{aligned} \tag{6.2}$$

Adding the Detection Probability of Electrons The previous calculation of the SNR ignored the fact that electrons produced in different depths of the cuboid differ in their probability to escape from the material. Furthermore, the final electron counts result from the detection efficiency η of the detector. This introduces an additional source of noise. Here, we assume the detector to have a constant quantum efficiency (η). We assume that the probability for an electron produced in a depth z to escape is to a good approximation exponentially decaying with a constant $c_{escape} < 0$. Any escaped electron is then detected with a probability of η. This yields a detection probability of $p_i(z) \approx \eta \exp[c_{i,escape} z]$. The SNR can be deduced by applying the Wald equation, the Blackwell-Girshick equation and the linearity of mean and variance. Again, we start from the definition of the SNR

$$\begin{aligned} SNR[S] &:= \frac{\mathbb{E}[S]}{\sqrt{Var[S]}} \\ &= \frac{\int_0^{\Delta z} S[z]\,dz}{\sqrt{Var\left[\int_0^{\Delta z} S[z]\,dz\right]}} \end{aligned}$$

For the deduction of the SNR formula, we divide the distance Δz into M pieces of thickness δz ($\{(0, \delta z), (\delta z, 2\delta z), \ldots, ((M-1)\delta z, M\delta z = \Delta z)\}$). The number of detected electrons originating from the m-th layer of material i is called $X_{i,m}$. It is related to the number of emitted photoelectrons by

$$X_{i,m} \approx \sum_{a=0}^{Y_i[(m-1)\delta z, m\delta z]} W_{i,z=m\delta z,a}.$$

Here, $W_{i,z,a}$ is the distribution related to the escape probability. In our case, it is Bernoulli distributed with parameter $p_i(z)$. $Y_i[(m-1)\delta z, m\delta z]$ is defined as above, but with δz instead of Δz. The expected integrated signal results from the sum of all expected signals produced in the slices.

$$\begin{aligned}
\mathbb{E}[S] &= \mathbb{E}\left[\sum_{m=1}^{M} S_m\right] \\
&= \mathbb{E}\left[\sum_{m=1}^{M} \left(X_{1,m}[\delta z] - X_{2,m}[\delta z]\right)\right] \\
&\overset{Wald}{=} \sum_{m=1}^{M} \left(\mathbb{E}[W_{1,m\delta z}]\,\mathbb{E}[Y_1[(m-1)\delta z, m\delta z]] - \mathbb{E}[W_{2,m\delta z}]\,\mathbb{E}[Y_2[(m-1)\delta z, m\delta z]]\right) \\
&= \sum_{m=1}^{M} \left(\eta \exp[c_{1,escape} m\delta z]\,\mathbb{E}[N_1]\,\mu_1 \delta z - \eta \exp[c_{2,escape} m\delta z]\,\mathbb{E}[N_2]\,\mu_2 \delta z\right) \\
&= \eta N \sum_{m=1}^{M} \left(\exp[c_{1,escape} m\delta z]\,\mu_1 \delta z - \exp[c_{2,escape} m\delta z]\,\mu_2 \delta z\right)
\end{aligned}$$

As M goes to infinity, the following formula for the expected signal results.

$$\mathbb{E}[S] = \eta N \int_0^{\Delta z} \left(\exp[c_{1,escape} z]\,\mu_1 - \exp[c_{2,escape} z]\,\mu_2\right) \mathrm{d}z$$

Similarly, the integrated variance can be determined by using the linearity of the variance.

$$\begin{aligned}
Var[S] &= Var\left[\sum_{m=1}^{M} S_m\right] \\
&= Var\left[\sum_{m=1}^{M} \left(X_{1,m}[\delta z] - X_{2,m}[\delta z]\right)\right] \\
&= \sum_{m=1}^{M} Var\left[X_{1,m}[\delta z] - X_{2,m}[\delta z]\right] \\
&\overset{6.3}{=} \sum_{m=1}^{M} \left(Var[X_{1,m}[\delta z]] + Var[X_{2,m}[\delta z]]\right) \\
&\overset{6.4}{=} \sum_{m=1}^{M} N\eta \left(\exp[c_{1,escape} m\delta z]\,\mu_1 \delta z + \exp[c_{2,escape} m\delta z]\,\mu_2 \delta z\right)
\end{aligned}$$

Letting M go to infinity, the following formula for the standard variance of signal results.

$$Var[S] = N\eta \int_0^{\Delta z} \exp[c_{1,escape} z]\,\mu_1 + \exp[c_{2,escape} z]\,\mu_2 \mathrm{d}z$$

These auxiliary equations were used:

$$\begin{aligned} Var[X_{1,m}[\delta z] - X_{2,m}[\delta z]] &= Var[X_{1,m}[\delta z]] + Var[X_{2,m}[\delta z]] \\ &\quad -2Cov[X_{1,m}[\delta z], X_{2,m}[\delta z]] \\ &= Var[X_{1,m}[\delta z]] + Var[X_{2,m}[\delta z]] \end{aligned} \tag{6.3}$$

$$\begin{aligned} Var[X_{i,m}[\delta z]] &\overset{Black}{=} \mathbb{E}[Y_i[(m-1)\delta z, m\delta z]]\, Var[W_{i,m\delta z,1}] \\ &\quad +\mathbb{E}[W_{i,m\delta z,1}]^2\, Var[Y_i[(m-1)\delta z, m\delta z]] \\ &\overset{6.1}{=} N\mu_i \delta z \eta \exp[c_{i,escape} m\delta z]\,(1 - \eta \exp[c_{i,escape} m\delta z]) \\ &\quad + (\eta \exp[c_{i,escape} m\delta z])^2\, N\mu_i \delta z \\ &= N\mu_i \delta z \eta \exp[c_{i,escape} m\delta z] \end{aligned} \tag{6.4}$$

Finally, the signal to noise ratio including the detection efficiency η and the depth dependent escape probability is given by

$$\begin{aligned} SNR &= \frac{\int_0^{\Delta z} S[z]\,dz}{\sqrt{Var\left[\int_0^{\Delta z} S[z]\,dz\right]}} \\ &= \frac{\eta N \int_0^{\Delta z} (\exp[c_{1,escape} z]\,\mu_1 - \exp[c_{2,escape} z]\,\mu_2)\,\mathrm{d}z}{\sqrt{N\eta \int_0^{\Delta z} \exp[c_{1,escape} z]\,\mu_1 + \exp[c_{2,escape} z]\,\mu_2 \mathrm{d}z}} \\ &= \sqrt{\eta N} \frac{\int_0^{\Delta z} (\exp[c_{1,escape} z]\,\mu_1 - \exp[c_{2,escape} z]\,\mu_2)\,\mathrm{d}z}{\sqrt{\int_0^{\Delta z} \exp[c_{1,escape} z]\,\mu_1 + \exp[c_{2,escape} z]\,\mu_2 \mathrm{d}z}}. \end{aligned} \tag{6.5}$$

Therefore, we now have an equation that relates the SNR, the number of incident photons and the feature size for FIB-SXM imaging.

6.3.2 Signal to Noise Ratio for the Transmission Mode

Now, we compare the signal to noise ratio result for FIB-SXM with the one for TXM imaging which is currently the most commonly used soft X-ray imaging method for cells. The exact SNR in the transmission X-ray microscope depends

on the contrast mechanism and the experimental setup. Here, we study a best case scenario. We assume that the microscope generates a perfect image of the sample, and the only noise present results from the probabilistic nature of the photon sample interaction. In a real system, this is not achievable since only a fraction of photons are collected and the detector introduces additional noise. Absorption contrast and phase contrast imaging are now separately studied in this scenario.

Absorption Contrast in TXM

As previously stated, the SNR is defined as the quotient of the expected signal to the standard variation of the signal, i.e. $SNR := \frac{\mathbb{E}[S]}{SD[S]}$ where $\mathbb{E}[S]$ and $SD[S]$ are the mean and standard variation of the signal (S). We now consider the signals produced by two cuboids which differ only in the material. Due to the different X-ray optical properties of the materials, both cuboids absorb a different number of the arriving photons. The photons which are transmitted by the cuboid photons then generate the detected signal (Y_i) . The signal is the difference between the two detected photon counts $S = Y_1 - Y_2$.

We start again with the number of incoming photons N_i. As before, this number is usually described by a Poisson distribution. Secondly, each of these photons has a certain (independently identically distributed) probability to be absorbed in the cuboid. The probability for a photon to be transmitted depends only on the thickness and optical properties of the cuboid. It is given by $p_i = \exp[-\mu_i \Delta z]$. Where μ_i and Δz are the absorption coefficient and thickness of the cuboid. The amount of transmitted photons is hence $Y_i = \sum_{l=1}^{N_i} Z_{i,l}$, with $Z_{i.l}$ a Bernoulli distribution with parameter p_i.

The variance of the signal is therefore

$$Var[S] = Var[Y_1 - Y_2].$$

$$Var[S] = \mathbb{E}[N_1](2(\exp[-\mu_1\Delta z] + \exp[-\mu_2\Delta z]) - (\exp[-2\mu_1\Delta z] + \exp[-2\mu_2\Delta z])).$$

while the expected value is

$$\mathbb{E}[S] = \mathbb{E}[N_1](\exp[-\mu_1\Delta z] - \exp[-\mu_2\Delta z]).$$

Therefore, the signal to noise ratio equals

$$\begin{aligned} SNR[S] &= \frac{\mathbb{E}[S]}{SD[S]} \\ &= \frac{\mathbb{E}[N_1](\exp[-\mu_1\Delta z] - \exp[-\mu_2\Delta z])}{\sqrt{\mathbb{E}[N_1](2(\exp[-\mu_1\Delta z] + \exp[-\mu_2\Delta z]) - (\exp[-2\mu_1\Delta z] + \exp[-2\mu_2\Delta z]))}}. \end{aligned}$$

In order to simplify this expression, the square root is approximated by its Taylor series

$$\begin{aligned} SNR[S] &= \frac{\mathbb{E}[N_1]\left(\exp[-\mu_1\Delta z]-\exp[-\mu_2\Delta z]\right)}{\sqrt{\mathbb{E}[N_1]\left(2\left(\exp[-\mu_1\Delta z]+\exp[-\mu_2\Delta z]\right)-\left(\exp[-2\mu_1\Delta z]+\exp[-2\mu_2\Delta z]\right)\right)}} \\ &\approx \sqrt{\mathbb{E}[N_1]}\left(\left(-\mu_1+\mu_2\right)\Delta z+\left(\mu_1^2-\mu_2^2\right)\Delta z^2+\dots\right) \\ &\quad\cdot\left(\frac{1}{\sqrt{2}}+\frac{1}{2}\left(\mu_1^2+\mu_2^2\right)(\Delta z)^2+\dots\right) \\ &\approx \sqrt{N}\frac{1}{\sqrt{2}}\left(-\mu_1+\mu_2\right)\Delta z \end{aligned} \tag{6.6}$$

Zernike Phase Contrast in TXM

Zernike phase contrast was developed for light microscopy in the early 1930's by Zernike [109] and later adapted to X-ray microscopy [78]. The key idea behind Zernike phase contrast is to impose a bias onto the detected field. Therefore, the signal generated by a cuboid is

$$Y_i = \left|A_i \exp[i\Delta\varphi_i] + B\exp[i\varphi_B]\right|^2.$$

Here, $B\exp[i\varphi_B]$ is the bias, $\Delta\varphi_i$ and A_i are the phase difference and amplitude generated by the cuboid. The bias $B\exp[i\varphi_B] \in \mathbb{C}$ is usually generated through a phase shifting element in a conjugate plane to the condenser of the objective. The phase shifting element is adapted to the Fourier components of the illumination created by the condenser. For the sake of simplicity, we assume that the bias is not influenced by the cuboid.

We are again interested in differentiating between two cubes of material 1 and material 2. Let the signal be the difference between the two detected photon counts $S = Y_1 - Y_2$. The expected signal is

$$\begin{aligned} \mathbb{E}[S] &= \mathbb{E}[Y_1 - Y_2] \\ &= \mathbb{E}[Y_1] - \mathbb{E}[Y_2]. \end{aligned}$$

The expected signal generated by one cube is

$$\begin{aligned} \mathbb{E}[Y_i] &= \mathbb{E}\left[A_i^2 + A_i B\left(\exp[i\left(\Delta\varphi_i - \varphi_B\right)] + \exp[i\left(\varphi_B - \Delta\varphi_i\right)]\right) + B^2\right] \\ &= \mathbb{E}\left[A_i^2\right] + \mathbb{E}\left[A_i B\left(\exp[i\left(\Delta\varphi_i - \varphi_B\right)] + \exp[i\left(\varphi_B - \Delta\varphi_i\right)]\right)\right] + \mathbb{E}\left[B^2\right] \\ &= N_0\exp[-\mu_i\Delta z] + B^2 + 2B\cdot\sqrt{N_0}\exp\left[-\frac{1}{2}\mu_i\Delta z\right]\cos\left[\left(\Delta\varphi_i - \varphi_B\right)\right]. \end{aligned}$$

The difference in the phase shift $\Delta\varphi_i$ depends on the material and the thickness. We use a macroscopic model and therefore, it is assumed that this difference is a deterministic function of the sample thickness.

We assume that the number of detected photons Y_i is again Poisson distributed. Then, the variance of Y_i is

$$Var[Y_i] = N_0 \exp[-\mu_i \Delta z] + B^2 + 2B \cdot \sqrt{N_0} \exp\left[-\frac{1}{2}\mu_i \Delta z\right] \cos[(\Delta\varphi_i - \varphi_B)].$$

Therefore, the SNR of the signal S is approximately

$$SNR[S] = \frac{\mathbb{E}[Y_1 - Y_2]}{\sqrt{Var[Y_1 - Y_2]}}$$

$$\approx \frac{N_0\left(e^{-\mu_1\Delta z} - e^{-\mu_2\Delta z}\right) + 2B \cdot \sqrt{N_0}\left(e^{-\frac{1}{2}\mu_1\Delta z}\cos[\Delta\varphi_1 - \varphi_B] - e^{-\frac{1}{2}\mu_2\Delta z}\cos[\Delta\varphi_2 - \varphi_B]\right)}{\sqrt{N_0\left(e^{-\mu_1\Delta z} + e^{-\mu_2\Delta z}\right) + 2B^2 + 2B \cdot \sqrt{N_0}\left(e^{-\frac{1}{2}\mu_1\Delta z}\cos[\Delta\varphi_1 - \varphi_B] + e^{-\frac{1}{2}\mu_2\Delta z}\cos[\Delta\varphi_2 - \varphi_B]\right)}}.$$

A common choice for the free parameters B and φ_B are $B = \sqrt{N_0}$ and $\varphi_B = \pm\frac{\pi}{2}$. Then, the equation simplifies to

$$\begin{aligned} SNR[S] &= \frac{\mathbb{E}[Y_1 - Y_2]}{\sqrt{Var[Y_1 - Y_2]}} \\ &\approx \frac{\sqrt{N_0}\left(\exp[-\mu_1\Delta z] - \exp[-\mu_2\Delta z] + \exp\left[-\frac{1}{2}\mu_1\Delta z\right](\pm\sin[(\Delta\varphi_1)]) - \exp\left[-\frac{1}{2}\mu_2\Delta z\right](\pm\sin[(\Delta\varphi_2)])\right)}{\sqrt{\exp[-\mu_1\Delta z] + \exp[-\mu_2\Delta z] + 2 + 2\left(\exp\left[-\frac{1}{2}\mu_1\Delta z\right](\pm\sin[(\Delta\varphi_1)]) + \exp\left[-\frac{1}{2}\mu_2\Delta z\right](\pm\sin[(\Delta\varphi_2)])\right)}}. \end{aligned}$$

6.3.3 Signal to Noise Ratio for X-ray Diffraction Microscopy

An analysis of both the signal to noise ratio and the damage threshold for biological samples for CDI and X-ray diffraction microscopy can be found in [42]. It is based on the diffraction pattern of a single voxel and produces the same general scaling of the dose as in the TXM case. Specifically, the dose scales with the inverse of the fourth power of the resolution ([42] eq. 3)

$$N_0 = \frac{P}{r_e^2 \lambda^2 |\tilde{\rho}_r|^2 d^4}.$$

Here, N_0 is the number of incident X-rays per unit area, d is the size of the voxel, r_e is the classical electron radius, $\tilde{\rho}_r$ the relative electron density (which takes into account the reduced contrast between water and protein) and P is the number of scattered photons that are detected.

The same paper contains an approximation of the maximal tolerable dose. For a cryogenic biological sample, the dose (D) should be less than ([42] eq. 5)

$$D \lessapprox 10^8 \text{Gy} \cdot resolution\,[\text{nm}].$$

In this paper, it is assumed that the relationship between the dose D near the surface and the number of incident photons per unit area is given by

$$D = \frac{\mu N_0 h \nu}{\varepsilon}.$$

Here, ε is the density, μ is the absorption coefficient, ν is the frequency of the photons and h is the Plank constant. For water at 2.4 nm ($\varepsilon \approx 1\frac{g}{cm^3}$, $\mu \approx \frac{1}{9}\,\mu m^{-1}$), one gray corresponds to one hundred photons per square micrometer $\left(1\,\text{Gy} \approx 100\,\frac{\text{photon}}{\mu m^2}\right)$, while one gray corresponds for cellular membranes under the same conditions to twelve photons per square micrometer $\left(1\,\text{Gy} \approx 12\,\frac{\text{photon}}{\mu m^2}\right)$ (see table 4.1). For 30 nm resolution, the results are compatible with [81].

6.3.4 Comparison of the Signal to Noise Ratios

The following example shows that the different scaling laws for the signal to noise ratio favor the FIB-SXM for high resolution imaging.

Example: Protein Cube in Water As an example, the SNR of a cube of proteins (chromatin) and a cube of water (ice) are compared. The following parameters are used

$$\begin{aligned}(\delta, \beta)_{Chromatin} &\approx \left(8.36 \cdot 10^{-4},\, 1.57 \cdot 10^{-4}\right)\\ (\delta, \beta)_{Water} &\approx \left(5.310^{-4},\, 0.21 \cdot 10^{-4}\right).\end{aligned}$$

In figure 6.4, we plot the required photon density over the size of a cube for an SNR of five and compare it to the damage threshold. The optical properties of the materials are given in table 4.1. Equation (6.2), equation (6.5) and equation (6.6) yield the following results for the required incident flux (ρ) in photons per square micrometer. For the simplest case that all photoelectrons are detected, the SNR of the FIB-SXM is

$$SNR \overset{6.2}{=} \frac{\sqrt{N\Delta z}\,(\mu_1 - \mu_2)}{\sqrt{(\mu_1 + \mu_2)}}.$$

Therefore, the photon density (ρ_{photon}) for a prescribed SNR is

$$\rho_{photon} = \frac{SNR^2\,(\mu_1 + \mu_2)}{(\mu_1 - \mu_2)^2\,\Delta z^3}.$$

If the detection probability of photoelectrons is included, the photon density results from the changed SNR

$$SNR \overset{6.5}{=} \sqrt{\eta N}\frac{\int_0^{\Delta z} \exp\left[c_{1,escape} z\right] \mu_1 - \exp\left[c_{2,escape} z\right] \mu_2 \, \mathrm{d}z}{\sqrt{\int_0^{\Delta z} \exp\left[c_{1,escape} z\right] \mu_1 + \exp\left[c_{2,escape} z\right] \mu_2 \, \mathrm{d}z}}.$$

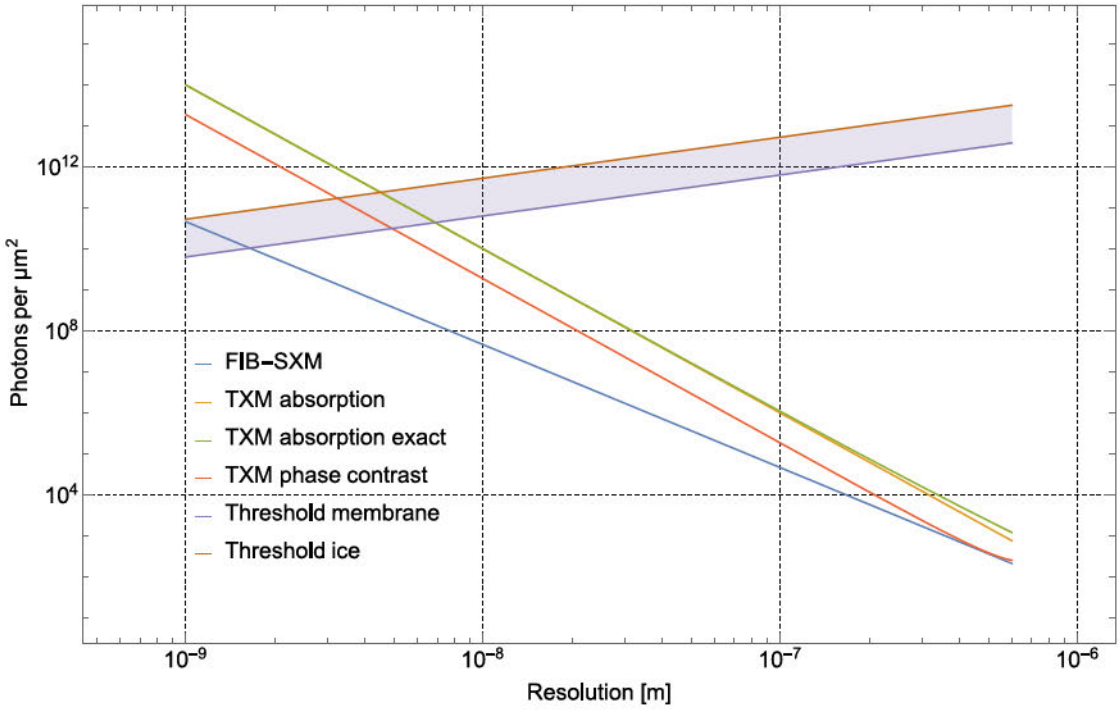

Figure 6.4: *Plot of the required photon density over the size of the protein / water cube for an SNR of five at $\lambda = 2.4\,\mathrm{nm}$. An enlarged plot of the interesting region between 1 nm and 30 nm is shown in figure 6.5.*

Therefore, the photon density (ρ_{photon}) for a prescribed SNR is under these conditions

$$\rho_{photon} = \frac{SNR^2 \int_0^{\Delta z} \exp\left[c_{1,escape} z\right] \mu_1 + \exp\left[c_{2,escape} z\right] \mu_2 \, \mathrm{d}z}{\eta \Delta z^2 \left(\int_0^{\Delta z} \exp\left[c_{1,escape} z\right] \mu_1 - \exp\left[c_{2,escape} z\right] \mu_2 \, \mathrm{d}z\right)^2}.$$

In both cases, the photon density increases roughly inversely to the third power of the size of the detected object. As the following example shows, the photon density increases faster for the transmission microscope, namely roughly inversely to the fourth power of the size of the feature.

For pure absorption contrast imaging, the SNR in the transmission microscope is

$$SNR \overset{6.6}{=} \sqrt{N}\frac{1}{\sqrt{2}}\left(-\mu_1+\mu_2\right)\Delta z.$$

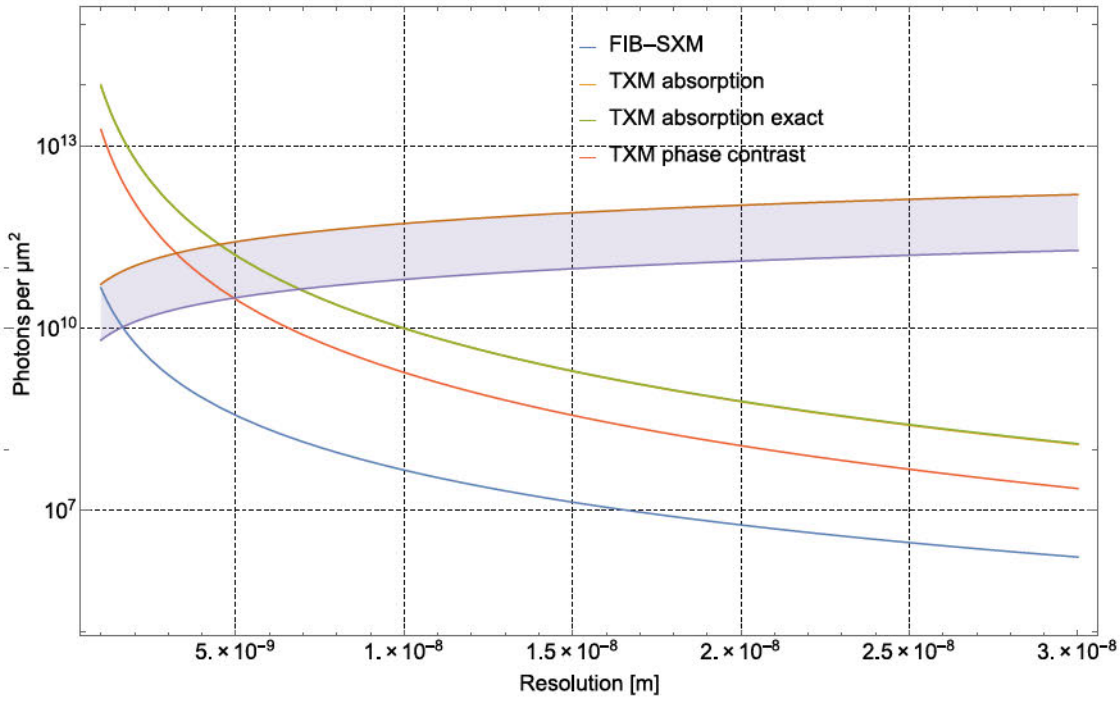

Figure 6.5: *Detailed plot of the required photon density over the size of the cube of chromatin for an SNR of five at $\lambda = 2.4\,\mathrm{nm}$. One should be aware that the plot assumes an optic with 100% efficiency. In practice, high resolution FZPs have efficiencies of about 10 % [103].*

This results in a photon density of

$$\rho_{photon}^{(absor.)} = \frac{2\,SNR^2}{\left(\mu_1-\mu_2\right)^2\Delta z^4}.$$

According to these calculations, FIB-SXM solves a fundamental problem of soft X-ray transmission imaging of biological samples. As the plot in figure 6.4 shows, FIB-SXM drastically decreases the dose that is required for a prescribed resolution and signal to noise ratio. Therefore, this method allows higher resolution than other soft X-ray transmission methods.

Summary

In this chapter, we have discussed the new soft X-ray imaging method FIB-SXM. The numerical simulations revealed an increased image quality for cell imaging in comparison to the current standard TXM. It was also shown, that FIB-SXM significantly reduces the required dose. This is a significant advantage, since the dose is currently often a limiting factor for high resolution soft X-ray imaging. Since FIB-SXM uses only a small X-ray spot, this method potentially suppresses the charging problems which occur in photoemission electron microscopy (PEEM). Additionally, the lateral resolution in the FIB-SXM is already provided by the size of the scanned X-ray spot. Therefore, in principle all emitted electrons originating from the spot can contribute to the photoelectron signal. For comparison, in the high resolution mode of the PEEM only a small fraction of the emitted electrons are collected by the electron column [79]. Therefore, the required dose for FIB-SXM might also be significantly lower compared to high resolution PEEM.

Chapter 7

Holography with Beam Shaping Optical Elements

The soft X-ray imaging methods studied in the previous chapters aim for high resolution 3D imaging. However, all these X-ray optical setups are not suited for ultra-fast imaging with spatially coherent femtosecond pulses. Modern free electron lasers (FEL) emit fs-pulses with very high brilliance and high photon numbers. Time resolved imaging on the length scale of a few nm with ultra-short time resolution would give new insight into fast dynamic processes, for example in magnetism [18]. For this purpose, novel X-ray imaging methods have to be developed which make use of the high coherent photon flux and permit full-field imaging.

In the visible light region, holography - originally invented by Gabor in 1948 [25] - became a routine method with the introduction of lasers in the visible light range. In this chapter, we will investigate the potential performance of a novel X-ray holography setup employing advanced diffractive optical elements (DOE).

7.1 Introduction to DOE Based Holography

Holography as an X-ray imaging method was already proposed in 1964 [92, 106] and the first experiments were conducted a year later [93]. For X-ray imaging, in-line and Fourier transform holography (FTH) are mainly used.

The optical setup for soft X-ray in-line holography was already described in chapter 2 and is shown in figure 2.4b. A typical in-line holography setup consists of a focusing optic, a sample and a detector. The focus of the beam lies a bit in front of or behind the sample. The defocused beam passes through the sample and the resulting diffracted wave (U_s) interferes with the non-diffracted beam (U_0) on the detector. The divergence of the non-diffracted beam defines the numerical

aperture and therefore the resolution. However, the image quality of the resulting in-line holograms suffer due to the so-called twin image problem, which is caused by an overlap of the virtual and the real image. This problem is suppressed in Fourier transform holography by separating both images (see also [62] chapter 4.3 or equation (7.2)).

In general, the setup for Fourier transform holography consists of a reference pinhole and a sample area (see figure 7.1, [18]). As described in section 2.2.3, the interference signal between light scattered from the sample and light scattered from the reference is detected in the far field. The reconstruction is done via Fourier transform. The resulting image can be split into four components including two components that are essentially convolutions between the image of the reference and the sample. Therefore, the size of the pinhole defines also the resolution. In most experiments, the reference is created by milling small, well defined pinholes into an opaque membrane which also contains a transparent area for the sample. A decreased pinhole diameter increases the resolution, but reduces at the same time the amount of photons in the reference wave, which increases the required exposure times[1]. This problem can be slightly reduced by setups with multiple pinholes [51] or extended reference [32]. However, these types of references scatter the light inhomogeneously, resulting in a bright central spot and a fast declining signal for high spatial frequencies.

To address both the problem of the decreased photon numbers in the reference wave with the decreased pinhole size and the fast decline of the reference wave for high spatial frequencies at the same time, we propose to use a single diffractive optical element (DOE) which generates simultaneously a homogeneous illumination profile for the sample area and a diffraction limited reference. This X-ray optical setup is shown in figure 7.2.

The DOE based setup has several advantages in comparison to standard Fourier transform holography. The DOE generates the required reference spot and homogeneous illumination of the sample at the same time. The focal length of the DOE depends on its diameter, its outermost zone width, the order of diffraction and the wavelength. By choosing these parameters, one can achieve a significant distance between sample and DOE. Therefore, the sample no longer has to be close to an opaque screen. The DOE based setup allows to use cryogenic samples and allows to image larger samples via raster scanning and stitching of the resulting images. The scanning process also reduces the effect of speckles. The intensity distributions in the sample and reference area are a free design parameter and can be optimized for a strong signal[2]. Additionally, a larger part of the incident X-rays

[1]The signal to noise ratio also depends on the ratio between the number of photons in the reference wave and sample wave. To maximize the signal used in Fourier transform holography, both photon numbers should be similar. See also equation (7.2).

[2]The image of the hologram results from the interference between reference and sample. To

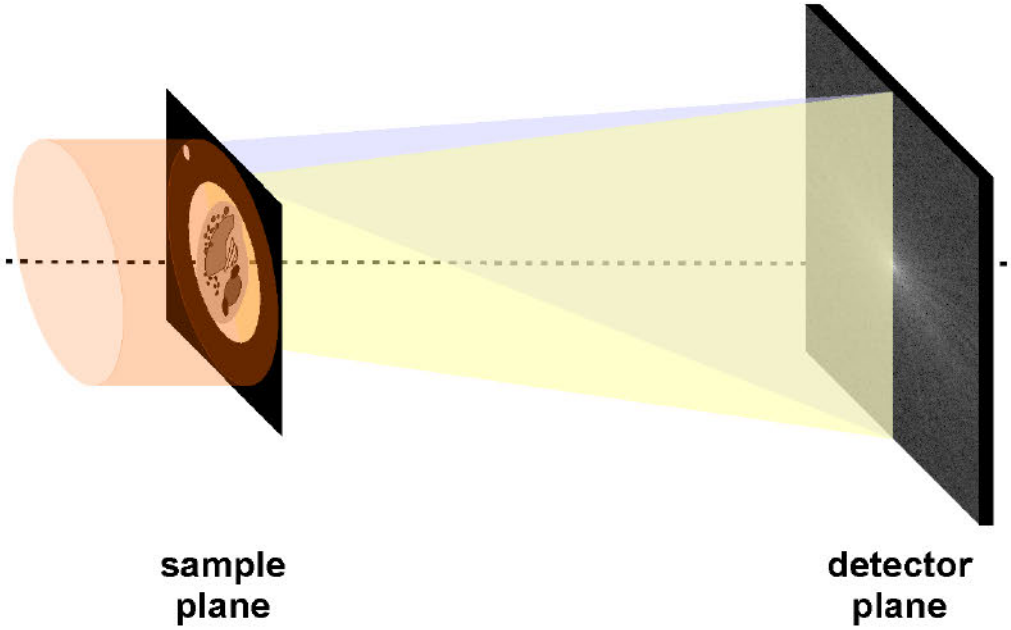

Figure 7.1: *Fourier transform holography setup. The diffracted light from the reference and sample interfere in the far field and generate the hologram.*

is used. The diffractive optical element can be relatively large, which allows to use a widened FEL beam and reduces damage to the DOE due to heating. Therefore, the DOE can endure the exposure to pulses of an FEL and potentially allows for single shot imaging at FELs. In this type of FTH-setup, the light is more homogeneously distributed over the detector, which reduces the required dynamic range of the detector.

7.2 The Computer Aided Design of Diffractive Optical Elements for Holography

For the imaging quality of DOE based FTH, it is essential to design a DOE which creates a well suited illumination profile. Here,we describe an algorithm for the design of binary masks for such DOEs. For simplicity, the algorithm is divided into

maximize the corresponding signal the photons should have equal probability to originate from the reference or from the sample area.

$$\begin{aligned} I_{detector}[x,y] &= |\psi_{reference} + \psi_{sample}|^2 [x,y] \\ &= \psi_{ref}\overline{\psi_{ref}} + \psi_{sam}\overline{\psi_{ref}} + \psi_{ref}\overline{\psi_{sam}} + \psi_{sam}\overline{\psi_{sam}}. \end{aligned}$$

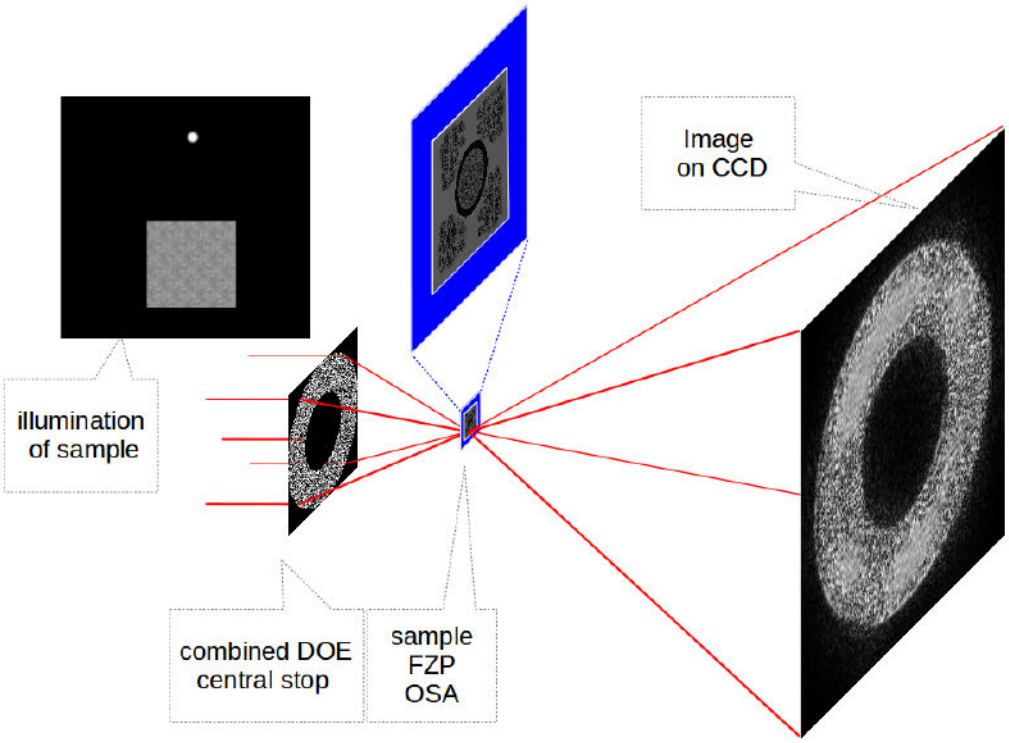

Figure 7.2: *Fourier transform holography setup based on a diffractive optical element. The illumination of the sample and the reference are generated by the DOE. The test sample consist of four structured arrays and a Fresnel zone plate in the center of the waver. The FZP was used to verify the created illumination. The window in the wafer of the sample in combination with the central stop on the DOE selects the order of diffraction used for imaging.*

three main steps. Firstly, a continuous complex transmission function that transforms the inbound illumination into an optimal profile for the FTH experiment is determined. This transmission function has to fulfill some additional constraints. For example, we choose that it has to be purely phase shifting. Secondly, the transmission function is approximated by a binary mask. The binary mask is later used as pattern of the DOE. Finally, the DOE pattern has to be verified since the first steps include approximations (Fresnel approximation respectively wide-angle near and far field approximation NFFA) which could result in numerical artifacts. The verification is done by first modifying the inbound wave with the transmission function of the DOE. The modified wave is then propagated into the focal plane of the DOE by a convolution based propagator (see also equation (2.6)). Experimentally, the designed DOE pattern is written into an e-beam resist by electron beam lithography. Planar nanotechnology is used to create the final DOE.

For the approximation of the DOE's transmission function by a binary mask, the phase of the inbound illumination and the field that generates the profile for the FTH experiment have to be compared. In order to compare the phases of both fields, a function (ϕ) that approximates the phase of the fields has to be determined. This leads naturally to the two dimensional phase unwrapping problem, which will be discussed in the following.

7.2.1 Least Square Approximation of the 2D Phase Unwrapping Problem by the Fourier Transform

In many applications (e.g. synthetic aperture radar (SAR)/ magnetic resonance imaging (MRI)), the function of interest $\phi : \mathbb{R}^2 \to \mathbb{R}$ is not directly measurable but instead a wrapped version $\psi : \mathbb{R}^2 \to (-\pi, \pi]$ is measured. The relationship between the two functions is given by

$$\exp[i\,\phi] \stackrel{!}{=} \exp[i\,\psi]\,. \tag{7.1}$$

This equation includes already the main problems. The lifting of the function ψ is not unique. If ϕ is continuous, it is unique up to a constant. For an overview of the 2 dimensional phase unwrapping problem see [28]. The subsequent calculations are also based on [28].

In most applications, ϕ is not necessarily a continuous function and, therefore, additional information is needed to deduce the correct ϕ from ψ. One example in polar coordinates for a non-continuous function ϕ is produced by the function $\hat{\psi}$,

$$\hat{\psi} : (r, \theta) \in \mathbb{R} \times (-\pi, \pi] \mapsto \theta.$$

A general problem for discretised versions of this equation is that the slope between two adjacent points x_1 and x_2 is only defined up to a multiple of π.

$$\begin{aligned} \exp[i\ (\phi[x_1] - \phi[x_2])] &= \exp[i\ (\phi[x_1] - \phi[x_2] + 2\pi \cdot m)] \\ &= \exp[i\ (\psi[x_1] - \psi[x_2])] \end{aligned}$$

Therefore, the discretised version of equation (7.1) is in general not even well posed for smooth functions ϕ.

If ϕ is smooth and its first derivatives are bounded, one solution is to use a finer discretization so that the maximal difference of the value of ϕ between neighboring points is smaller than π. Unfortunately, this approach is not feasible for many applications, including the design of the diffractive optical elements used for our experiments. Nevertheless, for some applications, it is enough to find a sufficiently good approximation $\hat{\phi}$ to ϕ which satisfies the condition that $\hat{\phi}$ has small first derivatives.

A good approximation should minimize the distance between the wrapped version ψ and the projected approximation $\hat{\phi}$ and should minimize the difference of the slopes

$$\hat{\phi} = \underset{\phi}{\operatorname{argmin}} \sum_i \sum_j \left|\phi_{i+1,j} - \phi_{i,j} - \Delta^x_{i,j}\right|^2 + \sum_i \sum_j \left|\phi_{i,j+1} - \phi_{i,j} - \Delta^y_{i,j}\right|^2 .$$

The discretised slopes are here only defined up to a multiple of 2π due to $\Delta^x_{i,j} := \arg\left[\exp\left[i\ (\psi_{i+1,j} - \psi_{i,j})\right]\right]$ and $\Delta^y_{i,j} := \arg\left[\exp\left[i\ (\psi_{i,j+1} - \psi_{i,j})\right]\right]$. The solution to this problem is a discrete version of Poisson's equation (see for example chapter 5 [28]).

From the continuous version $\frac{\partial^2}{\partial x^2}\phi\left[x,y\right] + \frac{\partial^2}{\partial y^2}\phi\left[x,y\right] = \rho$, a discrete one can be defined as

$$(\phi_{i+1,j} - 2\phi_{i,j} + \phi_{i-1,j}) + (\phi_{i,j+1} - 2\phi_{i,j} + \phi_{i,j-1}) = \rho_{i,j}.$$

Therefore, the solution to the problem is given by the following set of equations

$$\begin{aligned} \rho_{i,j} &= \left(\Delta^x_{i,j} - \Delta^x_{i-1,j}\right) + \left(\Delta^y_{i,j} - \Delta^y_{i,j-1}\right) \\ \rho_{i,j} &= \left(\phi_{i+1,j} - 2\phi_{i,j} + \phi_{i-1,j}\right) + \left(\phi_{i,j+1} - 2\phi_{i,j} + \phi_{i,j-1}\right). \end{aligned}$$

One way of finding a solution is based on the Fourier transform and extends the functions ρ, ϕ and ψ to periodic functions $\tilde{\rho}, \tilde{\phi}$ and $\tilde{\psi}$.

If the functions ρ, ϕ and ψ are defined on an $N+1 \times M+1$ grid, the extension is done by mirror reflection. The mirror reflection is defined in the following way:

$\phi : \{0 \ldots N\} \times \{0 \ldots M\} \to \mathbb{R}$ and $\psi \{0 \ldots N\} \times \{0 \ldots M\} \to (-\pi, \pi]$

$$\tilde{\psi}_{i,j} = \begin{cases} \psi_{i,j} & 0 \leq i \leq M,\ 0 \leq j \leq N \\ \psi_{2M-i,j} & M < i < 2M,\ 0 \leq j \leq N \\ \psi_{i,2N-j} & 0 \leq i \leq M,\ N < j < 2N \\ \psi_{2M-i,2N-j} & M < i < 2M,\ N < j < 2N \end{cases}$$

$$\begin{aligned} \tilde{\Delta}^x_{i,j} &:= \arg\left[\exp\left[i\left(\tilde{\psi}\left(i+1,j\right) - \tilde{\psi}\left(i,j\right)\right)\right]\right] \\ \tilde{\Delta}^y_{i,j} &:= \arg\left[\exp\left[i\left(\tilde{\psi}\left(i,j+1\right) - \tilde{\psi}\left(i,j\right)\right)\right]\right] \end{aligned}$$

$$\tilde{\rho}_{i,j} = \left(\tilde{\Delta}^x_{i,j} - \tilde{\Delta}^x_{i-1,j}\right) + \left(\tilde{\Delta}^y_{i,j} - \tilde{\Delta}^y_{i,j-1}\right).$$

By applying the two dimensional Fourier transform on the extended equation

$$\left(\tilde{\phi}_{i+1,j} - 2\tilde{\phi}_{i,j} + \tilde{\phi}_{i-1,j}\right) + \left(\tilde{\phi}_{i,j+1} - 2\tilde{\phi}_{i,j} + \tilde{\phi}_{i,j-1}\right) = \tilde{\rho}_{i,j},$$

(a) Original image **(b)** $\Delta_{max} = 1.5\pi$ **(c)** $\Delta_{max} = 2\pi$ **(d)** $\Delta_{max} = 3\pi$ **(e)** $\Delta_{max} = 8\pi$

Figure 7.3: *Different examples for reconstructed $\tilde{\phi}$ from wrapped data. The Fourier transform based method was used. The maximal difference between neighboring pixels is in* **(a)** *original* **(b)** 1.5π, *in* **(c)** 2π, *in* **(d)** 3π *and in* **(e)** 8π. *For high Δ_{max} values, the over smoothing of this operation is reflected in the color bar and is obvious from visual inspection of the images.*

a relationship between the Fourier transforms $P = \mathcal{FFT}[\tilde{\rho}]$ and $\Phi = \mathcal{FFT}\left[\tilde{\phi}\right]$ of $\tilde{\rho}$ and $\tilde{\phi}$ follows. From the resulting equation

$$\Phi_{m,n} = \frac{P_{m,n}}{2\cos[\pi m/M] + 2\cos[\pi n/N] - 4},$$

the estimate for ϕ is obtained by applying an inverse Fourier transform on Φ.

This method is not suitable for discontinuous functions ϕ or step sizes with discrete jumps above π as the examples in figure 7.3 emphasize. In the next section, this approximate solution to the phase unwrapping problem is used to design (higher order) diffractive optical elements.

7.2.2 Creating Diffractive Optical Elements with Substructure Width Resolution

In the Fourier transform holography setup, the numerical aperture of the DOE determines the achievable resolution. In practice, the numerical aperture of the DOE is limited by the precision of the nano-production method. The dependency of the resolution of a DOE and of a Fresnel zone plate are similar. For Fresnel zone plates, the Rayleigh resolution is given by $\Delta = \frac{1.22}{m} dr_N$. Here, dr_N is the outermost zone width and an essential parameter of the fabrication technique. In chapter 8, positioning errors in the manufacturing process of Fresnel zone plates are further discussed. The parameter m is the order of diffraction that is used for

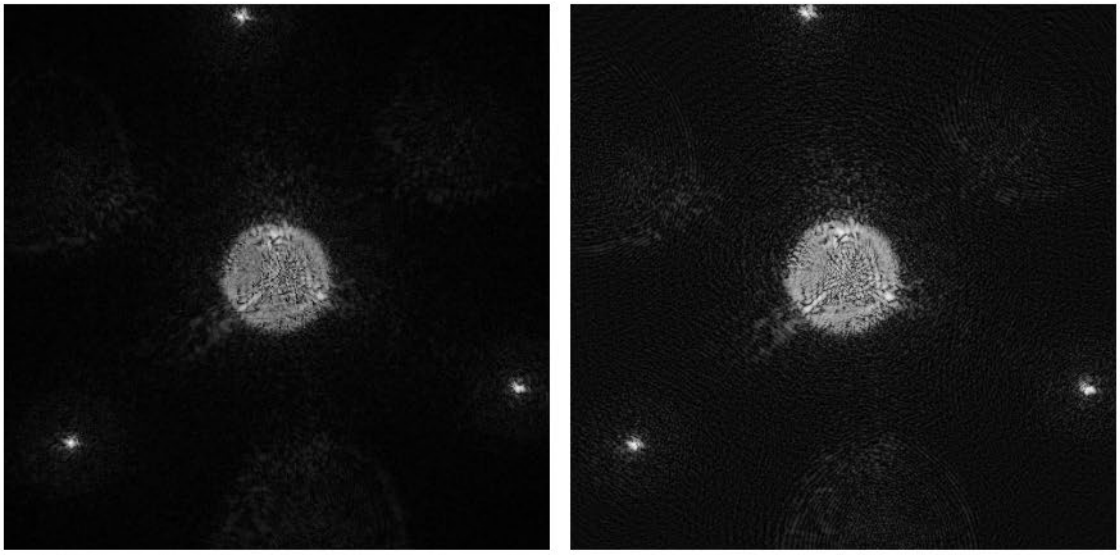

(a) Focus iterative optimizer (continuous) **(b)** Focus binary DOE

Figure 7.4: *Examples for the described algorithms for the generation of higher order DOEs. (In the print version, the color scale is nonlinear.)*
(a) *Focus as predicted by the iterative optimizer. This focal pattern is generated by a purely phase shifting continuous DOE.*
(b) *Focal pattern for the generated third order, binary DOE. The computation uses the convolution based algorithm as described in chapter 3.*

the imaging process. Therefore, with a prescribed outermost zone width, an image with higher resolution can be achieved by using a higher diffraction order. However, the efficiency of higher orders decreases for thin Fresnel zone plates proportionally to $\frac{1}{m^2}$. Since, for full-field microscopy, the Fresnel zone plate is situated between object and detector, the efficiency directly influences the dose needed for a given resolution. The use of a higher order also requires an increased stability of the zone thickness and exactness of the position.

Similarly, diffractive optical elements can be designed to use higher orders of diffraction to increase the resolution at the cost of a decreased efficiency. An algorithm for the design of such optics will now be presented. It is based on the propagators described in chapter 3 and the phase unwrapping algorithm presented in the previous section. The main steps are:

1. Defining the target intensity distribution in the focal plane of the DOE
2. Computing a holographic first estimate of the field in the plane of the DOE
3. Finding a least squares estimate for a continuous lift of the phase in the plane of the DOE

4. Propagating the resulting field into the focal plane of the DOE
5. Adapting the computed amplitudes to amplitudes that fit better the target intensity
6. Back propagation to the plane of the DOE
7. Restarting at 3. until a good approximation is found

A test of this algorithm is shown in figure 7.4. Note that this algorithm has several other applications aside from holography. Therefore several other methods for the design of diffractive optical elements exist, but those use the first order of diffraction [102, 108, 49]. Examples for such applications could be the design of condensers for improved dark and bright field soft X-ray full-field microscopes, as presented in appendix D.

7.3 Analysis of Experimental Data

7.3.1 Introduction

In the following, two proof of concept holography experiments are described. These experiments were conducted respectively at the U41 TXM beamline located at the Helmholtz Zentrum Berlin and at a plasma based soft X-ray laser (XRL [91]) located at the Max Born Institute.

7.3.2 Experimental Data and its Analysis

The holography experiment was conducted at the U41 TXM beamline at BESSY II. The optical setup of the experiment is diagrammed in figure 7.2. Parts of the TXM setup were modified for the experiment. The previously described algorithm was used to design the binary diffractive optical element (DOE) for the experiment. The DOE has a diameter of 250 µm and a central stop of 150 µm. It has an outermost zone width of 50 nm and a focal length of 5.2 mm at a wavelength of $\lambda = 3.84\,\mathrm{nm}$. The DOE and a test sample were fabricated in an electron beam based lithography process at the Helmholtz Zentrum Berlin.

Experiments showed that the condenser stage of the TXM is not sufficiently vibration-free for aligning the DOE. Therefore, we designed an adapter which was directly mounted to the TXM chamber. This direct mounting removed vibrations. However, the position and tilt of the DOE could no longer be changed. As test sample, we used 120 nm high gold structures on a Si_3N_4 membrane. As described before, the sample consists of four square areas which include a pattern of „T“ in various orientations. Each area also includes four Siemens stars which have spikes

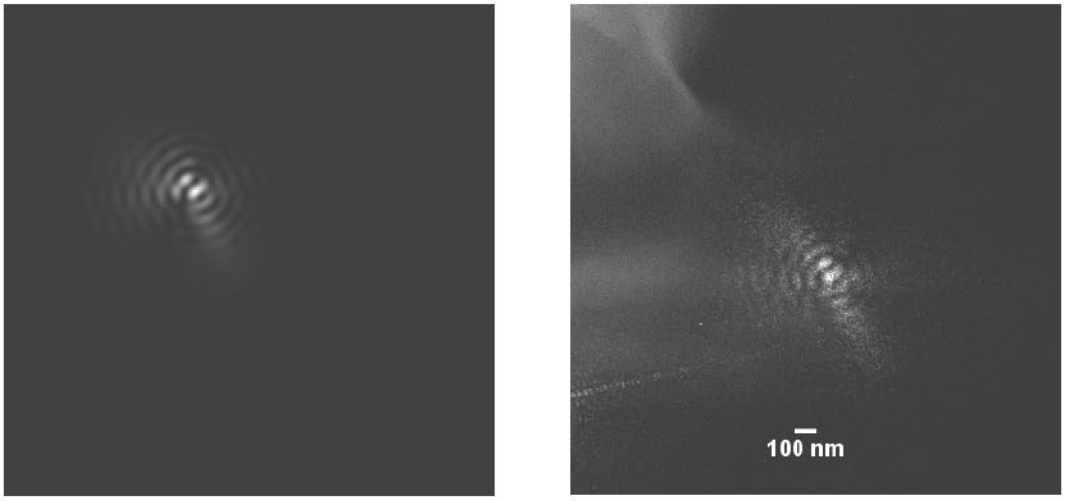

(a) predicted reference **(b)** measured reference

Figure 7.5: *A comparison between the numerical prediction and the measured reference spot produced by the DOE shows a good agreement.*

between 20 nm and 100 nm width. In the center of the sample, a high resolution FZP with 201 zones and an outermost zone width of 39.1 nm is included. This zone plate was later used to image the focal pattern of the DOE. Due to the space constraints in the TXM, we did not include a separate pinhole for the order sorting aperture (OSA). Instead, the window of the DOE wafer and the central stop of the DOE were matched so that the 100 nm width of the wafer formed an order sorting aperture. As detector, we used the thinned, backside illuminated CCD from the TXM (Roper Scientific, PI SX1300). The distance between the focal plane of the DOE and the CCD was approximately 32 cm. Under these conditions, the numerical aperture is $NA \approx 0.04$. Therefore, the best achievable resolution is theoretically about 50 nm.

During the experiment, we first tested the performance of the DOE by imaging the light distribution in the focal plane of the DOE with a high resolution FZP. A visual comparison between the numerically predicted and the measured focal spot shows a good agreement as seen in figure 7.5.

In a second step, the test sample was introduced. The Fresnel zone plate on the test sample was then used to image the light distribution in the focal pattern of the DOE again. This step was used to estimate the positioning between DOE and test sample. Afterwards, we shifted the sample into the focal plane of the DOE and raster scanned one of the square test areas. The scanned area is 40 x 40 µm at a step width of 2 µm. Since the thinned wafer window also acted as order sorting aperture (OSA), we could not remove the sample. Therefore, it was not possible to acquire flat field images, that is images without sample. These flat

field images are usually required for normalizing the holograms. Therefore, the underlying illumination profile has to be interpolated from the experimental data.

The fact that we used pre-existing components of the TXM simplified the design and reduced the costs and amount of time required to assemble the experiments, but some parameters of the setup were not available with the precision required for the evaluation of the experiment. Therefore, these parameters have to be inferred from the experimental data. These parameters include the exact distances between sample and detector as well as the positions of the sample during the scan. These two parameters are essential for the reconstruction of an extended field of view.

7.3.3 Analysis of the Experimental Data

During the evaluation of the experimental data, one challenge was that some of the necessary parameters had to be inferred from the data before any reconstruction could be attempted. Some of those parameters are intrinsically well known, e.g. the photon energy is given by the monochromator and is recorded during the experiment. Other parameters have to be estimated from prior knowledge, e.g. the distance between DOE and CCD can be recovered from the used wavelength, the knowledge about the focal length of the DOE and the experimental images.

The first step of the evaluation consists of estimating the illumination without the sample. In analogy to photography, we will call this illumination and its resulting distribution in the plane of the detector the „flat field“. As previously stated, it was not possible to directly measure the flat field in the experiment. Therefore, an algorithm was implemented which estimates the flat field from an image series. A naive estimate of the flat field is the mean of the image series. A better estimator is the median. Due to the large amount of data, the computation of the median is not viable. Instead, an online algorithm for variance, skewness and mean is used to estimate the median for the absolute intensity as well as the real and imaginary part of the Fourier transform holographic reconstruction. The estimated median is then used as estimator for the flat field.

In the second step, the illumination created by the DOE is numerically interpolated from the experimental data and the prior knowledge of the focal pattern of the DOE. For this, the mean wavelength of the used radiation is needed. We use that the photon energy is recorded in the log files of the experiment and is for all practical purposes constant (see table 7.1). Then, we use the equation $E = hc/\lambda$. Here, E is the energy in [eV], λ is the wavelength, h is Planck's constant $\approx 4.1 \cdot 10^{-15} eV \cdot s$ and c is the speed of light. With this mean wavelength, the resulting focal light distribution is calculated for the fully coherent case. This calculation is based on the prior knowledge of the DOE.

	value	standard deviation
mean E	322.9997eV	0.0027eV
mean λ	3,8385nm	0.032pm
distance to CCD	0.3196m	$\approx$ 0.002m

Table 7.1: *Parameters from the experiment at the U41 TXM beamline.*

This predicted light distribution is then used to calculate the intensity on the detector for various distances. The previously computed estimation of the flat field from the experimental image series and the new theoretical estimator are compared. From this comparison, the position and orientation of the focal plane in relation to the detector are estimated. The distance between detector and focal plane relates the size and resolution of the detector to the pixel size and number in the holographic reconstruction. The exact relationship depends on the numerical Fresnel propagator used. Here, it is assumed to be $\Delta_2 = \frac{\lambda z_{1,2}}{\Delta_1 N}$, in accordance with appendix A. Δ_i is the resolution in the i^{th} plane, $z_{1,2}$ is the distance between first and second plane and N is the number of pixels along the considered dimension.

Now, two different reconstruction techniques can be applied. One can either reconstruct an approximation of the complex transmission function of the object by using a ptychographic reconstruction. This approach was tried but proved difficult due to the uncertainties in the relative, lateral positioning of the sample between images. However, a new algorithm is currently in development and the first results are promising. The algorithm is based on the extended ptychography iterative engine (ePIE [50, 20]) and includes an alignment step which is based on the diffraction pattern.

For the second reconstruction technique, the inverse Fourier transform of the measured intensity is used. The theoretical background for this approach is that the far field pattern is in the Fraunhofer approximation proportional to the Fourier transform of the original field. In a Fourier transform holography experiment, the intensity on the detector results from an interference between the reference and the scattered field $I_{detector} = |\psi_{reference} + \psi_{sample}|^2$. The following calculation shows that a Fourier transform leads to a reconstruction of the sample. First, we expand the expression for the intensity

$$\begin{aligned} I_{detector}[x,y] &= |\psi_{reference} + \psi_{sample}|^2 [x,y] \\ &= \left((\psi_{ref} + \psi_{sam}) \cdot \overline{(\psi_{ref} + \psi_{sam})}\right)[x,y] \\ &= \psi_{ref}\overline{\psi_{ref}} + \psi_{sam}\overline{\psi_{ref}} + \psi_{ref}\overline{\psi_{sam}} + \psi_{sam}\overline{\psi_{sam}}. \end{aligned} \tag{7.2}$$

Here, the field is partitioned into the reference (ψ_{ref}) and sample signal (ψ_{sam}) on the detector. Now, we show how an estimator of the field of the sample is computed from this expansion by an inverse Fourier transform. Let z_0 be the plane containing the reference and the sample. Let z_1 be the plane of the detector. We introduce the reference (U_{ref}) and sample signal (U_{sam}) in the z_0 plane. Then, according to equation (2.8)

$$\begin{aligned}\psi\left[x_1, y_1, z_1\right] &\approx -\frac{i\,\exp\left[ik\left(z_1 - z_0\right)\right]}{\lambda\left(z_1 - z_0\right)} \exp\left[\frac{ik\left(x_1^2 + y_1^2\right)}{2\left(z_1 - z_0\right)}\right] \\ &\int_{\mathbb{R}^2} U\left[x_0, y_0, z_0\right] \exp\left[\frac{-ik}{\left(z_1 - z_0\right)}\left(x_0\, x_1 + y_0\, y_1\right)\right] \mathrm{d}x_0\, \mathrm{d}y_0.\end{aligned}$$

A simple substitution ($x' = x_0 \cdot \frac{1}{\lambda(z_1 - z_0)}$ and $y' = y_0 \cdot \frac{1}{\lambda(z_1 - z_0)}$) shows that this is equivalent to

$$\begin{aligned}\psi\left[x_1, y_1, z_1\right] &\approx \frac{\exp\left[ik\left(z_1 - z_0\right)\right]}{i\,\lambda^3\left(z_1 - z_0\right)^3} \exp\left[\frac{ik\left(x_1^2 + y_1^2\right)}{2\left(z_1 - z_0\right)}\right] \\ &\cdot \mathcal{F}\left[U\left[\lambda\left(z_1 - z_0\right)x', \lambda\left(z_1 - z_0\right)y', z_0\right]\right].\end{aligned}$$

Applying the last equation to equation (7.2) yields

$$\begin{aligned}I &= \psi_{ref}\overline{\psi_{ref}} + \psi_{sam}\overline{\psi_{ref}} + \psi_{ref}\overline{\psi_{sam}} + \psi_{sam}\overline{\psi_{sam}} \\ &\approx \frac{1}{\lambda^6\left(z_1 - z_0\right)^6} \\ &\Big(\mathcal{F}\left[U_{ref}\left[\lambda\left(z_1 - z_0\right)x', \lambda\left(z_1 - z_0\right)y', z_0\right]\right]\overline{\mathcal{F}\left[U_{ref}\left[\lambda\left(z_1 - z_0\right)x', \lambda\left(z_1 - z_0\right)y', z_0\right]\right]} + \\ &\cdots \\ &\mathcal{F}\left[U_{sam}\left[\lambda\left(z_1 - z_0\right)x', \lambda\left(z_1 - z_0\right)y', z_0\right]\right]\overline{\mathcal{F}\left[U_{sam}\left[\lambda\left(z_1 - z_0\right)x', \lambda\left(z_1 - z_0\right)y', z_0\right]\right]}\Big).\end{aligned}$$

We use an inverse Fourier transform and apply the convolution theorem (E.6). Omitting the argument of the functions, we get:

$$\begin{aligned}\mathcal{F}^{-1}\left[I\right] &= \frac{1}{\lambda^6\left(z_1 - z_0\right)^6} \\ &\mathcal{F}^{-1}\Big[\mathcal{F}\left[U_{ref}\right]\overline{\mathcal{F}\left[U_{ref}\right]} + \mathcal{F}\left[U_{sam}\right]\overline{\mathcal{F}\left[U_{ref}\right]} \\ &+\mathcal{F}\left[U_{ref}\right]\overline{\mathcal{F}\left[U_{sam}\right]} + \mathcal{F}\left[U_{sam}\right]\overline{\mathcal{F}\left[U_{sam}\right]}\Big] \\ &= \frac{1}{\lambda^6\left(z_1 - z_0\right)^6} \\ &\Big(\mathcal{F}^{-1}\left[\mathcal{F}\left[U_{ref}\right]\right] * \mathcal{F}^{-1}\left[\overline{\mathcal{F}\left[U_{ref}\right]}\right] + \mathcal{F}^{-1}\left[\mathcal{F}\left[U_{sam}\right]\right] * \mathcal{F}^{-1}\left[\overline{\mathcal{F}\left[U_{ref}\right]}\right] \\ &+\mathcal{F}^{-1}\left[\mathcal{F}\left[U_{ref}\right]\right] * \mathcal{F}^{-1}\left[\overline{\mathcal{F}\left[U_{sam}\right]}\right] + \mathcal{F}^{-1}\left[\mathcal{F}\left[U_{sam}\right]\right] * \mathcal{F}^{-1}\left[\overline{\mathcal{F}\left[U_{sam}\right]}\right]\Big).\end{aligned}$$

$$\mathcal{F}^{-1}[I] = \frac{1}{\lambda^6 (z_1 - z_0)^6} \Big(U_{ref} * (\overline{U_{ref}} \circ -Id) + \underline{U_{sam} * (\overline{U_{ref}} \circ -Id)} + \underline{U_{ref} * (\overline{U_{sam}} \circ -Id)} + U_{sam} * (\overline{U_{sam}} \circ -Id) \Big).$$

For the last step, we used properties of the Fourier transform (see equation (E.4)). The two underlined terms in the last equation are the FTH reconstructions of the sample. Obviously, these reconstructions are blurred by the shape of the reference. Therefore, a small and well defined reference is essential. For an optimal holography signal, the underlined terms should be large in comparison to the non-underlined terms. This can be achieved during the design of the DOE by optimizing the illumination profile which the DOE generates.

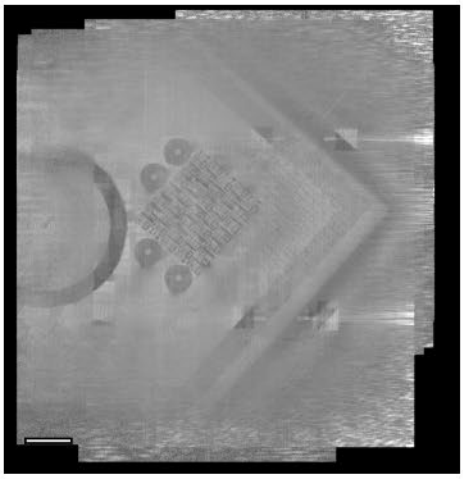

(a) Reconstruction

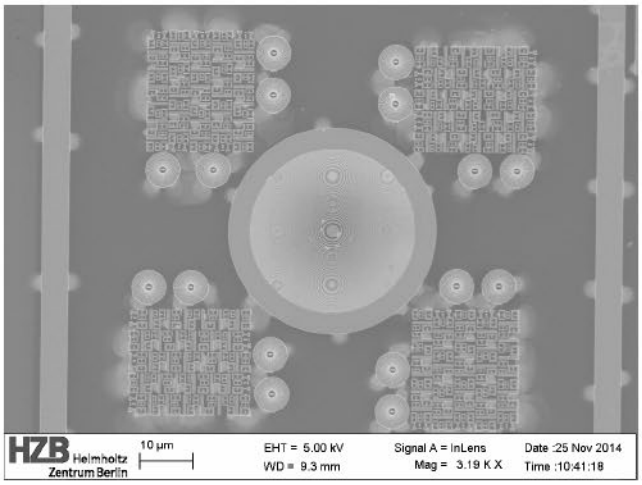

(b) SEM image of a processed wafer with sample.

Figure 7.6: *The sample consists of various gold structures on a thin Si_3N_4 membrane. In the center of the thinned wafer, an FZP is visible. The FZP was used to measure the intensity in the focal plane of the DOE.*
(a) *Full view of the reconstruction from stitched holograms.*
(b) *SEM image of the sample.*

In the next step, the extended test sample is reconstructed. This is done by stitching together FTH reconstructions which were taken at different, lateral positions. The stitching process includes a weighted averaging which reduces the deterioration of the resolution by speckles. The quality and resolution of the resulting image is restricted by the precision of the positioning used for the stitching. Since the logged positions are not sufficiently precise for the reconstruction, they are only used for a rough first alignment and are sequentially improved by a semi-

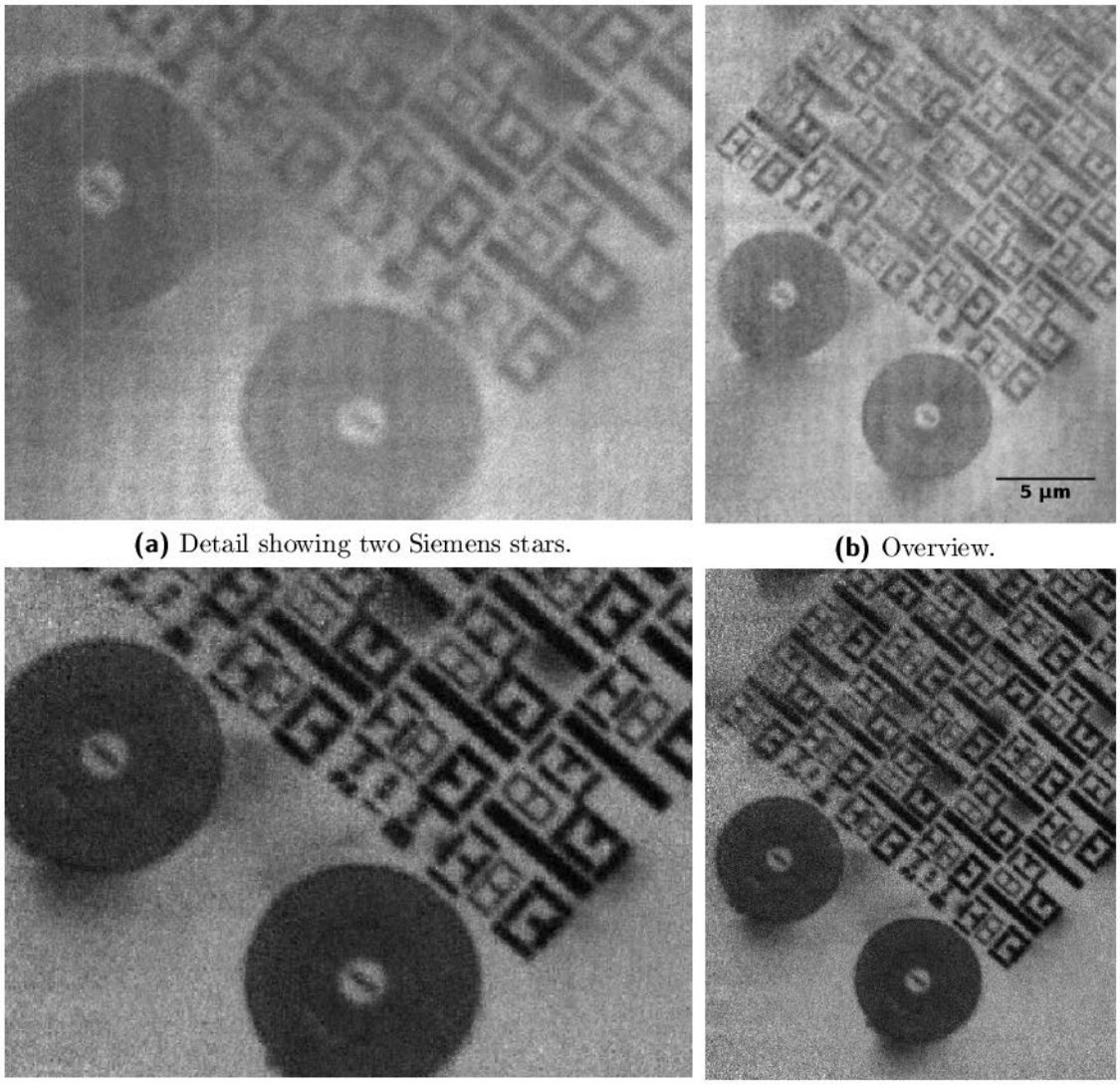

(a) Detail showing two Siemens stars.

(b) Overview.

(c) Detail using ePIE.

(d) Overview using ePIE.

Figure 7.7: *Details from the FTH reconstruction shown in figure 7.6a.*
(a) *Detail from the reconstruction, showing two Siemens stars with a diameter of 6.5 µm and outermost spikes of 100 nm (not resolved).*
(b) *Detail from the reconstruction, the orientation of the strongly absorbing lines seems bent which is an alignment artifact.*
(c) *and* ***(d)*** *Preliminary results from a modified ePIE based reconstruction. The same region as in (a) and (b) is shown. A significant increase in contrast and resolution was achieved.*

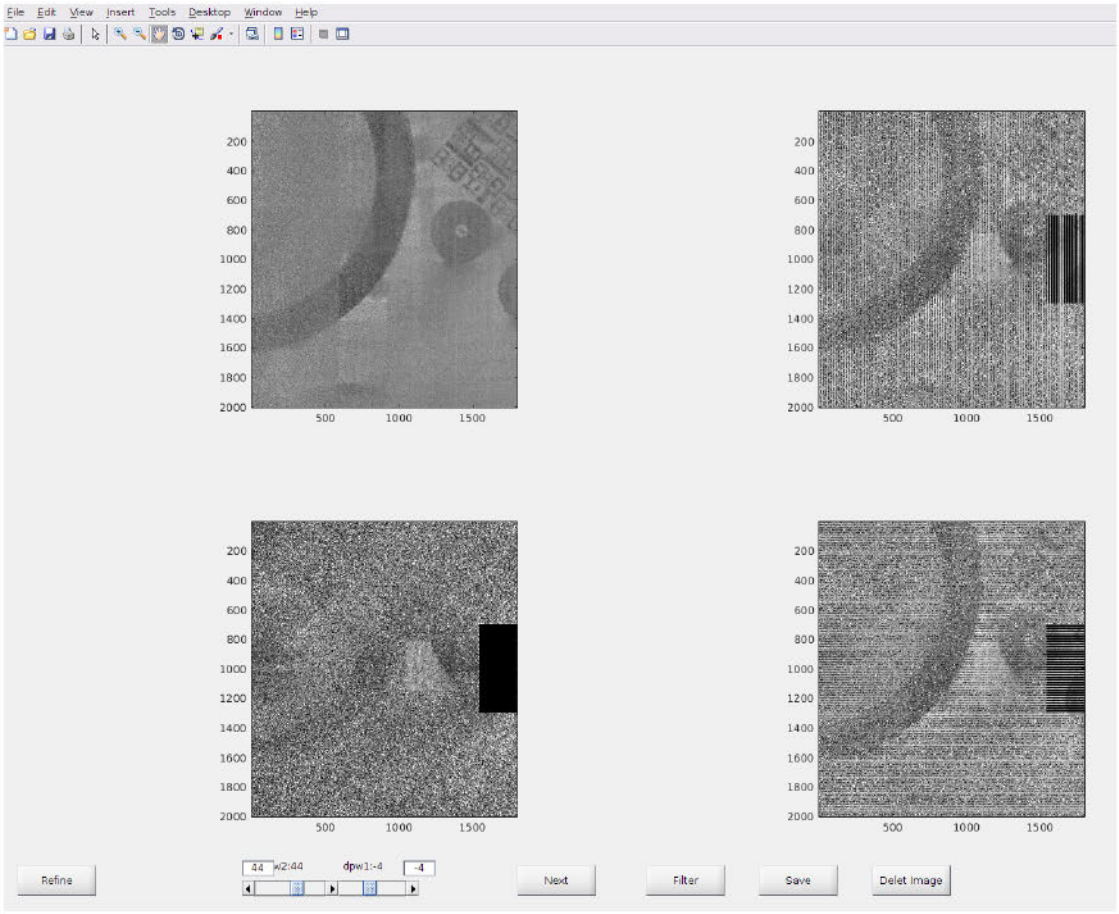

Figure 7.8: *GUI for the semi-manual positioning and stitching. Several positions on the sample were scanned during the experiment. In a semi-manual post process, the exact positions of the scan are estimated.*

automatic alignment algorithm. Different alignment methods were tested. Due to the strong speckle noise in the single images, the supplied image-registration routines in Matlab did not work reliably. The most successful approach was based on normalized cross-correlation. The position was found by picking the maximum of the correlation in a neighborhood of the logged position. It was necessary to preprocess the experimental images to take into account the inhomogeneous illumination. A GUI for the semi-automatic positioning was developed. It is shown in figure 7.8. The corrected positioning data was then used to generate an image of the test sample. The reconstruction is shown in figure 7.6a and figure **??**. This reconstruction takes into account the effects introduced by the photon statistics. An SEM image of the test structure is shown in figure 7.6b. The structure width of the „T“ is 100 nm, 200 nm and 300 nm respectively.

Conclusion and Outlook

From our experiments, we can conclude that the method basically works, although it is hard to make any conclusive statements on the achievable resolution or contrast transfer. This is mainly due to the strong speckle background in the single images and the imprecisely known stitching positions. We saw that some images in the series look sharper than others. It is known that an incoherent summation of holograms leads to a reduction of the speckles which are present in the reconstruction [52]. Therefore, it seems likely that the method could achieve the predicted resolution of about 80 nm. Since the DOE has an outermost zone width of 50 nm, this resolution is worse than the one of a TXM with a similar optic. The use of a DOE working in a higher order of diffraction could improve the resolution at the cost of lower efficiency. In contrast to other optic based full-field methods, the use of a higher diffraction order does not increase the dose on the sample since the DOE is situated in front of the sample.

An interesting effect is that not only the brightly illuminated sample field was recovered but also the surrounding area, as seen in figure 7.6a. Some images in the raster series were unusable since the reference was blocked by a highly absorbing structure. In the next experiment at a plasma based X-ray laser (XRL), we tried to circumvent this problem by splitting the reference into three spots. Unfortunately, the experiment showed a flaw in the design, and no reconstruction was feasible (see also the description and analysis of the experiment in the supplement section §C.3). Nevertheless, from the experimental data and the theoretical analysis, it can be concluded that the concept should also work with XRLs.

Summary

In this chapter, we introduced a new holography method. The method is based on Fourier transform holography. It requires a diffractive optical element and is aimed for fs imaging at free electron lasers. This approach removes some of the restrictions of classical Fourier transform holography setups. A new method for the design of the required diffractive optical element was developed. As far as we know, this design method has the unique feature that it can also be used to generate diffractive elements that use higher order diffraction. The proof of concept experiments revealed that the method works, but further experiments are needed to establish the exact performance.

Chapter 8

Impact of Random Positioning Errors on the Resolution of Fresnel Zone Plates

The previous chapters showed that diffractive optical elements, in particular Fresnel zone plates are the key optical elements for high resolution imaging. Hence, improvements in nano-fabrication leads directly to improvements in the imaging system. This chapter is based on a paper [67] in which we analyzed the impact of random positioning errors on the resolution of Fresnel zone plates. Let us recall that for soft X-rays, the refractive index is close to unity with similar magnitudes for the real and imaginary part. Due to the small phase shift and the high absorption, classical refractive lenses are very inefficient in the photon energy range between 0.1 - 5 keV. For hard X-rays, the absorption is sufficiently small to utilize refractive lenses but several such lenses have to be stacked to form a compound refractive lens (CRL) [89]. The main properties of Fresnel zone plates are already described in chapter 2. Their imaging performance is mainly characterized by two parameters: the numerical aperture and the diffraction efficiency. As diffractive optics, they have many diffraction orders but only one selected order can be used for imaging while all other orders must be blocked. With increased photon energy, the ratio between the height of a zone and its width (aspect ratio) has to be increased to efficiently focus X-rays.

Today's most successful fabrication method for FZP is electron beam lithography followed by planar etching techniques [68, 97, 8]. However, the smallest outermost zone period which determines the zone plate resolution is limited by the minimum electron beam diameter, electron scattering effects and the generation of secondary electrons in the electron beam resist during electron beam lithography. The achievable aspect ratio is limited by the dry etching process since the etching process is not fully anisotropic when constructing narrow nanostructures

[64, 22, 48]. To overcome these limitations, so-called sputtered sliced or jelly roll FZP's have been developed [70, 16].

These FZP's are produced by alternately coating a micro-wire with two different materials according to the required zone plate pattern. In principal, the width of the coated zone layers can be as small as a few atomic diameters. In addition, there is no limitation on the achievable aspect ratio. As the outermost zone width determines the achievable resolution with FZP's, this manufacturing method is potentially suited to develop X-ray optics providing sub-10 nm resolution. However, the theoretical resolution limit given by the outermost zone width might be unattainable due to aberrations introduced by zone positioning errors influencing the focal spot. Several different types of systematic positioning errors were previously studied and tolerable upper bounds were given [99]. However, the manufacturing process for a sputtered sliced FZP is likely to introduce random zone positioning errors. The effect of such errors on the achievable resolution of zone plate optics has not been described.

Here, we use scalar wave theory to determine the effect of random positioning errors by simulating the propagation of an incidental plane X-ray wave onto an erroneous FZP. The algorithms that we use are based on a numerical evaluation of the Rayleigh-Sommerfeld diffraction integral and will be further explained in section 8.2.

8.1 The Focal Spot of an FZP Without Positioning Errors

The numerical aperture (NA) of a lens defines the maximal resolution that can be achieved. According to the Rayleigh criterion, it is $0.61\lambda/\mathrm{NA}$. The NA of a Fresnel zone plate depends on its smallest zone period and the order of diffraction. It is equal to the angle of diffraction of a transmission grating of this periodicity. Therefore, the spatial resolution in the first order of diffraction provided by a full FZP without central stop is given by 0.61 times the outermost zone period. The fact that Fresnel zone plates produce for each diffraction order a focus, requires the use of an order selecting mechanism for imaging. In scanning transmission microscopy (STXM), this is a central stop in combination with an order sorting aperture. As known in microscopy, blocking the inner parts of a lens reduces the full width half maximum (FWHM) of the central peak and increases the intensity of the side lobes of the focal spot pattern [88]. For X-ray microscopy, low-dose imaging is essential. The radiation dose required to detect an object detail is proportional to $(C_{obj} \cdot MTF)^{-2}$ where C_{obj} denotes the object contrast and the modulation transfer function (MTF) describes how strongly a spatial frequency of

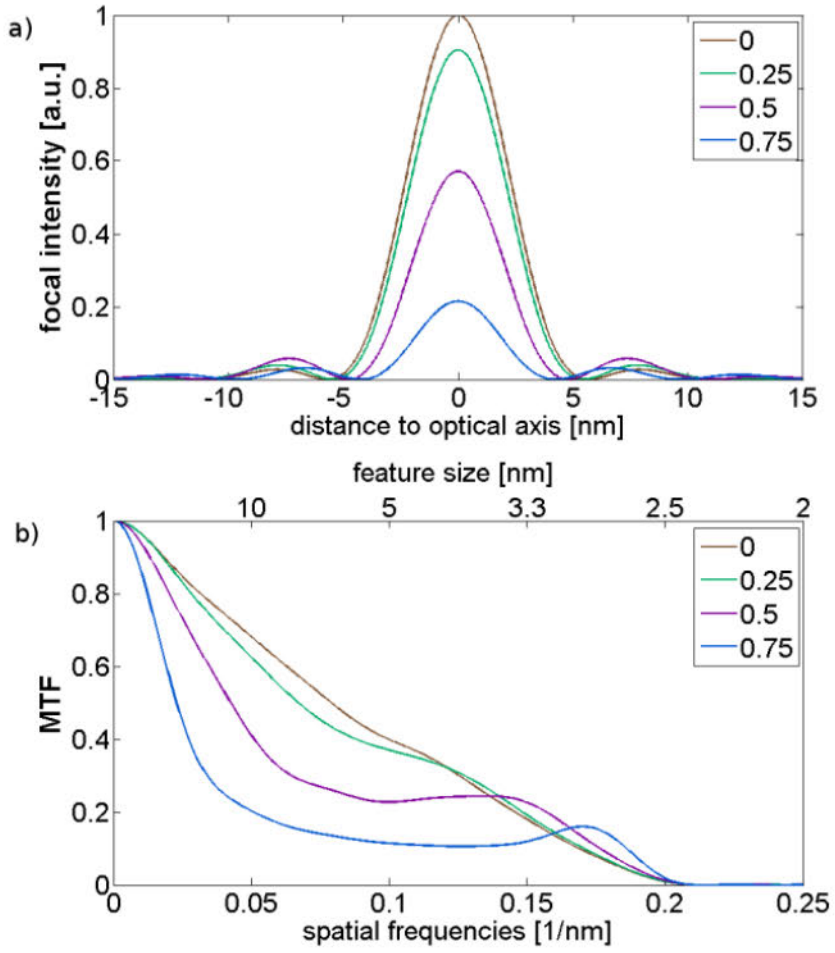

Figure 8.1: ***(a)*** *Impact of the central stop on the focal spot pattern of an FZP. Four different central stop diameters are considered: 0 (brown), 25 (green), 50 (purple) and 75% (blue).* ***(b)*** *Corresponding MTF for the focal spot pattern in (a). The calculations were performed for an FZP with 5 nm outermost zone width and a focal length of 50 µm at λ=0.157 nm.*

an object is transferred into the image plane [83]. Therefore, the MTF needs to be optimized to ensure optimal X-ray imaging conditions.

The MTF is the real part of the optical transfer function (OTF). For linear, shift invariant systems, the OTF can be approximated by the Fourier transform of the image of a point source. An experimental realization of such a system is the scanning transmission X-ray microscope (see figure 2.5). The STXM works by

scanning a sample through a focused X-ray beam and detecting the local change in transmission. In good approximation, the image formation in the STXM can be described by the convolution of the object transmission with the FZP focal intensity distribution.

In our theoretical analysis of the FZP performance, the focal spot is calculated by discretizing the FZP on an adapted polar grid and numerically evaluating the Rayleigh-Sommerfeld diffraction integral using an adapted algorithm described in [5]. From the intensity distribution of the focal spot, the MTF is computed using a Matlab implementation of the Hankel transform [33]. Figure 8.1(a) shows the resulting focal intensity distributions for different central stop diameters. As expected, the side lobes increase while the FWHM of the central peak decreases with increasing central stop size. Figure 8.1(b) shows the effect of the central stop on the MTF. Note that the MTF significantly decreases in the spatial frequency range of $0 - 0.13\,nm^{-1}$ with increasing central stop size.

The shape of the focal spot and its resultant MTF determines the imaging performance of an STXM. Since the Fresnel zone plate with central stop forms a focal spot with large side lobes, the convolution of the object transmission and the intensity of the focal spot creates a halo around each point. As a result, the imaging process is no longer linear in intensities and requires a careful interpretation of the images. For example, structures which are smaller than the distance between central peak and the first maximum of the side lobes are effectively doubled by this halo. For lenses without a central stop, the MTF drops continuously as a function of the spatial frequency. However, with increasing central stop size the MTF rises again and reaches its maximum value close to the cutoff frequency. Note that this increase is a consequence of the halo and does not necessarily help to improve the visibility of the object structures. For FZP with random positioning errors, the situation is even more complex.

8.2 Simulating Positioning Errors

Depending on the FZP manufacturing method, the zone positions might deviate from their set points. It is known that errors in the positioning of the zones reduce the efficiency and the imaging properties [99, 103]. In the following, we will describe the dominating positioning errors occurring in e-beam lithography and in the production of sputtered sliced FZP's. The main sources of positioning errors in e-beam lithography are thermal drift, beam position drift due to charging, non-linearities in the deflection unit and write field calibration errors. In state-of-the-art e-beam systems, the positioning error is expected to be less than 5 nm for FZP's with diameters below 250 µm. The nano-structuring process, which is required to transfer the zone plate pattern into a suitable material, could potentially cause

additional positioning errors. For example, a local shift of the zone structures due to insufficient adhesion of the zones to the underlying material layer could be introduced in very narrow zone structures with high aspect ratios during the development or electroplating processes. This error depends on the chosen process, the material parameters and the zone width. However, in state-of-the-art FZP's generated by electron beam lithography, this error is significantly less than half of the outermost zone width (see for example SEM micrographs in [7]).

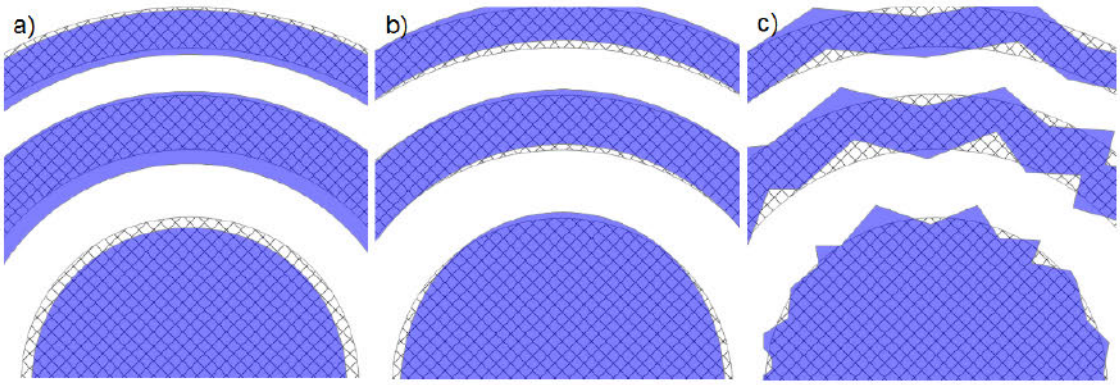

Figure 8.2: *Illustration of the different types of positioning errors which are considered in this thesis. a) Random fluctuations in the deposited zone width. b) Systematic shift of the zones due to an elliptical wire substrate. c) Random positioning errors caused by the roughness of the substrate. The erroneous FZP pattern is shown in color. The zone positions for the ideal FZP pattern are also indicated (cross-hatched).*

The main sources of positioning errors for sputtered sliced FZP's are the substrate and the deposition process. The accuracy of the FZP starts with the roughness and roundness of the micro-wire substrate that is used. The deposition process with its probabilistic nature leads to uncertainties in thickness and position of the deposited materials. In contrast to the errors occurring in e-beam lithography, these errors propagate within the FZP layer system. We simulate the influence of these errors on the imaging performance of an STXM.

For the simulations, we discretize the FZP with its possible errors and propagate into the focal spot by numerically solving the Rayleigh-Sommerfeld diffraction integral. For this numerical solution, it is important that errors introduced by the discretization are negligible compared to the amplitude of the positioning errors. Figure 8.2 shows an overview of the different errors which are considered in this work. If the zones are perfectly centered rings with varying width, a discretization on a polar grid is advisable (see figure 8.2). We use this type of discretization to study the influence on the MTF of an erroneous deposition rate combined with an additional surface error. We assume that the fluctuations are independent and

identically distributed so that we can simulate them by normal distributions. For this type of computation, the same algorithm that we used to compute the effect of the central stop is also suitable.

However, we also consider effects that are better suited for discretization on an orthogonal grid, for example, the effects of non-perfect wire substrates (see figure 8.2(b)-(c)). The deviation of the substrate from its perfect circular shape can be divided into a slowly varying elliptical (figure 8.2(b)) and a fast oscillating roughness (figure 8.2(c)) part. We assume that the position of the n-th zone is shifted proportional to the deviation of the micro-wire substrate due to its roughness. Furthermore, we include a damping of this error proportionally to the inverse of the mean radius of the n-th zone. This damping simulates a smoothing by the deposited material as claimed in [15]. The roughness of the sputtering base is simulated by a realization of a random function of the angular position which is based on a random walk and includes some smoothing.

On an orthogonal grid, a different algorithm is required and so we adapted an algorithm described in [87]. It assumes that a monochromatic plane wave is incident on the FZP. Since the FZP consists of zones with different refractive indices, the incident wave is partially absorbed and phase shifted. The algorithm assumes that the FZP is a 2D pattern without extension of the zones along the optical axis. This approximation is valid for most currently used FZP's. For thick FZP's with very high aspect ratio zone structures, the scalar wave equation has to be solved taking volume diffraction effects into account [103, 80]. In this case, the diffraction behavior of FZP's is much more complex and cannot be described by the presented methods.

The wave field and the effect of the FZP are discretized on an orthogonal grid. At each vertex, a complex number represents the value of the field at that point. If a vertex lies in an opaque zone of the FZP, we modify the complex number at that vertex to allow for the absorption and phase shifting induced by the zone. All examples presented here are based on totally opaque-and-transparent zone plates. Finally, the modified wave is propagated into the focal plane by using a Fresnel diffraction based algorithm [87].

For the Fresnel diffraction based propagation of the wave field $U[x, y, z]$ from the plane $z = z_0$ to the plane $z' = z_1$, the following equation has to be solved: (see also equation (3.4))

$$U[x_1, y_1, z_1] \approx \frac{\exp[i\,k\,(z_1 - z_0)]}{i\,\lambda\,(z_1 - z_0)} \int_{-\infty}^{\infty}\int_{-\infty}^{\infty} U[x_0, y_0, z_0] \exp\left[i\,k\,\frac{(x_1 - x_0)^2 + (y_1 - y_0)^2}{2\,(z_1 - z_0)}\right] \mathbf{d}x_0\mathbf{d}y_0.$$

Again, λ denotes the wavelength and $k = \frac{2\pi}{\lambda}$ the wave number. Note that this equation is a convolution of the wave in the z_0 plane with the (paraxial) impulse response of free space propagation. Since both planes need to be resolved with sub diffraction limited accuracy, a convolution based solution is used.

The MTF of FZP's with positioning errors is calculated from the resulting focal spot intensity distribution by fast Fourier transform (FFT) and finally by averaging over circular rings in the spatial frequency domain.

8.3 The Impact of Different Errors

We already studied the impact of the central stop as shown in figure 8.1. With increased diameter, the central stop suppresses certain spatial frequencies; this corresponds to the plateau seen in the MTF. Structures of these dimensions will appear blurry in the image. Hence, the diameter of the central stop should be less than 50% of the total diameter of the FZP.

The micro-wire substrate of a sputtered sliced FZP might deviate from the perfect circular shape. The impact of the roughness of the substrate on the focal pattern is shown for different rms values in figure 8.3. The increase of the side lobes in the focal pattern translates into a decreased image quality (see figure 8.3, middle row). The resulting MTF's are shown in figure 8.4. As expected, the MTF decreases with increasing roughness of the substrate. It also shows that the rms roughness of the substrate should be significantly smaller than $dr_N/2$ to avoid a degradation of the MTF for high spatial frequencies. Furthermore, an elliptical substrate also introduces a systematic shift in the zones and hence results in an FZP with an additional astigmatism (figure 8.2(b), see also [99]).

In the following, FZP's with production errors are investigated. We divide the FZP's into two types according to their manufacturing process: deposited FZP's (d-FZP's) with their micro-wire substrate and e-beam lithography FZP's (e-FZP's). In d-FZP's, errors propagate over the zone plate layer system while the positioning errors from the different zones in e-FZP's are independent. Hence, for e-FZP's, the acceptable error is largely independent of the diameter while the acceptable errors of d-FZP's strongly depend on the diameter of the optic.

The impact of the variation of the zone width is shown in 8.5. For d-FZP's, two effects are included in the simulation. First, the deposition of material is a random process. Hence, each zone width is produced with an inherent variation. Since each zone consists of many atomic layers independently deposited onto each other, the resulting zone width error is approximately normally distributed with a standard deviation equal to the square root of the numbers of layers times the standard deviation (σ_R) of the thickness of a single layer.

Second, due to the change of material at each zone interface, an additional

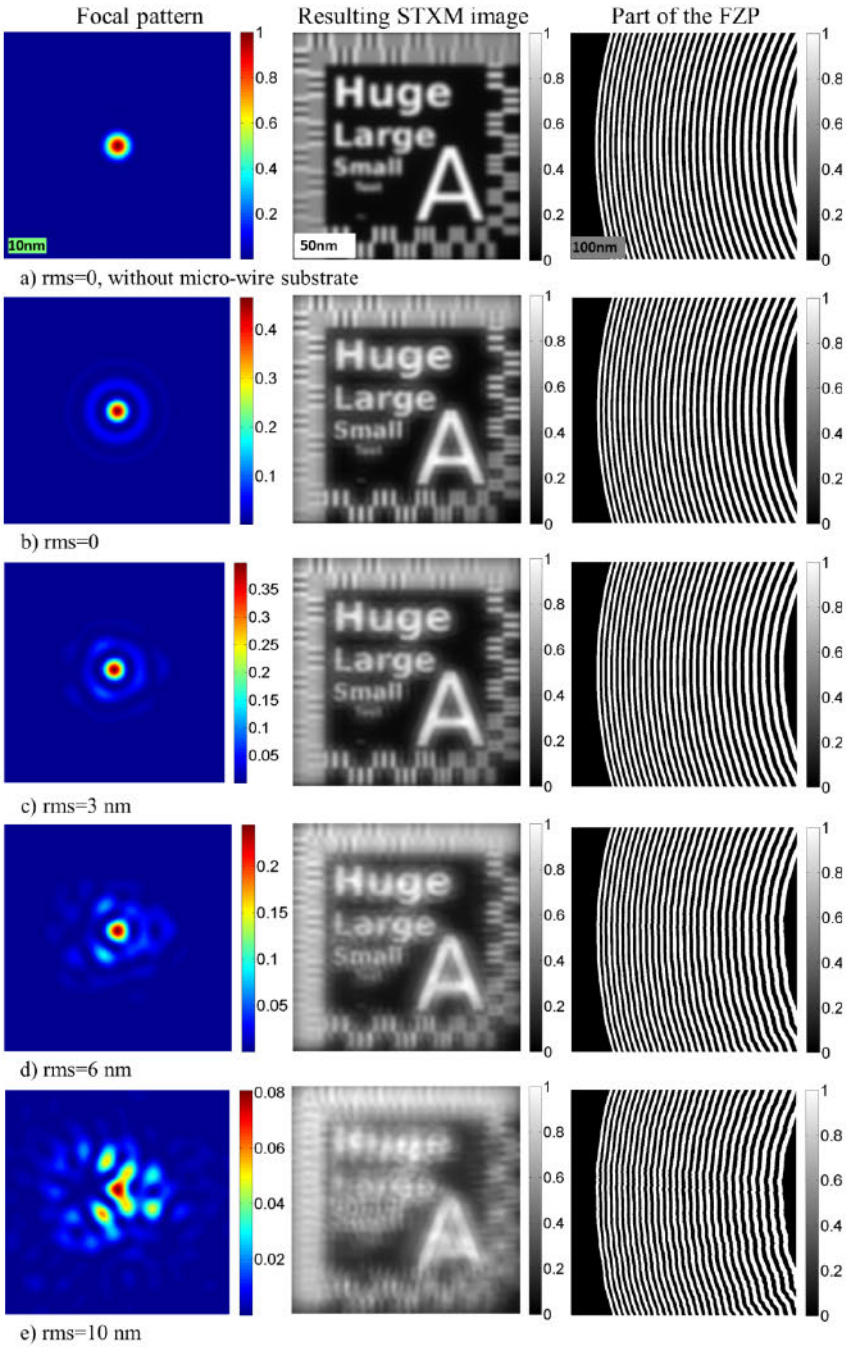

Figure 8.3: *Simulated images showing the impact of the substrate roughness (right column, see also figure 8.2(**c**)) on the focal pattern (left column) and hence the resolution (middle column) of the STXM. The simulation was performed for FZP's with an outermost zone width of $dr_N = 5$ nm and a diameter of 1.594 µm at a wavelength of 0.157 nm (see also [15]). Panel* **(a)** *shows the results for a perfect FZP without central stop. Panels* **(b)** *–* **(e)** *show the results for FZP's with central stop of 0.9 µm and different rms-values of 0 nm, 3 nm, 6 nm and 10 nm, respectively.*

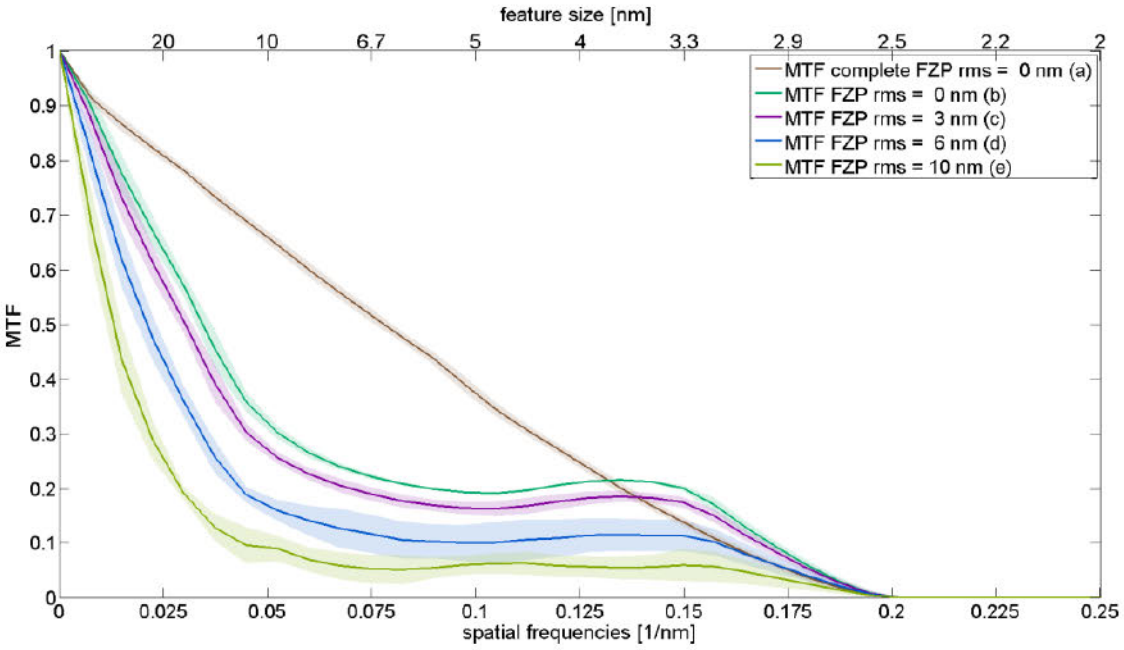

Figure 8.4: *Plots showing the mean MTF of the same FZP as shown in figure 8.3(a)-(e). With increasing rms-values of the micro-wire substrate, the MTF's already decrease strongly at moderate spatial frequencies. Note the increasing standard deviation (shaded) with increasing rms-values which is caused by the angular dependency of the MTF of non-circular FZP's.*

error is produced. For simplicity, this interface error is also assumed to be normally distributed with a standard deviation σ_N. As long as the expected deviation of the position of the outermost zone is smaller than $dr_N/2$, an average d-FZP will produce an Airy pattern as focal spot. If this condition is not satisfied, some of the outermost zones most likely no longer satisfy the necessary condition for constructive interference. This idea leads to the following "rule of thumb": Given the width (dr_N) of the outermost zone, the number (N) of zones and the radius (R) as well as the standard deviations of a single zone boarder σ_N (in nm per layer) and the standard deviation σ_R (in nm per ΔR) for a deposited distance (ΔR), the following inequality should be satisfied[1]:

$$\frac{dr_N}{2} > \sqrt{\sigma_N^2 N + \sigma_R^2 \frac{R}{\Delta R}}.$$

For e-FZP's, it is included that the position of each interface is normally

[1] The following equation is probably more convenient for practical applications. From $R \approx \sqrt{Nf\lambda}$ and $f \approx \frac{2R\,dr_N}{\lambda}$, the inequality can be approximated by $\frac{dr_N^4}{f\lambda} > \sigma_N^2 + \sigma_{dr_N}^2$. Here, σ_{dr_N} is the standard deviation for a layer thicknesss equal to the outermost zone width.

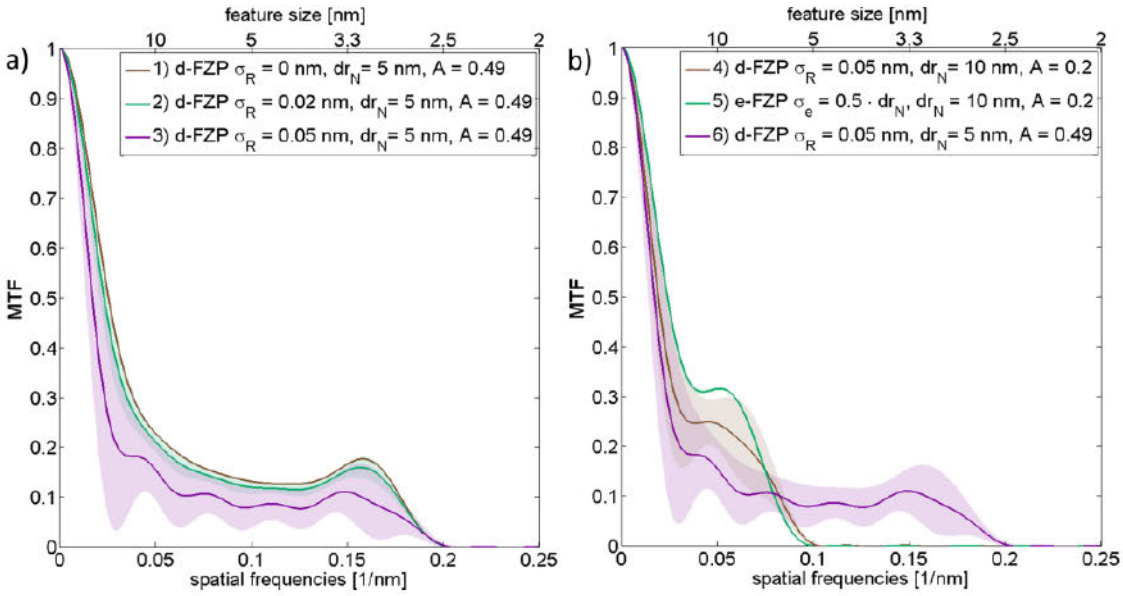

Figure 8.5: *Plots showing the MTF of d-FZP's and e-FZP's for different production parameters. The FZP's are assumed to consist of perfectly circular, concentric rings that are alternately opaque and transparent. All FZP's have a diameter of 50 µm. The border of each ring is perturbed as described in the text. The percentage of the FZP area obscured by the micro-wire substrate is denoted by A. In the left plot* **(a)**, *the standard deviation of the positioning error varied between 0.02 and 0.05 nm per each nm deposited. In this case, the condition* $\frac{dr_N}{2} > \sqrt{\sigma_R^2 \frac{R}{\Delta R}} = 0.05\,nm \cdot 86.6 \approx 4.33\,nm$ *is not satisfied for* σ_R *=0.05 nm (violet graph). In the green graph, the standard deviation is* σ_R *=0.02 nm satisfying the condition* $\frac{dr_N}{2} > \sqrt{\sigma_R^2 \frac{R}{\Delta R}} = 0.02\,nm \cdot 86.6 \approx 1.73\,nm$. *The brown line corresponds to a perfect FZP. The right plot* **(b)** *shows the MTF of an e-FZP and two d-FZP's. The FZP-parameters for the FZP 4) and 5) are identical, but the simulated positioning errors correspond to a d-FZP in 4) and an e-FZP in 5). The fact that the d-FZP 6) does not satisfy the above given condition and has additionally a large central wire reduces the MTF below the level of the FZP 4) and 5) for a large part of the frequency range.*

distributed around its prescribed position. As long as the standard deviation of the positioning error (σ_e) is smaller than the outermost zone width dr_N, most of the outermost zones most likely satisfy the condition for constructive interference. For relatively small d-FZP's such as the one used to simulate the effect of the roughness, the aberrations due to σ_N and σ_R are negligible. Our simulation shows that under these conditions, the main errors arise from the deviation of the substrate from a perfect cylindrical geometry. In our simulations, this deviation had to be smaller

than the width of the outermost zone in order to produce a focal spot close to an Airy pattern.

For practical applications in X-ray microscopy, the working distance of the FZP X-ray objectives plays an important role. For example, tomographic applications require tilting of the sample in the X-ray beam. To minimize the missing wedge effects in the reconstruction, tilt angles $\geq 60°$ are required. Therefore, in practice, the focal length of the FZP should be at least 0.5 mm. Assuming FZP's with dr_N =5 nm containing a micro-wire with half the diameter of the FZP diameter, operating at 1, 4 or 8 keV photon energy, the required number of deposited zones are 4700, 1164 and 582, respectively. The resulting deposition standard deviations σ_R are 0.014, 0.028 and 0.040 nm. In other words, the required deposition accuracies for an inner zone of 9 nm width are 0.042, 0.084 and 0.12 nm at 1, 4 and 8 keV, respectively.

Even for d-FZP's which are ideally manufactured, their utility for applications depends heavily on the photon energy used. For example, in the soft X-ray region, the efficiency of d-FZP's is significantly lowered by the smaller difference in the absorption and phase shift of the two alternating zone materials compared to e-FZP's with their vacuum against zone material contrast. Additionally, high efficiency soft X-ray optics with $dr_N \leq 10\,\text{nm}$ require tilted zone structures with radially increasing tilt angles (see [103, 80]). So far, no approach exists to manufacture such d-FZP optics.

For hard X-rays, efficient FZP's require very high aspect ratios, but zone tilting is less important due to the significantly lower numerical apertures. Furthermore, the absorption within the FZP is much lower than for soft X-rays and so, phase shift is dominant. However, for most applications, the focal length of currently produced d-FZP's is still too short. For high resolution d-FZP's with significantly larger working distances, many more zones are required which makes the position accuracy progressively worse. Nevertheless, d-FZP's are ideal candidates for nanoscale hard X-ray imaging but only if either the deposition accuracy can be extremely well controlled or the actual zone plate diameter can be measured and corrected during the fabrication process.

Summary

Our theoretical analysis of zone plates manufactured by deposition techniques shows the impact of the micro-wire substrate quality and the deposition accuracy on the achievable imaging performance. The substrate should be exactly circular and very smooth, which is nearly fulfilled for glass wire substrates [16]. The diameter of the wire substrate should be smaller than 50% of the FZP diameter to avoid negative effects on the MTF. We also studied the influence of the deposition accu-

racy on the focal spot. We find that the deposition accuracy for FZP with useful focal lengths for practical applications is a major challenge. This challenge could be overcome by in-situ measurements of the deposited layer thickness during the manufacturing process. In this case, the zone thickness can be corrected during the fabrication process which helps to suppress the propagating positioning error and relaxes the deposition rate accuracy. However, the accuracy of the measurement of the zone plate layer thickness needs to be at least half the outermost zone width. In [17] it was demonstrated that the in-situ measurements of the layer thickness can be performed indirectly by measuring the thickness on a plain substrate.

The analysis of the e-beam based manufacturing process showed that compared to sputtering-based zone-plate manufacture, a larger standard deviation in the local zone thickness is tolerable for e-beam manufacture of zone plates, since the local zone width errors do not propagate from layer to layer. However, the local precision of each zone has to be better than half the outermost zone width. For Fresnel zone plates with central stop which are used for imaging, the diameter of the central stop should be less than 50% of the FZP diameter. A unique feature of e-beam lithography is that one can also manufacture general diffractive optical elements.

Chapter 9

Summary and Outlook

Nanoscale X-ray imaging provides unprecedented views into matter. For many scientific areas, such as life and materials science, 3D views into complex structures are essential. The aim of this thesis was the understanding of the 3D nanoscale image formation with soft X-rays. Real space imaging methods like the transmission soft X-ray microscope or the scanning transmission microscope directly form the image of a sample, while reciprocal space methods like coherent diffraction imaging, ptychography and holography require numerical methods to generate the image.

Full-field soft X-ray transmission microscopy in combination with tomography is currently the most successful soft X-ray based approach for 3D imaging of biological cells. This approach is based on the assumption that the TXM images represent magnified projections of the sample for each tilt angle. The 3D imaging mode by tomography is based on the inverse Radon transform. For this approach, it is assumed that the TXM images represent at each tilt angle the integrated local absorption coefficient along the direction of projection. Experimental data shows that this assumption is no longer valid for high resolution soft X-ray optics. Ideally, the tilt range in tomography has to cover half a rotation (180°). However, in practice, experimental constraints often limit the maximal tilt to values of ±60°- ±70°. Soft X-ray microscopes, such as the BESSY II microscope, work in a partially coherent regime which also has a strong influence on the image formation process. In this thesis, numerical descriptions of the TXM at the electron storage ring BESSY II were developed to study all these effects which potentially arise from violations of the assumptions of tomography. Simulations taking into account the partially coherent object illumination, the depth of focus and the limited tilt range were compared to experimental data. The comparison of the images computed by simulations based on partially coherent and incoherent image formation showed that the partial coherence of the object illumination has to be taken into account to correctly simulate the TXM images. In addition, we studied the limiting effects

for soft X-ray transmission microscopy using an extended cell-like 3D phantom. As expected, we observed that an increased lateral resolution of the Fresnel zone plate decreases the fraction of the phantom that is imaged without blurring, reflecting the reduction of the depth of focus with increased numerical aperture of the objective. This also affects the tomographic 3D reconstruction. We found that only a cylinder around the rotational axis is resolved with the resolution provided by the Fresnel zone plate. The diameter of the cylinder is of the same order as the depth of focus. For samples that are larger than the depth of focus, we observed that the resolution degrades and severe artifacts appear with increased distance from the rotational axis. In addition, the partially coherent illumination leads to a violation of the assumption of a purely absorption contrast based image formation. In practice, all these artifacts are mixed with the missing wedge artifacts. The latter results from a limitation of the tilt angle. From the observed effects, we conclude that new tomography approaches are necessary to achieve an isotropic resolution close to 10 nm for extended biological samples. Potential solutions can be divided into two categories.

The first category contains approaches that extend the depth of focus either by developing new advanced algorithms for tomography, for example by using focal series and deconvolution to increase numerically the depth of focus, or the use of higher photon energies. The latter approach solves the problems related to the limited depth of focus, because the depth of focus increases linearly with the photon energy. Unfortunately, the absorption contrast between water and organic material is extremely weak for photon energies above the water window, which leads to a significant increase of the dose required for imaging of biological material. For high resolution imaging this poses a severe problem since the dose rises far beyond the dose induced damage threshold of such samples. Phase contrast imaging mainly overcomes these contrast related problems. Zernike phase contrast has been shown to work well for X-rays. However, such images no longer represent the linear local absorption coefficient. Instead the image represents a phase dependent signal. Current experimental setups use a phase ring in the focal plane of the objective to generate Zernike phase contrast. This ring is relatively large which results in a spatial frequency dependent mix of Zernike phase and absorption contrast. In this thesis, a new diffractive optical element (DOE) based condenser setup was proposed which has the potential to significantly reduce the spatial frequency dependency of the contrast. In addition, it permits use of a significantly larger fraction of the incident X-rays for the image formation.

Solutions in the second category consist of novel soft X-ray imaging methods which overcome the previously mentioned limitations. In this thesis, one approach for such a solution, which is inspired by confocal light microscopy was investigated. Confocal transmission soft X-ray microscopy is an approach for direct 3D imag-

ing by optical sectioning. The performance of this novel sort of X-ray microscopy setup was studied by theoretical and numerical means. In light microscopy, the confocal microscope is based on fluorescent dyes. Since individual dye molecules emit the fluorescent light independently, the image formation process is incoherent. However, confocal soft X-ray microscopy cannot be based on fluorescence due to dose considerations. The image formation in the confocal scanning transmission soft X-ray microscope is based on diffraction, which does not introduce an incoherent step during image formation. We showed that the image formation in the confocal transmission soft X-ray microscope requires a coherent description. We found that the resolution of the confocal soft X-ray microscope is anisotropic for both the incoherent as well as the coherent case. In comparison to the incoherent case, the depth resolution decreases even further in the coherent confocal scanning soft X-ray microscope. We also compared the predicted images of a confocal and a full-field transmission soft X-ray microscope. From the results, it is concluded that the confocal system does not exhibit significant advantages over TXM imaging for extended biological samples.

All previously studied X-ray imaging methods have fundamental restrictions in their achievable 3D resolution. In the search for an X-ray based microscopy method that can provide isotropic nanoscale 3D resolution, we studied a novel combination based on scanning soft X-ray microscopy (SXM) with photoelectron detection and high precision surface removal by focused ion beam (FIB) milling. In this so-called slice and view method, a nanoscale soft X-ray focal spot is scanned over the surface of the sample and the locally emitted electrons are detected. In the soft X-ray photon energy range photoelectrons are mainly generated by the X-ray absorption process. Due to the relatively low photon energy, the generated photoelectrons escape from a thin surface layer of 3 - 8 nm. Therefore, this method provides an excellent depth resolution given by the escape depth of the electrons. The lateral resolution depends only on the resolution of the Fresnel zone plate objective and the coherence of the illumination. In practice, current Fresnel zone plates provide focal spots of 10 nm. Therefore, the new FIB-SXM 3D imaging method potentially provides a resolution of at least 10 nm in all directions.

Organic material is very radiation sensitive, therefore, we also investigated the required dose for imaging of biological material in the FIB-SXM mode. As a result, we found that this microscope has the potential to reduce the dose by three orders of magnitude compared to both the transmission mode in the TXM and lens-less methods. The dose reduction is mainly due to the fact that the contrast of the photoelectron signal represents the relatively large difference in the local absorption coefficient, while the transmission based soft X-ray imaging methods detect the very small differences in the local transmission of water and the organic cellular structures. The numerical simulations revealed that FIB-SXM improves

significantly the 3D image quality for biological cells in comparison to the currently used TXM based tomography. It potentially achieves an isotropic 3D resolution below 10 nm at a signal to noise level above the Rose criterion. Therefore, this method potentially solves a fundamental 3D resolution problem in X-ray imaging.

Aside from high resolution 3D imaging, in this thesis new setups for high resolution 2D imaging with ultra-short X-ray pulses were investigated. Today free electron lasers provide spatially coherent, high photon flux pulses with femtosecond duration. Such pulses potentially allow imaging ultra-fast processes in complex samples with nanoscale resolution. However, high resolution full-field imaging with short pulses is still an unsolved problem. As a solution, we propose a novel approach based on Fourier transform holography, which is based on diffractive optical elements. In this approach, the diffractive optical element illuminates the sample and simultaneously generates the reference wave. In first proof of concept experiments at the electron storage ring BESSY II, we showed that Fourier transform holography based on the novel DOE nearly accomplishes the expected imaging performance. It can even be used to image large sample areas by stitching of overlapping images. Although, the resolution in holography is still significantly lower than the resolution achievable with a TXM, it does permit use of short X-ray pulses for time-resolved imaging. In the future, the recently developed algorithm proposed in this thesis could be applied to design diffractive optical elements optimized for higher orders of diffraction, which increase the effective numerical aperture leading to higher resolution. Since the outermost zone width is currently the limiting factor for the fabrication of diffractive optical elements by e-beam lithography, the use of higher orders of diffraction based diffractive optical elements significantly improves the images. Potentially this holography setup generates time-resolved images with single shots at spatial resolutions similar to current X-ray microscopes at electron storage ring with their exposure times in the second range.

In summary, in this thesis different X-ray optical setups for high resolution 3D imaging were investigated. From all the investigated methods, the novel FIB-SXM approach is the most promising candidate for nanoscale 3D imaging. FIB-SXM imaging promises to provide higher resolution 3D images than other X-ray methods. In addition, artifacts that are currently limiting other tomography based soft X-ray methods are removed. Nevertheless, improvements of the various TXM imaging modes is also important, since FIB-SXM can only be applied to relatively small samples regions since it is a raster scanning method. Therefore, a workflow that includes a lower resolution preliminary study of 3D samples by TXM tomography is advisable to locate the regions of interest. For the preliminary studies of whole cells in the TXM, the new setups for Zernike phase contrast and dark field imaging might provide a further improvement step. In general, X-

ray imaging offers a large penetration depth, good element contrast and short wavelength for microscopy. In addition, soft X-ray microscopy bridges the gap in resolution and permitted sample thickness between optical microscopy and electron microscopy. This unique combination make X-ray imaging in general a valuable tool for many applications in life and materials sciences.

Acknowledgment

I wish to thank all my coworkers who always supported me, endured all my questions and always found the time to discuss ideas with me. Dr. Stefan Rehbein, Dr. Stephan Werner, Dr. Peter Guttmann, Dr. James McNalley and Dr. Sergey Kapishnikov made the time that I work with them at the Helmholtz Zentrum Berlin not only an educational one, but also enjoyable. In Prof. Gerd Schneider I found a great supervisor. He helped me a lot by being at the same time supportive but also sufficiently critical.

Although our experiments were in the end not as successful as we hoped, I was glad to have the good fortune to work with Dr. Holger Stiel, Dr. Johannes Tümmler and Dr. Robert Jung as well as Klaus Föllmer from the Max Born Institut.

I thank Prof. Günter Schmahl and Prof. Stefan Kowarik for valuable discussions.

Finally, I thank my girlfriend Stephanie and my family for their patience and support.

Selbstständigkeitserklärung

Hiermit erkläre ich, die Dissertation selbstständig und nur unter Verwendung der angegebenen Hilfen und Hilfsmittel angefertigt zu haben. Ich hab mich anderwärts nicht um einen Doktorgrad beworben und besitze einen entsprechenden Doktorgrad nicht. Ich erkläre die Kenntnisnahme der dem Verfahren zugrunde liegenden Promotionsordnung der Mathematisch-Naturwissenschaftlichen Fakultät der Humboldt-Universität zu Berlin vom 18.11.2014.

Berlin, den 27.02.2017 Christoph Pratsch

Bibliography

[1] D. Attwood. *Soft X-Rays and Extreme Ultraviolet Radiation: Principles and Applications*. Cambridge University Press, 2007. ISBN 9781139643429.

[2] A. V. Baez. A study in diffraction microscopy with special reference to x-rays. *Journal of the Optical Society of America*, 42(10):756–762, Oct 1952. doi: 10.1364/JOSA.42.000756.

[3] S. Baumbach, B. Kanngiesser, W. Malzer, H. Stiel, and T. Wilhein. A laboratory 8 keV transmission full-field X-ray microscope with a polycapillary as condenser for bright and dark field imaging. *Review of Scientific Instruments*, 86(8), AUG 2015. ISSN 0034-6748. doi: 10.1063/1.4929602.

[4] E. Betzig, G. H. Patterson, R. Sougrat, O. W. Lindwasser, S. Olenych, J. S. Bonifacino, M. W. Davidson, J. Lippincott-Schwartz, and H. F. Hess. Imaging intracellular fluorescent proteins at nanometer resolution. *Science*, 313 (5793):1642–1645, SEP 2006. ISSN 0036-8075. doi: 10.1126/science.1127344.

[5] Q. Cao and J. Jahns. Comprehensive focusing analysis of various fresnel zone plates. *Journal of The Optical Society of America A-Optics Image Science and Vision*, 21(4):561–571, APR 2004. ISSN 1084-7529. doi: 10.1364/JOSAA.21.000561.

[6] J. L. Carrascosa, F. Javier Chichon, E. Pereiro, M. Josefa Rodriguez, J. Jesus Fernandez, M. Esteban, S. Heim, P. Guttmann, and G. Schneider. Cryo-X-ray tomography of vaccinia virus membranes and inner compartments. *Journal of Structural Biology*, 168(2):234–239, NOV 2009. ISSN 1047-8477. doi: 10.1016/j.jsb.2009.07.009.

[7] W. Chao, J. Kim, S. Rekawa, P. Fischer, and E. H. Anderson. Demonstration of 12 nm resolution fresnel zone plate lens based soft X-ray microscopy. *Optics Express*, 17(20):17669–17677, SEP 2009. ISSN 1094-4087. doi: 10.1364/OE.17.017669.

[8] W. Chao, P. Fischer, T. Tyliszczak, S. Rekawa, E. Anderson, and P. Naulleau. Real space soft x-ray imaging at 10 nm spatial resolution. *Optics Express*, 20(9), APR 2012. ISSN 1094-4087. doi: 10.1364/OE.20.009777.

[9] H. Chapman, C. Jacobsen, and S. Williams. A characterisation of dark-field imaging of colloidal gold labels in a scanning transmission X-ray microscope. *Ultramicroscopy*, 62(3):191–213, FEB 1996. ISSN 0304-3991. doi: 10.1016/0304-3991(96)00003-4.

[10] H. N. Chapman, A. Barty, M. J. Bogan, S. Boutet, M. Frank, S. P. Hau-Riege, S. Marchesini, B. W. Woods, S. Bajt, H. Benner, R. A. London, E. Ploenjes, M. Kuhlmann, R. Treusch, S. Duesterer, T. Tschentscher, J. R. Schneider, E. Spiller, T. Moeller, C. Bostedt, M. Hoener, D. A. Shapiro, K. O. Hodgson, D. Van der Spoel, F. Burmeister, M. Bergh, C. Caleman, G. Huldt, M. M. Seibert, F. R. N. C. Maia, R. W. Lee, A. Szoeke, N. Timneanu, and J. Hajdu. Femtosecond diffractive imaging with a soft-X-ray free-electron laser. *Nature Physics*, 2(12):839–843, DEC 2006. ISSN 1745-2473. doi: 10.1038/nphys461.

[11] H. N. Chapman, A. Barty, S. Marchesini, A. Noy, S. R. Hau-Riege, C. Cui, M. R. Howells, R. Rosen, H. He, J. C. H. Spence, U. Weierstall, T. Beetz, C. Jacobsen, and D. Shapiro. High-resolution ab initio three-dimensional x-ray diffraction microscopy. *Journal of the Optical Society of America A-Optics Image Science and Vision*, 23(5):1179–1200, may 2006. doi: 10.1364/JOSAA.23.001179.

[12] H.-Y. Chen, D. M.-L. Chiang, Z.-J. Lin, C.-C. Hsieh, G.-C. Yin, I.-C. Weng, P. Guttmann, S. Werner, K. Henzler, G. Schneider, L.-J. Lai, and F.-T. Liu. Nanoimaging granule dynamics and subcellular structures in activated mast cells using soft x-ray tomography. *Scientific Reports*, 6, OCT 2016. ISSN 2045-2322. doi: 10.1038/srep34879.

[13] J. Cooley and J. Tukey. An algorithm for machine calculation of complex Fourier series. *Mathematics of Computation*, 19(90):297–&, 1965. ISSN 0025-5718. doi: 10.2307/2003354.

[14] J. Deng, D. J. Vine, S. Chen, Y. S. G. Nashed, Q. Jin, N. W. Phillips, T. Peterka, R. Rossc, S. Vogt, and C. J. Jacobsen. Simultaneous cryo X-ray ptychographic and fluorescence microscopy of green algae. *Proceedings of the National Academy of Sciences of the United States of America*, 112(8):2314–2319, FEB 2015. ISSN 0027-8424. doi: 10.1073/pnas.1413003112.

[15] F. Doering, A. L. Robisch, C. Eberl, M. Osterhoff, A. Ruhlandt, T. Liese, F. Schlenkrich, S. Hoffmann, M. Bartels, T. Salditt, and H. U. Krebs. Sub-5 nm hard X-ray point focusing by a combined kirkpatrick-baez mirror and multilayer zone plate. *Optics Express*, 21(16):19311–19323, AUG 2013. ISSN 1094-4087. doi: 10.1364/OE.21.019311.

[16] A. Duvel, D. Rudolph, and G. Schmahl. Fabrication of thick zone plates for multi-kilovolt X-rays. In MeyerIlse, W and Warwick, T and Attwood, D, editor, *X-Ray Microscopy, Proceedings*, volume 507 of *AIP Conference Proceedings*, pages 607–614, 2000. ISBN 1-56396-926-2.

[17] C. Eberl, F. Doring, T. Liese, F. Schlenkrich, B. Roos, M. Hahn, T. Hoinkes, A. Rauschenbeutel, M. Osterhoff, T. Salditt, and H.-U. Krebs. Fabrication of laser deposited high-quality multilayer zone plates for hard x-ray nanofocusing. *Applied Surface Science*, 307:638–644, JUL 15 2014. ISSN 0169-4332. doi: 10.1016/j.apsusc.2014.04.089.

[18] S. Eisebitt, J. Luning, W. Schlotter, M. Lorgen, O. Hellwig, W. Eberhardt, and J. Stohr. Lensless imaging of magnetic nanostructures by X-ray spectroholography. *Nature*, 432(7019):885–888, DEC 2004. ISSN 0028-0836. doi: 10.1038/nature03139.

[19] O. Ersoy. *Diffraction, Fourier Optics and Imaging*. Wiley Series in Pure and Applied Optics. Wiley, 2006. ISBN 9780470084991.

[20] H. Faulkner and J. Rodenburg. Movable aperture lensless transmission microscopy: A novel phase retrieval algorithm. *Physical Review Letters*, 93(2), JUL 2004. ISSN 0031-9007. doi: 10.1103/PhysRevLett.93.023903.

[21] M. Feit and J. Fleck. Light-propagation in graded-index optical fibers. *Applied Optics*, 17(24):3990–3998, 1978. ISSN 0003-6935. doi: 10.1364/AO.17.003990.

[22] Y. Feng, M. Feser, A. Lyon, S. Rishton, X. Zeng, S. Chen, S. Sassolini, and W. Yun. Nanofabrication of high aspect ratio 24 nm x-ray zone plates for X-ray imaging applications. *Journal of Vacuum Science & Technology B*, 25 (6):2004–2007, NOV 2007. ISSN 1071-1023. doi: 10.1116/1.2789447.

[23] J. Fienup. Reconstruction of an object from modulus of its Fourier-transform. *Optics Letters*, 3(1):27–29, 1978. ISSN 0146-9592. doi: 10.1364/OL.3.000027.

[24] J. R. Fienup. Phase retrieval algorithms: a comparison. *Applied Optics*, 21 (15):2758–2769, aug 1982. doi: 10.1364/AO.21.002758.

[25] D. Gabor. A new microscopic principle. *Nature*, 161(4098):777–778, 1948. ISSN 0028-0836. doi: 10.1038/161777a0.

[26] J. Geilhufe, B. Pfau, M. Schneider, F. Buettner, C. M. Guenther, S. Werner, S. Schaffert, E. Guehrs, S. Froemmel, M. Klaeui, and S. Eisebitt. Monolithic focused reference beam X-ray holography. *Nature Communications*, 5, JAN 2014. ISSN 2041-1723. doi: 10.1038/ncomms4008.

[27] R. Gerchberg and W. Saxton. Practical algorithm for determination of phase from image and diffraction plane pictures. *Optik*, 35(2):237+, 1972. ISSN 0030-4026.

[28] D. Ghiglia and M. Pritt. *Two-dimensional phase unwrapping: theory, algorithms, and software*. Wiley-Interscience publication. Wiley, 1998. ISBN 9780471249351.

[29] M. Gu. *Principles of Three Dimensional Imaging in Confocal Microscopes*. World Scientific, 1996. ISBN 9789810225506.

[30] M. Gu. *Advanced Optical Imaging Theory*. Springer Series in Optical Sciences. Springer, 2000. ISBN 9783540662624.

[31] E. Guehrs, A. M. Stadler, S. Flewett, S. Froemmel, J. Geilhufe, B. Pfau, T. Rander, S. Schaffert, G. Bueldt, and S. Eisebitt. Soft X-ray tomoholography. *New Journal of Physics*, 14, JAN 2012. ISSN 1367-2630. doi: 10.1088/1367-2630/14/1/013022.

[32] M. Guizar-Sicairos and J. R. Fienup. Holography with extended reference by autocorrelation linear differential operation. *Optics Express*, 15(26):17592–17612, DEC 2007. ISSN 1094-4087. doi: 10.1364/OE.15.017592.

[33] M. Guizar-Sicairos and J. Gutierrez-Vega. Computation of quasi-discrete Hankel transforms of integer order for propagating optical wave fields. *Journal of The Optical Society of America A-Optics Image Science and Vision*, 21(1):53–58, JAN 2004. ISSN 1084-7529. doi: 10.1364/JOSAA.21.000053.

[34] C. Hagen, P. Guttmann, B. Klupp, S. Werner, S. Rehbein, T. C. Mettenleiter, G. Schneider, and K. Gruenewald. Correlative vis-fluorescence and soft X-ray cryo-microscopy/tomography of adherent cells. *Journal of Structural Biology*, 177(2):193–201, FEB 2012. ISSN 1047-8477. doi: 10.1016/j.jsb.2011.12.012.

[35] R. Hegerl and W. Hoppe. Influence of electron noise on 3-Dimensional image-reconstruction. *Zeitschrift für Naturforschung Section A-A Journal of Physical Sciences*, 31(12):1717–1721, 1976. ISSN 0932-0784.

[36] S. Hell and M. Kroug. Ground-state-depletion fluorescence microscopy - a concept for breaking the diffraction resolution limit. *Applied Physics B-Lasers And Optics*, 60(5):495–497, MAY 1995. ISSN 0946-2171. doi: 10.1007/BF01081333.

[37] S. Hell and J. Wichmann. Breaking the diffraction resolution limit by stimulated-emission - stimulated-emission-depletion fluorescence microscopy. *Optics Letters*, 19(11):780–782, JUN 1 1994. ISSN 0146-9592. doi: 10.1364/OL.19.000780.

[38] M. Holler, A. Diaz, M. Guizar-Sicairos, P. Karvinen, E. Farm, E. Harkonen, M. Ritala, A. Menzel, J. Raabe, and O. Bunk. X-ray ptychographic computed tomography at 16 nm isotropic 3D resolution. *Scientific Reports*, 4, JAN 24 2014. ISSN 2045-2322. doi: 10.1038/srep03857.

[39] W. Hoppe. Diffraction in inhomogeneous primary wave fields. 1. principle of phase determination from electron diffraction interference. *Acta Crystallographica Section A-Crystal Physics Diffraction Theoretical and General Crystallography*, A 25(4):495–&, 1969. ISSN 0567-7394. doi: 10.1107/S0567739469001045.

[40] B. Hornberger, M. Feser, and C. Jacobsen. Quantitative amplitude and phase contrast imaging in a scanning transmission X-ray microscope. *Ultramicroscopy*, 107(8):644–655, AUG 2007. ISSN 0304-3991. doi: 10.1016/j.ultramic.2006.12.006.

[41] P. Horowitz and J. A. Howell. A scanning x-ray microscope using synchrotron radiation. *Science*, 178(4061):608–611, 1972. ISSN 0036-8075. doi: 10.1126/science.178.4061.608.

[42] M. Howells, T. Beetz, H. Chapman, C. Cui, J. Holton, C. Jacobsen, J. Kirz, E. Lima, S. Marchesini, H. Miao, D. Sayre, D. Shapiro, J. Spence, and D. Starodub. An assessment of the resolution limitation due to radiation-damage in X-ray diffraction microscopy. *Journal of Electron Spectroscopy and Related Phenomena*, 170(1 - 3):4–12, 2009. ISSN 0368-2048. doi: 10.1016/j.elspec.2008.10.008.

[43] B. Kanngiesser, W. Malzer, and I. Reiche. A new 3D micro X-ray fluorescence analysis set-up - first archaeometric applications. *Nuclear Instruments & Methods In Physics Research Section B-Beam Interactions With Materials and Atoms*, 211(2):259–264, OCT 2003. ISSN 0168-583X. doi: 10.1016/S0168-583X(03)01321-1.

[44] S. Kapishnikov, A. Weiner, E. Shimoni, P. Guttmann, G. Schneider, N. Dahan-Pasternak, R. Dzikowski, L. Leiserowitz, and M. Elbaum. Oriented nucleation of hemozoin at the digestive vacuole membrane in plasmodium falciparum. *Proceedings of the National Academy of Sciences of the United States of America*, 109(28):11188–11193, JUL 10 2012. ISSN 0027-8424. doi: 10.1073/pnas.1118120109.

[45] J. Kenney, J. Kirz, H. Rarback, R. Feder, D. Sayre, and M. Howells. Scanning soft-X-ray-ray microscopy with a Fresnel zoneplate at the national synchrotron light-source. *Proceedings Of The Society Of Photo-Optical Instrumentation Engineers*, 447:158–163, 1984. ISSN 0361-0748.

[46] C. Knöchel. *Anwendung und Anpassung tomographischer Verfahren in der Röntgenmikroskopie*. PhD thesis, Georg-August-Universität zu Göttingen, 2005.

[47] M. Knoll and E. Ruska. Das Elektronenmikroskop. *Zeitschrift fuer Physik*, 78(5-6):318–339, MAY 1932. ISSN 0044-3328. doi: 10.1007/BF01342199.

[48] M. Lindblom, J. Reinspach, O. von Hofsten, M. Bertilson, H. M. Hertz, and A. Holmberg. High-aspect-ratio germanium zone plates fabricated by reactive ion etching in chlorine. *Journal of Vacuum Science & Technology B*, 27(2):L1–L3, MAR-APR 2009. ISSN 1071-1023. doi: 10.1116/1.3089371.

[49] A. W. Lohmann and D. P. Paris. Binary fraunhofer holograms generated by computer. *Applied Optics*, 6(10):1739–&, 1967. doi: 10.1364/AO.6.001739.

[50] A. M. Maiden and J. M. Rodenburg. An improved ptychographical phase retrieval algorithm for diffractive imaging. *Ultramicroscopy*, 109(10):1256–1262, SEP 2009. ISSN 0304-3991. doi: 10.1016/j.ultramic.2009.05.012.

[51] S. Marchesini, S. Boutet, A. E. Sakdinawat, M. J. Bogan, S. Bajt, A. Barty, H. N. Chapman, M. Frank, S. P. Hau-Riege, A. Szoeke, C. Cui, D. A. Shapiro, M. R. Howells, J. C. H. Spence, J. W. Shaevitz, J. Y. Lee, J. Hajdu, and M. M. Seibert. Massively parallel X-ray holography. *Nature Photonics*, 2(9):560–563, SEP 2008. ISSN 1749-4885. doi: 10.1038/nphoton.2008.154.

[52] W. Martienssen and S. Spiller. Holographic reconstruction without granulation. *Physics Letters A*, A 24(2):126+, 1967. ISSN 0375-9601. doi: 10.1016/0375-9601(67)90517-8.

[53] J. G. McNally, S. Rehbein, C. Pratsch, S. Werner, P. Guttmann, and G. Schneider. 3D psf measurement for a soft X-ray microscope and comparison to theory. In *Imaging and Applied Optics 2016*, page CM3D.4. Optical Society of America, 2016. doi: 10.1364/COSI.2016.CM3D.4.

[54] C. Messaoudil, T. Boudier, C. Oscar Sanchez Sorzano, and S. Marco. Tomoj: tomography software for three-dimensional reconstruction in transmission electron microscopy. *BMC Bioinformatics*, 8, AUG 6 2007. ISSN 1471-2105. doi: 10.1186/1471-2105-8-288.

[55] J. Miao, P. Charalambous, J. Kirz, and D. Sayre. Extending the methodology of X-ray crystallography to allow imaging of micrometre-sized non-crystalline specimens. *Nature*, 400(6742):342–344, JUL 22 1999. ISSN 0028-0836. doi: 10.1038/22498.

[56] M. Minsky. Microscopy apparatus, Dec. 19 1961. US Patent 3,013,467.

[57] G. Morrison. Phase-contrast and dark-field imaging in x-ray microscopy. In Jacobsen, CJ and Trebes, JE, editor, *Proc. SPIE Soft X-ray microscopy*, volume 1741 of *PROCEEDINGS OF THE SOCIETY OF PHOTO-OPTICAL INSTRUMENTATION ENGINEERS (SPIE)*, pages 186–193. SOC PHOTO OPT INSTRUMENTAT ENGINEERS, 1993. ISBN 0-8194-0914-6. doi: 10.1117/12.138730.

[58] O. Myers. Studies of transmission zone plates. *American Journal Of Physics*, 19(6):359–365, 1951. ISSN 0002-9505. doi: 10.1119/1.1932827.

[59] R. Neutze, R. Wouts, D. van der Spoel, E. Weckert, and J. Hajdu. Potential for biomolecular imaging with femtosecond X-ray pulses. *Nature*, 406(6797): 752–757, AUG 17 2000. ISSN 0028-0836. doi: 10.1038/35021099.

[60] B. Niemann, D. Rudolph, and G. Schmahl. X-ray microscopy with synchrotron radiation. *Applied Optics*, 15(8):1883–1884, 1976. ISSN 0003-6935. doi: 10.1364/AO.15.001883.

[61] J. Otón, E. Pereiro, A. J. Pérez-Berná, L. Millach, C. O. S. Sorzano, R. Marabini, and J. M. Carazo. Characterization of transfer function, resolution and depth of field of a soft X-ray microscope applied to tomography enhancement by Wiener deconvolution. *Biomedical Optics Express*, 7(12):5092–5103, DEC 1 2016. ISSN 2156-7085. doi: 10.1364/BOE.7.005092.

[62] D. Paganin. *Coherent X-Ray Optics*. Oxford Science Publications. OUP Oxford, 2006. ISBN 9780198567288.

[63] H. Pattee. *The Compound Reflection X-ray Microscope*. Department of Physics, Stanford University., 1953.

[64] M. Peuker. High-efficiency nickel phase zone plates with 20 nm minimum outermost zone width. *Applied Physics Letters*, 78(15):2208–2210, APR 9 2001. ISSN 0003-6951. doi: 10.1063/1.1361285.

[65] B. Pfau, S. Schaffert, L. Müller, C. Gutt, A. Al-Shemmary, F. Büttner, R. Delaunay, S. Düsterer, S. Flewett, R. Frömter, et al. Ultrafast optical demagnetization manipulates nanoscale spin structure in domain walls. *Nature communications*, 3:1100, 2012.

[66] C. J. Powell and A. Jablonski. *NIST Electron Effective-Attenuation-Length Database - Version 1.3*. National Institute of Standards and Technology, Gaithersburg, MD, 2011.

[67] C. Pratsch, S. Rehbein, S. Werner, and G. Schneider. Influence of random zone positioning errors on the resolving power of fresnel zone plates. *Optics Express*, 22(25):30482–30491, DEC 15 2014. ISSN 1094-4087. doi: 10.1364/OE.22.030482.

[68] S. Rehbein, S. Heim, P. Guttmann, S. Werner, and G. Schneider. Ultrahigh-resolution soft-x-ray microscopy with zone plates in high orders of diffraction. *Physical Review Letters*, 103(11), SEP 11 2009. ISSN 0031-9007. doi: 10.1103/PhysRevLett.103.110801.

[69] S. Rehbein, P. Guttmann, S. Werner, and G. Schneider. Characterization of the resolving power and contrast transfer function of a transmission X-ray microscope with partially coherent illumination. *Optics Express*, 20(6):5830–5839, MAR 12 2012. ISSN 1094-4087. doi: 10.1364/OE.20.005830.

[70] D. Rudolph, B. Niemann, and G. Schmahl. Status of the sputtered sliced zone plates for X-ray microscopy. *Proceedings of the Society of Photo-Optical Instrumentation Engineers*, 316:103–105, 1981. ISSN 0361-0748.

[71] M. J. Rust, M. Bates, and X. Zhuang. Sub-diffraction-limit imaging by stochastic optical reconstruction microscopy (storm). *Nature Methods*, 3 (10):793–795, OCT 2006. ISSN 1548-7091. doi: 10.1038/nmeth929.

[72] A. Sakdinawat and Y. Liu. Phase contrast soft X-ray microscopy using zernike zone plates. *Optics Express*, 16(3):1559–1564, FEB 4 2008. ISSN 1094-4087. doi: 10.1364/OE.16.001559.

[73] D. Sayre. Some implications of a theorem due to Shannon. *Acta Crystallographica*, 5(6):843, 1952. ISSN 0108-7673. doi: 10.1107/S0365110X52002276.

[74] A. Schertel, N. Snaidero, H.-M. Han, T. Ruhwedel, M. Laue, M. Grabenbauer, and W. Möbius. Cryo FIB-SEM: Volume imaging of cellular ultrastructure in native frozen specimens. *Journal of Structural Biology*, 184(2):355–360, 2013. ISSN 1047-8477. doi: 10.1016/j.jsb.2013.09.024.

[75] G. Schmahl and D. Rudolph. High power zone plates as image forming systems for soft X-rays. *Optik*, 29(6):577–&, 1969. ISSN 0030-4026.

[76] G. Schmahl and D. Rudolph. *Proposal for a Phase Contrast X-ray Microscope*, pages 231–238. Springer Berlin Heidelberg, Berlin, Heidelberg, 1987. ISBN 978-3-642-72881-5. doi: 10.1007/978-3-642-72881-5_16.

[77] G. Schmahl, D. Rudolph, B. Niemann, and O. Christ. Zone-plate X-ray microscopy. *Quarterly Reviews of Biophysics*, 13(3):297–315, 1980. ISSN 0033-5835.

[78] G. Schmahl, D. Rudolph, G. Schneider, P. Guttmann, and B. Niemann. Phase-contrast X-ray microscopy studies. *Optik*, 97(4):181–182, OCT 1994. ISSN 0030-4026.

[79] T. Schmidt, U. Groh, R. Fink, E. Umbach, O. Schaff, W. Engel, B. Richter, H. Kuhlenbeck, R. Schlögl, H.-J. Freund, A. M. Bradshaw, D. Preikszas, P. Hartel, R. Spehr, H. Rose, G. Lilienkamp, E. Bauer, and G. Benner. XPEEM with energy-filtering: advantages and first results from the SMART project. *Surface Review and Letters*, 09(01):223–232, 2002. doi: 10.1142/S0218625X02001811.

[80] G. Schneider. Zone plates with high efficiency in high orders of diffraction described by dynamical theory. *Applied Physics Letters*, 71(16):2242–2244, OCT 20 1997. ISSN 0003-6951. doi: 10.1063/1.120069.

[81] G. Schneider. Cryo X-ray microscopy with high spatial resolution in amplitude and phase contrast. *Ultramicroscopy*, 75(2):85–104, NOV 1998. ISSN 0304-3991. doi: 10.1016/S0304-3991(98)00054-0.

[82] G. Schneider, S. Heim, P. Guttmann, S. Rehbein, and B. Niemann. Novel X-ray microscopes for 3-d and fs-imaging at BESSY. In *Proceedings 8th International Conference X-ray Microscopy*, volume 7, pages 349–52, 2006.

[83] G. Schneider, P. Guttmann, S. Heim, S. Rehbein, F. Mueller, K. Nagashima, J. B. Heymann, W. G. Mueller, and J. G. McNally. Three-dimensional cellular ultrastructure resolved by X-ray microscopy. *Nature Methods*, 7(12):985–U116, DEC 2010. ISSN 1548-7091. doi: 10.1038/NMETH.1533.

[84] G. Schneider, P. Guttmann, S. Rehbein, S. Werner, and R. Follath. Cryo X-ray microscope with flat sample geometry for correlative fluorescence and nanoscale tomographic imaging. *Journal of Structural Biology*, 177(2):212–223, FEB 2012. ISSN 1047-8477. doi: 10.1016/j.jsb.2011.12.023.

[85] M. Selin, E. Fogelqvist, A. Holmberg, P. Guttmann, U. Vogt, and H. M. Hertz. 3D simulation of the image formation in soft X-ray microscopes. *Optics Express*, 22(25):30756–30768, DEC 15 2014. ISSN 1094-4087. doi: 10.1364/OE.22.030756.

[86] D. A. Shapiro, Y.-S. Yu, T. Tyliszczak, J. Cabana, R. Celestre, W. Chao, K. Kaznatcheev, A. L. D. Kilcoyne, F. Maia, S. Marchesini, Y. S. Meng, T. Warwick, L. L. Yang, and H. A. Padmore. Chemical composition mapping with nanometre resolution by soft X-ray microscopy. *Nature Photonics*, 8 (10):765–769, OCT 2014. ISSN 1749-4885. doi: 10.1038/NPHOTON.2014.207.

[87] T. Shimobaba, J. Weng, T. Sakurai, N. Okada, T. Nishitsuji, N. Takada, A. Shiraki, N. Masuda, and T. Ito. Computational wave optics library for C plus plus: CWo plus plus library. *Computer Physics Communications*, 183 (5):1124–1138, MAY 2012. ISSN 0010-4655. doi: 10.1016/j.cpc.2011.12.027.

[88] M. Simpson and A. Michette. Imaging properties of modified fresnel zone plates. *Optica Acta*, 31(4):403–413, 1984. ISSN 0030-3909.

[89] A. Snigirev, V. Kohn, I. Snigireva, and B. Lengeler. A compound refractive lens for focusing high-energy X-rays. *Nature*, 384(6604):49–51, NOV 7 1996. ISSN 0028-0836. doi: 10.1038/384049a0.

[90] A. Späth, J. Raabe, and R. H. Fink. Confocal soft X-ray scanning transmission microscopy: setup, alignment procedure and limitations. *Journal of Synchrotron Radiation*, 22(1):113–118, Jan 2015. doi: 10.1107/S1600577514022322.

[91] H. Stiel, A. Dehlinger, K. A. Janulewicz, R. Jung, H. Legall, C. Pratsch, C. Seim, and J. Tuemmler. Nanoscale imaging using coherent and incoherent laboratory based soft x-ray sources. In Rocca, J and Menoni, C and Marconi, M, editor, *X-RAY LASERS 2014*, volume 169 of *Springer Proceedings in Physics*, pages 267–273, 2016. ISBN 978-3-319-19521-6; 978-3-319-19520-9. doi: 10.1007/978-3-319-19521-6_35.

[92] G. Stroke and D. Falconer. Attainment of high resolutions in wavefront-reconstruction imaging. *Physics Letters*, 13(4):306–309, 1964. doi: 10.1016/0031-9163(64)90022-8.

[93] G. W. Stroke. Lensless Fourier-transform method for optical holography. *Applied Physics Letters*, 6(10):201–&, 1965. ISSN 0003-6951. doi: 10.1063/1.1754131.

[94] J. Tuemmler, R. Jung, H. Stiel, P. V. Nickles, and W. Sandner. High-repetition-rate chirped-pulse-amplification thin-disk laser system with joule-level pulse energy. *Optics Letters*, 34(9):1378–1380, MAY 1 2009. ISSN 0146-9592.

[95] J. Vanroey, J. Vanderdonk, and P. Lagasse. Beam-propagation method - analysis and assessment. *Journal of the Optical Society of America*, 71(7): 803–810, 1981. ISSN 0030-3941. doi: 10.1364/JOSA.71.000803.

[96] I. Vartiainen, C. Holzner, I. Mohacsi, P. Karvinen, A. Diaz, G. Pigino, and C. David. Artifact characterization and reduction in scanning X-ray Zernike phase contrast microscopy. *Optics Express*, 23(10):13278–13293, MAY 18 2015. ISSN 1094-4087. doi: 10.1364/OE.23.013278.

[97] J. Vila-Comamala, K. Jefimovs, J. Raabe, T. Pilvi, R. H. Fink, M. Senoner, A. Maassdorf, M. Ritala, and C. David. Advanced thin film technology for ultrahigh resolution X-ray microscopy. *Ultramicroscopy*, 109(11):1360–1364, OCT 2009. ISSN 0304-3991. doi: 10.1016/j.ultramic.2009.07.005.

[98] L. Vincze, B. Vekemans, F. Brenker, G. Falkenberg, K. Rickers, A. Somogyi, M. Kersten, and F. Adams. Three-dimensional trace element analysis by confocal X-ray microfluorescence imaging. *Analytical Chemistry*, 76(22): 6786–6791, NOV 15 2004. ISSN 0003-2700. doi: 10.1021/ac0492741.

[99] Y. Vladimirsky and H. Koops. Moire method and zone plate pattern inaccuracies. *Journal of Vacuum Science & Technology B*, 6(6):2142–2146, NOV-DEC 1988. ISSN 1071-1023. doi: 10.1116/1.584103.

[100] S. Vogt, H. Chapman, C. Jacobsen, and R. Medenwaldt. Dark field X-ray microscopy: the effects of condenser/detector aperture. *Ultramicroscopy*, 87 (1-2):25–44, MAR 2001. ISSN 0304-3991.

[101] O. von Hofsten, M. Bertilson, M. Lindblom, A. Holmberg, and U. Vogt. Compact Zernike phase contrast X-ray microscopy using a single-element optic. *Optics Letters*, 33(9):932–934, May 2008. doi: 10.1364/OL.33.000932.

[102] E. H. Waller and G. von Freymann. Multi foci with diffraction limited resolution. *Opt. Express*, 21(18):21708–21713, Sep 2013. doi: 10.1364/OE.21.021708.

[103] S. Werner, S. Rehbein, P. Guttmann, and G. Schneider. Three-dimensional structured on-chip stacked zone plates for nanoscale X-ray imaging with high efficiency. *Nano Research*, 7(4):528–535, APR 2014. ISSN 1998-0124. doi: 10.1007/s12274-014-0419-x.

[104] S. Wilhelm, B. Gröbler, M. Gluch, and H. Heinz. *Confocal Laser Scanning Microscopy*. Zeiss Jena, 2006.

[105] G. J. Williams, E. Hanssen, A. G. Peele, M. A. Pfeifer, J. Clark, B. Abbey, G. Cadenazzi, M. D. de Jonge, S. Vogt, L. Tilley, and K. A. Nugent. High-resolution X-ray imaging of plasmodium falciparum-infected red blood cells. *Cytometry Part A*, 73A(10):949–957, OCT 2008. ISSN 1552-4922. doi: 10.1002/cyto.a.20616.

[106] J. Winthrop and C. Worthington. X-ray microscopy by successive Fourier transformation. *Physics Letters*, 15(2):124+, 1965. doi: 10.1016/0375-9601(65)90211-2.

[107] H. Wolter. Spiegelsysteme streifenden Einfalls als abbildende Optiken für Röntgenstrahlen. *Annalen der Physik*, 445(1-2):94–114, 1952. ISSN 1521-3889. doi: 10.1002/andp.19524450108.

[108] F. Wyrowski and O. Bryngdahl. Iterative fourier-transform algorithm applied to computer holography. *Journal of the Optical Society of America A-optics Image Science and Vision*, 5(7):1058–1065, July 1988. doi: 10.1364/JOSAA.5.001058.

[109] F. Zernike. Das Phasenkontrastverfahren bei der mikroskopischen Beobachtung. *Zeitschrift für Technische Physik*, 16:454–457, 1935.

Appendix A

Propagators and Comments to the Programming

A.1 Propagators

The different approximations presented in chapter 4 naturally lead to different implementations. Here, some of the most often used implementations are introduced and commented.

A.1.1 Angular Spectrum Method Based Propagators

The angular spectrum method is quite slow and awkward to use. But it does not suffer from the paraxial approximation. It was therefore used to verify the results of the other implementations.

For example, the iterations for the optimization of the diffractive optical elements for the FTH-experiments use a propagator from the near and far field approximation. The final binary mask was tested using the angular spectrum method. Due to the size of a few hundred micrometers and the outermost structure width of fifty nanometers, this is already a challenging computation for a desktop computer.

Commented Program

The matlab program on page 161 implements equation 3.2.

$$U[x_1, y_1, z_1] = \frac{1}{i\lambda}\int_{-\infty}^{\infty}\int_{-\infty}^{\infty} U[x_0, y_0, z_0] \cdot (z_1 - z_0) \cdot \frac{\exp\left[i\,k\sqrt{(z_1 - z_0)^2 + (x_1 - x_0)^2 + (y_1 - y_0)^2}\right]}{(z_1 - z_0)^2 + (x_1 - x_0)^2 + (y_1 - y_0)^2} \mathbf{d}x_0\mathbf{d}y_0$$

The following notations are used in the program.

U1 is the discretised version of $U[x_1, y_1, z_1]$.

U0 is the discretised version of $U[x_0, y_0, z_0]$.

dx are the resolutions in both planes.

lambda is the wavelength.

d is the distance between both planes.

FOV_min is the minimal field of view which should be visible in the output plane.

Line 1 contains the function header.
Line 2 defines the global variables scalfaktor, lambda and k .
Lines 3 to 6 initialize some constants.
Lines 7 and 9 compute the parameters for the partition of the input field, so that the field of view has the correct size.
Line 10 defines the convolution kernel which corresponds to the red part

$$\left((z_1 - z_0) \cdot \frac{\exp\left[i\,k\sqrt{(z_1 - z_0)^2 + (x_1 - x_0)^2 + (y_1 - y_0)^2}\right]}{(z_1 - z_0)^2 + (x_1 - x_0)^2 + (y_1 - y_0)^2}\right).$$

Lines 11 and 12 initialize some constants and variables.
Lines 13 and 14 start the iteration over all sub-partitions of the input field.
Line 15 prints the current position onto the screen.
Line 16 uses a sub-routine to compute the current positions in the sub-partition.
Lines 17 to 19 determine the current sub-partition of the convolution kernel.
Line 20 cuts out the correct sub-partition of the transmission function.
Line 21 computes the resulting output field of the sub-partition by convolving the product of the inbound illumination with the transmission function and using a subroutine to compute the convolution of the result with the current propagation kernel.
Line 22 updates the resulting output field.

Implementation of the propagator for the angular spectrum

```
1. function [U1]=C20160102_Distributed_fft_ASM(U0,dx,d,lambda1,FOV_min)
2. global scalfaktor lambda k
3. lambda=lambda1;
4. k=2*pi/lambda;
5. scalfaktor=dx;
6. L=size(U0,1);
7. W=ceil(((FOV_min)/dx));
8. N=2^round(log2(L/W));
9. W=L/N;
10. prop= @(ix,d) squeeze(d./(d.^2+ix(1,:,:).^2+ix(2,:,:).^2).*...
    exp(1i*k*(sqrt(d.^2+ix(1,:,:).^2+ix(2,:,:).^2))));
11. U1=zeros(W);
12. Z2=0;offset=0;
13. for VN=1:N
14. for VM=1:N
15. [VN,VM]
16. Out=(Ind2Kord((1-W):(2*W),(1-W):(2*W),VN,VM,L, N, W));
17. Out(1,:,:)=rot90(squeeze(Out(1,:,:)),2);
18. Out(2,:,:)=rot90(squeeze(Out(2,:,:)),2);
19. propagat=(prop(Out,d));
20. Z2= U0(W*(VN-1)+(1:W),W*(VM-1)+(1:W));
21. Z1=Falter((Z2,propagat);
22. U1=(U1+Z1);
23. end
24. end
25. end
```

Sub-functions for the propagator for the angular spectrum method.

```
1. function Out=Ind2Kord(IX,IY,IN,IM,L, N, W)
2. global scalfaktor lambda k
3. Out(1,:,:)=scalfaktor*(-(L+1)/2+(IN-1)*W+IX)'*ones(1,size(IY,2));
4. Out(2,:,:)=scalfaktor*ones(size(IX,2),1)*(-(L+1)/2+(IM-1)*W+IY);
5. end
```

```
1. function K=Falter(A,B)
2. as=size(A);
3. bs=size(B);
4. a1=zeros((as+bs));
5. b1=zeros((as+bs));
6. a1(1:as(1),1:as(2))=A;
7. b1(1:bs(1),1:bs(2))=B;
8. a1=ifft2(ifftshift(fftshift(fft2(b1)).*fftshift(fft2(a1))))/...
   ((as(1)+bs(1))*(as(2)+bs(2)));
9. K=a1((floor(bs(1)/2)+1):(floor(bs(1)/2)+as(1)),...
   (floor(bs(2)/2)+1):(floor(bs(2)/2)+as(2)));
10. end
```

A.1.2 Fresnel Approximation Based Propagators

Commented Program

The program on the next page implements the equation (3.4).

$$U[x_1, y_1, z_1] \approx \frac{\exp[i\,k\,z]}{i\,\lambda\,z} \exp\left[i\,k\,\frac{x_1^2+y_1^2}{2\,(z_1-z_0)}\right] \int_{-\infty}^{\infty}\int_{-\infty}^{\infty} U[x_0, y_0, z_0] \exp\left[i\,k\,\frac{x_0^2+y_0^2}{2\,(z_1-z_0)}\right] \exp\left[-i\,k\,\frac{x_1x_0+y_1y_0}{(z_1-z_0)}\right] \mathrm{d}x_0\mathrm{d}y_0.$$

The following notations are used in the program.

Uz is the discretised version of $U[x_1, y_1, z_1]$.

dz1/dz2 are the resolutions in the z_1 plane.

U0 is the discretised version of $U[x_0, y_0, z_0]$.

d1/d2 are the resolutions in the z_0 plane.

lambda is the wavelength.

z is the distance between the two planes.

Lines 1 to 4 contain the function name and a small explanation of the variable names used.
Line 5 defines k as the wave number.
Lines 6 and 7 determine the dimensions $(N1, N2)$ of the input field (Uz) along direction one and two.
Lines 8 and 9 compute the resulting resolution of the output field. These resolutions result from the definition of the fast Fourier transform.
Lines 10 to 16 generate two arrays which contain the index along direction one and two.
Line 17 implements the red part $\left(U[x_0, y_0, z_0]\exp\left[i\,k\,\frac{x_0^2+y_0^2}{2\,(z_1-z_0)}\right]\right)$ of the Fresnel approximation.
Line 18 computes first the Fourier transform of the red part and then multiplies the result with the blue part $\left(\frac{\exp[i\,k\,z]}{i\,\lambda\,z}\exp\left[i\,k\,\frac{x_1^2+y_1^2}{2\,(z_1-z_0)}\right]\right)$ of the Fresnel approximation.

Implementation of the propagator for the Fresnel approximation.

```
1. function [Uz,dz1,dz2]=C20131217_FFTFresnel(U0,z,lambda,d1,d2)
2. %FFT Fresnel propagator
3. % U0=input field, z=propagation distance, lambda=wavelength ,
4. % d1= resolution along direction 1, d2=resolution along direction 2
5. k=2*pi/lambda;
6. N1=size(U0,1);
7. N2=size(U0,2);
8. dz1=lambda*z/(d1*N1);
9. dz2=lambda*z/(d2*N2);
10. UN1=-(ceil(N1/2+0.5)-1);
```

```
11. ON1=(floor(N1/2+0.5)-1);
12. UN2=-(ceil(N2/2+0.5)-1);
13. ON2=(floor(N2/2+0.5)-1);
14. V1=(UN1:ON1);
15. V2=(UN2:ON2);
16. [Mesh1,Mesh2]=meshgrid(V1,V2);
17. U0=U0.*exp(1i*k/(2*z).*((d1*Mesh1').^2+(d2*Mesh2').^2));
18. Uz=exp(1i*k*z)/(1i*lambda*z).*exp(1i*k/(2*z)*...
    ((dz1*Mesh1').^2+(dz2*Mesh2').^2))*d1*d2.*...
    fftshift(fft2(fftshift(U0)));
19. end
```

Changes for Essentially Converging Fields

In the case that the input field produces an output field with much smaller extensions, it is more convenient to include a converging wave factor into the programming. Setting $Ud\left[x_0, y_0, z_0\right] := U\left[x_0, y_0, z_0\right] \cdot \exp\left[i\,k\,\frac{x_0^2+y_0^2}{2\,(z_1-z_0)}\right]$ creates a slower oscillating field which allows a coarser sampling of the input. For this field, equation (3.4) changes to

$$U\left[x_1, y_1, z_1\right] \approx \frac{\exp\left[i\,k\,z\right]}{i\,\lambda\,z} \exp\left[i\,k\,\frac{x_1^2+y_1^2}{2\,(z_1-z_0)}\right] \int_{-\infty}^{\infty}\int_{-\infty}^{\infty} Ud\left[x_0, y_0, z_0\right] \exp\left[-i\,k\,\frac{x_1 x_0 + y_1 y_0}{(z_1-z_0)}\right] \mathrm{d}x_0 \mathrm{d}y_0.$$

This formula is implemented in the program on this page which is identical to the program on the previous page except for the removal of line 17 and that

U0 is the discretised version of $Ud\left[x_0, y_0, z_0\right] = U\left[x_0, y_0, z_0\right] \cdot \exp\left[i\,k\,\frac{x_0^2+y_0^2}{2\,(z_1-z_0)}\right]$.

Program for the Fresnel approximation for essentially converging fields.

```
1. function [Uz,dz1,dz2]=C20131217_FFTFresnel_slow(U0,z,lambda,d1,d2)
2. %FFT Fresnel propagator for big input and small output
3. % U0=input field, z=propagation distance, lambda=wavelength ,
4. % d1= resolution along direction 1, d2=resolution along direction 2
```

```
5.  k=2*pi/lambda;
6.  N1=size(U0,1);
7.  N2=size(U0,2);
8.  dz1=lambda*z/(d1*N1);
9.  dz2=lambda*z/(d2*N2);
10. UN1=-(ceil(N1/2+0.5)-1);
11. ON1=(floor(N1/2+0.5)-1);
12. UN2=-(ceil(N2/2+0.5)-1);
13. ON2=(floor(N2/2+0.5)-1);
14. V1=(UN1:ON1);
15. V2=(UN2:ON2);
16. [Mesh1,Mesh2]=meshgrid(V1,V2);
17. Uz=exp(1i*k*z)/(1i*lambda*z).*exp(1i*k/(2*z)*...
    ((dz1*Mesh1').^2+(dz2*Mesh2').^2))*d1*d2.*...
    fftshift(fft2(fftshift(U0)));
18. end
```

Changes for Essentially Diverging Fields

In the case that the input field produces an output field with much larger dimensions, it is more convenient to include a diverging wave factor into the programming. Setting $Ud\left[x_1, y_1, z_1\right] := U\left[x_1, y_1, z_1\right] \cdot \exp\left[-i\,k\,\frac{x_1^2+y_1^2}{2\,(z_1-z_0)}\right]$ creates a much slower oscillating field which allows a coarser sampling of the output. For this field, equation (3.4) changes to

$$Ud\left[x_1, y_1, z_1\right] \approx \frac{\exp\left[i\,k\,z\right]}{i\,\lambda\,z} \int_{-\infty}^{\infty}\int_{-\infty}^{\infty} U\left[x_0, y_0, z_0\right] \exp\left[i\,k\,\frac{x_0^2+y_0^2}{2\,(z_1-z_0)}\right] \exp\left[-i\,k\,\frac{x_1 x_0 + y_1 y_0}{(z_1-z_0)}\right] \mathbf{d}x_0\mathbf{d}y_0.$$

This formula is implemented in the program on the following page which is identical to the program on page 163 except for a change in line 18 and that

Uz is the discretised version of $Ud\left[x_1, y_1, z_1\right] = U\left[x_1, y_1, z_1\right] \cdot \exp\left[-i\,k\,\frac{x_1^2+y_1^2}{2\,(z_1-z_0)}\right]$.

Program for the Fresnel approximation for essentially diverging fields.

```
1. function [Uz,dz1,dz2]=C20131217_FFTFresnel_slow_small_source(U0,z,lambda,d1,d2)
2. %%FFT Fresnel propagator for small input and a large output field
3. % U0=input field, z=propagation distance, lambda=wavelength ,
4. % d1= resolution along direction 1, d2=resolution along direction 2
5. k=2*pi/lambda;
6. N1=size(U0,1);
7. N2=size(U0,2);
8. dz1=lambda*z/(d1*N1);
9. dz2=lambda*z/(d2*N2);
10. UN1=-(ceil(N1/2+0.5)-1);
11. ON1=(floor(N1/2+0.5)-1);
12. UN2=-(ceil(N2/2+0.5)-1);
13. ON2=(floor(N2/2+0.5)-1);
14. V1=(UN1:ON1);
15. V2=(UN2:ON2);
16. [Mesh1,Mesh2]=meshgrid(V1,V2);
17. U0=U0.*exp(1i*k/(2*z).*((d1*Mesh1').^2+(d2*Mesh2').^2));
18. Uz=exp(1i*k*z)/(1i*lambda*z)*d1*d2.*fftshift(fft2(fftshift(U0)));
19. end
```

A.1.3 Near and Far Field Approximation Based Propagators

These propagators take the different dimensions of the input and the output field into account. The resulting approximation of equation (2.6)

$$U[x_1, y_1, z_1] = \frac{1}{i\lambda} \int_{-\infty}^{\infty} \int_{-\infty}^{\infty} U[x_0, y_0, z_0] \frac{z_1 - z_0}{r_{01}} \frac{\exp[i k r_{01}]}{r_{01}} \mathrm{d}x_0 \mathrm{d}y_0 \qquad (A.1)$$

is therefore better suited for high numerical aperture optics, such as high resolution soft X-ray Fresnel zone plates.

Since the formulas for the propagation differ depending on whether the input or the output plane is larger, the implementations differ, too.

First, the case that the input plane is much larger is considered.
The algorithm on the following page implements the formula

$$U[x_1,y_1,z_1] \approx \frac{1}{i\lambda}\exp\left[i\,k\frac{x_1^2+y_1^2}{2z}\right] \int_{\mathbb{R}^2} U\left[\frac{x_s}{\sqrt{1-\frac{x_s^2+y_s^2}{z^2}}},\frac{y_s}{\sqrt{1-\frac{x_s^2+y_s^2}{z^2}}},z_0\right]\frac{z}{z^2-x_s^2-y_s^2} \cdot\exp\left[i\,k\sqrt{\frac{z^4}{z^2-x_s^2-y_s^2}}\right]\exp\left[-i\,k\frac{(x_1x_s+y_1y_s)}{z}\right]\mathrm{d}x_s\mathrm{d}y_s.$$

Here, x_s and y_s are the regular equidistant grid points used in the Fresnel propagator.

The inverse formula is given by:

$$U\left[\frac{x_s}{\sqrt{1-\frac{x_s^2+y_s^2}{z^2}}},\frac{y_s}{\sqrt{1-\frac{x_s^2+y_s^2}{z^2}}},z_0\right] \approx \exp\left[-i\,k\sqrt{\frac{z^4}{z^2-x_s^2-y_s^2}}\right]\frac{z^2-x_s^2-y_s^2}{z}\int_{\mathbb{R}^2} i\lambda U[x_1,y_1,z_1] \cdot\exp\left[-i\,k\left(\frac{x_1^2+y_1^2}{2z}-\frac{(x_1x_s+y_1y_s)}{z}\right)\right]\mathrm{d}x_1\mathrm{d}y_1.$$

The following notations are used in the program on the next page.

Uz is the discretised version of $U[x_1,y_1,z_1]$.

dz1/dz2 are the resolutions in the z_1 plane.

U0 is the discretised version of $U\left[x_0=\frac{x_s}{\sqrt{1-\frac{x_s^2+y_s^2}{z^2}}},y_0=\frac{y_s}{\sqrt{1-\frac{x_s^2+y_s^2}{z^2}}},z_0\right]$.

Ud is a variable that stores an intermediate result.

d1/d2 are the resolutions in the z_0 plane of the equidistant grid attached to x_s and y_s.

lambda is the wavelength.

z is the distance between the two planes.

Lines 1 to 5 contain the function name and a small explanation of the variable names used.
Line 6 defines k as the wave number.
Lines 7 and 8 determine the dimensions $(N1, N2)$ of the input field (Uz) along directions one and two.

Lines 9 and 10 compute the resulting resolutions of the output field. These resolutions result from the definition of the fast Fourier transform.
Lines 11 to 17 generate two arrays which contain the index along directions one and two.

Line 18 defines the function $myr := \frac{z}{z^2-x_s^2-y_s^2}\exp\left[i\,k\sqrt{\frac{z^4}{z^2-x_s^2-y_s^2}}\right]$.
Line 19 implements the red part

$$\left(U\left[\frac{x_s}{\sqrt{1-\frac{x_s^2+y_s^2}{z^2}}},\frac{y_s}{\sqrt{1-\frac{x_s^2+y_s^2}{z^2}}},z_0\right]\frac{z}{z^2-x_s^2-y_s^2}\exp\left[i\,k\sqrt{\frac{z^4}{z^2-x_s^2-y_s^2}}\right]\right)$$

of the approximation.
Line 20 computes at first the Fourier transform of the red part and then multiplies the result by the blue part $\left(\frac{1}{i\lambda}\exp\left[i\,k\frac{x_1^2+y_1^2}{2z}\right]\right)$ of the near field approximation.

Program for the near field approximation.

```
1. function [Uz,dz1,dz2]=NFFA_Taylor(U0,z,lambda,d1,d2)
2. % NFFA FFT Fresnel Propagator size of U0 >>Uz
3. % U0=Field in z0 ,z=Propagation distance ,lambda=wavelength ,
4. % d1= resolution in z0 plane first direction ,d2=resolution in z0 plane second
   direction
5. % !!!The Sampling of U0 is no longer equidistant!!      !
6. k=2*pi/lambda;
7. N1=size(U0,1);
8. N2=size(U0,2);
9. dz1=lambda*z/(d1*N1);
10. dz2=lambda*z/(d2*N2);
11. UN1=-(ceil(N1/2+0.5)-1);
12. ON1=(floor(N1/2+0.5)-1);
13. UN2=-(ceil(N2/2+0.5)-1);
14. ON2=(floor(N2/2+0.5)-1);
15. V1=(UN1:ON1);
16. V2=(UN2:ON2);
```

17. `[Mesh1,Mesh2]=meshgrid(V1,V2);`
18. `myr=@(x,y,z)...`
    `(z./(z.^2-x.^2-y.^2)).*exp(1i*k.*sqrt((z.^4./(z.^2-x.^2-y.^2))));`
19. `Ud=U0.*myr(d1*Mesh1',d2*Mesh2',z);`
20. `Uz=1/(1i*lambda).*exp(1i*k*(dz1*Mesh1'.^2+dz2*Mesh2'.^2)./(2*z))...`
    `*d1*d2.*fftshift(fft2(fftshift(Ud)));`
21. `end`

Changes for Essentially Converging Fields

For the near field approximation, only the case of an essentially converging field is needed. The field is again separated into a fast oscillating converging field and a slowly varying modification

$$Ud\left[x_0, y_0, z_0\right] = U\left[x_0, y_0, z_0\right] \cdot \exp\left[i\,k\sqrt{\left(z_1 - z_0\right)^2 + x_0^2 + y_0^2}\right].$$

From $\sqrt{z^2 + x_0^2 + y_0^2} = \sqrt{\frac{z^4}{z^2 - x_s^2 - y_s^2}}$, it follows

$$Ud\left[x_0, y_0, z_0\right] = U\left[x_0, y_0, z_0\right] \cdot \exp\left[i\,k\sqrt{\frac{z^4}{z^2 - x_s^2 - y_s^2}}\right].$$

Therefore, in the new program A.1.3 in line 19, the red part is reduced to

$$\left(Ud\left[\frac{x_s}{\sqrt{1 - \frac{x_s^2+y_s^2}{z^2}}}, \frac{y_s}{\sqrt{1 - \frac{x_s^2+y_s^2}{z^2}}}, z_0\right] \frac{z}{z^2 - x_s^2 - y_s^2}\right).$$

Program for the near field approximation for an essentially converging field.

1. function [Uz,dz1,dz2]=NFFA_Taylor_slow(U0,z,lambda,d1,d2)
2. % NFFA FFT Fresnel Propagator size of U0 >>Uz
3. % U0=Field in z0 ,z=Propagation distance ,lambda=wavelength ,
4. % d1= resolution in z0 plane first direction ,d2=resolution in z0 plane second direction
5. % !!!The Sampling of U0 is no longer equidistant!!!
6. k=2*pi/lambda;

```
7.  N1=size(U0,1);
8.  N2=size(U0,2);
9.  dz1=lambda*z/(d1*N1);
10. dz2=lambda*z/(d2*N2);
11. UN1=-(ceil(N1/2+0.5)-1);
12. ON1=(floor(N1/2+0.5)-1);
13. UN2=-(ceil(N2/2+0.5)-1);
14. ON2=(floor(N2/2+0.5)-1);
15. V1=(UN1:ON1);
16. V2=(UN2:ON2);
17. [Mesh1,Mesh2]=meshgrid(V1,V2);
18. myr=@(x,y,z) (z./(z.^2-x.^2-y.^2));
19. Ud=U0.*myr(d1*Mesh1',d2*Mesh2',z);
20. Uz=1/(1i*lambda).*exp(1i*k*(dz1*Mesh1'.^2+dz2*Mesh2'.^2)./(2*z))...
    *d1*d2.*fftshift(fft2(fftshift(Ud)));
21. end
```

The case that the input plane is much smaller than the output plane is considered.

The algorithm on the facing page implements the formula

$$
\begin{aligned}
&U\left[x_1\left[x_s,y_s\right],y_1\left[x_s,y_s\right],z_1\right]\\
&\approx \frac{1}{i\lambda}\exp\left[i\,k\sqrt{\frac{z^4}{z^2-x_s^2-y_s^2}}\right]\left(\frac{z^2-x_s^2-y_s^2}{z^3}\right)\\
&\int_{\mathbb{R}^2} U\left[x_0,y_0,z_0\right)]\exp\left[i\,k\frac{x_0^2+y_0^2}{2\,z}\right]\exp\left[-i\,k\frac{x_s x_0+y_s y_0}{z}\right]\mathrm{d}x_0\mathrm{d}y_0.
\end{aligned}
$$

Here, x_s and y_s are the regular equidistant grid points used in the Fresnel propagator.

The inverse formula is given by:

$$
\begin{aligned}
U\left[x_0,y_0,z_0\right)] \;=\; & i\lambda\exp\left[-i\frac{2\pi}{\lambda}\frac{x_0^2+y_0^2}{2\,z}\right]\int_{\mathbb{R}^2} U\left[x_1\left[x_s,y_s\right],y_1\left[x_s,y_s\right],z_1\right]\\
&\left(\frac{z^3}{z^2-x_s^2-y_s^2}\right)\exp\left[i\frac{2\pi}{\lambda}\frac{x_s x_0+y_s y_0}{z}-\sqrt{\frac{z^4}{z^2-x_s^2-y_s^2}}\right]\mathrm{d}x_s\mathrm{d}y_s.
\end{aligned}
$$

The following notations are used in program on the current page.

Uz is the discretised version of $U\left[x_1 = \frac{x_s}{\sqrt{1-\frac{x_s^2+y_s^2}{z^2}}}, y_1 = \frac{y_s}{\sqrt{1-\frac{x_s^2+y_s^2}{z^2}}}, z_1\right]$.

dz1/dz2 are the resolutions in the z_1 plane of the equidistant grid attached to x_s respectively y_s.

U0 is the discretised version of $U[x_0, y_0, z_0]$.

d1/d2 are the resolutions in the z_0 plane.

lambda is the wavelength.

Lines 1 to 5 contain the function name and a small explanation of the variable names.
Line 6 defines k as the wave number.
Lines 7 and 8 determine the dimensions $(N1, N2)$ of the input field (Uz) along directions one and two.
Lines 9 and 10 compute the resulting resolutions of the output field. These resolutions result from the definition of the fast Fourier transform.
Lines 11 to 17 generate two arrays which contain the index along directions one and two.
Line 18 defines the function $myr := \exp\left[i\,k\sqrt{\frac{z^4}{z^2-x_s^2-y_s^2}}\right]\left(\frac{z^2-x_s^2-y_s^2}{z^3}\right)$.
Line 19 implements the red part

$$\left(U[x_0, y_0, z_0)]\exp\left[i\,k\frac{x_0^2+y_0^2}{2\,z}\right]\right)$$

of the approximation.
Line 20 computes at first the Fourier transform of the red part and then multiplies the result by the blue part $\left(\frac{1}{i\lambda}\exp\left[i\,k\sqrt{\frac{z^4}{z^2-x_s^2-y_s^2}}\right]\left(\frac{z^2-x_s^2-y_s^2}{z^3}\right)\right)$ of the far field approximation.

Program for the far field approximation.

1. function [Uz,dz1,dz2]=NFFA_Taylor_small_input(U0,z,lambda,d1,d2)
2. % NFFA FFT Fresnel Propagator size of U0 << Uz
3. % U0=Field in z0 ,z=Propagation distance ,lambda=wavelength ,
4. % d1= resolution in z0 plane first direction ,d2=resolution in z0 plane second direction

```
5.  % !!!The Sampling of Uz is no longer equidistant!!!
6.  k=2*pi/lambda;
7.  N1=size(U0,1);
8.  N2=size(U0,2);
9.  dz1=lambda*z/(d1*N1);
10. dz2=lambda*z/(d2*N2);
11. UN1=-(ceil(N1/2+0.5)-1);
12. ON1=(floor(N1/2+0.5)-1);
13. UN2=-(ceil(N2/2+0.5)-1);
14. ON2=(floor(N2/2+0.5)-1);
15. V1=(UN1:ON1);
16. V2=(UN2:ON2);
17. [Mesh1,Mesh2]=meshgrid(V1,V2);
18. myr=@(x,y,z) ...
    ((z.^2-x.^2-y.^2)./(z.^3)).*exp(1i*k.*sqrt((z.^4./(z.^2-x.^2-y.^2))));
19. Ud=U0.*exp(1i*k*((d1*Mesh1').^2+(d2*Mesh2').^2/(2*z)));
20. Uz=1/(1i*lambda).*myr(dz1*Mesh1',Mesh2',2*z)*...
    d1*d2.*fftshift(fft2(fftshift(Ud)));
21. end
```

Changes for Essentially Diverging Fields

For the far field approximation, only the case of an essentially diverging field is needed.

The field is again separated into a fast oscillating converging field and a slowly varying modification $Ud[x_1, y_1, z_1] = U[x_1, y_1, z_1] \cdot \exp\left[-i\,k\sqrt{(z_1 - z_0)^2 + x_1^2 + y_1^2}\right]$.

From $\sqrt{z^2 + x_1^2 + y_1^2} = \sqrt{\frac{z^4}{z^2 - x_s^2 - y_s^2}}$, it follows $Ud[x_1, y_1, z_1] = U[x_1, y_1, z_1] \cdot \exp\left[-i\,k\sqrt{\frac{z^4}{z^2 - x_s^2 - y_s^2}}\right]$.

Therefore, in the new program A.1.3 in lines 18 and 20, the blue part is reduced to

$$\frac{1}{i\lambda}\frac{z^2 - x_s^2 - y_s^2}{z^3}.$$

Program for the far field approximation for a diverging field.

```
1. function [Uz,dz1,dz2]=NFFA_Taylor_small_input_slow(U0,z,lambda,d1,d2)
2. %% NFFA FFT Fresnel Propagator size of U0 << Uz
3. % U0=Field in z0 ,z=Propagation distance ,lambda=wavelength ,
4. % d1= resolution in z0 plane first direction ,d2=resolution in z0 plane second direction
5. % !!!The Sampling of Uz is no longer equidistant!!!
6. k=2*pi/lambda;
7. N1=size(U0,1);
8. N2=size(U0,2);
9. dz1=lambda*z/(d1*N1);
10. dz2=lambda*z/(d2*N2);
11. UN1=-(ceil(N1/2+0.5)-1);
12. ON1=(floor(N1/2+0.5)-1);
13. UN2=-(ceil(N2/2+0.5)-1);
14. ON2=(floor(N2/2+0.5)-1);
15. V1=(UN1:ON1);
16. V2=(UN2:ON2);
17. [Mesh1,Mesh2]=meshgrid(V1,V2);
18. myr=@(x,y,z) ((z.^2-x.^2-y.^2)./(z.^3));
19. Ud=U0.*exp(1i*k*((d1*Mesh1').^2+(d2*Mesh2').^2/(2*z)));
20. Uz=1/(1i*lambda).*myr(dz1*Mesh1',Mesh2',2*z)...
    *d1*d2.*fftshift(fft2(fftshift(Ud)));
21. end
```

A.2 Scope of the Propagators

The above described propagators all include some approximations. Therefore, it is essential to be aware of the innate limits of each propagator.

A.2.1 Angular Spectrum Method Based Propagators

The angular spectrum method based propagator uses the scalar wave approximation and the approximation that the field is well described by a single value per pixel.

Therefore, if either the polarization of the wave is important or the dimensions of a pixel is chosen to be too large, the propagator fails to approximate the real field.

Three significant drawbacks make this propagator unsuited for most of the computations done in this work. Firstly, it is not directly invertible. This is a serious problem for algorithms, that have to iterate between an input and an output plane. Secondly, the discretization has to be chosen equal in both the input and the output plane. Thirdly, the computation time and memory usage scale faster with the size of the problem than it does for other propagators.

A.2.2 Fresnel Approximation Based Propagators

These propagators use the scalar wave approximation assuming that the field is well described by a single value per pixel and that the field is essentially concentrated in a small region around the optical axis.

As with the angular spectrum method, if either the polarization of the wave is important or the dimensions of a pixel is chosen to be too large, the propagators fail to approximate the real field. Additionally, there is now a limit on the axial spread of the field and the minimal distance between input and output planes. This limits the use of this type of propagators to low numerical apertures.

Nevertheless, the discretization in the input and output plane is no longer equal but related by an equation to the resolution, dimensions and distance of the other plane. In some cases, it is possible to increase the discretization of one of the planes by using an advantageous geometry such as essentially converging or diverging fields.

The Fresnel approximation is a good approximation if the following conditions are true.

- Polarization is not important, for example, for unpolarized light sources and homogeneous isotropic non-attenuating mediums of propagation.

- The distance (r_{01}) between two points in the input and output planes in equation A.1

$$U[x_1, y_1, z_1] = \frac{1}{i\,\lambda} \int_{-\infty}^{\infty} \int_{-\infty}^{\infty} U[x_0, y_0, z_0] \, \frac{z_1 - z_0}{r_{01}} \frac{\exp[i\,k\,r_{01}]}{r_{01}} \, \mathrm{d}x_0 \mathrm{d}y_0$$

is well approximated by the second order Taylor approximation of the square root. This condition is deduced from the third term of the fourth order Taylor approximation of the square root

$$r_{01} \approx (z_1 - z_0) + \frac{(x_1 - x_0)^2 + (y_1 - y_0)^2}{2\,(z_1 - z_0)} - \frac{\left((x_1 - x_0)^2 + (y_1 - y_0)^2\right)^2}{8\,(z_1 - z_0)^3}.$$

The first two orders are already sufficiently good if

$$\begin{aligned} \exp\left[-i\,k\,\frac{\left((x_1 - x_0)^2 + (y_1 - y_0)^2\right)^2}{8\,(z_1 - z_0)^3}\right] &\approx 1 \\ \Longrightarrow\; k\,\frac{\left((x_1 - x_0)^2 + (y_1 - y_0)^2\right)^2}{8\,(z_1 - z_0)^3} &\ll 1 \\ \Longrightarrow\; k\frac{(L_1 + L_0)^4}{8} &\ll (z_1 - z_0)^3 \end{aligned}$$

and

$$\begin{aligned} (z_1 - z_0) + \frac{(x_1 - x_0)^2 + (y_1 - y_0)^2}{2\,(z_1 - z_0)} &\gg \frac{\left((x_1 - x_0)^2 + (y_1 - y_0)^2\right)^2}{8\,(z_1 - z_0)^3} \\ \Longrightarrow\; (z_1 - z_0) &\gg (L_1 + L_0) \geq |x_1 - x_0| + |y_1 - y_0| \end{aligned}$$

Here, L_1 and L_0 are the maximal, radial distances to the optical axis in the input and output planes respectively.

- The errors due to the discretization also produce small artifacts.
  For simplicity, a quadratic grid is assumed.
  Let Δx_0 and Δx_1 be the discretization step sizes in the input and output planes respectively, and N the number of pixels along one dimension, then the following conditions arise:

  - The discretization in either the input or output plane introduces a discretization in the other plane due to the properties of the fast Fourier transform. Therefore, one obtains

    $$\Delta x_0 N = \frac{\lambda z}{\Delta x_1}.$$

  - Since $L_1 = \Delta x_1 N/2$ and $L_0 = \Delta x_0 N/2$, the minimal distance $z = z_1 - z_0$ also depends on the discretization.

Starting with the discretization Δx_i of either the input or the output field, one gets

$$k\frac{(L_1+L_0)^4}{8} = k\frac{N^4(\Delta x_1+\Delta x_0)^4}{128} = k\frac{\left(\Delta x_i N+\frac{\lambda z}{\Delta x_i}\right)^4}{128} \ll z^3.$$

Expanding the fourth exponent of this expression yields the following conditions that must also be true:

* $\frac{k}{128}\left(\frac{\lambda}{\Delta x_i}\right)^4 \ll \frac{1}{z}$ which implies $z \ll \frac{128\lambda}{2\pi}\left(\frac{\Delta x_i}{\lambda}\right)^4$.
* $\binom{4}{3}\frac{k}{128}\left(\frac{\lambda}{\Delta x_i}\right)^3 z^3\Delta x_i N \ll z^3$ which implies

$$N \ll \frac{32}{2\pi}\frac{\Delta x_i^2}{\lambda^2}.$$

* $\binom{4}{2}\frac{k}{128}\left(\frac{\lambda}{\Delta x_i}\right)^2 z^2(\Delta x_i N)^2 \ll z^3$ which implies $\frac{12\pi\lambda N^2}{128} \ll z$ or equivalently

$$N \ll \frac{8}{\sqrt{6}}\frac{\sqrt{z}}{\sqrt{\lambda}}.$$

* The last condition is $\sqrt[3]{k\left(\frac{\Delta x_i N}{128}\right)^4} \ll z$

A.2.3 Near and Far Field Approximation Based Propagators

The near and far field approximation based propagators rely on three conditions, namely that the scalar wave approximation holds, that the field is well described by a single value per pixel and that the fields are essentially concentrated in either the input or output plane to a small region around the optical axis.

As in the previous methods, if either the polarization of the wave is important or the dimensions of a pixel is chosen to be too large, the propagators fail to approximate the real field. Again, there is a limit on the minimal distance between the input and output planes.

Nevertheless, the discretizations in the input and output planes are no longer equal but instead related by an equation involving the resolution, dimensions and distance to the other plane. In some cases, it is possible to increase the discretization of one of the planes by using an advantageous geometry such as essentially converging or diverging fields. These propagators are not limited to low numerical apertures!

These approximations are good approximations if the following conditions are true.

For the near field approximation:

- The distance (r_{01}) between two points in the input and output planes in equation A.1

$$U[x_1, y_1, z_1] = \frac{1}{i\lambda}\int_{-\infty}^{\infty}\int_{-\infty}^{\infty} U[x_0, y_0, z_0]\,\frac{z_1 - z_0}{r_{01}}\,\frac{\exp[i\,k\,r_{01}]}{r_{01}}\,\mathbf{d}x_0\mathbf{d}y_0$$

is well approximated by the near field approximation of the square root $\left(r_{01} \approx \sqrt{z^2 + x_0^2 + y_0^2}\sqrt{1+h}\right)$. The function h is given by:

$$\begin{aligned} h &= \frac{x_1^2 + y_1^2}{z^2 + x_0^2 + y_0^2} - \frac{2\,(x_1 x_0 + y_1 y_0)}{z^2 + x_0^2 + y_0^2} \\ &\overset{(x_0^2+y_0^2 \ll z^2)}{\approx} \frac{x_1^2 + y_1^2}{z^2} - \frac{2\,(x_1 x_0 + {}_1\, y_0)}{z^2 + x_0^2 + y_0^2}. \end{aligned}$$

The condition for this is deduced from the third term of the fourth order Taylor approximation of the square root of $\sqrt{1+h}$. The Taylor expansion of $\sqrt{1+h}$ yields

$$\begin{aligned} \sqrt{1+h} &= 1 + \frac{h}{2} - \frac{h^2}{8}\ldots \\ &\approx 1 + \frac{h}{2}. \end{aligned}$$

The first order is already sufficiently good if

$$\begin{aligned} &\exp\left[-i\,k\,\frac{h^2}{8}\sqrt{z^2 + x_0^2 + y_0^2}\right] \\ = \exp&\left[\frac{-i\,k}{8}\frac{\left(x_1^2 + y_1^2 - 2\,(x_1 x_0 - y_1 y_0)\right)^2}{\left(z^2 + x_0^2 + y_0^2\right)^2}\sqrt{z^2 + x_0^2 + y_0^2}\right] \approx 1. \end{aligned}$$

Which is valid if

$$\begin{aligned} \Longrightarrow\quad k\,\frac{\left(x_1^2 + y_1^2 - 2\,(x_1 x_0 - y_1 y_0)\right)^2}{8\sqrt{\left(z^2 + x_0^2 + y_0^2\right)^3}} &\ll 1 \\ \Longrightarrow\quad k\frac{L_1^4}{8} &\ll z^3 \\ k^2\frac{\left(2\,L_1^2 - 4\,L_1 L_0\right)^4}{64} &\overset{L_1 \ll L_0}{\approx} k^2 4\,(L_1 L_0)^4 \ll \left(z^2 + 2L_0^2\right)^3. \end{aligned}$$

- The errors due to the discretization also produce small artifacts.
  For simplicity, a quadratic grid is assumed.
  Let Δx_0 and Δx_1 be the discretization step sizes of the regular grid in the input and output planes respectively, and N be the number of pixels along one dimension. Then the following conditions arise.
  Since the grid in the input plane is no longer equidistant but rather determined by $x_0 = \frac{x_s}{\sqrt{1-\frac{x_s^2+y_s^2}{z^2}}}$ and $y_0 = \frac{y_s}{\sqrt{1-\frac{x_s^2+y_s^2}{z^2}}}$, the conditions for the discretization are a bit more complicated.

  - The regular discretization in either the input or output plane introduces a regular discretization in the other plane due to the properties of the fast Fourier transform. Therefore, one obtains:

$$\Delta x_0 N = \frac{\lambda z}{\Delta x_1}.$$

  - Since $L_1 = \Delta x_1 N/2$ and $L_0 = \frac{\Delta x_0 N/2}{\sqrt{1-\frac{(\Delta x_0 N/2)^2+(\Delta y_0 N/2)^2}{z^2}}}$, the minimal distance $z = z_1 - z_0$ also depends on the discretization.
    Starting with the output discretization Δx_1, one obtains

$$\begin{aligned} k\frac{L_1^4}{8} = \left(\frac{\lambda z}{\Delta x_0}\right)^4 /128 &\ll z^3 \\ \Longrightarrow z &\ll 128\frac{(\Delta x_0)^4}{\lambda^4} \end{aligned}$$

    and

$$\begin{aligned} k^2 4\left(L_1 L_0\right)^4 &\ll \left(z^2+2L_0^2\right)^3 \\ \Longrightarrow \frac{k^2\lambda^4 N^4}{64\left(1+\frac{\left(\frac{\lambda}{\Delta x_1}\right)^2}{2-4\left(\frac{\lambda}{2\Delta x_1}\right)^2}\right)^3\left(1-2\left(\frac{\lambda}{2\Delta x_1}\right)^2\right)^2} &\ll z^2. \end{aligned}$$

For the far field approximation:

- The distance (r_{01}) between two points in the input and output plane in equation A.1

$$U\left[x_1, y_1, z_1\right] = \frac{1}{i\,\lambda}\int_{-\infty}^{\infty}\int_{-\infty}^{\infty} U\left[x_0, y_0, z_0\right]\frac{z_1 - z_0}{r_{01}}\frac{\exp\left[i\,k\,r_{01}\right]}{r_{01}}\,\mathrm{d}x_0\mathrm{d}y_0$$

is well approximated by the far field approximation of the square root

$$\left(r_{01} \approx \sqrt{z^2 + x_1^2 + y_1^2}\sqrt{1+h}\right).$$

The function h is here given by:

$$\begin{aligned} h &= \frac{x_0^2 + y_0^2}{z^2 + x_1^2 + y_1^2} - \frac{2\left(x_1 x_0 + y_1 y_0\right)}{z^2 + x_1^2 + y_1^2} \\ &\overset{\left(x_1^2+y_1^2 \ll z^2\right)}{\approx} \frac{x_0^2 + y_0^2}{z^2} - \frac{2\left(x_1 x_0 + y_1 y_0\right)}{z^2 + x_1^2 + y_1^2}. \end{aligned}$$

The condition for this is deduced from the third term of the fourth order Taylor approximation of the square root of $\sqrt{1+h}$. The Taylor expansion of $\sqrt{1+h}$ yields

$$\begin{aligned} \sqrt{1+h} &= 1 + \frac{h}{2} - \frac{h^2}{8}\ldots \\ &\approx 1 + \frac{h}{2}. \end{aligned}$$

The first order is already sufficiently good if

$$\begin{aligned} &\exp\left[-i\,k\,\frac{h^2}{8}\sqrt{z^2 + x_1^2 + y_1^2}\right] \\ = \exp&\left[\frac{-i\,k}{8}\frac{\left(x_0^2 + y_0^2 - 2\left(x_1 x_0 - y_1 y_0\right)\right)^2}{\left(z^2 + x_1^2 + y_1^2\right)^2}\sqrt{z^2 + x_1^2 + y_1^2}\right] \approx 1. \end{aligned}$$

This results in the following conditions

$$\begin{aligned} k\,\frac{\left(x_0^2 + y_0^2 - 2\left(x_1 x_0 - y_1 y_0\right)\right)^2}{8\sqrt{\left(z^2 + x_1^2 + y_1^2\right)^3}} &\ll 1 \\ \Longrightarrow\; k\frac{L_0^4}{8} &\ll z^3 \\ k^2\frac{\left(2\,L_0^2 - 4\,L_1 L_0\right)^4}{64} &\overset{L_0 \ll L_1}{\approx} k^2 4\left(L_1 L_0\right)^4 \ll \left(z^2 + 2L_1^2\right)^3. \end{aligned}$$

- The errors due to the discretization also produce small artifacts.
  For simplicity, a quadratic grid is assumed.
  Let Δx_0 and Δx_1 be the discretization step sizes of the regular grid in the input and output planes respectively, and N be the number of pixels along

one dimension. Then the following conditions arise:
Since the grid in the input plane is no longer equidistant but rather determined by $x_1 = \frac{x_s}{\sqrt{1-\frac{x_s^2+y_s^2}{z^2}}}$ and $y_1 = \frac{y_s}{\sqrt{1-\frac{x_s^2+y_s^2}{z^2}}}$, the conditions for the discretization are a bit more complicated.

- The regular discretization in either the input or output plane introduces a regular discretization in the other plane due to the properties of the fast Fourier transform. Therefore, one obtains

$$\Delta x_0 N = \frac{\lambda z}{\Delta x_1}.$$

- Since $L_1 = \frac{\Delta x_1 N/2}{\sqrt{1-\frac{(\Delta x_1 N/2)^2+(\Delta y_1 N/2)^2}{z^2}}}$ and $L_0 = \Delta x_0 N/2$, the minimal and maximal allowable distance $z = z_1 - z_0$ also depends on the discretization.
Starting with the output discretization Δx_0, one obtains

$$\begin{aligned} k\frac{L_0^4}{8} = \left(\frac{\lambda z}{\Delta x_1}\right)^4 /128 &\ll z^3 \\ \Longrightarrow z &\ll 128\frac{(\Delta x_1)^4}{\lambda^4} \end{aligned}$$

and

$$\begin{aligned} k^2 4\left(L_1 L_0\right)^4 &\ll \left(z^2+2L_1^2\right)^3 \\ \Longrightarrow \frac{k^2\lambda^4 N^4}{64\left(1+\frac{1}{8\left(\frac{\Delta x_0}{\lambda}\right)^2-4}\right)^3\left(1-2\left(\frac{\lambda}{2\Delta x_0}\right)^2\right)^2} &\ll z^2. \end{aligned}$$

A.2.4 Examples

The following examples were used to verify that the approximations were working. They also show some of the weaknesses of the algorithms (A.2).

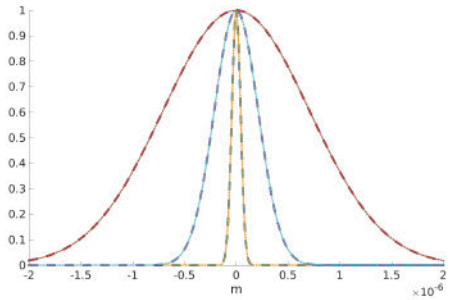

(a) Cut through the peak

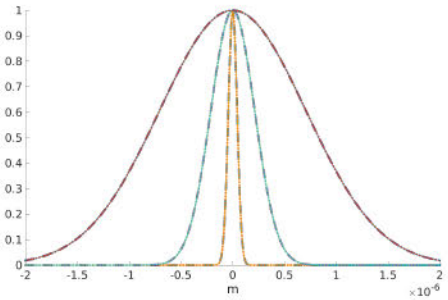

(b) Cut through the peak

Figure A.1: *Gaussian beams are propagated to their waist by the presented algorithms. Cuts of the resulting intensities through the peak for a waist of* $20\,nm$, $100\,nm$ *and* $1\,\mu m$ *are compared. The parameters of the propagation are* $\lambda = 2.4\,nm$, *distance between planes* $z = 0.5\,m$, *discretization in focal plane* $\Delta x = 6\,nm$ *and a field of view edge length of* $2000\,pxl = 12\,\mu m$. *For the simulation in* ***(b)****, a partition into a slowly oscillating function and a converging wave was used.*
In both cases the algorithms yield almost identical results to the theoretical prediction.

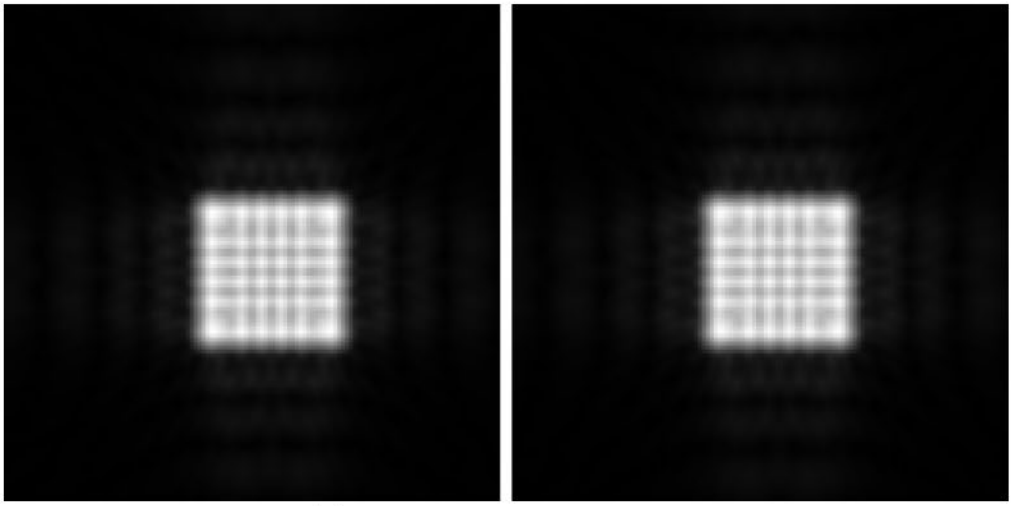

(a) Intensity of the reconstruction

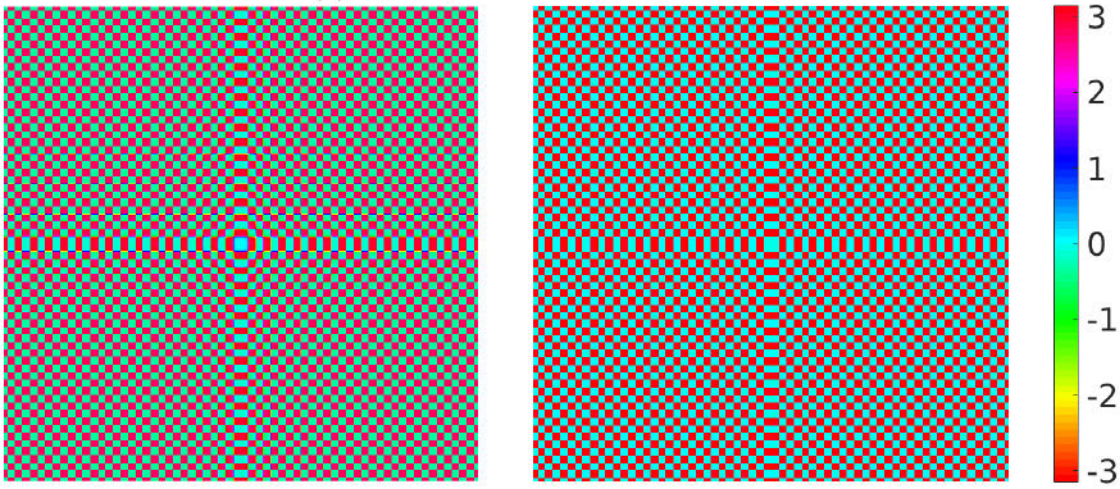

(b) Phase of the slowly varying function

Figure A.2: *For the left image in* **(a)**, *a homogeneous white square on a black background was back-propagated with the Fresnel propagator and the resulting field forward propagated with the angular spectrum method.*
For the right image, the same white square was back-propagated with the NFFA propagator and the resulting field was again forward propagated with the angular spectrum method.
Since in both cases, the version of the code that eliminates the fast oscillating converging parts of the wave were used, an additional interpolation step interpolates the data on a finer grid and includes the fast oscillating term before the ASM is applied.
The left image in **(b)** *is the phase of the slowly varying function created by the back-propagation with the Fresnel propagator and the right image is the phase produced by the NFFA propagator.*

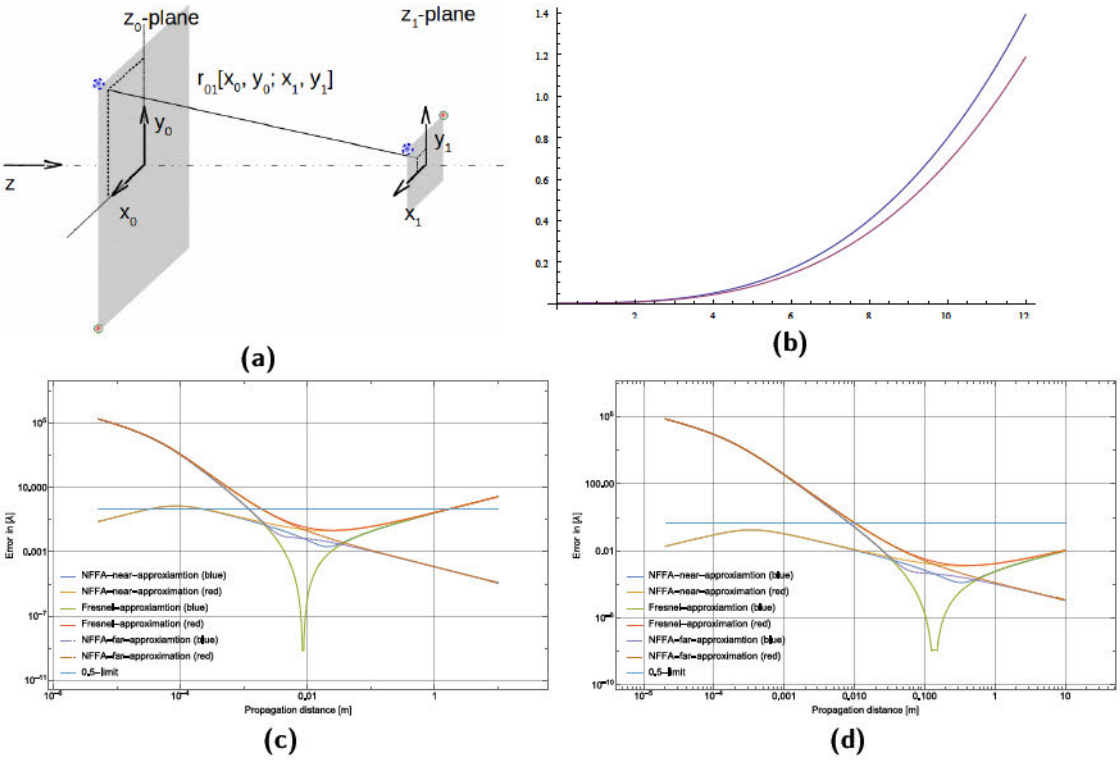

Figure A.3: *Panel* ***(a)*** *shows the dependency of the distance* $r_{01}\,[x_0, y_0; x_1, y_1]$ *on the position of the points of interested in the two planes. The blue (dashed) and red dots mark the positions used for estimating the maximal positioning errors. If the field of view is in one plane much larger than in the other, then the larger plane dominates the approximation errors of the distance in the Fresnel approximation. Panel* ***(b)*** *shows a comparison of the approximation error plotted over the distance between the two planes in units of the bigger plane. The smaller plane is here fifty times smaller than the bigger one. Both graphs show the quotient of the error of the Fresnel approximation divided by the error of the NFFA. The points* (x_0, y_0) *and* (x_1, y_1) *are chosen in such a way that they represent extremal cases for both approximations. The graphs in (c) and (d) show the errors of the approximated distance (equation (3.3) and equation (3.5)) in units of the wavelength over the propagation distance (compare also figure 3.2). In* ***(c)*** *the size of the input plane is a square of 100 µm and is discretized by* 512×512 *points. In* ***(d)*** *the size of the input plane is 400 µm at the same discretization.*

Appendix B

Simulation of the Transmission and Confocal Microscope

Here, the basis for the numerical analysis of the optical system is the Rayleigh-Sommerfeld diffraction formula for the propagation of monochromatic waves in a homogeneous medium. With this formula the propagation between two planes is given by equation (3.1)

$$U[x_1, y_1, z_1] = \frac{1}{i\lambda} \int_{-\infty}^{\infty} \int_{-\infty}^{\infty} U[x_0, y_0, z_0] \frac{z_1 - z_0}{r_{01}} \frac{\exp[i k r_{01}]}{r_{01}} \mathrm{d}x_0 \mathrm{d}y_0.$$

As previously deduced, the Fresnel approximation (3.4) can be used for faster computation in the case of small numerical apertures

$$U[x_1, y_1, z_1] \approx \frac{\exp[i k (z_1 - z_0)]}{i\lambda (z_1 - z_0)} \exp\left[i k \frac{x_1^2 + y_1^2}{2 (z_1 - z_0)}\right] \cdot \int_{-\infty}^{\infty} \int_{-\infty}^{\infty} U[x_0, y_0, z_0] \exp\left[i k \frac{x_0^2 + y_0^2}{2 (z_1 - z_0)}\right] \exp\left[-i k \frac{x_1 x_0 + y_1 y_0}{(z_1 - z_0)}\right] \mathrm{d}x_0 \mathrm{d}y_0. \quad \text{(B.1)}$$

This formula can be nested and also generalized to approximate the propagation in an inhomogeneous medium.

These two features allow the analysis of the transmission X-ray microscope and the confocal transmission X-ray microscope. The numerical analysis for both systems uses similar ideas since the general setup of both is similar. Both use two lenses of which the first one produces the illumination for the sample and the second one images the sample. See also figure B.1. Next, we deal with the details of the imaging process.

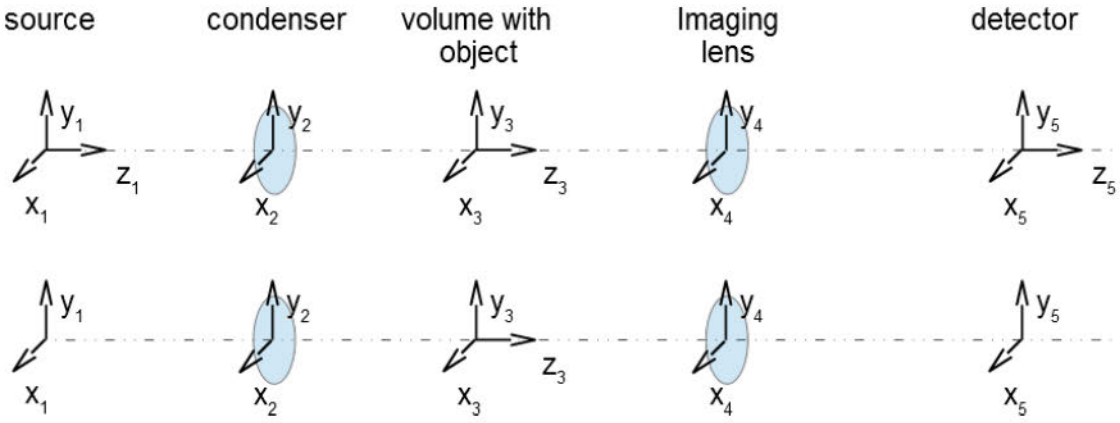

Figure B.1: *Coordinates used for the simulation. The second row shows the simplifications.*

B.1 Theoretical Background of the Simulation

In this section, the imaging process in an X-ray transmission microscope (TXM) is studied. The assumptions include again the paraxial approximation. Like a confocal microscope, the TXM contains a condenser which focuses the incoming radiation onto the sample and the imaging Fresnel zone plate. Although the exact setup in the experiment varies, we assume here that the condenser is essentially an annular lens with relatively low numerical aperture. The imaging Fresnel zone plate is simulated by an ordinary lens. These approximations are sufficiently good for a comparison between TXM and confocal XM. This is due to the fact that the condenser usually produces a hollow cone illumination. All but one order of diffraction of the Fresnel zone plate is therefore suppressed on the detector since the detector is located in the geometric shadow of those orders. Starting again from equation (B.1), the two optics are studied separately.

Firstly, the condenser is considered. Its shape and size in combination with the features of the source of radiation introduce a certain degree of coherence into the imaging process. For the following considerations, the source is assumed to consist of a finite amount of independent point sources. This approximation can be applied to radiation from synchrotrons or plasma based X-ray sources.

Secondly, the imaging Fresnel zone plate is considered. Due to the geometry of most X-ray microscopes, it suffices to assume its imaging properties to be identical to those of an ordinary (refractive) thin lens. The objects studied in an X-ray microscope are typically weakly scattering so that the first Born approximation is usable.

The propagation through the optical system is here split into three segments. The propagation from the source through the condenser to the start face of the

sample and the propagation from the end face of the sample through the imaging lens to the detector can be described by a nesting of free space propagations and modifications by transmission functions that are restricted to a thin plane. Therefore, the Rayleigh-Sommerfeld diffraction integral can be directly applied to these segments. The problematic segment is the propagation through the sample since equation (B.1) is only valid for a homogeneous medium. Since the field propagates essentially in the forward direction, the method presented in the next paragraph is a good approximation.

For this method, the sample is separated into z-slices. The propagation through a slice is separated into a propagation through a homogeneous medium and a perturbation due to the inhomogeneity of the slice. The propagation is done by taking the field at the position before the slice and propagating it in free space to the plane of the second optic. From there, it is back propagated to the end of the slice. The inhomogeneities are assumed to create a perturbation of the resulting field similar to the one a plane wave would experience.

B.1.1 Mathematical Formulation of the Simulation

Let the sample have a z dimension from $z_3^{(min)}$ to $z_3^{(max)}$. The sample is separated into z-slices of thickness Δz_3. A point in the starting face of the n^{th} slice has therefore the form

$$\left(x_3, y_3, z_3^{(min)} + (n-1)\,\Delta z_3\right).$$

The end face of the n^{th} slice contains points of the form

$$\left(x_3, y_3, z_3^{(min)} + n\Delta z_3\right).$$

The ansatz for the homogeneous propagation is to do a forward propagation to the lens in the plane $z_4 = 0$ followed by a back-propagation to the plane $z_3^{(min)} + n\Delta z_3$. The distance between the planes $z_3 = 0$ and $z_4 = 0$ is d_{34}.
The resulting perturbations by the inhomogeneities are approximated by

$$\begin{aligned} T_{z_3^{(min)}+n\Delta z_3}\left[x_3, y_3\right] \;:=\; & \exp\Big[i\,k\,\Big(-\overline{\delta}\left[x_3, y_3, z_3^{(min)} + n\Delta z_3\right] \\ & +i\overline{\beta}\left[x_3, y_3, z_3^{(min)} + n\Delta z_3\right]\Big)\,\Delta z_3\Big], \end{aligned}$$

where $\overline{\delta}$ and $\overline{\beta}$ are the averaged δ and β values of a voxel.
For the numerical implementations, all variables have to be discrete. Let $N_x \times N_y$ be the size of the discrete field U. The discrete FFT based propagators correlate the resolution $(\Delta x_4, \Delta y_4)$ in the z_4 plane to the resolution $\left(\Delta x_3^{(n)}, \Delta y_3^{(n)}\right)$ in the $z_3^{(n)} := z_3^{(min)} + n\Delta z_3$ plane via

$$\begin{aligned}\Delta x_3^{(n)} &= \frac{\lambda\left(z_4 - z_3^{(n)}\right)}{\Delta x_4 \cdot N_x} \\ &= \frac{\lambda\left(z_4 - z_3^{(min)} - n\Delta z_3\right)}{\Delta x_4 \cdot N_x}\end{aligned}$$

and

$$\Delta y_3^{(n)} = \frac{\lambda\left(z_4 - z_3^{(min)} - n\Delta z_3\right)}{\Delta y_4 \cdot N_y}.$$

Therefore, the resolution along the z axis in the sample changes.

Also, the forward propagators used for the simulation factorize the field $U[x_4, y_4, z_4]$ into a fast oscillating diverging wave and a slowly varying rest.

$$U^{(n-1)}[x_4, y_4, z_4] = U_{slow}^{(n-1)}[x_4, y_4, z_4] \cdot \exp\left[i\,k\,\frac{x_4^2 + y_4^2}{2\left(z_4 - z_3^{(n-1)}\right)}\right]$$

The back-propagation step is a bit shorter. Therefore, the slowly oscillating part has to be modified by

$$\begin{aligned}&U_{slow}^{(n)}[x_4, y_4, z_4] \\ &= U_{slow}^{(n-1)}[x_4, y_4, z_4] \cdot \exp\left[i\,k\left(\frac{1}{z_4 - z_3^{(n-1)}} - \frac{1}{z_4 - z_3^{(n)}}\right)\frac{x_4^2 + y_4^2}{2}\right].\end{aligned} \tag{B.2}$$

The resulting back-propagated field is modified by $T_{z_3^{(n)}}$ to approximately include the perturbation due to the inhomogeneity in the optical properties of the slice.

The computation of $T_{z_3^{(n)}}$ from a phantom is also quite intensive on the computational side.

The phantom consists in our case of a set of five tuples. The first three entries contain the position of a dot while the fourth and fifth entry contain the delta and beta values for 510eV respectively 310eV.

$$phantom[n] = (x, y, z, \delta_{510eV} + i\beta_{510eV}, \delta_{310eV} + i\beta_{310eV})$$

Each five tuple represents a small randomly chosen sub volume of the structure of the sample. Let z_3^* be so that the sub-tuple $(x = 0,\ y = 0,\ z = 0)$ of the phantom is located in $(x_3 = 0,\ y_3 = 0,\ z_3 = z_3^*)$. The z-slice from $z_3^{(n-1)}$ to $z_3^{(n)}$includes then all tuples in the phantom which have a third entry between $z_3^{(n-1)} - z_3^* < z \leq z_3^{(n)} - z_3^*$.

For the confocal microscope, the minimal value for $z_3^{(1)}$ depends on the scanning range. Let $z_{scan} = (-m : n) \cdot \Delta z_{scan}$ be the scanning range and $z_{phantom}^{(min)}$, $z_{phantom}^{(max)}$ be respectively the minimal and maximal z component of the phantom. Then, $z_3^{(1)} = -m \cdot \Delta z_{scan} + z_3^* + z_{phantom}^{(min)}$ and the maximal value for $z_3^{(max)}$ results from $z_3^{(max)} = n \cdot \Delta z_{scan} + z_3^* + z_{phantom}^{(max)}$.

The number (N_z) of z-slices is then $\frac{z_3^{(max)} - z_3^{(1)}}{\Delta z_3}$ rounded up.

For the transmission microscope, the limits $z_3^{(1)}$ and $z_3^{(max)}$ depend only on the parameters of the phantom.

$$\begin{aligned} z_3^{(1)} &= z_3^* + z_{phantom}^{(min)} \\ z_3^{(max)} &= z_3^* + z_{phantom}^{(max)} \end{aligned}$$

For sparse objects, it can be convenient to group propagations of empty slices together to reduce the number of Fourier transforms and lighten the computational load.

These z dimensions also influence the minimal size of the discrete field in the plane $z_3^{(1)}$. Due to the numerical aperture (NA) of the lens, the borders of the field contain some erroneous data after the back propagation. To reduce this effect, a sufficiently large padding is included. To estimate the size of the padding, it is assumed that the errors propagate with the same angular spread as the opening angle of the lens. The minimal dimension is

$$d_3^{min} = NA * 2 \left(z_3^{(max)} - z_3^{(min)} + (n + m + 1) \cdot \Delta z_{scan} \right) + FOV. \tag{B.3}$$

For faster computations, it is good to change the way the phantom is stored. If the step sizes Δz_{scan} and Δz_3 are chosen such that Δz_3 divides Δz_{scan}, the phantom can conveniently be stored as a structured array. The indexing of the structured array corresponds then to a Δz_3 binning. This saves computational time since the points for each slice are already in one bin. This is also true for the TXM simulation.

For the confocal system, the use of a structured array allows using the index of the array as a loop controlling variable.

Here, two different types of illumination in the TXM are considered. The former U41 beamline at the Helmholtz Zentrum Berlin used a moving condenser to illuminate the full sample. The direct image of the source is in this setup small in relation to the field of view.

Another example is the TXM at the TU-Berlin (BLIX) which uses a relatively large incoherent source.

In order to approximate the illumination for the second case, a series of illumination profiles is computed from a series of random source profiles. Each resulting

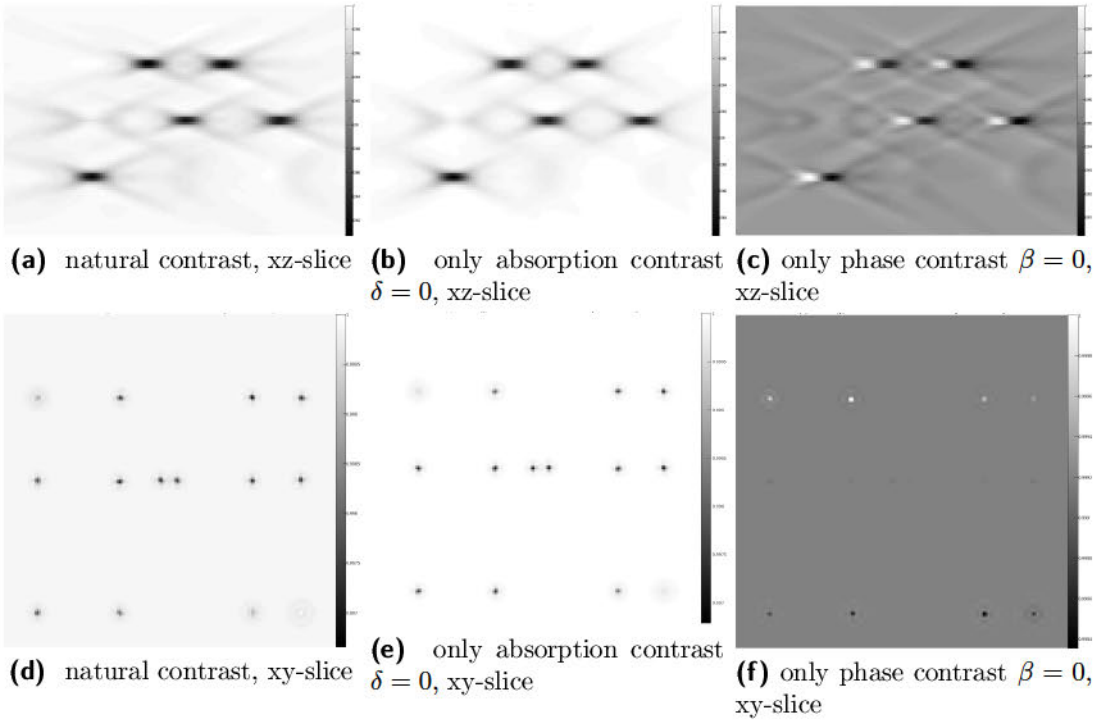

(a) natural contrast, xz-slice **(b)** only absorption contrast $\delta = 0$, xz-slice **(c)** only phase contrast $\beta = 0$, xz-slice

(d) natural contrast, xy-slice **(e)** only absorption contrast $\delta = 0$, xy-slice **(f)** only phase contrast $\beta = 0$, xy-slice

Figure B.2: *The upper row* ***(a-c)*** *of images shows confocal images at* $\lambda = 2.4\,nm$ *of some 10nm spheres with the density of cellular membranes. The effects of absorption and phase shift are quite different, and are shown in (b) and (c). Due to the asymmetry in the resolution, the images are squeezed in the direction of the optical axis by a factor of three. The field of view is* $400\,nm$ *high and* $1.8\,\mu m$ *long. In the second row* ***(d-f)****, images of* $3\,nm$ *spheres are shown. The field of view is* $400\,nm \times 400\,nm$*. The central row of dots are in the focal plane, while in the upper and lower row the dots are situated in planes* $10\,nm$*,* $20\,nm$*,* $40\,nm$ *and* $80\,nm$ *away from the focal plane.*
In both cases, the two lenses have matching numerical apertures of $NA \approx 0.21$*.*

illumination is propagated through the sample and the resulting intensities are accumulated in the plane of the detector.

In order to approximate the illumination for the first case, a series of illumination profiles is computed from a series of random condenser positions. Each resulting illumination is propagated through the sample and the resulting intensities are accumulated in the plane of the detector.

Again, the fact that the first two propagation distances do not satisfy the lens law leads to a multiplicative factor.

The random condenser positions are simulated by propagating an off-axis Gaus-

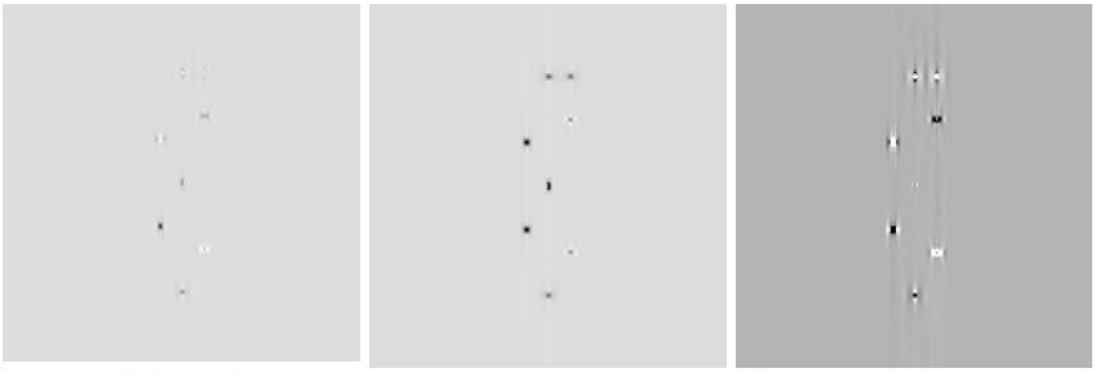

(a) xy cut
natural contrast

(b) xy cut
only absorption contrast $\delta = 0$

(c) xy cut
only phase contrast $\beta = 0$

Figure B.3: *TXM based tomographic reconstruction of a similar phantom as in B.2 a-c. The phantom consists of some 10nm spheres. The lens has a numerical aperture of $NA \approx 0.21$. The effects of absorption and phase shift are quite different and are shown in* ***(b)*** *and* ***(c)****.*

sian beam profile through the lens which contains also a small shift, i.e., if the Gaussian beam in plane z_1 is centered at $x_1 = \tilde{x}$, $y_1 = \tilde{y}$, then the condenser is also centered at $x_2 = \tilde{x}$, $y_2 = \tilde{y}$. Also, the image is centered at $x_3 = \tilde{x}$, $y_3 = \tilde{y}$. Therefore, the resulting pattern can be approximated by a laterally shifted image of a centered source at $(x_1, y_1) = (0, 0)$. Again, multiple sources can be put into one run and different runs change the position of the sources and their relative phase.

B.2 Implementation

B.2.1 Implementation of the Confocal Microscopy Simulation

The following matlab code was used to generate the raw data for the image in figure B.2. The implementation follows the theoretical description in section §B.1. Some of the sub routines used are not included but have already been presented in appendix A.

Commented Program

The following parameters are used.

lambda, the wavelength, here $2.4nm$.

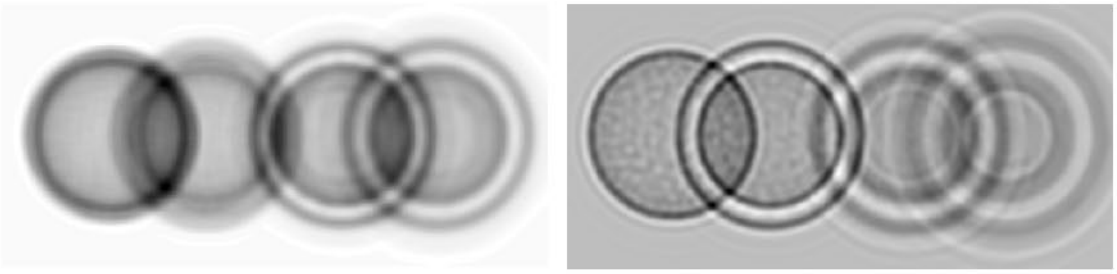

(a) Confocal STXM image xy **(b)** Partially coherent TXM image xy

Figure B.4: *Comparison of the imaging performance of a confocal STXM and a partially coherent TXM. The images show four spheres. Each sphere has a diameter of 300 nm and simulates a 4 nm thick cellular membrane. They are separated in depth by 300 nm. (See also figure 5.4)*
For the confocal simulation ***(a)*** *and for the TXM simulation* ***(b)****, a 10 nm FZP objective in combination with a 40 nm FZP condenser was used.*

Vol_per_dot is a parameter for the generation of the phantom. It defines the volume that is represented by one point of the phantom.

do1 do2 do3 do4 are the distances respectively between the source, condenser, in focus plane, FZP objective and the detector.

r12_min r12_max r34_min r34_max are the outer and inner radii of the optics.

xs ys zs are arrays that define the points that are scanned.

dxs dys dzs are the distances between neighboring points.
For Example zs=-30:30 and dzs=30e-9 yields a z scanning range of -900nm to 900 nm in 30 nm steps.

dz is the z resolution used for the full coherent propagation through the sample.

The following variables are used.

scanedImage is used to store the intensities for each position of the scan. Thus it represents the confocal image of the sample.

Raw_Phantom is the randomized representation of the phantom. The first three entries contain the position and the fourth and fifth the optical density of each "dot".

Lines 1 to 2 contain the function name and a small explanation of the aim of the program.

Lines 3 to 31 contain definitions of parameters and initialization of deduced constants or variables.
Lines 32 to 33 and lines 114 to 141 initialize the phantom.
Lines 34 to 38 initialize deduced constants or variables.
Lines 39 to 48 sort the phantom into bins for faster numerical evaluation in the propagation loop.
Lines 49 to 70 initialize the parameters for the field of view. This includes a padding which reduces the artifacts introduced at the border as described in equation (B.3).
Lines 71 to 74 control the loop over all points in the confocal image.
Lines 75 to 82 generate the inbound coherent illumination
Lines 83 and 103 control the propagation loop for one point in the confocal image.
Lines 84 to 93 propagate the current scalar field to the end of the current slice. For computational efficiency, empty slices are grouped together. It is the discretized version of equation (B.2).
Lines 94 to 102 compute the optical density of the phantom and allow for the modification of the field introduced by the phantom.
Line 104 propagates the field to the second optic.
Lines 105 to 107 modify the field by the transmission function of the second optic.
Line 108 propagates the field to the detector.
Line 109 stores the resulting signal in the array "scanedImage".

```
1. function Confocl_microscope
2. % simulates the confocal microscope
3. %% Parameters
4. lambda=2.4e-9; % wavelength
5. % parameters of the phantom
6. Vol_per_dot=8e-27; % Volume per dot
7. % parameters of the optics:
8. do1=9.67522;
9. % Distance to focus [m]
10. do2=371E-6/2;
11. % Diameter of first optic [m]
12. r12_min=40E-6/4;
13. r12_max=40E-6;
```

```
14. % Distance second optic to CCD (do4) [m] and focal length
15. f2=370E-6/2; % focal length
16. do4=1.9;
17. % Diameter of second optic [m]
18. r34_min=0;%40E-6/2;
19. r34_max=40E-6;
20. % scanning range of the confocal microscope
    (a constant step size is assumed!)
21. xs=-20:20;
22. ys=0:0;
23. zs=-30:30;
24. dxs=10e-9;
25. dys=20e-9;
26. dzs=30e-9;
27. % scanning resolution in the simulation along the z direction
    (Attention, other resolutions follow from the other parameters!)
28. dz=dzs/4;
29. %% Initializing
30. k=2*pi/lambda;
31. scanedImage=zeros(size(xs,2),size(ys,2),size(zs,2));
32. %% Initializing the phantom
33. [Raw_Phantom,Vol_per_dot]=DOTGENERATOR_V2(Vol_per_dot);
34. zmin=min(Raw_Phantom(3,:));
35. zmax=max(Raw_Phantom(3,:));
36. %% Changing it to an adapted struc-array:
37. mycount=0;
38. DOTS.DOTS=[]
39. for my_z=floor(zmin/dz):floor(zmax/dz) % Sorting the dots into fitting bins
```

```
40. mycount=mycount+1;
41. DOTS(mycount).DOTS=...Raw_Phantom(...
    :,find(and(Raw_Phantom(3,:)>=dz*my_z,Raw_Phantom(3,:)<(dz*(my_z)+dz))));
42. DOTS(mycount).z=my_z*dz;
43. if isempty( DOTS(mycount).DOTS)
44.  DOTS(mycount).isfull=0;
45. else
46.  DOTS(mycount).isfull=1;
47. end
48. end
49. %% Initializing the FOV
50. f1=do1*do2/(do1+do2);
51. do3=do4*f2/(do4-f2);
52. % Computing the minimal size of U that can be used for the simulation
53. NA_max=max(r12_max/do2,r34_max/do3); % Maximum of the two numerical apertures
54. min_dim=NA_max*2*(zmax-zmin+(zs(end)-zs(1))*dzs)+...
    max((xs(end)-xs(1))*dxs,(ys(end)-ys(1))*dys); %Minimal dimensions of the starting
    field
55. myz_start=do2+zmin+dzs*min(zs);
56. d2=lambda*myz_start/(min_dim);
57. N=2*ceil((1.2*r12_max/d2));
58. % resulting resolution in plane 3
59. d3=lambda*myz_start/(d2*N);
60. N1=N;
61. N2=N;
62. d2_1=d2;
63. d2_2=d2;
64. UN1=-(ceil(N1/2+0.5)-1);
65. ON1=(floor(N1/2+0.5)-1);
```

```
66. UN2=-(ceil(N2/2+0.5)-1);
67. ON2=(floor(N2/2+0.5)-1);
68. V1=(UN1:ON1);
69. V2=(UN2:ON2);
70. [Mesh1,Mesh2]=meshgrid(V1,V2);
71. %% Propagation through the sliced medium
72. for my_ind_z=1:size(zs,2)
73. for my_ind_x=1:size(xs,2)
74. for my_ind_y=1:size(ys,2)
75. % propagation from start to start of phantom
76. U=exp(-1i*k*((d2_1*Mesh1').^2+(d2_2*Mesh2').^2)...
    .*(1/(2*(do2))-1/(2*myz_start)));
77. U(((d2_1*Mesh1').^2+(d2_2*Mesh2').^2)<r12_min^2)=0;
78. U(((d2_1*Mesh1').^2+(d2_2*Mesh2').^2)>r12_max^2)=0;
79. [U,d3_1,d3_2]=C20131217_FFTFresnel_slow(U,do2+do3-myz_start,lambda,d2_1,d2_2);
80. z_last=myz_start;
81. % Header:  (converging)
82. % [Uz,dz1,dz2]=C20131217_FFTFresnel_slow(U0,z,lambda,d1,d2)
83. for my_z_ind=1:size(DOTS,2)
84. % computing the current slice
85. if DOTS(my_z_ind).isfull==1
86. [U,d4_1,d4_2]=C20131217_FFTFresnel_slow_small_source(...
    U,do2+do3-z_last,lambda,d3_1,d3_2);
87. % Header:  (diverging)
88. % [Uz,dz1,dz2]=C20131217_FFTFresnel_slow_small_source(U0,z,lambda,d1,d2)
89. U=U.*exp(1i*k*((d4_1*Mesh1').^2+(d4_2*Mesh2').^2).*(1/(2*(do2+do3-z_last))...
    -1/(2*(do2+do3-(do2+zs(my_ind_z)*dzs+DOTS(my_z_ind).z)))));
90. z_last=do2+zs(my_ind_z)*dzs+DOTS(my_z_ind).z;
```

```
91. [U,d3_1,d3_2]=C20131217_IFFTFresnel_slow_small_source(...
    U,do2+do3-(do2+zs(my_ind_z)*dzs+DOTS(my_z_ind).z),lambda,d4_1,d4_2);

92. % Header:

93. % [U0,d1,d2]=C20131217_IFFTFresnel_slow_small_source(Uz,z,lambda,dz1,dz2)

94. zwDOTS=DOTS(my_z_ind).DOTS;

95. % Removing the points outside the FOV

96. zwDOTS=zwDOTS(:,and(round((zwDOTS(1,:)+xs(my_ind_x)*dxs)/d3_1+N1/2+1)>0...
    ,round((zwDOTS(1,:)+xs(my_ind_x)*dxs)/d3_1)<N1/2));

97. zwDOTS=zwDOTS(:,and(round((zwDOTS(2,:)+ys(my_ind_y)*dys)/d3_2+N2/2+1)>0...
    ,round((zwDOTS(2,:)+ys(my_ind_y)*dys)/d3_2)<N2/2));

98. T=accumarray(...
    {[1 N1 (round((zwDOTS(1,:)+xs(my_ind_x)*dxs)/d3_1)+N1/2+1)],...
    [1 N2 round((zwDOTS(2,:)+ys(my_ind_y)*dys)/d3_2)+N2/2+1]},...
    [0 0 zwDOTS(4,:)]);

99. Tvol=accumarray(...
    {[1 N1 (round((zwDOTS(1,:)+xs(my_ind_x)*dxs)/d3_1)+N1/2+1)],...
    [1 N2 round((zwDOTS(2,:)+ys(my_ind_y)*dys)/d3_2)+N2/2+1]},...
    [0 0 ones(size(zwDOTS(4,:)))]);

100. T=(Vol_per_dot/(d3_1*d3_2*dz))*T./(max(1,Vol_per_dot*Tvol/(d3_1*d3_2*dz)));

101. U=U.*exp(1i*k*T*dz);

102. end

103. end


104. [U,d4_1,d4_2]=C20131217_FFTFresnel_slow_small_source(...
     U,do2+do3-z_last,lambda,d3_1,d3_2);

105. U=U.*exp(1i*k*((d4_1*Mesh1').^2+(d4_2*Mesh2').^2)...
     .*(1/(2*(do2+do3-z_last))-1/(2*do3)));

106. U(((d4_1*Mesh1').^2+(d4_2*Mesh2').^2)<r34_min^2)=0;

107. U(((d4_1*Mesh1').^2+(d4_2*Mesh2').^2)>r34_max^2)=0;

108. [U5,d5_1,d5_2]=C20131217_FFTFresnel_slow(U,do4,lambda,d4_1,d4_2);

109. scanedImage(my_ind_x,my_ind_y,my_ind_z)=
     sum(sum(abs(U5(end/2+1+(-2:2),end/2+1+(-2:2))).^2));

110. end
```

```
111. end
112. end
113. end
114. function [DOTS,Vdis]=DOTGENERATOR_V2(Vdis)
115. % Generates Point object (DOTS) [size(DOTS)=5xN] 1=x,2=y,3=z,4=optical
116. % properties at 520eV 5=optical properties at 310eV
117. Vdis=Vdis;%dx*dy*dz/16; %"Volume" of one dot
118. DOTS=[];
119. %% Generating a sphere of radius rz and with middle hsmx,hsmy,hsmz
120. %%%%%%%%%%%%%%%%%%%%%%%%%%%%
121. % Sets of hollow spheres %
122. %%%%%%%%%%%%%%%%%%%%%%%%%%%%
123. % Center
124. hsmx=[0 100e-9 0 -100e-9 -100e-9 ];
125. hsmy=[ 0 0 15e-9 0 0];
126. hsmz=[-500e-9 500e-9 500e-9 200e-9 -200e-9];
127. %outer Radius
128. hsrco=[10 10 10 10 10]*10^-9;
129. %inner Radius
130. hsrci=0*hsrco;% optional
131. % optical density (membranes)
132. hsdoc=(-0.000909493479+ 1i*0.000211989463)*ones(size(hsrco));
133. hsdoc310=(-0.00186587463+ 1i*0.00114491396)*ones(size(hsrco));
134. Ndis=ceil(4/3*pi*(hsrco.^3-hsrci.^3)./Vdis);
135. mysphere=@(r,vphi,vpsi,hsmx,hsmy,hsmz,hsdoc,hsdoc310) [...
     r.*cos(vphi).*cos(vpsi)+hsmx;...
     r.*(sin(vphi).*cos(vpsi))+hsmy;...
     r.*(sin(vpsi))+hsmz; hsdoc*ones(size(vphi));hsdoc310*ones(size(vphi))];
136. % adding the sphere to the dots:
```

```
137. for myi=1:size(hsmx,2)
138. DOTS=[DOTS mysphere(...
     (((hsrco(myi)^3-hsrci(myi)^3).*rand(1,Ndis(myi)))+hsrci(myi)^3).^(1/3),...
     2*pi*rand(1,Ndis(myi)),asin(2*rand(1,Ndis(myi))-1),...
     hsmx(myi),hsmy(myi),hsmz(myi),hsdoc(myi),hsdoc310(myi))];
139. end
140. end
```

B.2.2 Implementation of the Incoherent Microscopy Simulation

The following matlab code was used to generate the raw data for the incoherent examples. The implementation is based on the incoherent point spread function of a regular refractive lens. This approximation is reasonable, since the number of zones of the Fresnel zone plate is large (>100). A numerical comparison between the focal spot of the Fresnel zone plate and its refractive counterpart showed very little difference. The comparison was done by evaluating a formula given in [5] and a formula given in [30].

The main steps of the program have already been described in section 4.2.1.

Algorithm

```
1. function Incoherent_TXM
2. %% Initializing Phantom:
3. % x ray
4. z=620;% length
5. y=620;% height
6. x=620;% width
7. % Resolution [m]
8. % x-ray
9. dz=5*10^-9;
10. dy=5*10^-9;
11. dx=5*10^-9;
12. Vol_per_dot=8e-27;
```

```
13. lambda1=2.4*10.^-9;% wavelength x-ray
14. k1=2*pi ./lambda1;
15. % Tomogram properties
16. myangle=-90:90;
17. %% Start PSF1
18. k=k1;
19. lambda=lambda1;
20. f=370E-6;
21. do4=1.9;
22. do3=do4*f/(do4-f);
23. raussen=(44.391)*10.^-6;
24. rinnen=0;
25. myInt=@(r,z,x1,y1,x3,y3) exp(-1./2.*1i.*k.*r.^2.*z./(do3.*(do3-z))).*2.*pi.*r.
26. *besselj(0,...
    (k.*r.*sqrt((-x1-(x3*(do3-z))/do4).^2 +(-y1-(y3*(do3-z))/do4).^2 )./(do3-z)));
27. [X3,Y3]=meshgrid((-100:1:100)*dy,(-100:1:100)*dx);
28. figure(2)
29. PSF1=[]
30. for myzdist=-floor(z/2):1:ceil(z/2)
31. disp(myzdist)
32. %subplot(9,1,5+myzdist)
33. q=integral(@(r) myInt(r,myzdist*dz,0,0,X3.*(do4/(do3-myzdist*dz)),...
    Y3.*(do4/(do3-myzdist*dz))),rinnen,raussen,'ArrayValued',true);%
34. % plot(X3(101,:),abs(q(101,:)).^2,'color',[(ceil(z/(2))+myzdist)/(2*ceil(z/(2)))
    (ceil(z/(2))-myzdist)/(2*ceil(z/(2))) 0.5])
35. % title(num2str(myzdist))
36. % drawnow
37. if max(size(PSF1))<1
38. PSF1=zeros(1,size(q,1),size(q,2));
```

```
39. PSF1(1,:,:)=abs(q).^2;
40. myind=1;
41. else
42. myind=myind+1;
43. PSF1(myind,:,:)=abs(q).^2;
44. end
45. end
46. PSF1=PSF1/sum(sum(sum(PSF1)));
47. [DOTS,~]=DOTGENERATOR(Vol_per_dot);
48. DOTS(1,:)=DOTS(1,:)+x*dx/2;
49. DOTS(2,:)=DOTS(2,:)+y*dy/2;
50. DOTS(3,:)=DOTS(3,:)+z*dz/2;
51. for myang=1:size(myangle,2)% start tomographic projections
52. disp(myangle(myang))
53. projA=zeros(x,y);
54. %% Rotationsmatrix+Translation x=> y=A*x+t und dx=> dy=A*dy
55. % a1 b1 c1 t1
56. % a2 b2 c2 t2
57. % a3 b3 c3 t3
58. % 0 0 0 1
59. Rot=@(phi,psi,t1,t2,t3) [cos(phi),sin(phi) 0 0;-sin(phi),cos(phi) 0 0 ;...
    0 0 1 0; 0 0 0 1]*[1,0 0 0;0,cos(psi),sin(psi), 0 ;0 -sin(psi) cos(psi) 0; 0
    0 0 1]...
    *[1 0 0 t1;0 1 0 t2;0 0 1 t3;0 0 0 1];
60. centerofrot=[0.5; 0.5; 0.5; 0].*[x; y; z; 0]; %(defines the center of rotation)
61. translationv=[0 0 0];% (in [nm])
62. rotscaler=[dx; dy; dz; 1];
63. rotationv=[0 2*pi*myangle(myang)/360 ]; % in [rad]
```

```
64. fixpM=((Rot(rotationv(1),rotationv(2),translationv(1),translationv(2),...
    translationv(3))*(-centerofrot.*rotscaler)))+centerofrot.*rotscaler;
65. vDOTS=DOTS;
66. vcx=DOTS(1,:);
67. vcy=DOTS(2,:);
68. vcz=DOTS(3,:);
69. vc= [vcx;vcy;vcz;ones(size(vcz))];
70. vc=((Rot(rotationv(1),rotationv(2),translationv(1),translationv(2),...
    translationv(3))*vc)+fixpM*ones(1,size(vc,2)));
71. vDOTS(1:3,:)=vc(1:3,:);
72. vDOTS(1,:)=ceil(vDOTS(1,:)/dx);
73. vDOTS(2,:)=ceil(vDOTS(2,:)/dy);
74. vDOTS(3,:)=ceil(vDOTS(3,:)/dz);
75. zDOTS=find(and(vDOTS(1,:)>0,vDOTS(1,:)<(x+1)));
76. vDOTS=vDOTS(:,zDOTS);
77. zDOTS=find(and(vDOTS(2,:)>0,vDOTS(2,:)<(y+1)));
78. bvDOTS=vDOTS(:,zDOTS);
79. %%%%%%%%%%%%%%%%%%%%%%%%%%%%%%%%%%%%%%%%%%%%
80. % SIMULATING THE ABSORPTION IMAGE OF THE ROTATED OBJECT
81. %%%%%%%%%%%%%%%%%%%%%%%%%%%%%%%%%%%%%%%%%%%%
82. for my_big_z=1:100:z %coarse z-steps
83. zDOTS=find(and(bvDOTS(3,:)>my_big_z-1,bvDOTS(3,:)<my_big_z+100));
84. vDOTS=bvDOTS(:,zDOTS);
85. for myz=my_big_z:min(z,my_big_z+99)% start fine steps
86. try
87. mySlice=ones(size(projA));
88. zDOTS=find(vDOTS(3,:)==myz);
89. mySlice=mySlice+(accumarray({[1 y vDOTS(2,zDOTS)],[1 x vDOTS(1,zDOTS)]},...
    [0 0 vDOTS(4,zDOTS)]))/(Vol_per_dot/(dx*dy*dz));
```

```
90. projA=projA+mySlice;
91. catch err
92. 'error'
93. rethrow(err);
94. end
95. %%%%%%%%%%%%%%%%%%%%%%%%
96. % DO IMAGING IN TXM MODE %
97. %%%%%%%%%%%%%%%%%%%%%%%%
98. if or(any(zDOTS~=0),or(myz==z,myz==1))
99. try
100. if myz==1
101. Bild=zeros(size(mySlice));
102. multBild=ones(size(Bild));
103. NBild=Bild; % Stores flatimage
104. mumean=mean(mean(mySlice));
105. Bild=Bild+Falter(-1+real(exp((1i*2*pi*dz/lambda1)*1i*imag(mySlice))).^2,...
     abs(squeeze(PSF1(myz,:,:))));
106. mygrSlice=mumean*ones(size(mySlice)+size(squeeze(PSF1(myz,:,:))));
107. mygrSlice(floor(size(PSF1,2)/2)+(1:size(mySlice,1)),...
     floor(size(PSF1,3)/2)+(1:size(mySlice,1)))=mySlice;
108. mygrSlice=Falter(real(exp((1i*2*pi*dz/lambda1)*1i*imag(mygrSlice))).^2,...
     (size(PSF1,2)+size(mygrSlice,1))*(size(PSF1,3)+size(mygrSlice,2))*...
     abs(squeeze(PSF1(myz,:,:)))/(sum(sum(abs(squeeze(PSF1(myz,:,:)))))));
109. multBild=multBild...
     .*mygrSlice(floor(size(PSF1,2)/2)+(1:size(mySlice,1)),...
     floor(size(PSF1,3)/2)+(1:size(mySlice,1)));
110. NBild=NBild+Falter(ones(size(NBild)),abs(squeeze(PSF1(myz,:,:))))/size(PSF1,1);
111. else
112. mygrSlice(floor(size(PSF1,2)/2)+(1:size(mySlice,1)),...
     floor(size(PSF1,3)/2)+(1:size(mySlice,1)))=mySlice;
```

```
113. Bild=Bild+Falter(-1+real(exp((1i*2*pi*dz/lambda1)*1i*imag(mySlice))).^2,...
     abs(squeeze(PSF1(myz,:,:))));

114. mygrSlice=Falter(real(exp((1i*2*pi*dz/lambda1)*1i*imag(mygrSlice))).^2,...
     (size(PSF1,2)+size(mygrSlice,1))*(size(PSF1,3)+size(mygrSlice,2))*...
     abs(squeeze(PSF1(myz,:,:)))/(sum(sum(abs(squeeze(PSF1(myz,:,:)))))));

115. multBild=multBild.*mygrSlice(floor(size(PSF1,2)/2)+(1:size(mySlice,1)),...
     floor(size(PSF1,3)/2)+(1:size(mySlice,1)));

116. NBild=NBild+Falter(ones(size(NBild)),abs(squeeze(PSF1(myz,:,:))))/size(PSF1,1);

117. end

118. if myz==z

119. if myang==1

120. %initializing

121. Bildser=zeros(size(mySlice,1),size(mySlice,2),size(myangle,2));

122. Bildser2=Bildser;

123. Bildsermult=Bildser;

124. Bildproj=Bildser;

125. end

126. Bildser(:,:,myang)=(NBild+Bild)./NBild;

127. Bildsermult(:,:,myang)=multBild;

128. Bildproj(:,:,myang)=real(exp((1i*2*pi*dz/lambda1)*1i*imag(projA))).^2;

129. end

130. catch err

131. 'error'

132. rethrow(err)

133. end

134. end

135. end % singel z-step

136. end % coarse z-steps

137. end
```

```
%% Results:
Result_of_additive_approach=(Bildser/(max(Bildser(:))));
Result_of_multiplicative_approach=single(Bildsermult/(max(Bildsermult(:))));
Result_of_projection=single( Bildproj/(max( Bildproj(:))));
end

function K=Falter(A,B)
% fft-convolution operator of size:  size(A)
as=size(A);
if size(B,1)>2*size(A,1)
mycut=floor((size(B,1)-2*size(A,1))/2);
B=B((mycut+1):(end-mycut),:);
end
if size(B,2)>2*size(A,2)
mycut=floor((size(B,2)-2*size(A,2))/2);
B=B(:,(mycut+1):(end-mycut));
end
bs=size(B);
a1=zeros((as+bs));
b1=zeros((as+bs));
a1(1:as(1),1:as(2))=A;
b1(1:bs(1),1:bs(2))=B;
a1=ifft2(ifftshift(fftshift(fft2(b1)).*fftshift(fft2(a1))))/...
((as(1)+bs(1))*(as(2)+bs(2)));
K=a1((floor(bs(1)/2)+1):(floor(bs(1)/2)+as(1)),...
(floor(bs(2)/2)+1):(floor(bs(2)/2)+as(2)));
end
```

Examples

In figure B.5 the effect of under sampling and defocus on the tomographic reconstruction is studied. Figure 4.7 shows that the incoherent simulation matches key features of the experimental data but ignores some effects like the asymmetry of the defocusing effects.

B.2.3 Implementation of the Partially Coherent Microscopy Simulation

The following matlab code was used to generate the raw data for the image in figure B.3. The implementation is similar to the one for the confocal microscope. It follows the theoretical description in section §B.1. Again, some of the sub routines used are not included but have already been presented in appendix A or are identical to the ones in section B.2.1.

Algorithm

```
1. function partial_coheren_TXM
2. % simulates the transmission microscope
3. %% Parameters
4. lambda=2.4e-9; % wavelength
5. % dimensions of the phantom
6. Vol_per_dot=8e-27; % Volume per dot
7. % parameters of the optics:
8. r12_min=40E-6/8;
9. r12_max=40E-6/2;
10. f1=370E-6/2; % used to be f
11. do1=(1.5)*f1;
12. do2=3*f1;
13. % Diameter of first optic [m]
14. r12_min=40E-6/4;
15. r12_max=40E-6;
16. % Distance to second optic (do3) and second optic to CCD (do4) [m]
```

```
17. f2=370E-6/2; % used to be f
18. do4=1.9;
19. % Diameter of second optic [m]
20. r34_min=0;%40E-6/2;
21. r34_max=40E-6;
22. % FOV of the transmission microscope
23. x_FOV=1600e-9;
24. y_FOV=1600e-9;
25. dz=(30e-9)/4;
26. % covered angles
27. myangle=-90:90;
28. %% Initalizing
29. k=2*pi/lambda;
30. %% Initializing the phantom
31. [Raw_Phantom,Vol_per_dot]=DOTGENERATOR_V2(Vol_per_dot);
32. H2Odoc=(-0.000511537655+1i*2.0818954E-05);
33. for myang=1:size(myangle,2)
34. New_Phantom=Raw_Phantom;
35. disp(myangle(myang))
36. %% Rotating the phantom
37. Rot=@(phi,psi,t1,t2,t3) [cos(phi),sin(phi) 0 0;-sin(phi),cos(phi) 0 0 ;0 0 1
    0; 0 0 0 1]...
    *[1,0 0 0;0,cos(psi),sin(psi), 0 ;0 -sin(psi) cos(psi) 0; 0 0 0 1]*[1 0 0 t1;0
    1 0 t2;0 0 1 t3;0 0 0 1];
38. centerofrot=[0; 0; 0; 0];
39. translationv=[0 0 0];% (in [nm])
40. rotscaler=[1;1;1;1];%[dx; dy; dz; 1];
41. rotationv=[0 2*pi*myangle(myang)/360 ]; % in [rad]
```

```
fixpM=((Rot(rotationv(1),rotationv(2),translationv(1),translationv(2),...
translationv(3))*(-centerofrot.*rotscaler)))+centerofrot.*rotscaler;
vcx=New_Phantom(1,:);
vcy=New_Phantom(2,:);
vcz=New_Phantom(3,:);
vc= [vcx;vcy;vcz;ones(size(vcz))];
vc=((Rot(rotationv(1),rotationv(2),translationv(1),translationv(2),...
translationv(3))*vc)+fixpM*ones(1,size(vc,2)));
New_Phantom(1:3,:)=vc(1:3,:);
%% Changing it to an adapted struc array:
zmin=min(New_Phantom(3,:));
zmax=max(New_Phantom(3,:));
mycount=0;
try
clear ('DOTS')
catch
end
DOTS.DOTS=[];
for my_z=floor(zmin/dz):floor(zmax/dz) % Sorting the DOTS into fitting bins
mycount=mycount+1;
DOTS(mycount).DOTS=New_Phantom(:,find(and(New_Phantom(3,:)>=dz*my_z,...
New_Phantom(3,:)<(dz*(my_z)+dz))));
DOTS(mycount).z=my_z*dz;
if isempty( DOTS(mycount).DOTS)
DOTS(mycount).isfull=0;
else
DOTS(mycount).isfull=1;
end
end
```

```
68. if myang==1
69. %% Initializing the illumination
70. f1=do1*do2/(do1+do2);
71. do3=do4*f2/(do4-f2);
72. % Computing the minimal size of U that can be used for the simulation
73. NA_max=max(r12_max/do2,r34_max/do3); % Maximum of the two numerical apertures
74. min_dim=NA_max*2*(zmax-zmin)+max(x_FOV,y_FOV); %Minimal dimensions of the starting
    field
75. myz_start=do2+zmin;
76. d2=lambda*myz_start/(min_dim);
77. N=2*ceil((2*r12_max/d2));
78. % resulting resolution in the planes 3 and 1
79. d1=lambda*do1/(N*d2);
80. d1_1=d1;
81. d1_2=d1;
82. d3=lambda*myz_start/(d2*N);
83. % Generating the inbound wavefront
84. N1=N;
85. N2=N;
86. d2_1=d2;
87. d2_2=d2;
88. UN1=-(ceil(N1/2+0.5)-1);
89. ON1=(floor(N1/2+0.5)-1);
90. UN2=-(ceil(N2/2+0.5)-1);
91. ON2=(floor(N2/2+0.5)-1);
92. V1=(UN1:ON1);
93. V2=(UN2:ON2);
94. [Mesh1,Mesh2]=meshgrid(V1,V2);
```

```
95. end
96. Image_on_ccd=[];
97. Image_on_ccd_sans_obj=[];
98. %% Propagation through the sliced medium
99. tic
100. Ubar=0;
101. U=exp(-((d1_1*Mesh1').^2+(d1_2*Mesh2').^2).*(1/(do1/do2*(x_FOV/2*y_FOV/2))));
102. projA=ones(size(U));
103. tic
104. for my_num_of_illum=1:1000
105. U=exp(-((d1_1*Mesh1').^2+(d1_2*Mesh2').^2).*(1/(do1/do2*(x_FOV/2*y_FOV/2))));
106. U=(U/8>rand(size(U))).*exp(1i*pi*2*rand(size(U)));
107. Ubar=U+Ubar;
108. [U,d2_1,d2_2]=C20131217_FFTFresnel_slow_small_source(U,do1,lambda,d1_1,d1_2);
109. U=U.*exp(-1i*k*((d2_1*Mesh1').^2+(d2_2*Mesh2').^2).*...
     (1/(2*(do2))-1/(2*myz_start)));
110. U(((d2_1*Mesh1').^2+(d2_2*Mesh2').^2)<r12_min^2)=0;
111. U(((d2_1*Mesh1').^2+(d2_2*Mesh2').^2)>r12_max^2)=0;
112. [U,d3_1,d3_2]=C20131217_FFTFresnel_slow(U,myz_start,lambda,d2_1,d2_2);
113. % Header:  (converging)
114. z_last=myz_start;
115. for my_z_ind=1:size(DOTS,2)
116. if my_z_ind==1
117. % normalizes the illumination
118. [Un,d4_1,d4_2]=C20131217_FFTFresnel_slow_small_source(U,...
     do2+do3-z_last,lambda,d3_1,d3_2);
119. Un=Un.*exp(1i*k*((d4_1*Mesh1').^2+(d4_2*Mesh2').^2).*...
     (1/(2*(do2+do3-z_last))-1/(2*do3)));
120. Un(((d4_1*Mesh1').^2+(d4_2*Mesh2').^2)<r34_min^2)=0;
```

```
121. Un(((d4_1*Mesh1').^2+(d4_2*Mesh2').^2)>r34_max^2)=0;

122. [Un,d5_1,d5_2]=C20131217_FFTFresnel_slow(Un,do4,lambda,d4_1,d4_2);

123. end

124. % computing the current slice

125. if or(DOTS(my_z_ind).isfull==1,DOTS(min(size(DOTS,2),my_z_ind+1)).isfull==1)

126. [U,d4_1,d4_2]=C20131217_FFTFresnel_slow_small_source(U,...
     do2+do3-z_last,lambda,d3_1,d3_2);

127. % Header:  (diverging)

128. % [Uz,dz1,dz2]=C20131217_FFTFresnel_slow_small_source(U0,z,lambda,d1,d2)

129. U=U.*exp(1i*k*((d4_1*Mesh1').^2+(d4_2*Mesh2').^2)...
     .*(1/(2*(do2+do3-z_last))-1/(2*(do2+do3-(do2+DOTS(my_z_ind).z)))));

130. z_last=do2+DOTS(my_z_ind).z;

131. [U,d3_1,d3_2]=C20131217_IFFTFresnel_slow_small_source(U,...
     do2+do3-(do2+DOTS(my_z_ind).z),lambda,d4_1,d4_2);

132. % Header:

133. % [U0,d1,d2]=C20131217_IFFTFresnel_slow_small_source(Uz,z,lambda,dz1,dz2)

134. zwDOTS=DOTS(my_z_ind).DOTS;

135. % Removing the points outside the FOV

136. zwDOTS=zwDOTS(:,and(round((zwDOTS(1,:))/d3_1+N1/2+1)>0,...
     round((zwDOTS(1,:))/d3_1)<N1/2));

137. zwDOTS=zwDOTS(:,and(round((zwDOTS(2,:))/d3_2+N2/2+1)>0,...
     round((zwDOTS(2,:))/d3_2)<N2/2));

138. try

139. T=accumarray(...

140. {[1 N1 (round((zwDOTS(1,:))/d3_1)+N1/2+1)],...

141. [1 N2 round((zwDOTS(2,:))/d3_2)+N2/2+1]},...

142. [0 0 zwDOTS(4,:)]);

143. Tvol=accumarray(...

144. {[1 N1 (round((zwDOTS(1,:))/d3_1)+N1/2+1)],...
```

```
145. [1 N2 round((zwDOTS(2,:))/d3_2)+N2/2+1]},...
146. [0 0 ones(size(zwDOTS(4,:)))]);
147. T=(Vol_per_dot/(d3_1*d3_2*dz))*T./(max(1,Vol_per_dot*Tvol/(d3_1*d3_2*dz)));
148. catch
149. 'error'
150. end
151. U=U.*exp(1i*k*T*dz);
152. projA=real(projA.*abs(exp(1i*k*T*dz)));
153. end
154. end
155. [U,d4_1,d4_2]=...
     C20131217_FFTFresnel_slow_small_source(U,do2+do3-z_last,lambda,d3_1,d3_2);
156. U=U.*exp(1i*k*...
     ((d4_1*Mesh1').^2+(d4_2*Mesh2').^2).*(1/(2*(do2+do3-z_last))-1/(2*do3)));
157. U(((d4_1*Mesh1').^2+(d4_2*Mesh2').^2)<r34_min^2)=0;
158. U(((d4_1*Mesh1').^2+(d4_2*Mesh2').^2)>r34_max^2)=0;
159. [U5,d5_1,d5_2]=C20131217_FFTFresnel_slow(U,do4,lambda,d4_1,d4_2);
160. if isempty(Image_on_ccd)
161. Image_on_ccd=abs(U5.^2);
162. Image_on_ccd_sans_obj=abs(Un.^2);
163. else
164. Image_on_ccd=Image_on_ccd+abs(U5.^2);
165. Image_on_ccd_sans_obj=Image_on_ccd_sans_obj+abs(Un.^2);
166. end
167. end
168. toc
169. if myang==1
170. Image_series(:,:,myang)=Image_on_ccd;
```

```
171. Image_proj(:,:,myang)=projA;
172. Image_series_I(:,:,myang)=Image_on_ccd_sans_obj;
173. else
174. Image_series(:,:,myang)=Image_on_ccd;
175. Image_proj(:,:,myang)=projA;
176. Image_series_I(:,:,myang)=Image_on_ccd_sans_obj;
177. end
178. end
179. %%%%%%%%%%%%%%%%%%%%%%%
180. % STORES THE TOMOGRAM %
181. %%%%%%%%%%%%%%%%%%%%%%%
182. Result_as_is=single(Image_series/(max(Image_series(:))));
183. Result_normalized_by_flatfield=Image_series./(Image_series_I+
     (Image_series_I==0));
184. Result_projection=single(Image_proj/(max(Image_proj(:))));
185. toc
186. end
```

Examples

In figure B.6, the effect of the partial coherence on a tomographic reconstruction is studied. A comparison of figure 4.9 and figure 4.7 shows that the simulation with partial coherence matches the experimental data better than the incoherent simulation.

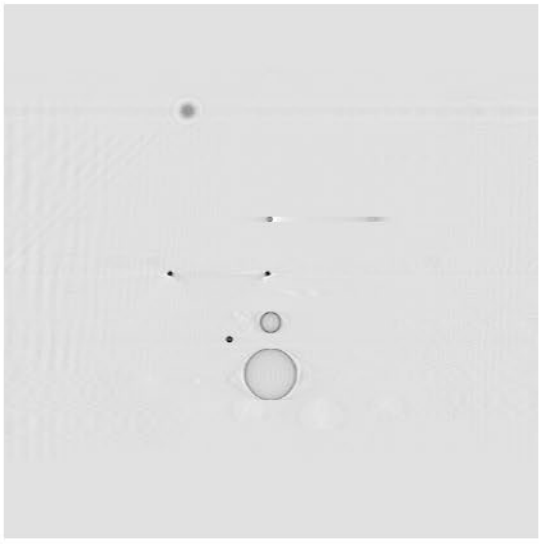

(a) xy-slice, linear projection based, tilts: -90°:1°:90°

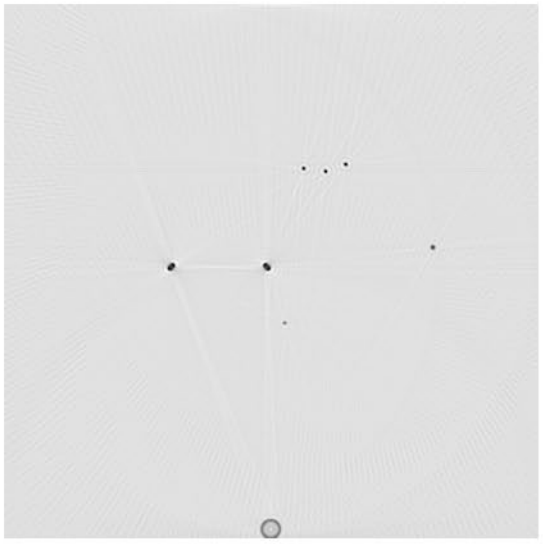

(b) xz-slice, linear projection based, tilts: -90°:1°:90°

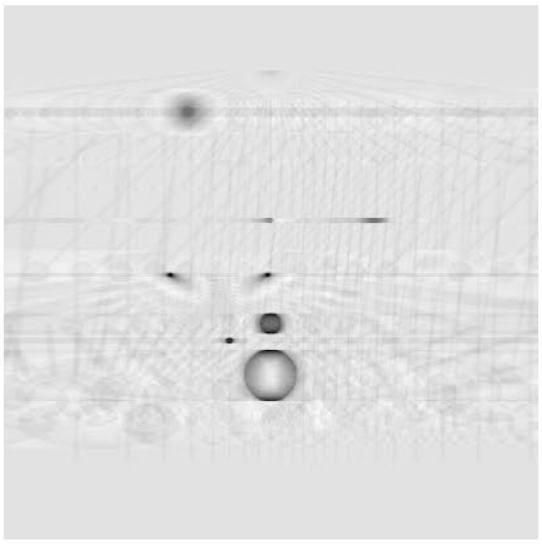

(c) xy-slice, linear projection based, tilts: -90°:6°:90°

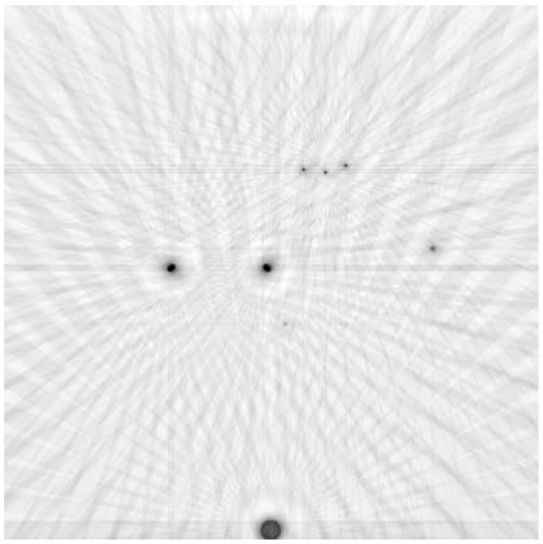

(d) xz-slice, linear projection based, tilts: -90°:6°:90°

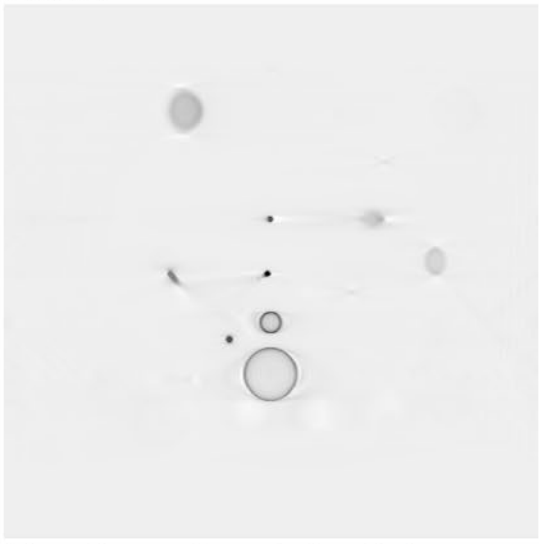

(e) xy-slice, incoherent FZP with $dr_N = 10\,nm$ based, tilts: -90°:1°:90°

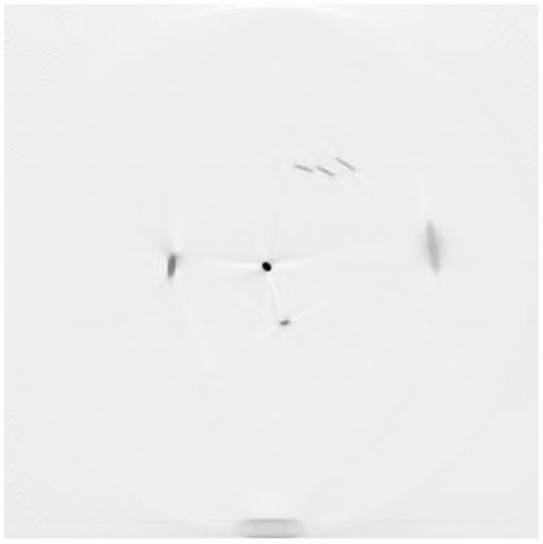

(f) xz-slice, incoherent FZP with $dr_N = 10\,nm$ based, tilts: -90°:1°:90°

Figure B.5: *Comparison of under sampling and defocus on the tomographic reconstruction. The field of view is* $3.1\,\mu m$.

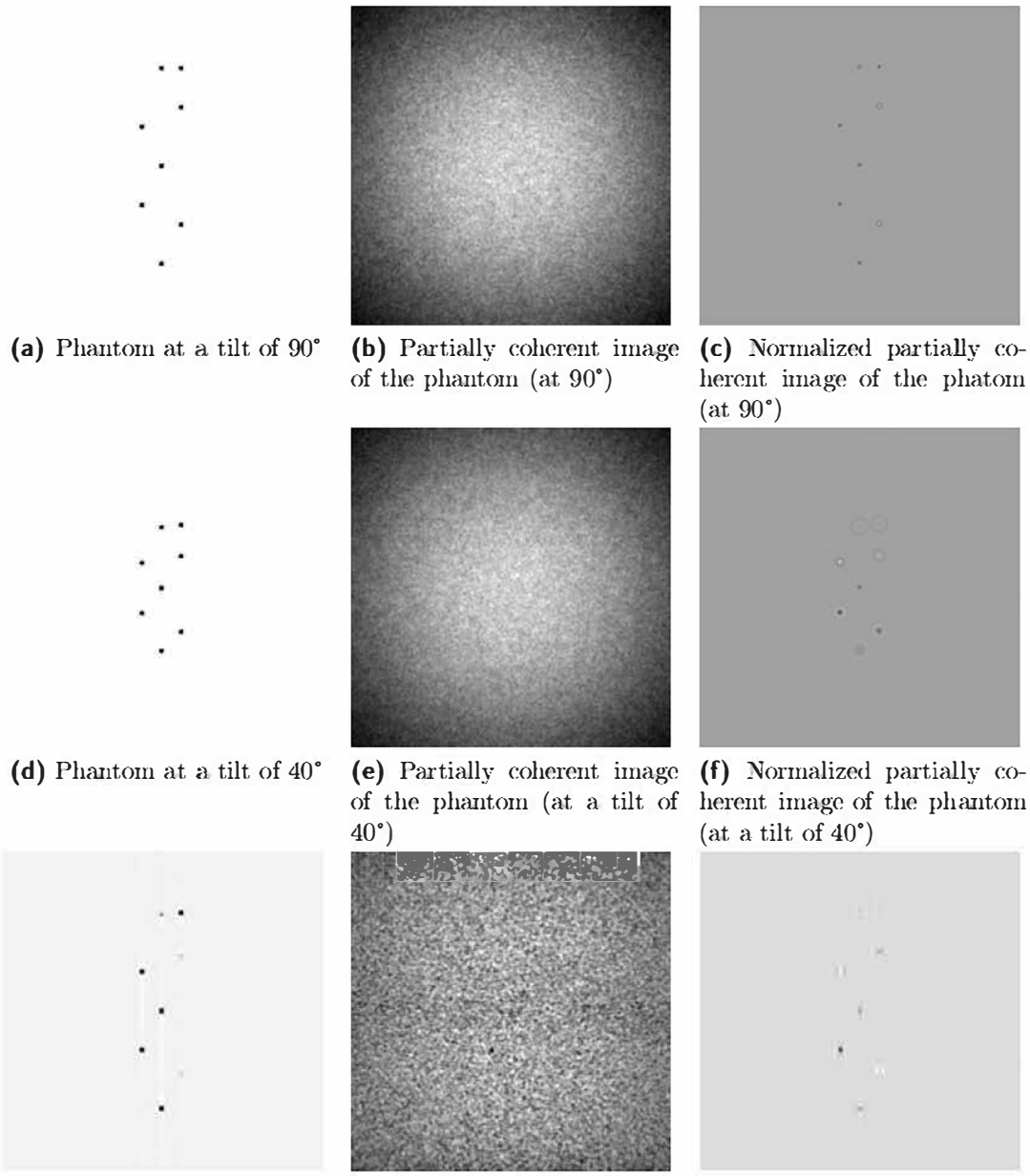

(a) Phantom at a tilt of 90°

(b) Partially coherent image of the phantom (at 90°)

(c) Normalized partially coherent image of the phatom (at 90°)

(d) Phantom at a tilt of 40°

(e) Partially coherent image of the phantom (at a tilt of 40°)

(f) Normalized partially coherent image of the phantom (at a tilt of 40°)

(g) Slice (XZ) of the tomographic reconstruction of the phantom

(h) Slice (XZ) of the tomographic reconstruction of the phantom from a -90°:1°:90° partially coherent image series.

(i) Slice (XZ) of the tomographic reconstruction from a -90°:1°:90° normalized partially coherent image series.

Figure B.6: *These examples show that the partial coherence leads to significant changes in the image of a sample in comparison to the incoherent approximation. The interpretation of the images is problematic due to contrast inversion. Surprisingly, the reconstruction works also for the unnormalized images although the object is almost invisible in the images of the tilt series. The most likely explanation is that the noise in the partially coherent image series is uncorrelated and hence its impact on the reconstruction is reduced.*
The partial coherence was taken into account by averaging over random source distributions. The normalized images were divided by the intensity pattern generated without sample.

Appendix C

Phase Unwrapping and Generating DOEs

C.1 Phase Unwrapping

Program C.1 implements the unweighted least-squares phase unwrapping algorithm presented on page 111. Due to the use of Matlab®, the discrete versions of ϕ and ψ now start at 1 instead of 0. They also end respectively at $N+1$ and $M+1$ instead of N and M. They are hence defined as $\phi^{Matlab} : \{1, 2, \ldots, N+1\} \times \{1, 2, \ldots, M+1\} \to \mathbb{R}$ and $\psi^{Matlab}\{1, 2, \ldots, N+1\} \times \{1, 2, \ldots, M+1\} \to (-\pi, \pi]$ with $\arg\left[\exp\left[i\phi^{Matlab}\right]\right] = \psi^{Matlab}$. The mirror reflection has to change accordingly. For example, the mirror reflection of ψ is

$$\tilde{\psi}_{i,j} = \begin{cases} \psi_{i,j} & 1 \leq i \leq M+1,\ 1 \leq j \leq N+1 \\ \psi_{2M+2-i,j} & M+1 < i < 2M+1,\ 1 \leq j \leq N+1 \\ \psi_{i,2N+2-j} & 1 \leq i \leq M+1,\ N+1 < j < 2N+1 \\ \psi_{2M+2-i,2N+2-j} & M+1 < i < 2M+1,\ N+1 < j < 2N+1. \end{cases}$$

The following notations are used in the program.

psi is the discrete version of ψ.

psi_big is the discrete version of the extension by mirror reflection of ψ.

rho is the discretised version of ρ.

PHI_FT is the discrete least-squares approximation of ϕ.

Line 1 is the function header.
Line 2 defines the extension by mirror reflection of ψ.

Line 3 initializes rho, which is a discrete version of ρ.
Line 4 defines rho. There are different discrete versions of the base equation $\triangle\phi = \rho$. A five point star version is

$$\tilde{\rho}_{i,j} = \left(\tilde{\Delta}^{x}_{i,j} - \tilde{\Delta}^{x}_{i-1,j}\right) + \left(\tilde{\Delta}^{y}_{i,j} - \tilde{\Delta}^{y}_{i,j-1}\right).$$

The corresponding implementation is:

```
rho=(mod((psi_big(:,[2:end 1 ])-psi_big)+pi,2*pi)-pi...
-mod((psi_big-psi_big(:,[end 1:end-1]))+pi,2*pi)+pi...
+mod((psi_big([2:end 1],:)-psi_big)+pi,2*pi)-pi...
-mod((psi_big-psi_big([end 1:end-1],:))+pi,2*pi)+pi)
```

A nine point version of the same equation is used in the implementation shown here.
Line 5 computes the fast Fourier transform of $\tilde{\rho}$.
Line 6 uses the symmetry of rho to eliminate some numerical artifacts by restriction to the real part of P.
Line 7 computes $\Phi_{m,n} = \frac{P_{m,n}}{2\cos[\pi m/M]+2\cos[\pi n/N]-4}$.
Line 8 sets $\Phi[1,1] = 0$.
Line 9 computes the inverse Fourier transform of Φ.
Line 10 restricts the result to the original format.

Fast Fourier transform based unweighted least-squares phase unwrapping.

1. `function PHI_FT=fft_unwrap(psi)`

2. ```
   psi_big=...
   [psi,psi(:,(end-1):-1:2);psi((end-1):-1:2,:),psi((end-1):-1:2,(end-1):-1:2)];
   ```

3. `rho=zeros(size(psi_big));`

4. ```
   rho=(mod((psi_big(:,[2:end 1 ])-psi_big)+pi,2*pi)-pi...
   -mod((psi_big-psi_big(:,[end 1:end-1]))+pi,2*pi)+pi...
      +mod((psi_big([2:end 1],:)-psi_big)+pi,2*pi)-pi...
      -mod((psi_big-psi_big([end 1:end-1],:))+pi,2*pi)+pi)/2 ...
      +(mod((psi_big([2:end 1 ],[2:end 1 ])-psi_big)+pi,2*pi)-pi...
      -mod((psi_big-psi_big([end 1:end-1],[end 1:end-1]))+pi,2*pi)+pi...
      +mod((psi_big([2:end 1],[end 1:end-1])-psi_big)+pi,2*pi)-pi...
      -mod((psi_big-psi_big([end 1:end-1],[2:end 1]))+pi,2*pi)+pi)/4;
   ```

5. `P=fft2((rho));`

6. `P=real(P);`

```
7. P=P./...
   (2*cos(2*pi*((0:size(P,1)-1)/(size(P,1)))'*ones(1,size(P,2)))...
   +2*cos(2*pi*(ones(size(P,1),1)*(0:size(P,2)-1)/(size(P,2))))-4);

8. P(1,1)=0;

9. PHI_FT=ifft2((P));

10. PHI_FT=real(PHI_FT(1:size(psi,1),1:size(psi,2)));

11. end
```

Scope of the Algorithm

This algorithm is useful to find least-squares approximations to the phase problem, as long as the correct field only contains regular points. That is, each path around all points results in a vanishing integrated phase. If this condition is not satisfied, the algorithm computes a field that has minimal wrapped mean square distance. One example for such an irregular point is shown in figure C.1.

If the phase contains some points with a high difference in the phase but the image contains no residues, the Fourier least-squares phase unwrapping algorithm yields locally good results but might not find a solution which is a globally close match to the image. One example is shown in figure C.2. The Itoh algorithm fails under those conditions. In fact, it is a good feature for the design of DOEs that the Fourier least-squares phase unwrapping algorithm removes any residues from the phase.

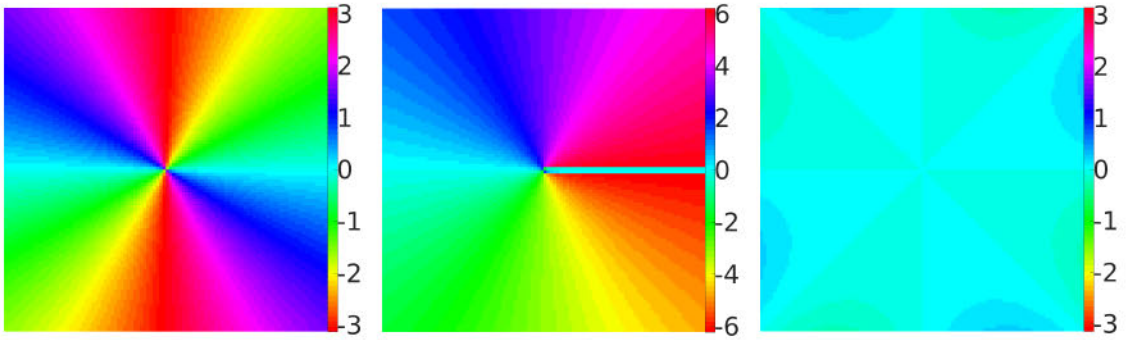

(a) original phase

(b) recovered phase with the Itoh algorithm

(c) recovered phase with the Fourier least-squares phase unwrapping algorithm

Figure C.1: The effect of residues on the Itoh and the Fourier least-squares phase unwrapping algorithm.

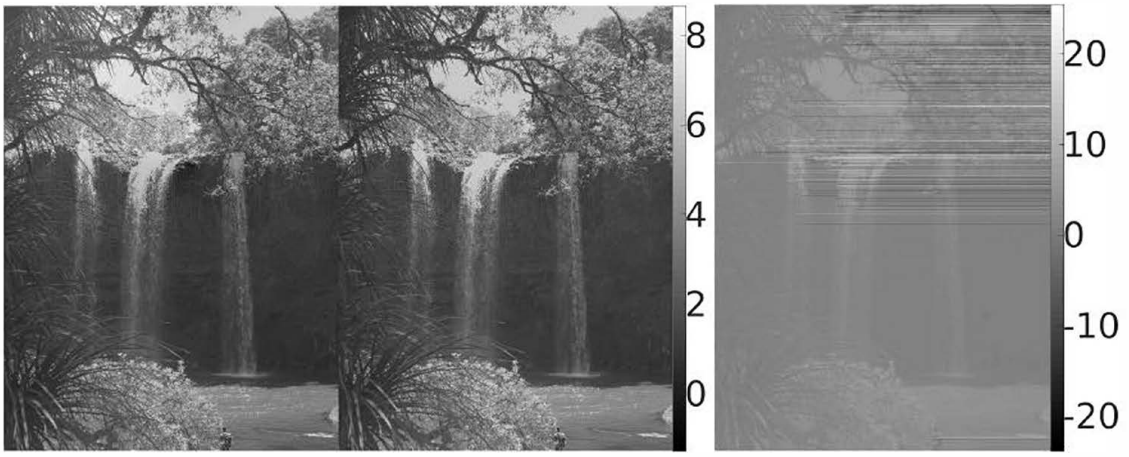

(a) Respectively original image, recovered image with least-squares and Itoh method $\Delta_{max} = 1.5\pi$

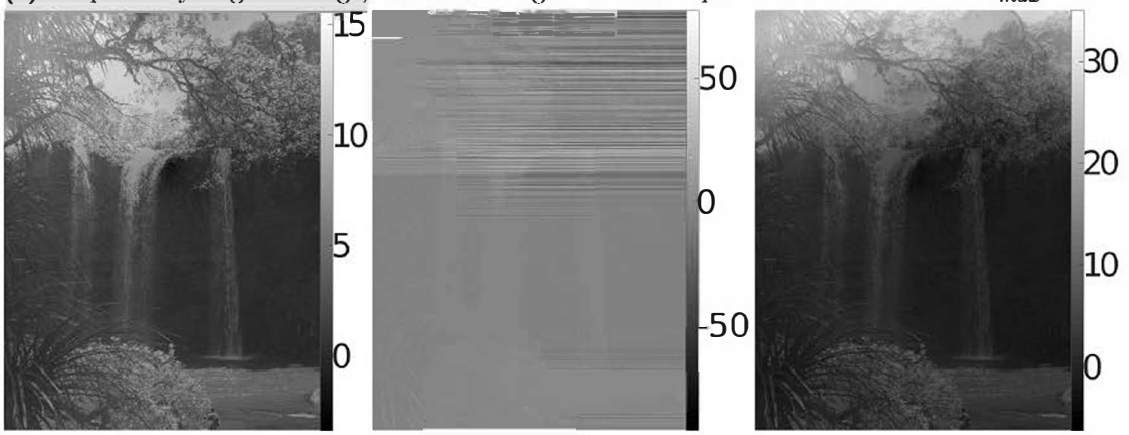

(b) recovered image $\Delta_{max} = 2\pi$ **(c)** Itoh method $\Delta_{max} = 2\pi$ **(d)** recovered image $\Delta_{max} = 3\pi$

Figure C.2: *Different examples for reconstructed ϕ from wrapped data. The Fourier transform based method and the Itoh method have been used. The maximal difference between neighboring pixels is in* **(a)** 1.5π, *in* **(b)** *and* **(c)** 2π, *and in* **(d)** 3π.

C.2 Generating DOEs Using High Orders of Diffraction

The main steps for the design of a DOE are (see also figure C.3):

1. Defining the target intensity in the focal plane of the DOE

2. Computing a holographic first estimate of the field in the plane of the DOE

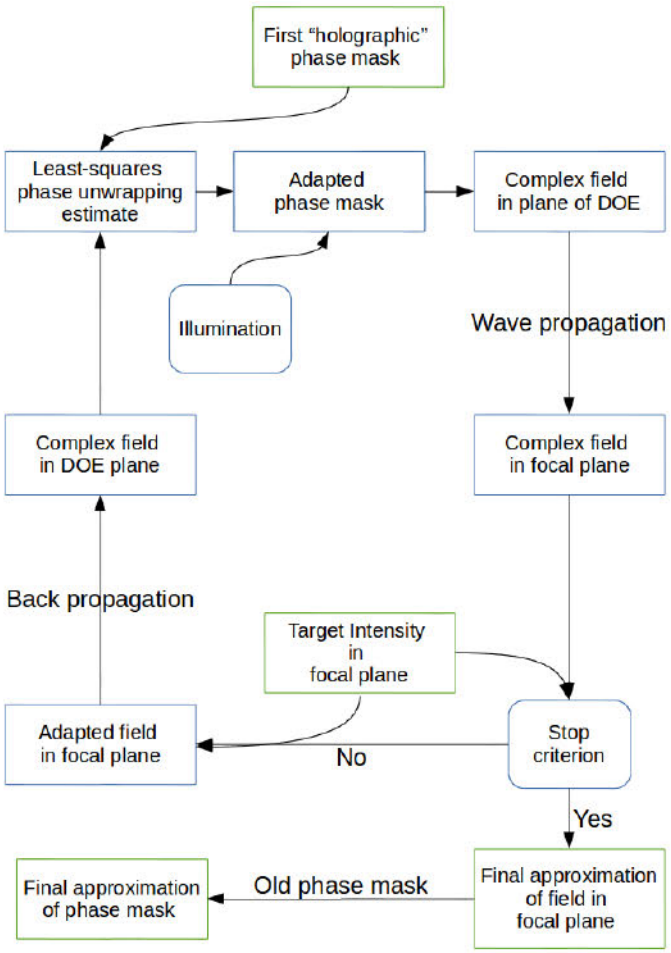

Figure C.3: *Algorithm for the design of higher order DOEs.*

3. Finding a least-squares estimate for a continuous lift of the phase in the plane of the DOE

4. Propagating the resulting field into the focal plane of the DOE

5. Adapting the computed amplitudes to amplitudes that fit better the target intensity

6. Back propagation to the plane of the DOE

7. Restarting at 3. untill a good approximation is found

The least-squares phase unwrapping algorithm is applied in the third step of this algorithm.

C.3 FTH Experiment at an XRL

An experiment at a soft X-ray laser (XRL) was conducted at the Max Born Institut (see figure C.4). The XRL was operated in grazing incidence pump (GRIP) geometry and produced coherent X-rays at 19.8 nm. It was pumped by two pulses of a high repetition rate 100 Hz thin disk laser (TDL) chirped pulse amplification (CPA) system [94]. The TDL system consisted of a front-end with a Yb:KGW oscillator, stretcher and Yb:KGW regenerative amplifier followed by two regenerative amplifiers and one multipass amplifier. The output of the front-end was divided into two pulses. Each of them was amplified in a regenerative amplifier to a level of about 100 mJ. Whereas the pulse from the first regenerative amplifier was compressed to a duration of about 200 ps using a grating compressor, the output of the second regenerative amplifier was given to a thin disk multipass amplifier which amplified the pulses to an energy of up to 400 mJ and compressed them in the grating compressor to about 2 ps pulse duration at an energy of 270 mJ. The long pulse (150 ps, E 70 mJ) was focused by a cylindrical and a spherical lens onto the target at normal incidence. The generated plasma column was then heated by the short pulse focused by a spherical mirror into the preformed plasma. We have found for our Mo slab target (50 mm length, 5 mm width) an optimum GRIP angle of about 24 degree. The target was attached to a motorized stage with four degrees of freedom allowing the adjustment along three axes as well as the continuous renewal of the target surface. The latter was important for our experiments, since we used a multi shot approach to maximize the signal to noise ratio.

The setup of the FTH experiment had to be adapted to the changed wavelength. Since we wanted to keep an outermost zone width of 50 nm, the longer wavelength of 18.9 nm resulted in a higher NA. Therefore, the focal length was drastically reduced. This was partially countered by using an 1.8 mm DOE with a focal length of 6.8 mm. Nevertheless, the distances between DOE, object and order sorting aperture are rather small. Therefore, a compact mechanical setup was needed. We solved this problem by attaching the DOE and the OSA to a common support. This support consists of a one inch Al cylinder which has recesses for the DOE, sample and OSA forming pinhole. The sample is mounted on a movable arm which allows for 3D positioning of the sample in relation to the DOE. The Al cylinder has five degrees of freedom so that we can align it with the XRL beam. The setup was designed with AutoDesk Inventor. The key components are shown

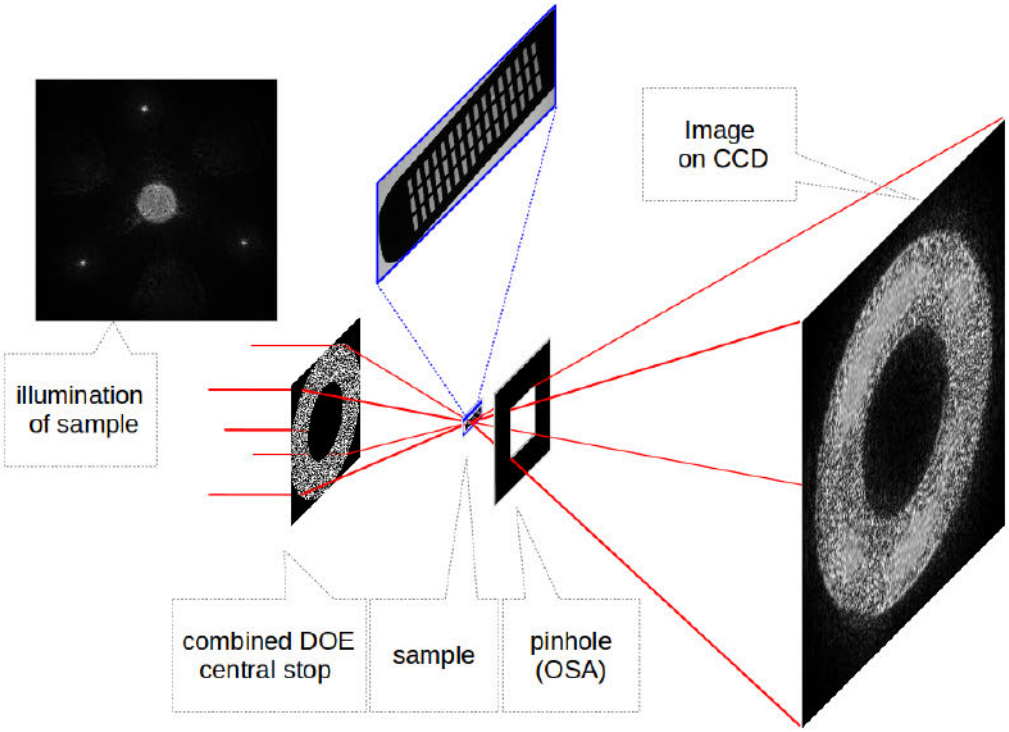

Figure C.4: *Fourier transform holography setup based on a diffractive optical element which generates three references. In this experiment, we included a pinhole between the sample and the CCD. In combination with the central stop on the DOE, this selected the order of diffraction used for imaging. We used three references to minimize and correct effects introduced by partially obscured references.*

in figure C.8. Due to the shorter wavelength, the DOE has a significantly larger NA and, therefore, we had to use the NFFA during the design process.

For this kind of experiment, we use the holders shown in figure C.5 which we also use in the TXM at the Hemlholtz Zentrum Berlin. On the holder, the sample is fixed to a thin carbon foil. The foil is between 13 and 20 nm thick and contains holes of approximately 2 µm in a 4 µm grid. Hence, it produces a small absorption ($<$10%) but good phase contrast signal at the wavelength of 19.8 nm. Numerical simulations predicted that it would be nearly impossible to see the foil in amplitude contrast. The low amplitude contrast of the foil is a desirable design parameter since it allows to image strongly absorbing objects by simply fixing them onto the foil.

For the first run of the experiment, the pure carbon foil was used as sample. Therefore, we had to find a way to get a phase contrast based imaging signal.

Again, numerical simulations were used to predict the properties of different imaging contrasts (see also figure C.6).

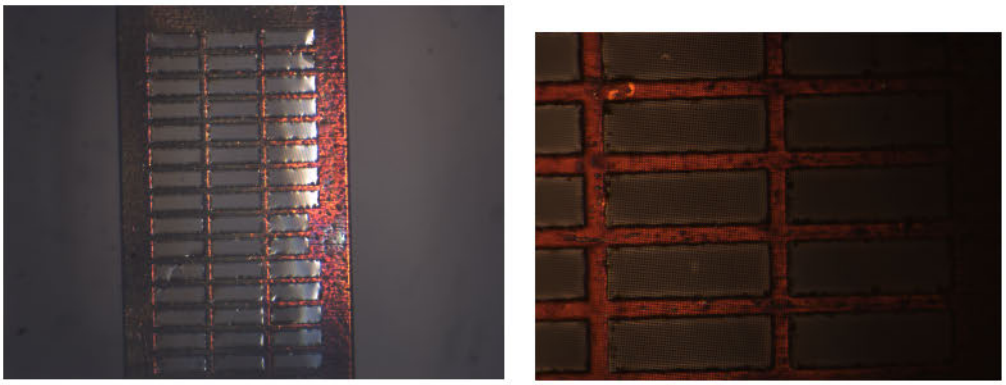

Figure C.5: *Holder for the sample and detailed view of the carbon foil. (Images taken with a light microscope.) The brighter dot is the region that was exposed to a higher X-ray dose during the experiment.*

Since the experimental setup contained no measurement of the position of the sample relative to the DOE, a method for finding the focal position had to be developed.

We used the fact that the thin carbon foil is situated on top of a coarser Au grid. The grid bars are strongly absorbing and can generate shadows on the CCD. The main idea was to look at the shadow of a bar at different defocused positions. By measuring the thickness of the shadow and applying the interception theorem, the correct focal distance can be estimated. A small correction has to be made due to the finite dimension of the image of the DOE.

In a first experiment, we saw that the nano-positioner produced so much infrared light that the X-ray signal was lost. Therefore, the nano-positioners had to be shut down during the measurements. Since the interruption of the current lead to the loss of the exact position, only a few single images were taken. One example is shown in figure C.7. In order to test the results and differentiate between numerical artifacts and real signal, the sample had to be moved in a well defined way. In a second session, we were therefore forced to include optical shielding into the experiment. Now, the positioning units could be left on during the data acquisition. Although we managed to block the infrared light produced by the attocubes, the nano-positioners did not perform with the shielding as expected. The exact problem is not known since the shielding and the moving parts of the experiment had no contact. Hence, a mechanical fault is unlikely. But we observed that with the shielding, the positioning units got very hot. This might have prevented their correct performance and also produced thermal expansion within the setup.

Conclusion

From these experiences, we deduce that the concept should in principle also work with XRLs. In order to prevent similar problems with alignment and positioning of the sample, future setups should contain some additional means to verify the correct positioning of all parts, e.g. a movable, low resolution Fresnel zone plate for direct X-ray imaging.

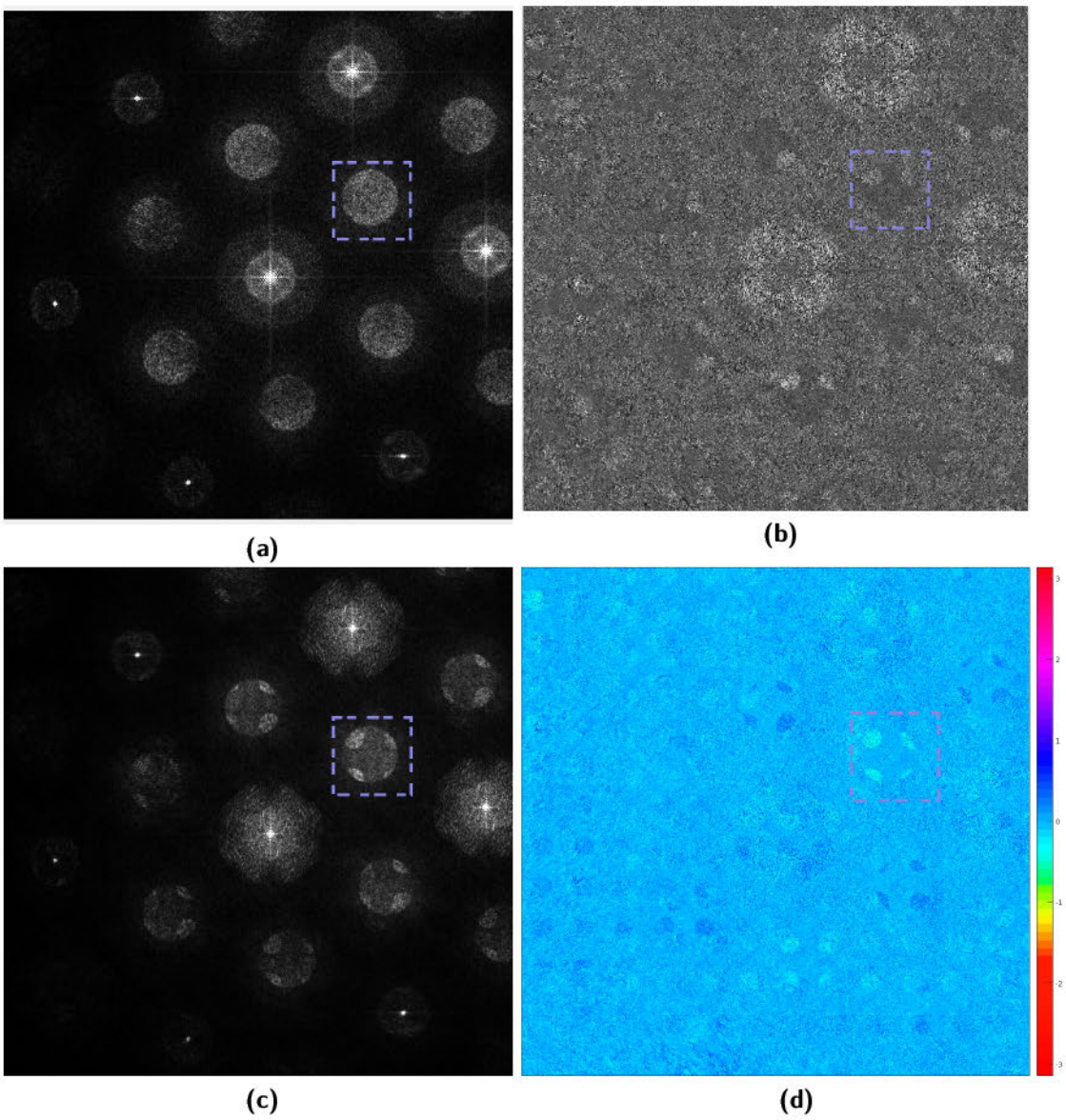

Figure C.6: *Numerically predicted images of the foil (image is in the blue square).*
(a) *Direct imaging (absorption contrast).*
(b) *Direct image divided by „flat field“ (absorption contrast).*
(c) *Phase sensitive image type I: absolute difference between direct image and „flat field“.*
(d) *Phase sensitive image type II: difference between argument of direct image and „flat field“.*

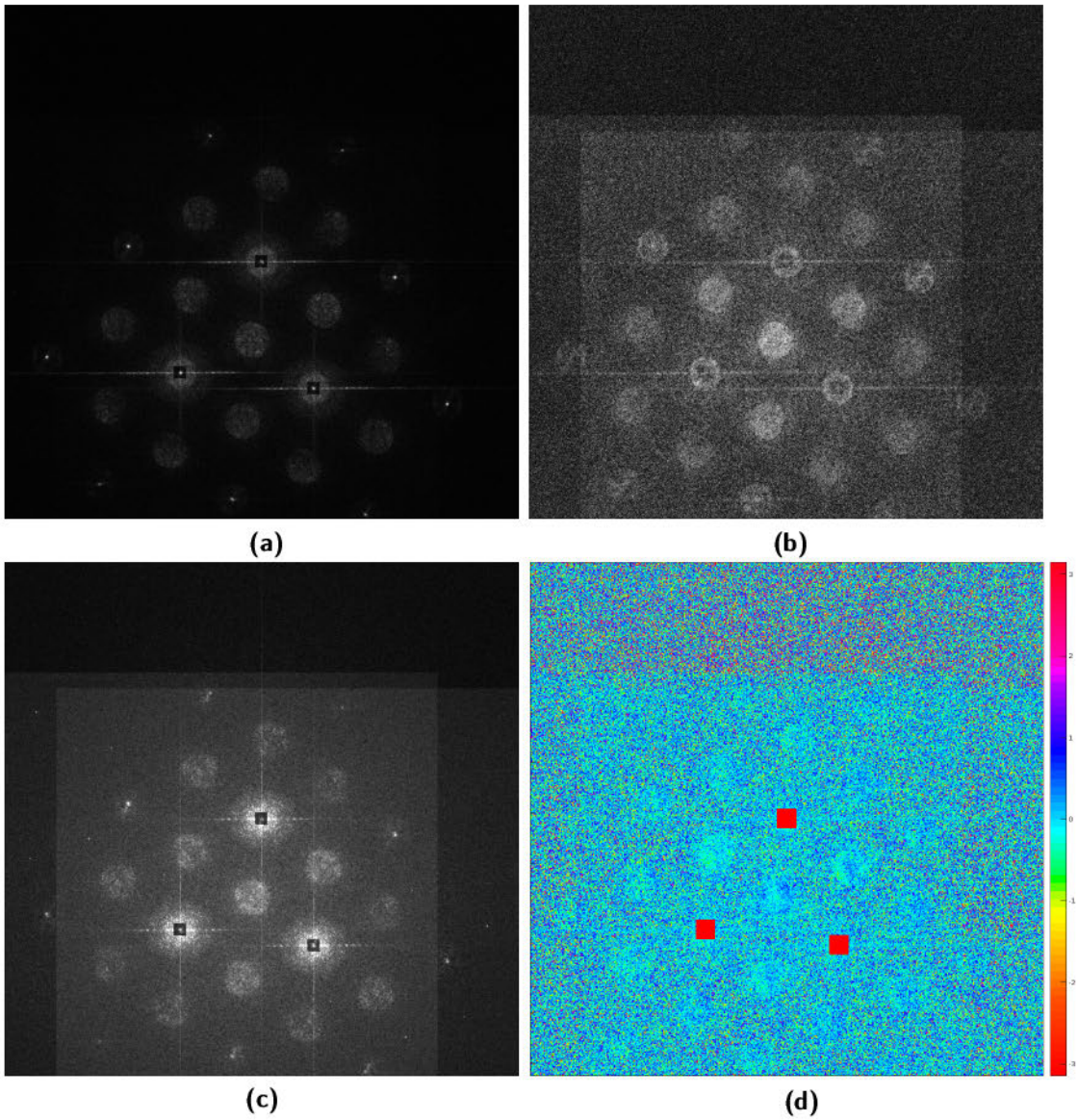

Figure C.7: *Experimental images of the foil.*
(a) *Direct imaging (absorption contrast) .*
(b) *Direct image divided by „flat field“ (absorption contrast).*
(c) *Phase sensitive image type I: absolute difference between direct image and „flat field“.*
(d) *Phase sensitive image type II: difference between argument of direct image and „flat field“.*

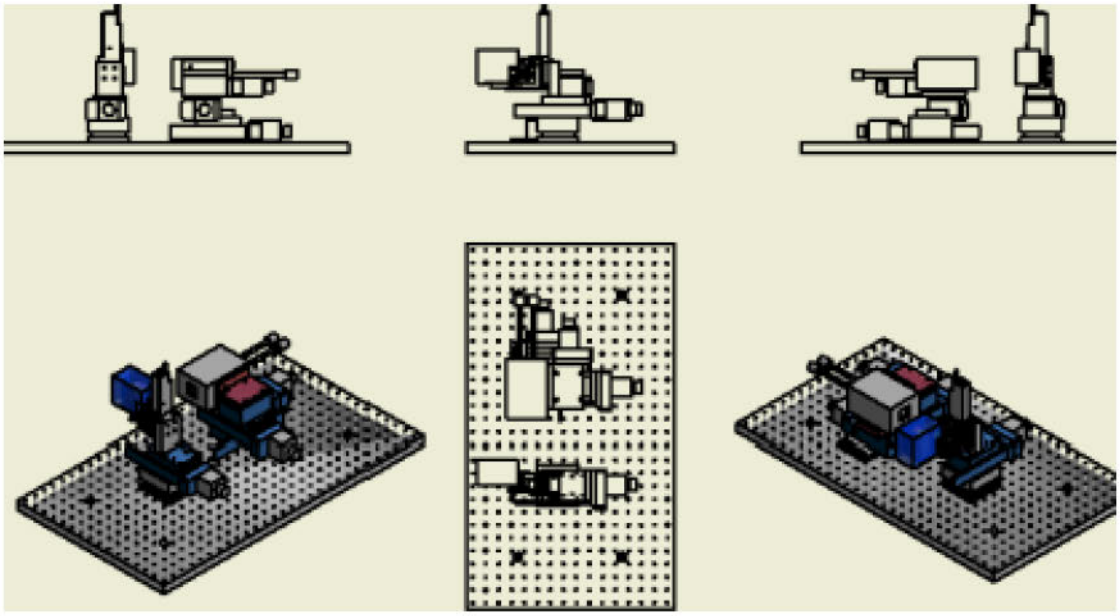

(a) Technical drawings of the experimental setup for the XRL based FTH experiment.

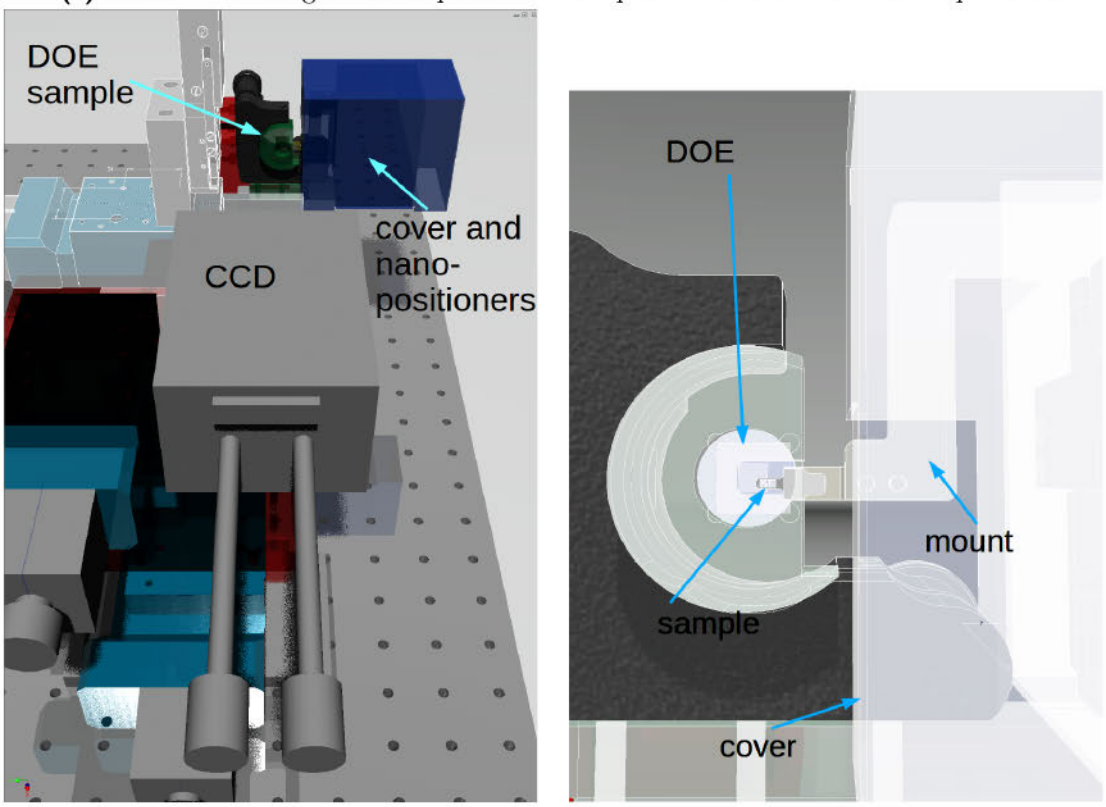

(b) 3D-rendering of selected parts of the XRL- FTH setup.

Figure C.8: *Design of the XRL based FTH experiment. The right image in figure b shows the compact combination of DOE, sample and pinhole.*

Appendix D

Potential Application of DOEs as Condensers for Transmission Microscopy

In this chapter, we present three novel, untested setups for soft X-ray imaging. Two of them potentially could improve existing contrast mechanisms and the last combines in-line holography and bright field TXM imaging. None of these setups have been implemented yet.

D.1 DOE Based Zernike Phase Contrast Imaging

Zernike phase contrast was developed for light microscopy in the early 1930's by Zernike [109]. The key idea behind Zernike phase contrast is diagrammed in figure D.1. A shift of the phase of the incident light after the light has been diffracted by the sample allows visualization of sample induced phase shifts. Its earliest implementation in soft X-ray microscopy used an annular ring condenser and a matching phase-shifting annular ring in the back-focal plane [78]. The X-ray optical setup is shown in figure D.2. New alternatives use specially designed objective Fresnel zone plates which essentially include the phase ring [101, 72]. The latter approach reduces the FOV and is therefore often not well suited for imaging extended samples.

The use of an annular ring condenser limits the light that reaches the sample and prevents the matching of the NA of condenser and objective. The opening angle of the condenser has to be relatively small since it directly correlates to the angular dimensions of the phase shifting ring. From a theoretical point of view, the limited NA of the condenser results in partially coherent image formation in this optical system, which results in artifacts due to partial coherence. Indeed,

such artifacts have been observed and partially characterized [96].

Therefore, we developed a new setup which is shown in figure D.2 (b). The key idea is to use a condenser that generates a ring shaped focus in front of the sample. This ring is then reproduced by the objective in a plane that satisfies the thin lens law. In this plane, a matching, phase shifting annular ring can be used to shift the undiffracted light with respect to the light diffracted by the sample. This ring can be significantly smaller with our approach than in the classical soft X-ray setup, thereby reducing the unwanted filtering of diffracted light. Additionally, the condenser can now be matched to the objective which reduces the impact of partial coherence effects on image formation (see also figure D.3). Therefore, this new setup minimizes artifacts present in the conventional soft X-ray Zernike phase methods.

The Construction of the Condenser for Zernike Phase Contrast.

We now show how such an annular ring condenser can be constructed. The construction is very similar to the one used for conventional Fresnel zone plates. We therefore recall the construction law for FZPs. The construction uses the rotational invariance of the system around the optical axis. One starts by calculating the optical path length between the focal point and the FZP. The path length (l) is directly related to the phase difference $(\Delta\varphi)$ incurred due to the larger propagation distance

$$\exp\left[i\Delta\varphi\right] = \exp\left[i\frac{2\pi}{\lambda}l\right].$$

Hard clipping the path length to $\left[0,\ \frac{\lambda}{2}\right]$ modulo λ yields the opaque zones of the Fresnel zone plate. The hard clipping is equivalent to selecting one half of the phase space.

The construction of the ring condenser follows a similar idea. The rotational invariance is again used. Instead of calculating the optical path length between two points, this time we use a weighted, path length based phase integral. The result is then hard clipped to $\Re > 0$ to generate the pattern of the condenser.

The path length (l) from a point (p_1) in the z_1 plane to a point (p_2) in the z_2 plane $(z_1 < z_2)$ is

$$l\left[p_1, p_2\right] := \left|p_1 - p_2\right| = \sqrt{\left|p_1 - p_2\right|^2}.$$

This distance results in a relative phase change of $\exp\left[-\frac{2\pi}{\lambda}i\left|p_1 - p_2\right|\right]$. Now, it is assumed that the point p_2 is part of the ring which the condenser generates. Let us assume that this ring has a diameter of r_2. We define for any circle (C_{r_1})

in the z_1 plane with radius $r_1 > 0$ which is centered around the optical axis, the integrated, weighted phase contribution as

$$\begin{aligned}\Phi_{p_2}[r_1] &:= \int_{C_{r_1}} \frac{\exp\left[-i\frac{2\pi}{\lambda} l\left[p_1[s], p_2\right]\right]}{l\left[p_1[s], p_2\right]} \mathrm{d}s \\ &= \int_0^{2\pi} \frac{\exp\left[-\frac{2\pi}{\lambda} i\sqrt{(z_2-z_1)^2 + r_2^2 + r_1^2 - 2r_2 \cdot r_1 \cos[\varphi]}\right]}{\sqrt{(z_2-z_1)^2 + r_2^2 + r_1^2 - 2r_2 \cdot r_1 \cos[\varphi]}} r_1 \,\mathrm{d}\varphi\end{aligned}$$

Hard clipping Φ to $\Re > 0$ generates a pattern of a condenser that produces a ring of radius r_2 at a focal length of $z_2 - z_1$. Using this condenser, the proposed Zernike contrast setup is readily implemented.

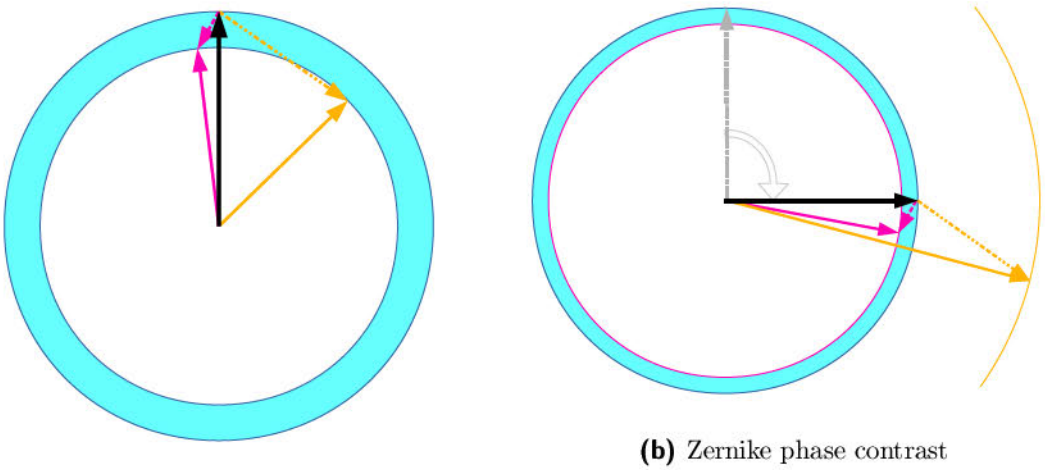

(a) Absorption contrast

(b) Zernike phase contrast

Figure D.1: *Visualization of the concept of Zernike phase contrast and comparison to absorption contrast. The total detected signal (colored arrows) is decomposed into the signal produced by the illumination (black arrow) and the signal generated by the sample (dashed arrows). The radius of the circles represents the detected amplitude. In* ***(a)****, the mechanism for absorption contrast is shown. Both samples generate the same amplitude (smaller circle). The samples are therefore indistinguishable in absorption contrast. In* ***(b)****, the concept of Zernike phase contrast is shown. The previously indistinguishable signals are now clearly separated (magenta and orange circle). This is achieved by shifting the phase of the incident illumination with respect to the signal generated by the sample.*

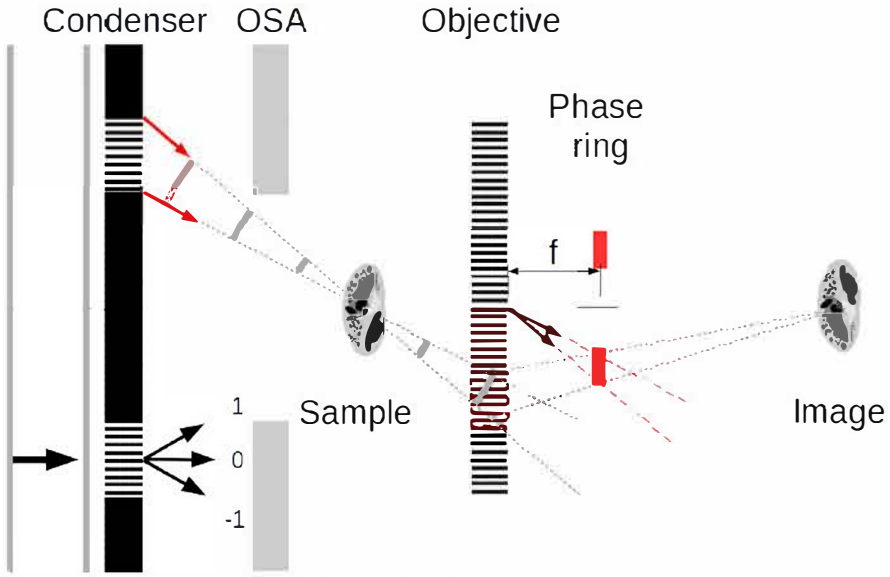

(a) Zernike phase contrast

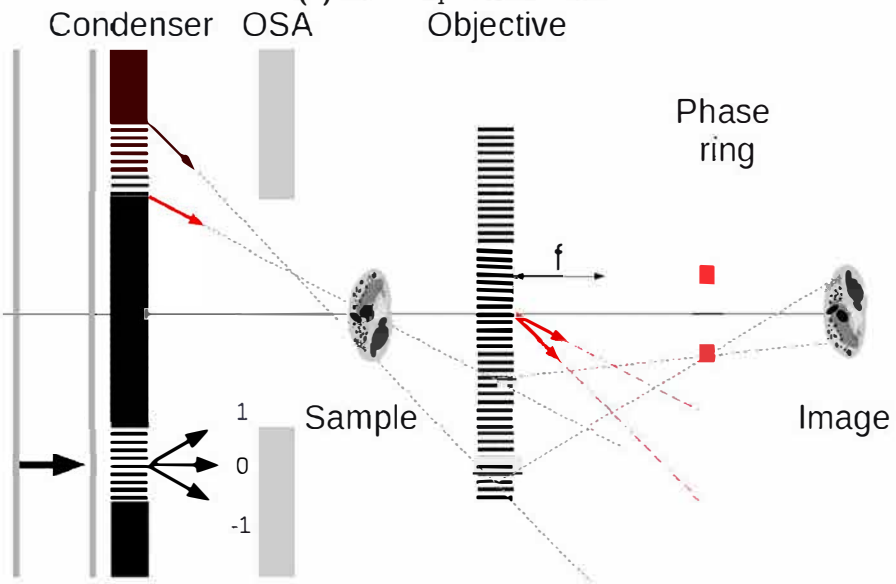

(b) Zernike phase contrast with DOE condenser

Figure D.2: *Optical setups for Zernike phase contrast.*
(a) In the classical soft X-ray implementation of Zernike phase contrast, the sample is illuminated by a ring shaped condenser zone plate. Since the distance between sample and condenser is relatively large, the ring aperture of the condenser also defines the Fourier components of the illumination as indicated by the red wave vectors. In the focal plane of the Fresnel zone plate objective, the light which was not diffracted by the sample is therefore located within the red area. A phase ring can then generate the phase shift required for Zernike phase contrast, but certain frequencies of the diffracted signal are also shifted. Alternatively, the zone positions in the red area of the objective can be switched to generate the phase shift.
(b) In this new approach, the condenser refocuses the light into a ring in front of the sample. This ring is imaged by the Fresnel zone plate. Now, a significantly smaller phase ring can be used to generate the phase shift of the non-diffracted light and the condenser can be matched to the NA of the objective eliminating effects generated by partial coherence.

D.1.1 Example for Zernike Phase Contrast

The TXM simulation presented in section B.2.3 was extended to include a phase ring. Due to the significant differences in the dimensions and resolution of the objective and its focal plane, it was not possible to use this algorithm to simulate the "classical" phase ring approach. However, for the DOE based approach, the distance between objective and phase ring is significantly larger and the difference in resolution between the plane of the phase ring and the objective is smaller. the simulation showed therefore some results, although the numerical propagators are outside their range of validity. The classical Zernike approach was here approximated by introducing the phase shift in the plane of the objective. A flat, purely phase shifting, Siemens star like object was introduced in the focal plane.

From the result, one can deduce that the method has some potential to overcome the problem of the frequency dependency of the contrast in classical Zernike phase contrast X-ray imaging.

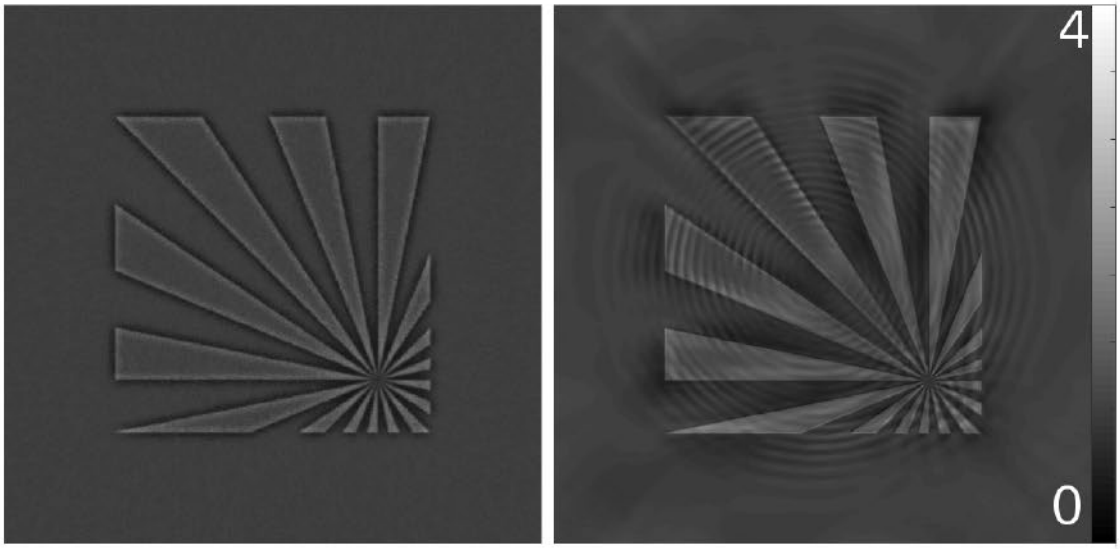

Figure D.3: Simulated Zernike phase contrast images of a phase object. The frequency dependence of the contrast in the "classical" approach shows in the large spikes (left). Strong numerical artifacts prevent a clear interpretation of the results of the new approach (right).

D.2 High Order DOEs for Dark Field TXM Imaging

Dark field imaging has proven to be a very effective tool for weakly scattering samples in light microscopy. Naturally, one would like to have this option available for full field soft X-ray microscopy. Although there have already been some implementations of dark field soft X-ray microscopy [9, 3], most of them yielded sub-optimal results. We propose here a new approach based on diffractive optical elements (DOE). This approach has the advantage of minimizing the dose on the sample and is except for the fabrication and computation of the DOE easily implemented or can easily be integrated into an existing TXM by changing the condenser. Theoretically, one could also use a capillary or Fresnel zone plate condenser with very high numerical aperture and large central stop. But these alternatives can only be used together with relatively large spatially incoherent sources or have to be moved during the exposure to generate a homogeneous illumination.

The Construction of the Condenser

The two most common ways to generate a soft X-ray dark field image are based on blocking the illumination after it has passed through the sample. This can either be done by inserting an absorbing ring into the focal plane of the objective, similar to the Zernike phase contrast setup (see figure D.2 (a)) or by blocking certain parts of the condenser as shown in figure D.4 (a).

These approaches also block certain parts of the light diffracted by the object which high pass filters the dark field image. The usual experimental implementation achieves the blocking of the illumination by restricting the illumination to a hollow cone. A problem with these approaches is that the numerical aperture of the illumination is smaller than the aperture of the objective. This leads automatically to a partially coherent imaging system. Such a system always shows artifacts which limits its usefulness. One could use a higher order FZP with a central stop and locate an objective FZP of similar outermost zone width in the core shadow of the central stop. But a classical high order, high NA condenser generates a very small focal spot. In order to use such a condenser for full field imaging, a homogeneous illumination has to be generated. This can either be accomplished by using a large incoherent source or by moving the condenser during the exposure. The latter option has to be used for undulator based sources which leads to an inhomogeneous and random illumination. Diffractive optical elements can solve this problem at the cost of lower efficiency. A setup for such a solution is presented in figure D.4.

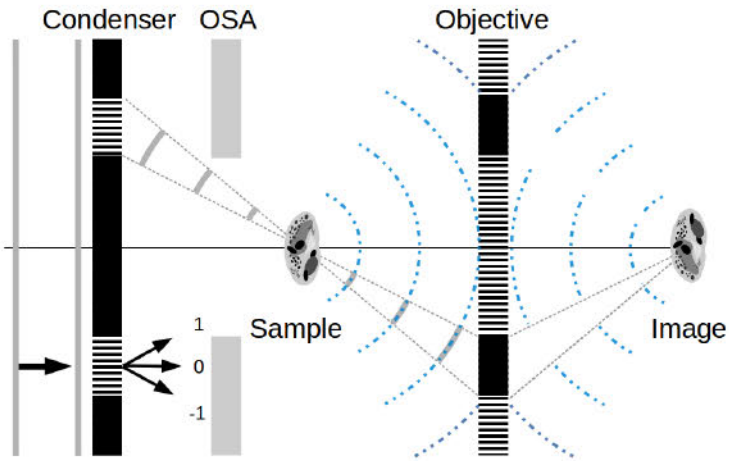

(a) Dark field as in [57, 100]

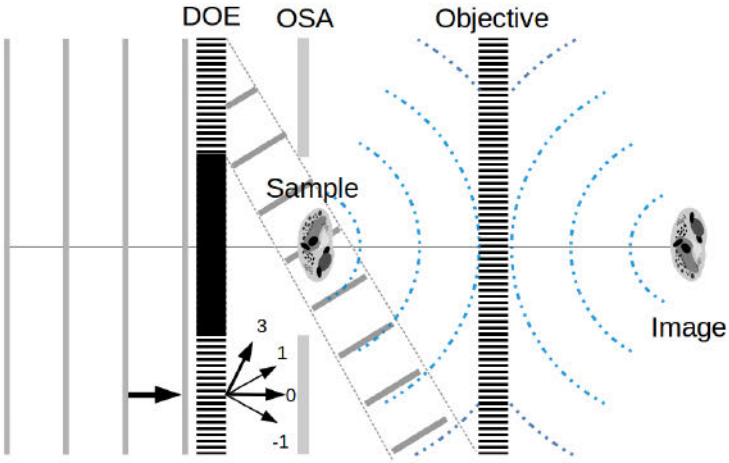

(b) Dark field based on DOE

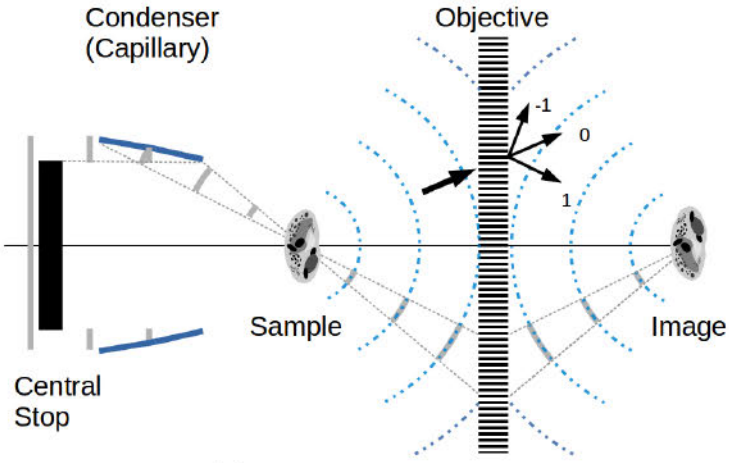

(c) Bright field TXM setup

In these sketches, the light scattered by the object is shown in blue. Grey dashed lines show the ray optical paths.
In (a), the condenser and objective use the same diffraction order. The dark field image is produced by restricting the illumination to a hollow cone and blocking the corresponding parts in the objective FZP. This also removes certain frequencies from the final image.
In (b), the sample is illuminated by using the third order of the DOE while the objective uses the first order. Therefore, all frequencies that fit into the NA of the objective are kept.
In (c), a typical TXM bright field setup is shown.

Figure D.4: *Soft X-ray dark and bright field imaging setups.* ***(a)*** *Dark field imaging based on blocked illumination,* ***(b)*** *dark field imaging based on a DOE and* ***(c)*** *bright field imaging with a capillary condenser.*

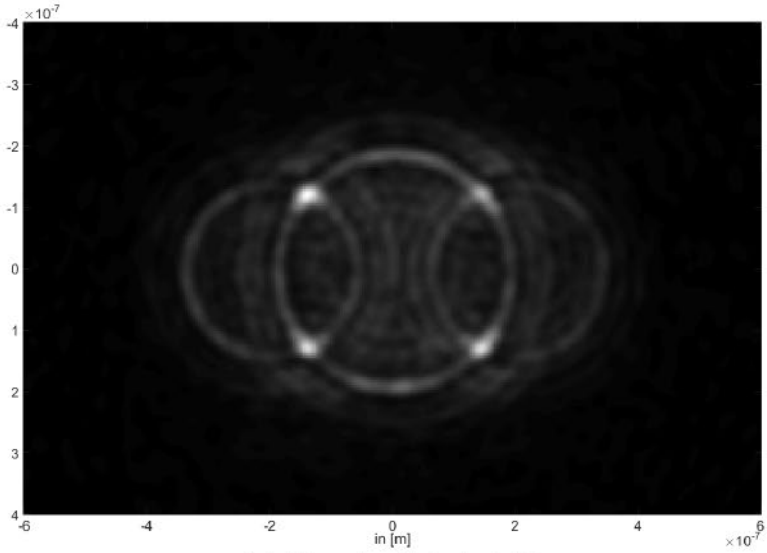

(a) "Standard" dark field

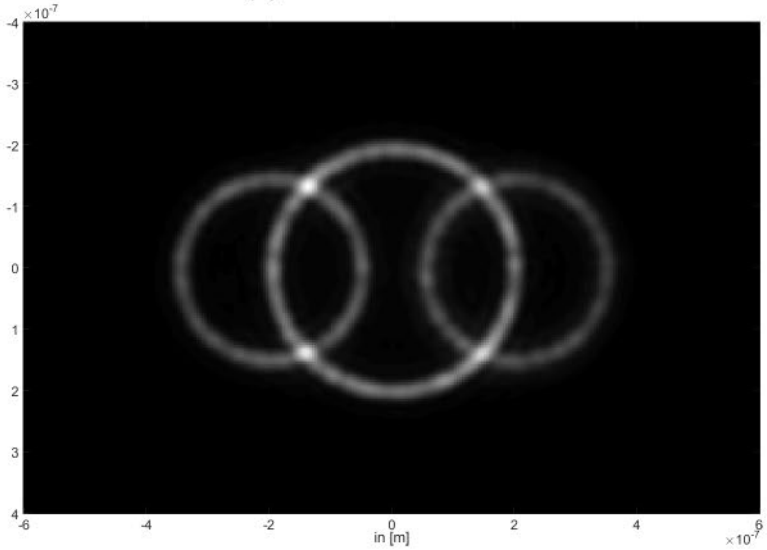

(b) DOE based dark field

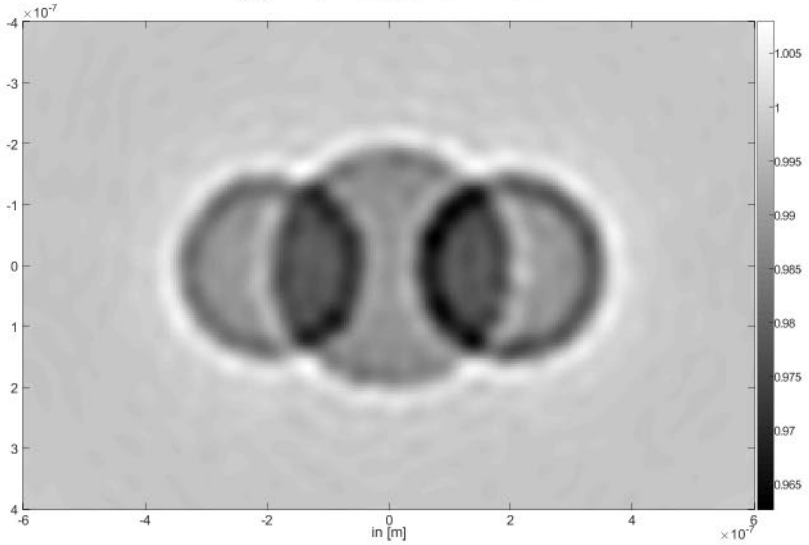

(c) TXM bright field

(a) *Dark field imaging based on blocked Fourier components,* ***(b)*** *dark field imaging based on a DOE and* ***(c)*** *bright field imaging based on a matching NA condenser. Soft X-ray dark and bright field image of three spheres. The difference in the contrast between dark and bright field imaging is obvious. The approach with a ring-like illumination leads to a blurrier dark field image (a) compared to the DOE based one (b). The same outermost zone width (25 nm) was used for all simulations.*

Figure D.5: *Simulation of soft X-ray based dark and bright field imaging.*

D.2.1 Simulation

For this simulation, we designed a binary DOE for the third order of diffraction. The pattern is generated as described in section 7.2. The aim is to generate as closely as possible a homogeneous, circular illumination. The central stop of the DOE is chosen to be large enough so that the objective Fresnel zone plate is located inside its core shadow. A pinhole between sample and DOE acts as order sorting aperture (OSA).

In this system, the condenser has a significantly larger numerical aperture than the objective zone plate. Therefore, the degree of coherence of this optical system depends mainly on the coherence of the source. The resolution should also be slightly better than in a TXM with matched NAs due to the higher numerical aperture of the condenser.

A comparison (see figure D.5) with the approach of [100] shows that the DOE based dark field generates significantly better images. The contrast also differs significantly from the one observed in a partially coherent soft X-ray transmission microscope. This method is therefore well suited as a means to differentiate objects with similar bright field images, e.g. one can use it to detect the positions of strongly scattering particles of subdiffraction limited size within a cell.

D.3 Using the Zeroth Order Transmitted Light of a FZP in TXM Imaging for In-line Holography

Currently, there are no good approaches for FEL based soft X-ray TXM imaging. We propose a setup with a novel condenser design which could be used at an FEL beamline. In addition, the limited efficiency of Fresnel zone plates, which poses a problem for Fresnel zone plate based transmission microscopy, is addressed. In transmission soft X-ray microscopy, the image is usually formed by the first diffractive order of the zone plate. This order contains only a small part (usually less than 10%) of the photons that illuminated the sample. Most photons (approximately 50%) stay in the zeroth order of diffraction. Since the radiation dose usually limits the resolution for biological samples, using these photons to increase the quality of the image is desirable. While the following approach cannot achieve this directly, it could potentially be used to improve the alignment of a tomographic series. According to the dose-fractionation theorem [35] this could also lead to a dose reduction.

The following setup combines a transmission soft X-ray microscope with a lens-less method to use a larger part of the incident photons. In this method, the condenser optic is a patchwork of squares. Each square contains a part of a

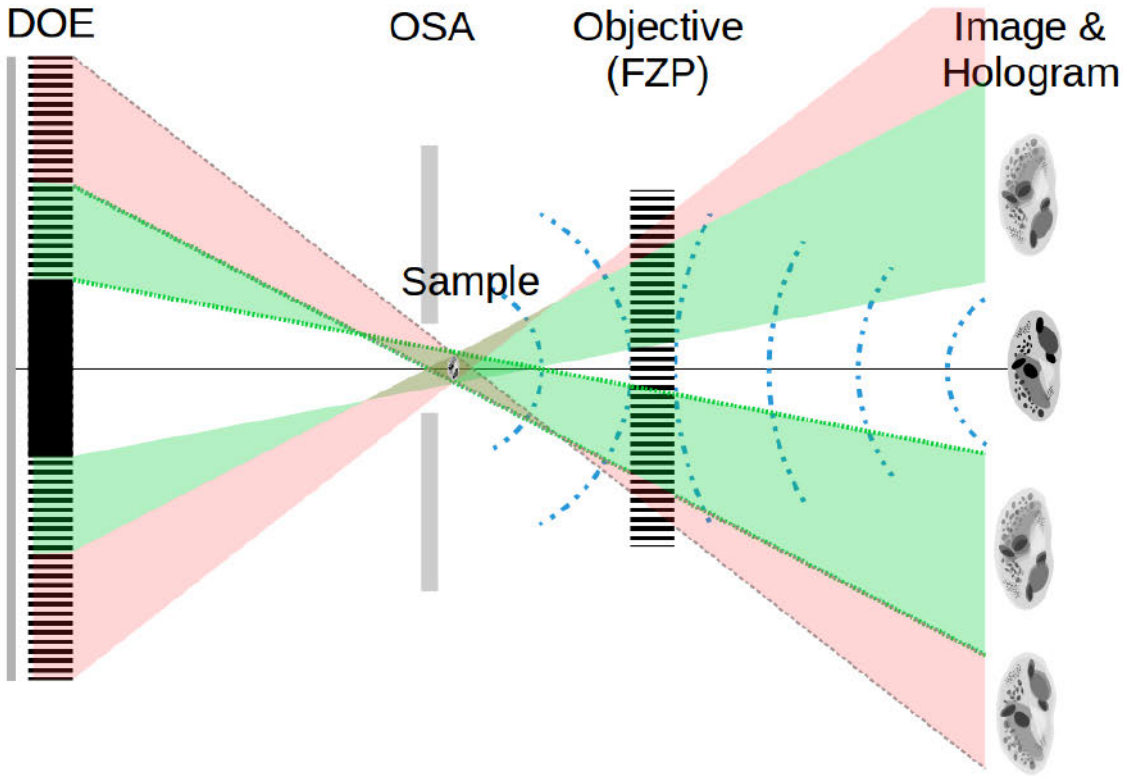

Figure D.6: *Setup for a combined in-line hologram and TXM experiment. The first order diffration of the FZP generates a regular TXM image while the non-diffracted part of the beam generates in-line holograms. Here, squares are shown alternately in red or green. These squares differ in their focal length. Due to the construction of the condenser, the sample area is almost homogeneously illuminated.*

Fresnel zone plate. The size of each FZP part is a little larger than the area that is coherently illuminated. The FZP parts alternately generate a focal point well before or behind the sample. As shown in figure D.6, the location of the focal point is chosen in such a way that the sample is fully illuminated by the beam. Since the beam patterns of the FZPs are mutually incoherent, the generated illumination is homogeneous and almost incoherent. Hence, it is well suited as illumination for transmission soft X-ray microscopy. Due to the construction, each square of the condenser generates an in-line hologram of the sample. This in-line hologram passes through the imaging high resolution FZP and can be detected in the zeroth order of the high resolution FZP. During the recording of any TXM image, several in-line holograms of the same area are generated. The zeroth order is not used in the usual TXM setup, therefore these additional holograms do not increase the dose. Since the holograms are all generated from the same area, it should

be possible to combine them to get a holographic image with slightly increased resolution.

Holographic images contain some 3D information. Therefore, the holograms could also be used in combination with fiducial markers to improve the alignment for tomographic reconstructions of the high resolution TXM data. This probably would help to make efficient use of the dose-fractionation theorem.

D.3.1 Construction of the Condenser

We now design such a condenser that consists of squares. We assume that the central area is opaque. This central stop forms an order sorting aperture in combination with a pinhole in front of the sample. We assume that the condenser homogeneously illuminates a square of width b and that each square of the condenser has an edge length of w. Let f be the distance between condenser and illuminated field. Then, the interception theorem yields two possible distances between the condenser and the focal spot, as shown in figure D.7

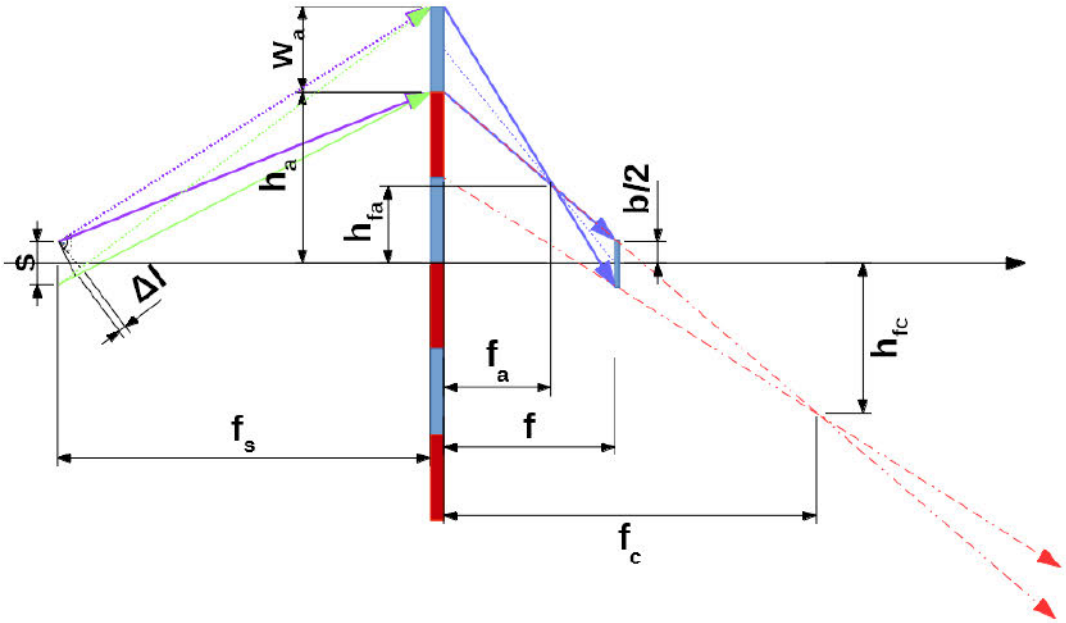

Figure D.7: *Sketch of the distances that define the pattern of the DOE.*

$$f_a = f\frac{w}{b+w}$$
$$f_c = f\left(\frac{w+b}{w}\right).$$

Here, f_a is a focus between the condenser and the illuminated field while f_c is a focus on the other side of the illuminated field. In order to illuminate the field homogeneously, each focus has to be off-axis. The exact position follows again from the interception theorem. Using the notation of figure D.7, the position is given by

$$h_{f_a} = \frac{f - f_a}{f}\left(h_a + \frac{w}{2}\right)$$
$$h_{f_c} = -\frac{f - f_c}{f}\left(h_c + \frac{w}{2}\right).$$

Example: A 3 x 3 Condenser

At the Helmholtz Zentrum Berlin, Fresnel zone plates with an outermost zone width down to $dr_N = 25\,\text{nm}$ are routinely used for TXM tomography. The FZP has a focal length of about 0.95 mm (see also table 2.1). We will now construct a matched condenser for a wavelength of $\lambda = 2.4\,\text{nm}$. At the position of the condenser, the lateral coherence length is approximately $l_c = 200\,\mu\text{m}$. Therefore, we set the width of each sub condenser part to $w = 300\,\mu\text{m}$. The field of view of the microscope is $b = 10\,\mu\text{m}$. We get the following values for our condenser:

Diameter:

$$\varnothing_{con} = 3 \cdot 300\,\mu\text{m} = 0.9\,\text{mm}.$$

Focal length:

$$f_{con} \approx \frac{\varnothing_{con}}{\varnothing_{FZP}} \cdot f_{FZP} = \frac{0.9\,\text{mm}}{0.09\,\text{mm}} \cdot 0.95\,\text{mm} = 9.5\,\text{mm}.$$

The sub-condensers have a focal length of $f_a = f_{con}\frac{w}{b+w} \approx 9.2\,\text{mm}$ respectively $f_c = f_{con}\frac{w}{w-b} \approx 9.8\,\text{mm}$.
Figure D.8 shows, that such a condenser can be realized for typical parameters of a TXM and that it generates a relatively homogeneous intensity distribution in the plane of the object. However, the simulations showed that this design leads to modulations along the edges of the illuminated square. Therefore a design which uses only the plane between the DOE and the object for all eight intermediate foci seems more favorable for TXM applications.

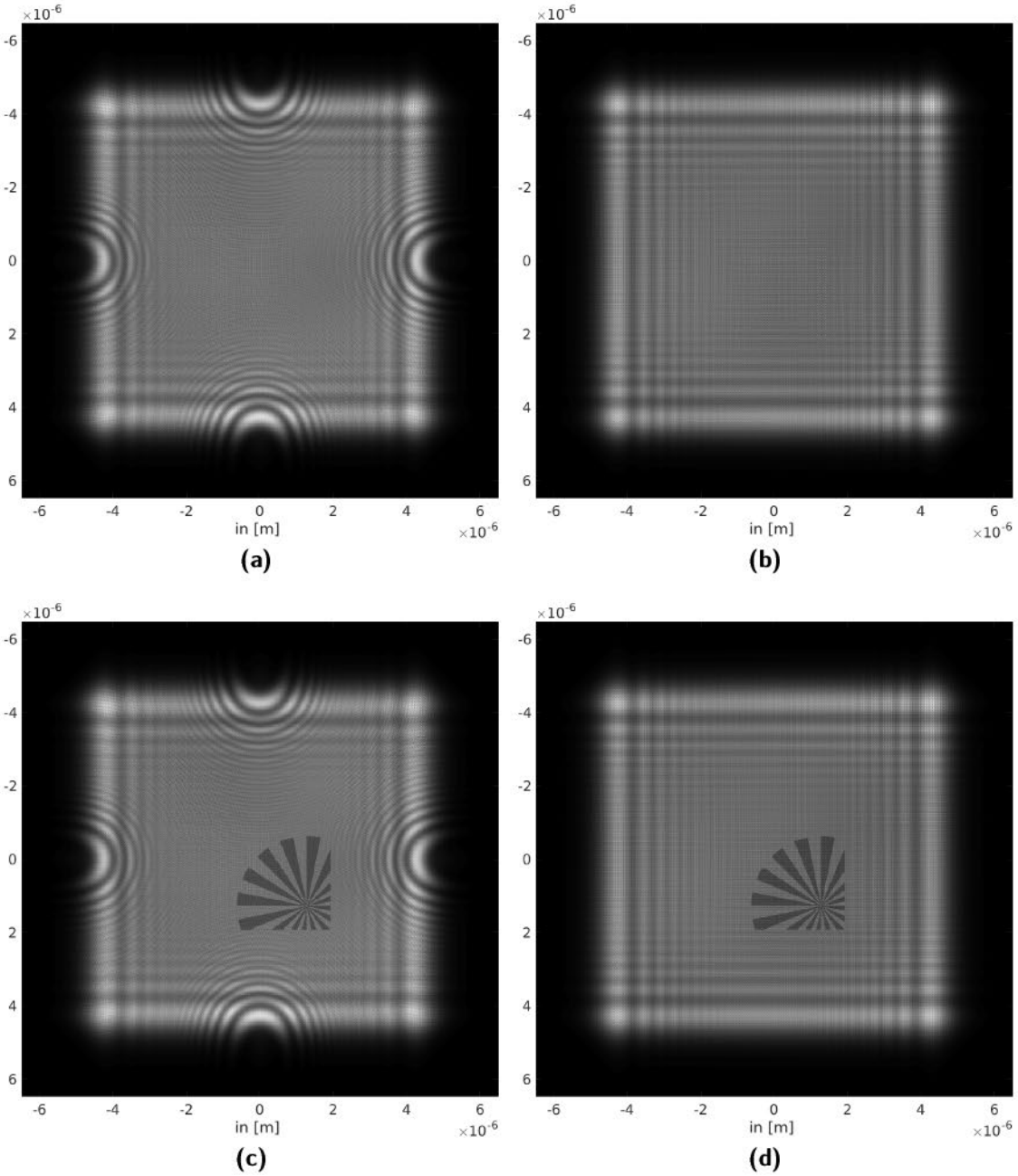

Figure D.8: *Predicted illumination in the sample area and resulting images of a Simens star based on 3×3 condensers under partially coherent conditions.*
(a, c) *using two planes as shown in figure D.7*
(b, d) *using only one plane (f_a) for the intermediate foci.*

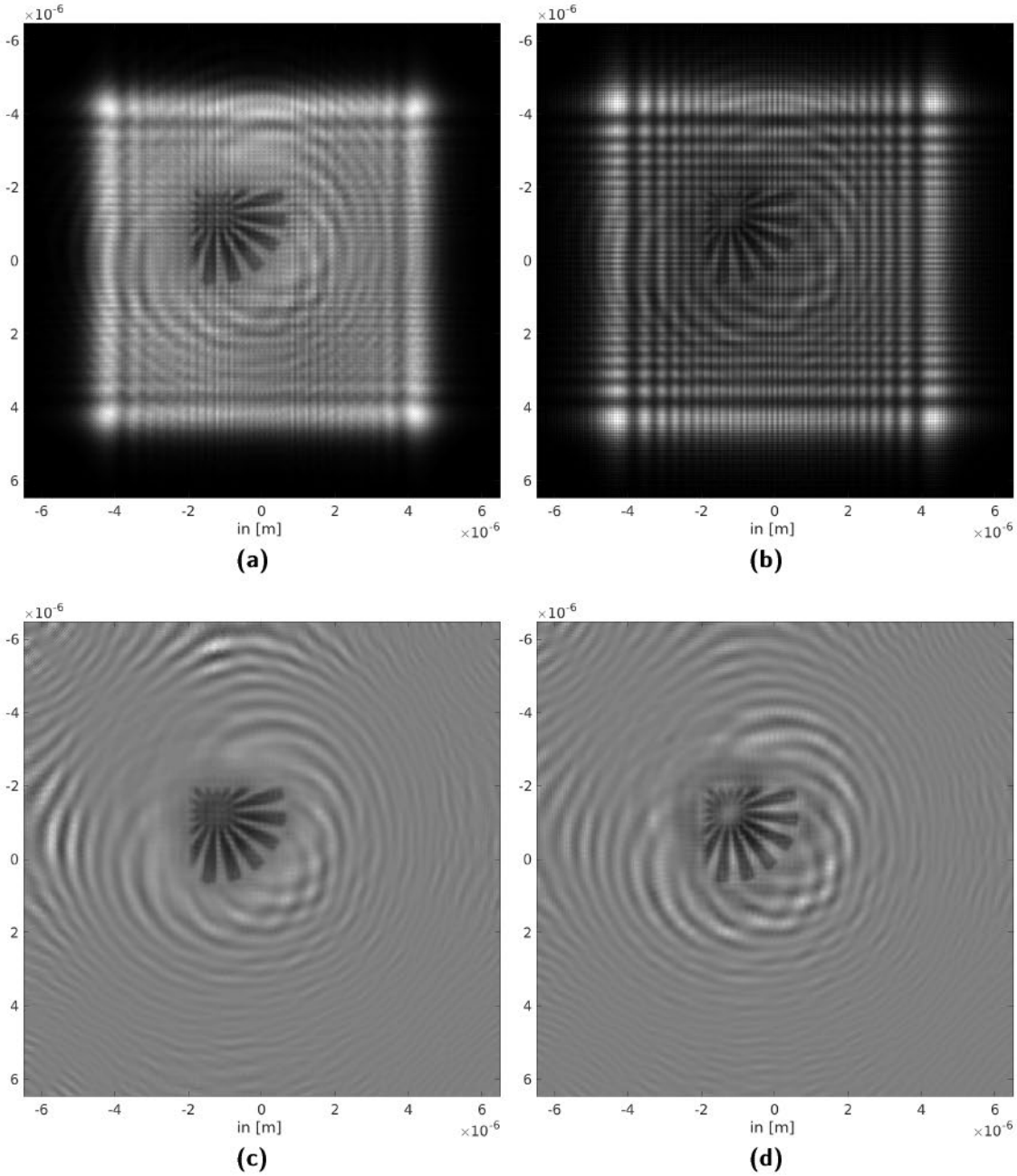

Figure D.9: *Predicted holograms based on 3×3 condensers under partially coherent conditions.*
(a) *using two planes and in* ***(c)*** *a normalization*
(b) *using only one plane* (f_a) *for the intermediate foci and in* ***(d)*** *a normalization*

Summary

In this chapter, we have introduced three new concepts for soft X-ray imaging setups. The aim of the first two is to improve existing setups for Zernike phase contrast and dark field microscopy. The third setup is based on a new condenser for full field, soft X-ray transmission microscopy. This latter setup has potentially two advantages. The condenser should improve the homogeneity of the illumination in comparison to a capillary condenser (at the cost of lower efficiency). It also allows combining TXM imaging and (low resolution) in-line holography. The holograms could be used for 3D alignment purposes. The improved alignment allows to use the dose-fractionation theorem to its full potential and could potentially reduce the dose for TXM tomography.

Appendix E

Additional Information and Programming

E.1 Generating a 3D Phantom

Code for the Simulation of the Two Phantoms

The following code produces the phantoms shown in chapter 4.

```
1. function Vergl_Phantome
2. % This function shows different phantoms in projection
3. % line + sphere
4. x=500;
5. y=500;
6. z=500;
7. dx=3e-9;
8. dy=3e-9;
9. dz=3e-9;
10. tic
11. [DOTS]=DOTGENERATORwithVOLUME(x,y,z,dx,dy,dz);
12. Phantom_DOTS=zeros(x,y,z);
13. Phantom_Voxel=zeros(x,y,z);
14. %%%%%%%%%%%%%%%%%%%%%%
```

```
% Generating the Phantom_DOTS
%%%%%%%%%%%%%%%%%%%%%%%%
vDOTS=DOTS;
vDOTS(1,:)= ceil(DOTS(1,:)/dx);
vDOTS(2,:)= ceil(DOTS(2,:)/dy);
vDOTS(3,:)=ceil(DOTS(3,:)/dz);
zDOTS=find(and(vDOTS(1,:)>0,vDOTS(1,:)<(x+1)));
vDOTS=vDOTS(:,zDOTS);
zDOTS=find(and(vDOTS(2,:)>0,vDOTS(2,:)<(y+1)));
bvDOTS=vDOTS(:,zDOTS);
for my_big_z=1:100:z %coarse z-steps
zDOTS=find(and(bvDOTS(3,:)>my_big_z-1,bvDOTS(3,:)<my_big_z+100));
vDOTS=bvDOTS(:,zDOTS);
for myz=my_big_z:min(z,my_big_z+99)% start fine steps
try
zDOTS=find(vDOTS(3,:)==myz);
mypreSlice=accumarray(...
{[1 y vDOTS(2,zDOTS)],...
[1 x vDOTS(1,zDOTS)]},...
[0 0 vDOTS(4,zDOTS)]);
myvolSlice=accumarray(...
{[1 y vDOTS(2,zDOTS)],...
[1 x vDOTS(1,zDOTS)]},...
[0 0 vDOTS(6,zDOTS)]);
myprevolSlice=myvolSlice/(dx*dy*dz);
mySlice(myvolSlice>1)=mypreSlice(myvolSlice>1)./myvolSlice(myvolSlice>1);
myvolSlice(myvolSlice>1)=1;
```

```
42. try
43. mySlice(myz,:,:)=mypreSlice;
44. catch err
45. 'ups'
46. rethrow(err);
47. end
48. catch err
49. 'ups'
50. rethrow(err);
51. end
52. if or(any(zDOTS~=0),or(myz==z,myz==1))
53. end
54. end % singel z-step
55. end % coarse z-steps
56. Phantom_DOTS=mySlice;
57. toc
58. projA=squeeze(sum(mySlice,1));
59. figure(2)
60. imagesc(imag(projA))
61. drawnow
62. %%%%%%%%%%%%%%%%%%%%%%%%
63. % Generating the Phantom_DOTS
64. %%%%%%%%%%%%%%%%%%%%%%%%
65. % Generating a full cylinder
66. % Starting Point
67. %%%%%%%%%%%%%%%%%%%%%%%%
68. %Initialization:
```

```
69. % Starting Point
70. fcx=dx*x*[0.3 ];
71. fcy=dy*y*[0.5 ];
72. fcz=dz*z*[0.5 ];
73. %direction (in real space)
74. fdcx=[1 ];
75. fdcy=[0 ];
76. fdcz=[1 ];
77. fds=sqrt(fdcz.^2+fdcy.^2+fdcx.^2);
78. fdcz=fdcz./fds;
79. fdcy=fdcy./fds;
80. fdcx=fdcx./fds;
81. %Radius [nm]
82. frc=[10 ]*10^-9;
83. % Length start
84. flcs=[-100 ]*10^-9;
85. % Length end
86. flc=[300 ]*10^-9;
87. % optical density (Chromatin)
88. fdoc=(-0.000836149149+ 1i*0.000156815062)*ones(size(flc));
89. fdoc310=(- 0.00229999027+ 1i*0.00062734884)*ones(size(flc));
90. [X,Y]=meshgrid(1:y,1:x);
91. for vz=1:z
92. TL=((dx.*X-fcx).*fdcx+(dy.*Y-fcy).*fdcy+(dz.*vz-fcz).*fdcz)<flc;
93. TL(TL)=((dx.*X(TL)-fcx).*fdcx+...
94. (dy.*Y(TL)-fcy).*fdcy+(dz.*vz-fcz).*fdcz)>flcs;
95. STL=((dx.*X(TL)-fcx).*fdcx+(dy.*Y(TL)-fcy).*fdcy+(dz.*vz-fcz).*fdcz);
```

```
TL(TL)=((dx.*X(TL)-STL.*fdcx-fcx).^2+(dy.*Y(TL)-STL.*fdcy-fcy).^2...
+(dz.*vz-STL.*fdcz-fcz).^2)<frc^2;
myzwPhantom=squeeze(Phantom_Voxel(:,:,vz));
myzwPhantom(TL)=myzwPhantom(TL)+fdoc;
Phantom_Voxel(:,:,vz)=myzwPhantom;
end
% Generating a hollow spheres %
% Center
hsmx=dx*x*[0.5];
hsmx=hsmx+[0.5 ]*10^-9;
hsmy=dy*y*0.5*ones(size(hsmx));
hsmz=dz*z*0.3*ones(size(hsmx));
hsmz=hsmz+[0 ]*10^-9;
hsmz(1)=dz*z*0.5;
%outer Radius
hsrco=[100 ]*10^-9;
%inner Radius
hsrci=hsrco-4*10^-9;
% optical density (membranes)
hsdoc=(-0.000909493479+ 1i*0.000211989463)*ones(size(hsrco));
hsdoc310=(-0.00186587463+ 1i*0.00114491396)*ones(size(hsrco));
for vz=1:z
TL=((dx.*X-hsmx).^2+(dy.*Y-hsmy).^2+(dz.*vz-fcz).^2)<hsrco^2;
TL(TL)=((dx.*X(TL)-hsmx).^2+(dy.*Y(TL)-hsmy).^2+(dz.*vz-fcz).^2)>hsrci^2;
myzwPhantom=squeeze(Phantom_Voxel(:,:,vz));
myzwPhantom(TL)=myzwPhantom(TL)+hsdoc;
Phantom_Voxel(:,:,vz)=myzwPhantom;
```

```
123. end
124. toc
125. projA2=squeeze(sum(Phantom_Voxel,1));
126. projA=squeeze(sum(Phantom_DOTS,2));
127. figure(1)
128. imagesc(imag([((projA2(100:400,100:400))).',projA(100:400,100:400)]));
129. colormap gray;axis off
130. figure(2)
131. projB2=squeeze(sum(Phantom_Voxel,3));
132. projB=squeeze(sum(Phantom_DOTS,1));
133. imagesc(imag([projA2(100:400,100:400).',projA(100:400,100:400);...
134. projB2(100:400,100:400),projB(100:400,100:400)]));
135. colormap gray;axis off;axis image
136. drawnow
137. end

138. function [DOTS]=DOTGENERATORwithVOLUME(x,y,z,dx,dy,dz)
139. % Generates point object (DOTS)
140. %
141. DOTS=[];
142. vDOTS=DOTS;
143. %% Generating a sphere of radius rz and with center hsmx,hsmy,hsmz
144. %%%%%%%%%%%%%%%%%%%%%%%%%%%%
145. % Sets of hollow spheres %
146. %%%%%%%%%%%%%%%%%%%%%%%%%%%%
147. % Center
148. hsmx=dx*x*[0.5];
149. hsmx=hsmx+[0.5 ]*10^-9;
```

```
150. hsmy=dy*y*0.5*ones(size(hsmx));
151. hsmz=dz*z*0.3*ones(size(hsmx));
152. hsmz=hsmz+[0 ]*10^-9;
153. hsmz(1)=dz*z*0.5;
154. %outer Radius
155. hsrco=[100 ]*10^-9;
156. %inner Radius
157. hsrci=hsrco-4*10^-9;
158. % optical densety (membranes)
159. hsdoc=(-0.000909493479+ 1i*0.000211989463)*ones(size(hsrco));
160. hsdoc310=(-0.00186587463+ 1i*0.00114491396)*ones(size(hsrco));
161. Vdis=(1)*10^-27; %"Volume" of one dot
162. Ndis=ceil(4/3*pi*(hsrco.^3-hsrci.^3)./Vdis);
163. mysphere=@(r,vphi,vpsi,hsmx,hsmy,hsmz,hsdoc,hsdoc310) ...
164. [r.*cos(vphi).*cos(vpsi)+hsmx;...
165. r.*(sin(vphi).*cos(vpsi))+hsmy;...
166. r.*(sin(vpsi))+hsmz; hsdoc*ones(size(vphi));hsdoc310*ones(size(vphi))] ;
167. % adding the sphere to the dots:
168. for myi=1:size(hsmx,2)
169. SA=mysphere((((hsrco(myi)^3-hsrci(myi)^3).*rand(1,Ndis(myi)))+...
     hsrci(myi)^3).^(1/3),...
170. 2*pi*rand(1,Ndis(myi)),asin(2*rand(1,Ndis(myi))-1),...
171. hsmx(myi),hsmy(myi),hsmz(myi),((Vdis)/(dx*dy*dz))*hsdoc(myi),...
172. ((Vdis)/(dx*dy*dz))*hsdoc310(myi));
173. DOTS=[DOTS [SA; Vdis*ones(1,size(SA,2))]];
174. end
175. %%%%%%%%%%%%%%%%%%%%%%%%%%
176. % Sets of full cylinders % (Chromatin)
```

```
177. %%%%%%%%%%%%%%%%%%%%%%%%%
178. %Initialization:
179. % Starting Point
180. fcx=dx*x*[0.3 ];
181. fcy=dy*y*[0.5 ];
182. fcz=dz*z*[0.5 ];
183. %direction (in real space)
184. fdcx=[1 ];
185. fdcy=[0 ];
186. fdcz=[1 ];
187. fds=sqrt(fdcz.^2+fdcy.^2+fdcx.^2);
188. fdcz=fdcz./fds;
189. fdcy=fdcy./fds;
190. fdcx=fdcx./fds;
191. %Radius [nm]
192. frc=[10 ]*10^-9;
193. % Length start
194. flcs=[-100 ]*10^-9;
195. % Length end
196. flc=[300 ]*10^-9;
197. % optical density (Chromatin)
198. fdoc=(-0.000836149149+ 1i*0.000156815062)*ones(size(flc));
199. fdoc310=(- 0.00229999027+ 1i*0.00062734884)*ones(size(flc));
200. % volume leads to number of points:
201. Ndis=ceil(2*pi*(frc.^2.*(flc-flcs))./Vdis);
202. focx=(fdcy+((fdcy.^2+fdcx.^2)==0))./...
203. (sqrt(fdcy.^2+fdcx.^2)+((fdcy.^2+fdcx.^2)==0));
```

```
204. focy=(-fdcx)./(sqrt(fdcy.^2+fdcx.^2)+((fdcy.^2+fdcx.^2)==0));
205. focz=zeros(size(focy));
206. fobx=focy.*fdcz-focz.*fdcy;
207. foby=focz.*fdcx-focx.*fdcz;
208. fobz=focx.*fdcy-focy.*fdcx;
209. for a=1:size(fobz,2)
210. % Checks for orthonormal frame!
211. FG=[fdcx(a) fobx(a) focx(a);fdcy(a) foby(a) focy(a);fdcz(a) fobz(a) focz(a)];
212. disp(a)
213. disp( FG*FG')
214. end
215. mycylinder=@(focx,focy,focz,fobx,foby,fobz,fcx,fcy,fcz,fdcx,fdcy,fdcz,...
216. fls,fdoc,fdoc310,vphi,vr) ...
217. [vr.*(sin(vphi)*focx+cos(vphi)*fobx)+fcx+fls*fdcx;...
218. vr.*(sin(vphi)*focy+cos(vphi)*foby)+fcy+fls*fdcy;...
219. vr.*(sin(vphi)*focz+cos(vphi)*fobz)+fcz+fls*fdcz;...
220. fdoc*ones(size(vphi));fdoc310*ones(size(vphi))];
221. for myi=1:size(fcx,2)
222. SA=mycylinder(focx(myi),focy(myi),focz(myi),fobx(myi),foby(myi),fobz(myi),...
223. fcx(myi),fcy(myi),fcz(myi),fdcx(myi),fdcy(myi),...
224. fdcz(myi),(flc(myi)-flcs(myi))*rand(1,Ndis(myi))+flcs(myi),...
225. ((Vdis)/(dx*dy*dz))*fdoc(myi),((Vdis)/(dx*dy*dz))*fdoc310(myi),
     2*pi*rand(1,Ndis(myi)),...
226. sqrt(frc(myi)^2*rand(1,Ndis(myi))));
227. DOTS=[DOTS [SA; Vdis*ones(1,size(SA,2))]];
228. end
229. end
```

E.2 Properties of the Fourier Transform

E.2.1 Fourier Transform

Definition (2D):

$$\begin{aligned} \mathcal{F}\left[g_{[x,y]}\right][v,w] &:= \int_{\mathbb{R}^2} g[x,y] \exp\left[-2\pi i\ (xv+yw)\right] \mathrm{d}x\,\mathrm{d}y \\ \mathcal{F}^{-1}\left[G_{[v,w]}\right][x,y] &:= \int_{\mathbb{R}^2} G[v,w] \exp\left[2\pi i\ (xv+yw)\right] \mathrm{d}v\,\mathrm{d}w \end{aligned} \tag{E.1}$$

Properties

1. Symmetry: (E.2)

$$\mathcal{F}\left[\mathcal{F}\left[g_{[x,y]}\right]\right][x,y] = g[-x,-y] \tag{E.2}$$

2. Asymmetry with conjugation:

$$\overline{\mathcal{F}\left[g_{[x,y]}\right]}[\xi] = \mathcal{F}\left[\overline{g}_{[x,y]}\right][-\xi] \tag{E.3}$$

and

$$\mathcal{F}^{-1}\left[\overline{G}_{[v,w]}\right][\xi] = \overline{\mathcal{F}^{-1}\left[G_{[v,w]}\right]}[-\xi] \tag{E.4}$$

Proof:

$$\begin{aligned} \mathcal{F}\left[g_{[x,y]}\right][v,w]: &= \int_{\mathbb{R}^2} g[x,y] \exp\left[-2\pi i\ (xv+yw)\right] \mathrm{d}x\,\mathrm{d}y \\ |\text{use } :v \to -\hat{v};\ w \to -\hat{w} &= \int_{\mathbb{R}^2} g[x,y] \exp\left[2\pi i\ (x\hat{v}+y\hat{w})\right] \mathrm{d}x\,\mathrm{d}y \\ &= \int_{\mathbb{R}^2} g[x,y] \overline{\exp\left[-2\pi i\ (x\hat{v}+y\hat{w})\right]} \mathrm{d}x\,\mathrm{d}y \\ &= \overline{\int_{\mathbb{R}^2} \overline{g[x,y]} \exp\left[-2\pi i\ (x\hat{v}+y\hat{w})\right] \mathrm{d}x\,\mathrm{d}y} \\ &= \overline{\mathcal{F}\left[\overline{g}_{[x,y]}\right][-v,-w]} \end{aligned}$$

Proof:

$$\begin{aligned}
\mathcal{F}^{-1}\left[\overline{G}_{[v,w]}\right][x,y] &= \overline{\int_{\mathbb{R}^2} \overline{G}[v,w]\exp\left[2\pi\, i\ (xv+yw)\right]\mathrm{d}v\,\mathrm{d}w} \\
&= \overline{\int_{\mathbb{R}^2} G[v,w]\exp\left[-2\pi\, i\ (xv+yw)\right]\mathrm{d}v\,\mathrm{d}w} \\
|\mathtt{use}: x\to-\hat{x};\ y\to-\hat{y} &= \overline{\int_{\mathbb{R}^2} G[v,w]\exp\left[2\pi\, i\ (\hat{x}v+\hat{y}w)\right]\mathrm{d}v\,\mathrm{d}w} \\
&= \overline{\mathcal{F}^{-1}\left[G_{[v,w]}\right]}[-x,-y]
\end{aligned}$$

3. Conjugation due to inversion:

$$\mathcal{F}\left[g_{[x,y]}\circ -Id_{[x,y]}\right][\xi] = \overline{\mathcal{F}\left[\overline{g}_{[x,y]}\right]}[\xi] \tag{E.5}$$

Proof:

$$\begin{aligned}
\mathcal{F}\left[g_{[x,y]}\circ -Id\right][v,w]: &= \int_{\mathbb{R}^2} g[-x,-y]\exp\left[-2\pi\, i\ (xv+yw)\right]\mathrm{d}x\,\mathrm{d}y \\
|\mathtt{use}: x\to-\hat{x};\ y\to-\hat{y} &= \int_{\mathbb{R}^2} g[\hat{x},\hat{y}]\exp\left[2\pi\, i\ (\hat{x}v+\hat{y}w)\right]\mathrm{d}\hat{x}\,\mathrm{d}\hat{y} \\
&= \int_{\mathbb{R}^2} g[\hat{x},\hat{y}]\,\overline{\exp\left[-2\pi\, i\ (\hat{x}v+\hat{y}w)\right]}\mathrm{d}\hat{x}\,\mathrm{d}\hat{y} \\
&= \overline{\int_{\mathbb{R}^2} \overline{g}[\hat{x},\hat{y}]\exp\left[-2\pi\, i\ (\hat{x}v+\hat{y}w)\right]\mathrm{d}\hat{x}\,\mathrm{d}\hat{y}} \\
&= \overline{\mathcal{F}\left[\overline{g}_{[x,y]}\right][v,w]}
\end{aligned}$$

4. Convolution theorem: (also holds for $\mathcal{F}^{-1}$ instead of $\mathcal{F}$)

$$\begin{aligned}
\mathcal{F}\left[g_{[x,y]}\cdot h_{[x,y]}\right] &= \mathcal{F}[g]*\mathcal{F}[h] \\
\mathcal{F}\left[g_{[x,y]}* h_{[x,y]}\right] &= \mathcal{F}[g]\cdot\mathcal{F}[h]
\end{aligned} \tag{E.6}$$

therefore,

$$\begin{aligned}
\mathcal{F}^{-1}\left[g_{[x,y]}\cdot h_{[x,y]}\right] &= \mathcal{F}^{-1}[g]*\mathcal{F}^{-1}[h] \\
\mathcal{F}^{-1}\left[g_{[x,y]}* h_{[x,y]}\right] &= \mathcal{F}^{-1}[g]\cdot\mathcal{F}^{-1}[h]
\end{aligned}$$

E.2.2 Properties of the Convolution

Commutative $f * g = g * f$

Associative $f * (g * h) = (f * g) * h$

Distributive $f * (g + h) = f * g + f * h$

Associative with scalar multiplication $a(f * g) = (af) * g$

Conjugation $\overline{f * g} = \overline{f} * \overline{g}$

E.3 Excerpt of Applied Theorems

E.3.1 Blackwell-Girshick Equation

Let N be a random variable with values in $\mathbb{N}$ and let $(X_i)_{i=1,2...}$ be a family of random variables which are independently, identically distributed. Furthermore, let the variances of X_1 and N be finite. Under these conditions the Blackwell-Girshick equation can be used to calculate the variance of $Y := \sum_{i=1}^{N} X_i$. The variance is then:

$$Var[Y] = Var[N]\, E[X_1]^2 + E[N]\, Var[X_1].$$

E.3.2 Wald's Equation

Let N be a random variable with values in $\mathbb{N}$ and let $(X_i)_{i=1,2...}$ be a family of random variables which are independently, identically distributed. Then Wald's equation can be used to calculate the expected value of $Y := \sum_{i=1}^{N} X_i$. The expected value is then:

$$E[Y] = E[N]\, E[X_1].$$

E.3.3 Taylor Expansions for the Moments of Functions of Random Variables

Let X be a random variable which has finite moments. Let f be a function of X. Furthermore let f be sufficiently differentiable. Then the first moment of $f[X]$ is

approximated by

$$\begin{aligned}\mathbb{E}[f[X]] &\approx \mathbb{E}\left[f[\mathbb{E}[X]] + f'[\mathbb{E}[X]](X - \mathbb{E}[X]) + \frac{1}{2}f''[\mathbb{E}[X]](X - \mathbb{E}[X])^2\right] \\ &= f[\mathbb{E}[X]] + \frac{1}{2}f''[\mathbb{E}[X]]\,Var[X].\end{aligned}$$

With the same assumptions the variance of $f[X]$ can be approximated by

$$Var[f[X]] \approx (f'[\mathbb{E}[X]])^2\,Var[X].$$